GHENT UNIVERSITY
FACULTY OF ENGINEERING AND ARCHITECTURE

UNIVERSITY OF LIÈGE
FACULTY OF APPLIED SCIENCES

MASTER'S DISSERTATION

FORMULATION OF A MACRO-ELEMENT FOR SUCTION CAISSON FOUNDATIONS UNDER AXIAL TENSILE LOAD

Graduation Studies conducted for obtaining the Master's Degree in Civil Engineering by Gilles CORMAN

Promotors: Prof. Adam Bezuijen — UGent
Prof. Frédéric Collin — University of Liège

Academic year 2016 - 2017

This thesis is dedicated to my Grandmother,
Thank you for having inspired me since my really first steps.

Acknowledgements

Throughout the progression of this master dissertation, I have benefited from the direct or indirect support of many persons. I would like to seize the opportunity of these few lines to show them my gratitude.

First of all, I would like to thank all the members of my committee, who took time to read this work, and especially my two promotors Prof. F. Collin and Prof. A. Bezuijen for making this joint adventure possible. Their guidance from near or far all along this thesis has allowed me to move forward serenely in my work.

Then, I would like to express my sincere acknowledgements to Benjamin Cerfontaine, for the long moments he spent even on weekends and public holidays to answer my questions, to put me on the right track and to help me master the computation software. This availability, patience and supervising at all times played a significant role in reaching the final result.

Apart from the academic circle, I would like to address particular thanks to my friends from university. It was a pleasure to benefit from mutual support during these years of master and to learn my future job with them. Special mention to the team of room -1/440 for the warm atmosphere that prevailed during these few working weeks.

I was given the opportunity to complete my studies in Ghent which was a rewarding experience to improve my language skills and to develop myself. I would like to give credit to all the people I met there for having made this language stay an unforgettable page of my life.

Last but not least, I will never thank my family enough for their support and their encouragements during this master dissertation, and throughout my entire academic path. Above all, the complicity with my brother, which remained intact no matter the distance that separated us, was not only an unconditional and unwavering support but also a source of confidence, strength, and motivation.

Thanks to all of them for having guided me in the right direction.

Gilles Corman,
7th June 2017

Summary

Abstract in English

Nowadays, the ongoing electricity demand along with environmental concerns and the search for energy autonomy have been setting the basis for a global development of renewable energies. Among these sources, offshore wind power shows an attractive potential. With the increasing number of wind farms put in place further away from the coastline and in deeper waters, innovative foundation systems are required to guarantee the economic viability of offshore projects. In this context, suction caissons emerge as a suitable and cost-effective solution, and are therefore extensively studied to come up with optimised design strategies. This thesis investigates the behaviour of suction caissons in clay under a vertical tensile load that may arise from specific environmental conditions. The aim is to develop a simplified design method for this specific case. To achieve this target, a 2D numerical study of suction caissons is performed by using the finite element software LAGAMINE (developed at the University of Liège). Different configurations of the soil-foundation model are simulated in order to point out and analyse the key physical factors of the components that are involved in the extraction resistance. The most representative of these parameters are finally assembled to formulate and calibrate a mechanical model of the tensile capacity consisting of rheological elements (springs, sliders, dampers…).

Samenvatting in het Nederlands

De behoeften voor elektriciteitsproductie samen met milieu uitdagingen en aspiraties van energie-onafhankelijkheid hebben tegenwoordig de wereldwijde uitbreiding van duurzame energiebronnen uitgestippeld. Onder deze bronnen, offshore windenergie heeft een enorm ontwikkelingspotentieel. Met het toenemende aantal windmolen, die steeds dieper en verder van de kust worden gebouwd, innovatieve funderingssystemen worden nu onmisbaar om de economische levensvatbaarheid van projecten op zee te waarborgen. In deze omstandigheden, maken zuigpalen een geschikte en rendabele optie uit, wat tot optimalisatie van ontwerpmethoden leidt. Dit rapport heeft ten doel deze funderingstechniek in kleigrond onder trekbelasting te onderzoeken. Het oogmerk is een eenvoudige methode te ontwikkelen voor de berekening van deze case studie. Om dit te bereiken, is een numerieke tweedimensionale analyse van een caisson gevoerd door middel van eindige elementen programma LAGAMINE (ontwikkeld aan de Universiteit van Luik). Verschillende configuraties van het grond - fundering model worden dan gesimuleerd om fysische factoren te benadrukken en te analyseren die in de treksterkte worden opgenomen. De meeste vertegenwoordigende parameters worden eindelijk geassembleerd zodat een mechanisch model van het trekgedrag bestaande uit reologische elementen (springveren, energieverspreiders en dempers) geformuleerd en gekalibreerd kan worden.

Résumé en français

Les besoins continus en électricité, couplés aux enjeux environnementaux et aux aspirations d'indépendance énergétique ont posé les jalons de l'expansion mondiale que connait actuellement le domaine des énergies renouvelables. Parmi celles-ci, l'énergie éolienne offshore présente un potentiel de développement énorme. Avec le nombre croissant de turbines installées toujours plus profondément et plus loin des côtes, des systèmes de fondation innovants deviennent indispensables pour assurer la pérennité économique des projets éoliens offshores. Dans ces conditions, les caissons à succion apparaissent comme une solution appropriée et rentable, ce qui accroit l'attrait porté à l'optimisation des méthodes de conception. Ce travail porte spécifiquement sur l'étude du comportement de ce type de fondations dans des sols argileux et sous charges de traction, imposées par les conditions environnementales. L'objectif est de développer une méthode de calcul simplifiée propre à ce cas d'étude. Pour y parvenir, une étude numérique en deux dimensions d'un caisson est réalisée à l'aide du logiciel éléments finis LAGAMINE (développé à l'Université de Liège). Différentes configurations du modèle sol - fondation sont simulées de manière à mettre en évidence et analyser les facteurs physiques des composants intervenant dans la résistance à la traction. Les paramètres les plus représentatifs sont ensuite combinés en vue de formuler et calibrer un modèle mécanique du comportement en traction à partir de divers éléments rhéologiques (ressorts, amortisseurs, dissipateurs...).

Content

Acknowledgements ..... **ii**

Summary ..... **iii**

Content ..... **v**

List of figures ..... **viii**

List of tables ..... **xii**

Nomenclature ..... **xiii**

List of acronyms ..... **xvii**

Chapter 1 Introduction **1**

1.1. Background 1

1.2. Objectives of the thesis 3

1.3. Structure of the thesis 3

Chapter 2 Foundations for offshore wind turbines **5**

2.1. Introduction 5

2.2. General outlook of the offshore wind market in Europe 5

2.3. Wind turbine elements 8

2.4. Support structures for offshore wind turbines 9

2.4.1. Bottom-mounted OWT structures 10

2.4.2. Moored floating OWT structures 14

2.4.3. Summary of supports for OWTs 18

Chapter 3 Suction caissons for offshore wind turbines **19**

3.1. Introduction 19

3.2. General description 19

3.3. Pros and cons 21

3.4. Conditions in marine environment 22

3.4.1. Soil conditions 22

3.4.2. Loading conditions 23

3.4.3. Typical loading magnitudes acting on OWTs 26

3.5. Installation procedure 29

3.5.1. Basic principles 29

3.5.2. Installation in sandy soil conditions 29

3.5.3. Installation in clay soil conditions 30
3.5.4. Analytical approach 30
3.5.5. Issues during installation 33
3.6. Design principles of suction caisson foundations 34
3.6.1. Vertical bearing capacity 34
3.6.2. Vertical pull-out (tensile) capacity 37
3.6.3. Horizontal capacity 38
3.6.4. Inclined capacity 40
Chapter 4 2D Finite Element Analysis 41
4.1. Introduction 41
4.2. Definition of the reference FE model 41
4.2.1. Problem statement 41
4.2.2. Numerical model implementation 43
4.2.3. Initial stress state in the soil 48
4.2.4. Initial loading state of the caisson 49
4.3. 1st Scenario - Drained conditions and linear-elastic soil 54
4.3.1. Assumptions 54
4.3.2. The FE model 54
4.3.3. Results 56
4.3.4. Influence of the main parameters 62
4.3.5. Comparison between numerical and analytical results 64
4.4. 2nd Scenario - Partially drained conditions and elastic soil 69
4.4.1. Assumptions 69
4.4.2. The FE model 69
4.4.3. Results 70
4.4.4. Influence of the main parameters 79
4.4.5. Comparison between numerical and analytical results 81
Chapter 5 Macro-element 89
5.1 Introduction 89
5.2 1st Simulation - Drained conditions and linear-elastic soil 89
5.2.1. Model 89
5.2.1.1. Rigid body motion 91
5.2.1.2. Soil free to move 91
5.3. 2nd Scenario - Partially drained conditions and elastic soil 95
5.3.1. Model 95
5.3.2. Parametric study 103

Chapter 6 Conclusion 107

6.1. Summary and conclusions 107

6.2. Perspectives 108

Appendix A 110

Appendix B. 111

Appendix C. 113

Appendix D 118

Appendix E 129

References 130

List of figures

FIGURE 1-1: Presumed alternative energy share of the total electricity generation [1].....1
FIGURE 1-2: Trends EU of the capacity of onshore and OWTs until 2030 [5].....2
FIGURE 2-1: Past, present and projected trends for wind power capacity and production, and for avoided **CO2** emissions in the EU [2].....5
FIGURE 2-2: Outlook of operational (green), and expected wind farms for the period 2016-2022 (red) in North-Western Europe [10][13].....6
FIGURE 2-3: Overview of the offshore market in Europe: In 2016 (a) and cumulative (b) [10].....7
FIGURE 2-4: Overview of the water depth [m] and the distance to the shore [km] for operating and planned farms at the end of 2016 in Europe (a)[12] and growth in the size of OWTs since 1991 (b) [1] ...8
FIGURE 2-5: Components of the rotor-nacelle assembly (a) [16] and support structure components (b) [17] 9
FIGURE 2-6: Share of the support structure for OWT in Europe : In 2016 (a) and cumulative (b)[10] 10
FIGURE 2-7: Monopod substructure : (a) gravity base monopod, (b) suction caisson monopod, (c) monopile – Multipod substructure : (d) gravity base multipod, (e) suction caisson multipod, (f) multipile – jacket substructure : (g) piled, (h) suction caisson anchored [23].....11
FIGURE 2-8: Installation of gravity based foundations [26].....12
FIGURE 2-9: Load components applied on: (a) monopile, (b) multipile [27].....13
FIGURE 2-10: Moored floating substructures : (a) Ballast stabilized configuration, (b) Mooring line stabilized configuration; Buoyancy stabilized configuration : (c) semi-submersible barge including water tank,(d) tri-floater tanks connected by an open space truss [34].....15
FIGURE 2-11: Mooring systems : (a) Catenary mooring system, (b) Taut mooring system, (c) Vertical mooring system [20].....15
FIGURE 2-12: Surface gravity anchor: (a) box anchor, (b) grillage and berm anchor [36].....16
FIGURE 2-13: Pile anchor: (a) Driven or drilled pile [35], (b) DPA [20].....17
FIGURE 2-14: Embedded anchor: (a) traditional drag anchor, (b) vertically loaded anchor [20].....17
FIGURE 2-15 : (a) Suction caisson anchor and installation of SEPLA's: (b) installation of suction caisson, (c) suction caisson retrieval, (d) plate anchor keying [39].....18
FIGURE 3-1 : Suction caisson component terminology based on vertical and horizontal cross sections 20
FIGURE 3-2 : (a) Typical loading on a 3,5-5MW OWT under extreme conditions, Equivalent loading acting on the OWT and reaction forces on the suction caisson in case of: (a) monopod, (b) multipod arrangement.....28
FIGURE 3-3 : Installation of a suction caisson in: (a) sand and (b) clay.....30
FIGURE 3-4 : Forces during installation: (a) Self-weight penetration, (b) suction-assisted penetration....33
FIGURE 3-5 : vertical bearing capacity in : (a) drained, (b) partially drained, (c) undrained conditions.36
FIGURE 3-6 : vertical pull-out capacity in: (a) drained, (b) partially drained, (c) undrained conditions..38
FIGURE 3-7 : failure mechanisms during fully drained, partly drained and fully undrained uplift.....38
FIGURE 3-8 : Soil failure mechanism under horizontal loading : (a) caisson anchor with optimal attachment depth, (b) monopod suction caisson [15].....39
FIGURE 3-9 : Soil failure mechanism under inclined loading: (a) elevation, (b) in-plane views [67].....40
FIGURE 4-1: typical tripod foundation: (a) Elevation view, (b) Plane view with the modelled part (red)[56].....41

Figure 4-2 : Iterative resolution of the nonlinear force-displacement relationship....42
Figure 4-3: (a) Plane-strain model and (b) axisymmetric model [80] 43
Figure 4-4 : Discretization of the interface finite element [64] 46
Figure 4-5 : Meshed geometry of the axisymmetric FE model with mechanical and hydraulic boundary conditions, details of the caisson lid and of the interfaces....46
Figure 4-6 : Loading applied to the caisson and initial stresses at the beginning of the extraction phase 49
Figure 4-7 : Orientation and colour code of reaction components in the initial state....53
Figure 4-8 : Contribution of each component (blue) to the total upward or downward reaction (red)...53
Figure 4-9: Definition of the four sub-cases examined in the 1st scenario 56
Figure 4-10: (a) Cancellation of the variation of water components, (b) variation of reaction components during an imposed displacement....57
Figure 4-11: Drained traction simulations: variations of the reaction components and variations of the reaction components to variation of the total load for (a) subcase 2 and (b) subcase 4....58
Figure 4-12 : Comparison of the mobilisation of friction components in the case of (a) a rigid body motion and (b) a soil free to move 60
Figure 4-13: Soil-caisson behaviour in the initial phase (a, black) and variation of vertical displacement in both rigid body movement (b) and released soil cases (c), Amplification Factor = 25%....60
Figure 4-14: Distribution of the shear and normal stresses along the caisson skirt in the cases of a rigid body motion (a)-(b) and of a soil free to move (c)-(d)-(e)-(f), 1st scenario....61
Figure 4-15: Influence of the main parameters on the friction components 63
Figure 4-16: (a) Linearly increasing shear stress profile with depth and (b) real shear stress profile bounded to the maximum available shear stress τmax....64
Figure 4-17: Comparison between the numerical and analytical computations of friction components for a purely rigid body movement (sub-case 1): Inner available friction (a) and outer available friction (b).65
Figure 4-18: Comparison between numerical and analytical computation of friction components for a rigid body movement (sub-case 2): Inner available friction (a) and outer available friction (b) 66
Figure 4-19: Superposition of the numerical and analytical curves when (a) no parameter, (b) 1 parameter and (c) 2 parameters are considered in the analytical formula (Outer friction component)....68
Figure 4-20: Superposition of numerical and analytical curves considering 1 parameter in the analytical expression (Inner friction component) 68
Figure 4-21: Definition of the two sub-cases examined in the second scenario 70
Figure 4-22: Variation of the reaction components during an imposed displacement, 2nd scenario 71
Figure 4-23: Partially drained traction simulation : variations of the reaction components and variations of the reaction components to variation of the total load for (a,b) sub-case 5 and (c,d) sub-case 6....73
Figure 4-24: Comparison of the (a) total reaction component, (b) inner friction component and (c) outer friction component between drained and partly drained conditions....73
Figure 4-25: Distribution of pore water pressures around the caisson for (a) a rigid body motion and (b) a soil free to move, rate of loading = $1 \times 10 - 6$ms and k = $10 - 7$ m/s....75
Figure 4-26: Results of the sub-case 6 for $k = 5.10 - 12$: (a) Load-displacement curves and (b) variations of vertical displacement, Amplification factor = 25% 76
Figure 4-27: Results of the sub-case 6 for $k = 5.10 - 15$: (a) Load-displacement curves and (b) variations of vertical displacement, Amplification factor = 25% 77
Figure 4-28: Coupling between plug uplift and seepage flow mechanisms....77
Figure 4-29: Distribution of the shear and the normal stresses along the caisson skirt in the case of a rigid body motion (a)-(b) and of a soil free to move (c)-(d)-(e)-(f), 2nd scenario....78
Figure 4-30: Influence of the main parameters on the friction components 81

FIGURE 4-31: Comparison between the numerical and the analytical computations of the friction components for a purely rigid body movement (sub-case 5): Inner available friction (a) outer available friction (b) and PWP component (c), 2nd scenario 83
FIGURE 4-32: Superposition of the numerical and the analytical curves considering (a) no calibration parameter, (b) 1 parameter and (c) 2 parameters in the analytical formula 85
FIGURE 4-33: Superposition of the numerical and the analytical curves considering 1 parameter in the analytical expression: (a) the friction is fully mobilised and (b) the critical suction is reached 85
FIGURE 4-34: Superposition of the numerical and the analytical curves considering (a) no calibration parameter and (b) one parameter $\xi pwp, u, II$ in the analytical formula 86
FIGURE 4-35: Superposition of numerical and analytical curves considering (a) no calibration parameter or (b) one parameter $\xi plug, u$ in the analytical formula (plug uplift component) 88
FIGURE 5-1: (a) Mechanical behaviour of a spring and a slider - (b) Rheological model for the 1st fully drained scenario [76] 91
FIGURE 5-2: Variation of the calibration parameter of the slider with the aspect ratio: (a) outer friction and (b) inner friction 92
FIGURE 5-3 : Variation of the calibration parameters $\xi out, d, \zeta out, d$ and $\zeta in, d$ with νc for 5 aspect ratio's 93
FIGURE 5-4 : Variation of the calibration parameters $\xi out, d, \zeta out, d$ and $\zeta in, d$ with $K\tau$ for 5 aspect ratio's 94
FIGURE 5-5 : Variation of the calibration parameters $\xi out, d, \zeta out, d$ and ζin, d with $K\tau$ for 5 aspect ratio's 94
FIGURE 5-6: Rheological model for the 2nd partly drained scenario in the case of a rigid body motion [76] 97
FIGURE 5-7: Variation of the calibration parameter of the slider with the aspect ratio: (a) outer friction and (b) inner friction 101
FIGURE 5-8: Rheological model for the 2nd partially drained scenario in the case of a soil free to move [76] 101
FIGURE 5-9: Activation of the rheological elements for (a) fully drained, (b) partly drained and (c) undrained conditions 103
FIGURE 5-10: Variation of the calibration parameter $\xi pwp, u, I$ with (a) the permeability and (b) the loading rate, for 5 distinct slenderness ratio's 104
FIGURE 5-11: Variation of the calibration parameter $\xi pwp, u, II$ with (a) the permeability and (b) the loading rate, for 5 distinct slenderness ratio's 105
FIGURE 5-12: Variation of the calibration parameter $\xi out, u$ with (a) the permeability and (b) the loading rate, for 5 distinct slenderness ratio's 106
FIGURE 5-13: Variation of the calibration parameter $\xi in, u$ with (a) the permeability and (b) the loading rate, for 5 distinct slenderness ratio's 106
FIGURE 5-14: Variation of the calibration parameter $\xi plug, u$ with (a) the permeability and (b) the loading rate, for 5 distinct slenderness ratio's 106
FIGURE B- 1 : Drained traction simulations: variations of the reaction components and variations of the reaction components to variation of the total load for sub-case 1 111
FIGURE B- 2: Drained traction simulations: variations of the reaction components and variations of the reaction components to variation of the total load for sub-case 2 111
FIGURE B- 3 : Drained traction simulations: variations of the reaction components and variations of the reaction components to variation of the total load for sub-case 3 112
FIGURE B- 4: Drained traction simulations: variations of the reaction components and variations of the reaction components to variation of the total load for sub-case 4 112
FIGURE C- 1 : Shear stress profile 114
FIGURE C- 2 : Stresses in soil element [75] 115

FIGURE D- 1 : Trend lines for the variation of $\zeta out, d$ and $\xi out, d$ with $\boldsymbol{\nu c}$.....119
FIGURE D- 2: Trend lines for the variation of $\zeta in, d$ with $\boldsymbol{\nu c}$ 119
FIGURE D- 3: Trend lines for the variation of $\zeta out, d$ with νc 120
FIGURE D- 4 : Trend lines for the variation of $\xi out, d$ with νc 120
FIGURE D- 5: Trend lines for the variation of $\zeta in, d$ with νc.....121
FIGURE D- 6 : Trend lines for the variation of $\zeta out, d$ with Ec 122
FIGURE D- 7 : Trend lines for the variation of $\xi out, d$ with Ec 122
FIGURE D- 8 : Trend lines for the variation of $\zeta in, d$ with Ec.....123
FIGURE D- 9 : Trend lines for the variation of $\xi pwp, u, I$ with k.....124
FIGURE D- 10 : Trend lines for the variation of $\xi pwp, u, I$ with the loading rate 124
FIGURE D- 11 : Trend lines for the variation of $\xi pwp, u, II$ with k.....125
FIGURE D- 12 : Trend lines for the variation of $\xi pwp, u, II$ with the loading rate.....125
FIGURE D- 13 : Trend lines for the variation of $\xi out, u$, with the permeability 126
FIGURE D- 14 : Trend lines for the variation of $\xi out, u$, with the loading rate 126
FIGURE D- 15 : Trend lines for the variation of $\xi in, u$, with the permeability.....127
FIGURE D- 16 : Trend lines for the variation of $\xi in, u$, with the loading rate.....127
FIGURE D- 17 : Trend lines for the variation of $\boldsymbol{\xi plug}, u$, with the permeability 128
FIGURE D- 18 : Trend lines for the variation of $\boldsymbol{\xi plug}, u$, with the loading rate 128
FIGURE E- 1 : Flow chart to assess the plug uplift mechanism.....129

List of tables

TABLE 2-1: Overview of the offshore wind market in 2016 and the cumulative market [10]....7
TABLE 3-1 : Indicative loading magnitudes for a 3,5-5MW OWT supported by one single suction caisson during a storm....27
TABLE 3-2 : Indicative loading magnitudes for the leeward caisson of a tripod substructure supporting a 3.5-5MW OWT during a storm....28
TABLE 4-1 : System of units used in the LAGAMINE program....42
TABLE 4-2: Geometrical parameters of the reference FE model....44
TABLE 4-3 : Parameters of the reference geometry, steel caisson, elastic clay soil and contact elements..48
TABLE 4-4: Set of simulation input values: parameters of the mechanical constitutive law of the interface elements, the soil and the caisson materials and execution data....55
TABLE 4-5: Linear elastic soil behaviour & drained configuration: simulation attributes....56
TABLE 4-6: Set of simulation input values: parameters of the mechanical constitutive law of interface elements, soil and caisson materials and execution data....70
TABLE 4-7: Linear elastic soil behaviour & drained configuration: simulation attributes....70
TABLE 4-8: Check of the consistency of the results....74
TABLE 5-1 : Normalisation of the main study parameters....89
TABLE 6-1: Summary of the different specific cases and their features....107
TABLE 6-2: Summary of the different components of the resistance and their related mechanical elements 109

Nomenclature

Latin symbols	Significance	Unit
A	Area of the OWT component	$[m^2]$
$A_{base,i}$	Inner cross section area of the caisson base	$[m^2]$
$A_{base,o}$	Outer cross section area of the caisson base	$[m^2]$
A_i	Inner surface area of the skirt (per unit meter of penetration)	$[m^2]$
A_o	Outer surface area of the skirt (per unit meter of penetration)	$[m^2]$
A_{tip}	Tip area of the suction caisson	[m]
a	Exponent of the inclined capacity failure envelope	[-]
b	Exponent of the inclined capacity failure envelope	[-]
$C_{D/M}$	Drag/Inertia coefficient	[-]
C_g	Geometrical factor of the OWT component	[-]
c	Cohesion of the soil	[-]
c_v	Coefficient of consolidation	$[mm^2/s]$
$D = B$	Mean diameter of the caisson	[m]
D_i	Inner caisson diameter	[m]
D_o	Outer caisson diameter	[m]
D_{tower}	Effective diameter or width of the submerged part	[m]
$d = u$	(Imposed) Displacement of the lid of the caisson	[m]
$d_q; d_c; d_\gamma$	Depth factors	[-]
$d(t)$	Imposed displacement of the lid (as a function of time)	[m]
E_c	Elastic modulus of the clay soil	[Pa]
E_k	Characteristic value of the environmental action	[kN]
$\mathrm{E_r}$	Relative error	[%]
E_s	Elastic modulus of the steel of the caisson	[GPa]
e	Void ratio	[-]
F	External applied force	[kN]
F_{waves}	Unitary wave-induced force vector normally acting on the member axis	[kN]
F_{wind}	Wind-induced force on the OWT	[kN]
f_{li}	Parameter 1 - factor of lateral influence	[-]
$f_{w,N}; f_{w,L}$	Fluid flow normal to the interface or oriented longitudinally	$[kg/(m^2s)]$
G	Shear modulus	[GPa]
G_k	Characteristic value of the permanent action	[kN]
G_s	Specific gravity	[-]
g	Gravitational acceleration of the earth	$[m/s^2]$

H	Horizontal load	$[N]$
$H_{(s)}$	(Significant) wave height	[m]
H_{ult}	ultimate lateral capacity of the caisson	[kPa]
h	Penetration depth	[m]
h_c	Penetration depth in clay	[m]
h_s	Penetration depth in sand	[m]
$h_{w,lid}(t)$	Heigh of the water column above the lid (as a function of the time)	[m]
i	Hydraulic gradient	$[-]$
J	Jacobian of the integration point	[-]
K	Lateral earth pressure coefficient	[-]
K_0	Horizontal earth pressure coefficient at rest	[-]
K_N	Normal penalty coefficient	$[N/m^3]$
K_T	Tangential penalty coefficient	$[N/m^3]$
$K(u)$	Integration matrix	[m/kN]
k	Coefficient of permeability	[m/s]
k_L	Longitudinal intrinsic permeability at the interface	$[m^2]$
$\mathrm{k_{int}}$	intrinsic permeability	$[m^2]$
L	Embedded skirt length	[m]
L_{plug}	Uplift length of the soil plug	[m]
M	Moment load	$[N \times m]$
N_c	Bearing capacity factor (cohesion)	[-]
N_p	Lateral bearing capacity factor varying with the slenderness ratio	[-]
N_q	Bearing capacity factor (overburden)	[-]
N_γ	Lateral bearing capacity factor	[-]
n	Porosity	[%]
$1/n$	Annual probability of occurrence of a storm	[-]
$\mathrm{P_{pwp}}$	Integral of the pore water pressure distribution	[N]
P_w	Buoyancy force on the caisson	[N]
p_N	Normal contact pressure	[Pa]
p	End bearing capacity	[kPa]
p_w	Water pressure	[kPa]
Q_i	Friction resistance on the inner skirt surface of the caisson	[kN]
Q_k	Characteristic value of the variable action	[kN]
Q_{lid}	Bearing capacity of the lower part of the lid of the caisson	[kPa]
Q_o	Friction resistance on the outer skirt surface of the caisson	[kN]
$Q_{phase\,1}$	Vertical capacity during self-weight installation	[kN]
Q_{phase2}	Vertical capacity during suction-assisted penetration	[kN]
Q_{pw}	PWP distribution on the lower part of the lid of the caisson	[kPa]
Q_{suct}	Penetration of the caisson base under suction	[kN]
Q_{tip}	End bearing capacity & overburden pressure on the skirt end	[kN]
S_{req}	Required suction for the installation of the suction caisson	[kPa]
r_m	Radius at which the shear stress becomes negligible	[m]
s	Applied suction	[Pa]
s_{crit}	Critical suction	[Pa]
$\overline{s_u}$	Average undrained shear strength over the penetration depth	[kPa]

$s_q; s_\gamma;\ s_c$	Shape factor for circular foundation	[-]
s_u	Undrained shear strength at the skirt end level	[kPa]
s_{u0}	Shear strength at mudline	[kPa]
T, T_{10}	Averaging period and 10-min mean wind period	[s]
T_p	Spectral peak period	[s]
T_w	Transmissivity	$[m/(Pas)]$
t	Thickness of the caisson skirt	[m]
U, U_{10}	Mean wind speed and 10-minute mean wind speed	[m/s]
u	Pore water pressure in the soil	[kPa]
$\frac{\partial u}{\partial t}$	Horizontal wave-induced velocity of water	[m/s]
$\frac{\partial^2 u}{\partial t^2}$	Horizontal wave-induced acceleration of water	$[m/s^2]$
u_0	Initial pore water pressure in the vertical direction	[Pa]
V	Vertical load	$[N]$
V_{plug}	Uplift volume of the soil plug	$[m^3]$
$V_{ult,d,\mathrm{I}}$	Vertical ultimate bearing capacity in drained conditions	[kPa]
$V_{ult,d,\mathrm{II}}$	Vertical ultimate pull-out capacity in drained conditions	[kPa]
$V_{ult,pd,\mathrm{I}}$	Vertical ultimate bearing capacity in partially drained conditions	[kPa]
$V_{ult,u,\mathrm{I}}$	Vertical ultimate bearing capacity in undrained conditions	[kPa]
V_{ult}	Ultimate vertical capacity of the caisson	[kPa]
v	Seepage velocity	$[m/s]$
W'	Effective submerged self-weight of the caisson	[kN]
W_{cais}	Weight of the caisson	[N]
W'_{plug}	Effective submerged weight of the soil plug	[kN]
W_{plug}	Resultant of the variation of the uplift movement of the soil plug confined within the skirt	[N]
W_w	Hydrostatic weight of water	[N]
W'	Effective submerged self-weight of the caisson	[kN]
w	Bulk density of the air	$[N/m^3]$
x	Abscissa coordinate of the integration point	[m]
z	Height above sea level	[m]

Greek symbols

α_i	Dimensionless inner adhesion factor	[-]
α_{in}	Factor for reduction of outside resistance	[-]
α_o	Dimensionless outer adhesion factor	[-]
α_{out}	Factor for reduction of inside resistance	[-]
α_{tip}	Factor for reduction of tip resistance	[-]
γ	Soil weight	$[kN/m^3]$
γ'	Effective soil weight	$[kN/m^3]$
γ'_c	Effective unit weight of clay soil	$[kN/m^3]$
γ'_{clay}	Effective unit weight of the clay	$[kN/m^3]$
γ'_s	Effective unit weight of sand soil	$[kN/m^3]$
$\gamma_{sat,clay}$	Saturated unit weight of the clay	$[kN/m^3]$

γ_w	Unit weight of water	$[kN/m^3]$
$\delta_q; \delta_c; \delta_\gamma$	Load inclination factors	[-]
ε_N	Normal strain rate	$[s^{-1}]$
ε_T	Tangential strain rate	$[s^{-1}]$
$\varepsilon_x; \varepsilon_y; \varepsilon_z$	Strains along the $x, y, z - axis$	[m]
$\rho_{s,clay}$	Particle density of the clay	$[kg/m^3]$
ρ_s	Bulk density of the steel	$[kg/m^3]$
ρ_w	Density of water	$[kg/m^3]$
$\delta_q; \delta_c; \delta_\gamma$	Load inclination factors	[-]
Σ'	Resistance of the in-situ soil	[N]
σ'	Effective stress in the soil	[kPa]
$\sigma_{h,0}$	Initial total stress in the horizontal direction	[Pa]
$\sigma'_{h,0}$	Initial effective stress in the horizontal direction	[Pa]
σ_U	Standard deviation of the 10-minute mean wind speed	[m/s]
σ_{tot}	Total vertical stress in the soil	[kPa]
$\sigma_{v,0}$	Initial total stress in the vertical direction	[Pa]
$\sigma'_{v,0}$	Initial effective stress in the vertical direction	[Pa]
τ	Shear stress	[Pa]
υ_c	Poisson's ratio of the clay	[-]
υ_s	Poisson's ratio of the steel	[-]
$\overline{\Phi}$	Value of shear stress at the integration point	[Pa]
$\Phi_{in}; \Phi_{out}$	Integral of the shear stresses along the skirt of the caisson	[N]
Φ^{max}	Maximum friction resistance	[N]
ϕ	Soil friction angle	[°]
θ	Inclination angle of the loading	[°]
λ	Wave length	[m]
μ_w	Fluid dynamic viscosity for water at 20°C	$[Pa\ s]$
μ	Friction coefficient of the interface	[-]
ρ	Rate of change of the shear strength with respect to the depth	[-]
ψ	Dilatation angle	[°]

Convention

$\blacksquare'$	Effective stress
$\Delta\blacksquare$	Variation
$\nabla\blacksquare$	Gradient
$\blacksquare_{max}$	Maximum value
$\blacksquare_{min}$	Minimum value
$\overline{\blacksquare}$	Value at the integration point
$\lvert\blacksquare\rvert$	Absolute value

List of acronyms

BC	Boundary Condition
DPA	Dynamically Penetrating Anchor
EU	European Union
EWEA	European Wind Energy Association
FE	Finite Element
FEA	Finite Element Analysis
GBF	Gravity Base Foundation
NC	Normally Consolidated clay
NIMBY	Not In My BackYard (syndrome)
OWE	Offshore Wind Energy
OWT	Offshore Wind Turbine
PWP	Pore Water Pressure
ROV	Remotely Operated Vehicle
SEPLA	Suction Embedded Plate Anchor
SLS	Serviceability Limit State
TLP	Tension Leg Platform
ULS	Ultimate Limit State
VLA	Vertically Loaded Anchor

Chapter 1
Introduction

1.1. Background

In the years post World-Wars period, an unprecedented techno-industrial revolution, together with significant technological advances were faced on a global scale. These progresses coupled with the continual population growth have led to increasing humankind energy needs and with them to the emergence of fossil fuels and nuclear industries.

However, the overconsumption of gas and petroleum supplies over the last decades has revealed the limited availability of these non-renewable energy sources, and the Chernobyl and Japan disasters have highlighted the dangerous nature of nuclear power, despite its cost and time efficiency. These global concerns resulted in the signing of the Kyoto Protocol by about 190 countries in 1997, and have initiated the worldwide development of alternative sources of energy, coming from renewable earth resources such as current, waves, sun rays, geothermal heat, biomass or wind. As of today's date, the aim is to progressively substitute the fossil energies by a combination of various emerging renewable energy sources, among which the wind power discussed in this thesis appears to be one of the most promising ways to generate clean energy.

At the end of 2015, wind power amounted to almost 4% of the global power generating capacity and provided one sixth of the renewable power capacity, only surpassed by hydropower which accounted for about 70% [1]. The alternative generating capacity share of the total electricity production at year-end 2015 is depicted in Figure 1-1.

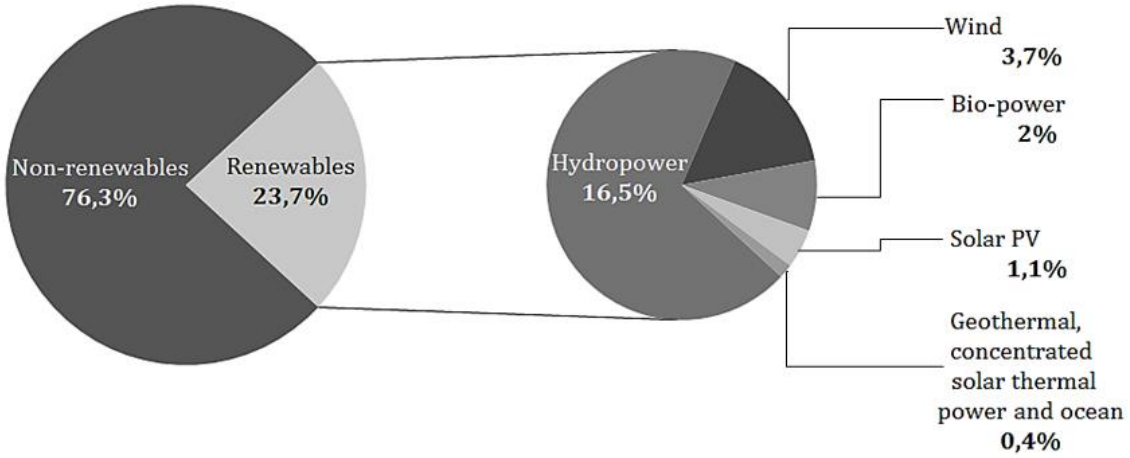

FIGURE 1-1: Presumed alternative energy share of the total electricity generation [1]

Although wind energy has achieved a phase of maturity during the last four decades, negative aspects are still pointed out, especially aesthetical and environmental impacts, noise and vibration generation, along with disturbances caused by cyclic shadow of the rotor blades [2]. Because of the intermittence of wind resources, the optimal electricity output is only generated for specific arrays of wind direction and velocity, which requires to combine wind power capacity with other consistent sources of energy [3]. Advantages of wind power arise from the fact that this means of electricity generation is green and non-polluting, naturally available and inexhaustible over time on earth's surface. Moreover the rapid growth of the wind power sector, together with the increasing population demand have contributed to lower the generation costs and to develop a really competitive alternative source of energy. Also the technological advances have made it possible to maximize the huge potential of wind energy by operating offshore wind spots in addition to onshore ones [4].

Even if the wind power market has two parallel axes of possible development to set itself up as one of the mainstream power sources (i.e. onshore and offshore), most of the future projects are expected to be based on offshore wind turbines (OWT). The projected annual installed and cumulated capacities of offshore wind energy (OWE) in Europe, shown in Figure 1-2, will increase steadily whereas the trend for onshore expansion is in reduction from now on and is foreseen to be surpassed by OWE by the year 2020 [5][6]. The main advantage of OWTs is their location in sites with regular high-speed and sustained wind conditions, which allow to increase the installation capacity and to deliver larger electricity amounts, compared to land-based projects [7]. At sea, there is a lot of available promising space, only constrained by the interactions with the fishing areas and the maritime corridors, while onshore sites are becoming even more confined, and often have to deal with the NIMBY syndrome. Thus, larger wind farms can emerge offshore, and provide high power output from large-scale wind turbines that sweep a greater area. It is also easier to ship big turbine components to farms under construction by sea [7][8]. However, while onshore wind energy rests on its certain maturity and the rather stable wind level to offer low costs, offshore market deals with development costs about two times larger. This comes mainly from the significant installation and maintenance expenses, derived from extreme environmental loads that are encountered away from the shore. These load conditions have required the design of specific and complex supports, which can amount up to 40% of the final installation cost [8] and which include especially suction caissons.

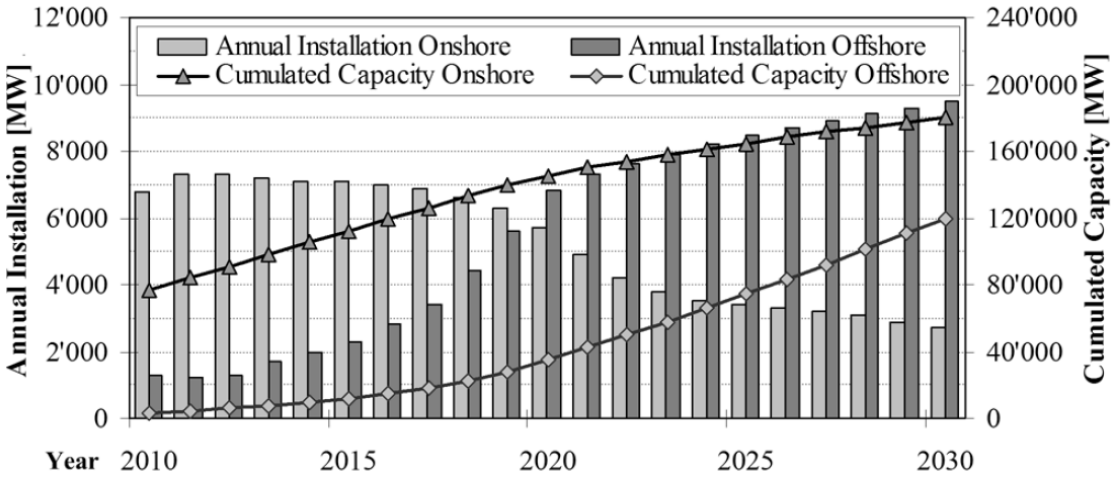

FIGURE 1-2: Trends EU of the capacity of onshore and OWTs until 2030 [5]

The suction caisson as a support solution for OWTs is intended to develop given its low environmental impact, its simple and cost-effective installation process and its applicability for water depth above 30m. The whole system constitutes a rather lightweight structure that copes with large cyclic environmental loads. This poses major challenges in the design of the caisson, since overturning moments induce large extraction forces on the structure. The design practice of suction caissons under tensile loads can be conducted either by limit equilibrium analysis or Finite Element Method (FEM).

The work presented in this thesis aims at investigating the behaviour of suction caissons under an axial tensile load in order to formulate a practical simplified design method.

1.2. Objectives of the thesis

The achievement of this work serves a dual purpose.

On the one hand, a numerical investigation of the behaviour of suction caissons upon axial tensile load is carried out. This aims at obtaining an overall understanding of the different modes of reaction of the caisson under traction loading and at estimating the effects of the different components included in the tensile capacity. To reach this goal, some suction caisson models with various aspect ratios are implemented in the finite element software package LAGAMINE (developed at the University of Liège). Then the simulations are performed using a step-by-step methodology that enables to analyse the caisson response on a case-by-case basis: starting from a rigid body motion in drained conditions, the analysis will then focus on a released soil in partially drained conditions.

On the other hand, since the conducted analysis helped identifying the key factors that have a strong influence on the resistance of the caisson, it is possible to formulate a simplified design method in the form of a macro-element. It is done by implementing a kind of component method by which the tensile capacity of the caisson is modelled as an assembly of individual basic components. All these components present a specific mechanical behaviour that contributes to the total capacity and that can be substituted by a rheological element having the same constitutive law. By putting these elements in series or in parallel, the effective load-displacement relationship of the caisson can be estimated.

1.3. Structure of the thesis

Chapter 1 gives an introduction to the master dissertation, composed of a general overview of the subject, of the formulation of the main objectives of the work, and of the explanation of the structure of the thesis.

Chapter 2 proposes an overall description of the offshore wind turbine sector. The current situation and the expected trends for the future are reviewed. The major components of an OWT are enumerated and described to get an idea of the functioning of the system. Finally, the existing types of support structures for OWT are discussed through a literature review.

Chapter 3 focuses on the suction caisson technology. A description of general aspects of this technique is proposed, and pros and cons are highlighted. The environmental conditions faced

by OWTs including soil and load types are investigated. Subsequently, the installation processes in clay and sand are given with some basic analytical rules. This chapter ends up with the design principles to be applied in order to reach the proper in-service performances of a suction caisson.

Chapter 4 deals with the numerical part of the thesis. The reference 2D model is first defined, and then the numerical analysis of the caisson under a displacement-controlled tensile load is carried out for different configurations. In each case, the numerical results are displayed, discussed, and then compared to analytical calculations, proposed in the literature.

Chapter 5 provides a practical prediction method of the behaviour of the caisson under a tensile load. Based on the findings of chapter 4, mechanical elements are associated to each part of the tensile resistance and then combined in order to formulate a macro-element of the suction caisson foundation, which will predict the extraction resistance (resp. the imposed displacement) for any imposed displacement (resp. extraction resistance).

Chapter 6 finally presents the conclusions of the thesis and some possible perspectives.

Chapter 2
Foundations for offshore wind turbines

2.1. Introduction

This chapter proposes an overall description of the offshore wind turbine sector. The current situation in the offshore wind energy market in Europe is firstly brought up, and the expecting trends for the near future are given. In a second phase, the main individual components of an OWT are described in order to understand the overall functioning of this technique. At the end, the support structures for OWTs are discussed through a literature review.

2.2. General outlook of the offshore wind market in Europe

As a consequence of the global climate change together with the upward trend of the price of the barrel of oil and the continuous development of alternatives energy processes over the last decades, many industrialized countries including the European Union (EU) states have undertaken significant efforts in the energy sector. The purpose of the EU's energy policy is on the one hand to reduce the dependency on the non-renewable energy sources and on the other hand to promote alternative energy sources [2][9][10]. Among these renewable sources, wind energy has experienced a rapid expansion since 1990, and has been widely supported by the EU to achieve the set of objectives that especially aims at increasing the share of the renewable energy mix by 20% by 2020 [11].

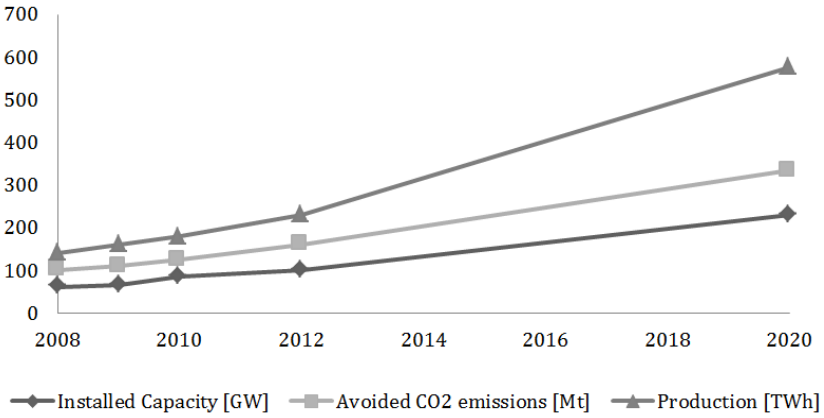

FIGURE 2-1: Past, present and projected trends for wind power capacity and production, and for avoided CO_2 emissions in the EU [2]

Nowadays, to stick to this energy policy while remaining cost-effective, young technologies starting with offshore wind energy have seen major advances, in the same way as did mature technologies such as onshore wind energy. The consequences of this policy are clearly visible in Figure 2-1 showing the trends for a wind power capacity and production as well as the avoided emissions in the EU [2][9].

The prospective development of the offshore wind energy market is reinforced by the figures of the European Wind Energy Association (EWEA) [10]. During the year 2016, nine new offshore wind farms were erected in Europe, namely seven in the North Sea (four in Germany, three in the Nederlands) and two in the Irish Sea on behalf of the United Kingdom. A wind farm refers to an arrangement of multiple onshore or OWTs, with a site access and a grid connection point [5]. All in all, 339 new offshore turbines were connected to the grid in 2016 in Europe that amounts to 1558MW of additional installed capacity.

Since the start of operation of the first OWT in 1991 until the end of 2016, a total amount of 3589 operating OWTs were distributed over 81 offshore wind farms in the European waters, and the majority of these parks are located in the North Sea, in the Baltic Sea and in the Irish Sea as depicted in Figure 2-2. Most of the turbines have been installed by the United Kingdom (41%), Germany (26,4%), Denmark (14,4%) and the Netherlands (10,2%), whereas the remaining installations are spread in the waters of six other EU state members. The cumulative capacity supplied by OWTs in Europe at the end of 2016 came to 12631 MW, which forms 8,21% of the total installed wind capacity of 153,7 GW, and 1,3% of the total EU electricity demand [10][12].

FIGURE 2-2: Outlook of operational (green), and expected wind farms for the period 2016-2022 (red) in North-Western Europe [10][13]

By 2020, the European offshore wind energy is expected to be twice as high as at present, with 24,6 GW of installed capacity. As of today's date, offshore deployment can count respectively

on 4,8 GW from wind farms under construction, on 24,2 GW from consented projects and on 7 GW from projects applying for permits while another 65,6 GW are foreseen by the EU countries. All the data's of the annual market in 2016 and of the cumulative market at the end of 2016 are reported in Table 2-1 and are illustrated in Figure 2-3 (a)(b) [10].

TABLE 2-1: Overview of the offshore wind market in 2016 and the cumulative market [10]

	ANNUAL MARKET IN 2016						CUMULATIVE MARKET SINCE 1991					
AREA	*farms*		*turbines connected*		*Capacity connected*		*farms*		*turbines connected*		*capacity connected*	
	No	*%*	*No*	*%*	*MW*	*%*	*No*	*%*	*No*	*%*	*MW*	*%*
UK	2	25	7	2,1	56	3,6	28	34,6	1472	41,01	5156	40,82
Germany	4	50	155	45,8	813	52,2	18	22,2	947	26,38	4108	32,52
Denmark							13	16,1	517	14,41	1271	10,06
Netherlands	3	37,5	177	52,4	691	44,3	6	7,4	365	10,17	1118	8,85
Belgium							6	7,4	182	5,08	712	5,63
Sweden							5	6,2	86	2,40	202	1,61
Finland							2	2,5	11	0,31	32	0,25
Ireland							1	1,2	7	0,2	25	0,20
Spain	-1	-12,5	-1	-0,3	-2	-0,1	1	1,2	1	0,02	5	0,04
Norway							1	1,2	1	0,02	2	0,02
TOTAL	8	100	338	100	1558	100	81	100	3589	100	12631	100

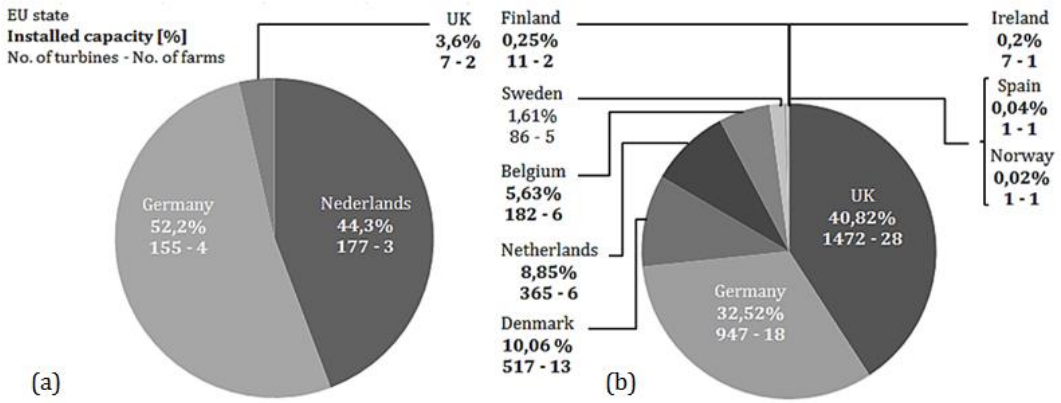

FIGURE 2-3: Overview of the offshore market in Europe: In 2016 (a) and cumulative (b) [10]

The quick rate of development of the offshore wind power sector enables to design wind parks even larger, further away from the coastline, and thus at increasing water depths, as shown in Figure 2-4 (a). Projects under construction and planned to be completed in the next two to three years will reach distances to the shore up to 150km and water depths up to 45m. The scale of online wind farms follows an upward trend since the early 2000s, and is correlated to the rising size and production capacity of individual windmills. In 25 years, the energy production of one single OWT has seen a twentyfold increase and the rotor diameter has been upscaled from 35m to more than 150m, an evolution apparent in Figure 2-4 (b) [5][10]. This continuous increase of the OWT dimensions attests to the rapid growth of the offshore wind market.

On a global scale, Europe is the leader of the offshore wind power industry and assembles the majority of the offshore wind parks. It is closely followed by China which provided a cumulative offshore wind capacity of 1627 MW by the end of 2016. The market is completed by smaller projects in the US and in Asia where offshore wind energy attempts to emerge [14].

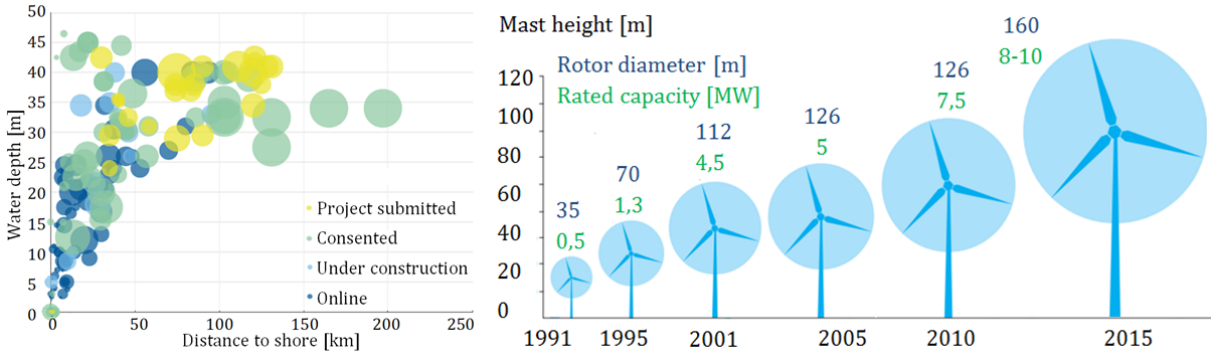

FIGURE 2-4: Overview of the water depth [m] and the distance to the shore [km] for operating and planned farms at the end of 2016 in Europe (a)[12] and growth in the size of OWTs since 1991 (b) **[1]**

2.3. Wind turbine elements

By definition, a wind turbine is a horizontal axis equipment that captures parts of the kinetic energy from the wind to convert it into usable electrical power [15][16]. Conventional wind turbines are made of an upper part, i.e. the rotor-nacelle assembly, and a lower part that consists of the support structure [17].

The top rotor-nacelle assembly is accessible by an enclosed ladder (1) inside the tower, and includes about ten major components highlighted in Figure 2-5 (a). The nacelle (3) is the top structural cover element used to transfer the load acting on the blades to the tower and which houses the key generating components. Among those components, the anemometer and wind vane (5) follow the variation of the wind direction and speed and deliver these measurements to the yaw control system (2) that orientates the nacelle in the optimal wind direction to maximize electrical energy generation. A rotor hub (10) at one extremity of the nacelle connects the blades (8) at their junction point. The blade pitch control (9) adjusts the angle of attack by turning the blades around its longitudinal axis, in order to combine an optimal efficiency with an admissible load rate. The gear box (7) connects the blades to the generator and increases the turning speed to a much higher number of rotations per minute that the electrical generator (4) requires to convert the mechanical energy into an electrical current. A braking system (6) is activated to stop the rotor in case of emergency situations or in case of maintenance works [16][17][18].

The bottom support structure is the part of the wind turbine that includes all the elements below the rotor-nacelle assembly, as presented in Figure 2-5(b). The tower (11) is the central segment usually made of tubular steel, concrete or steel lattice, which holds the access ladder and the electric cables (12) linked to the power grid. This structural part has a height depending on the blades size and on the wind conditions on site and is designed to support the weight of the rotor-nacelle assembly, as well as the load induced by the wind speed [13]. The substructure (13) is a mostly-submerged structural element that connects the tower to the foundation

system in case of OWT, and that is not present for land-based structures. The foundation (14) at the lowest part of the wind turbine is a geotechnical and structural system that carries and spreads the loads applied on the upper structure to the ground or the seabed [16][17][19]. Finally, scour protections are installed to avoid too pronounced erosion at the base of the structure, that may lead to the overall destabilization of the turbines.

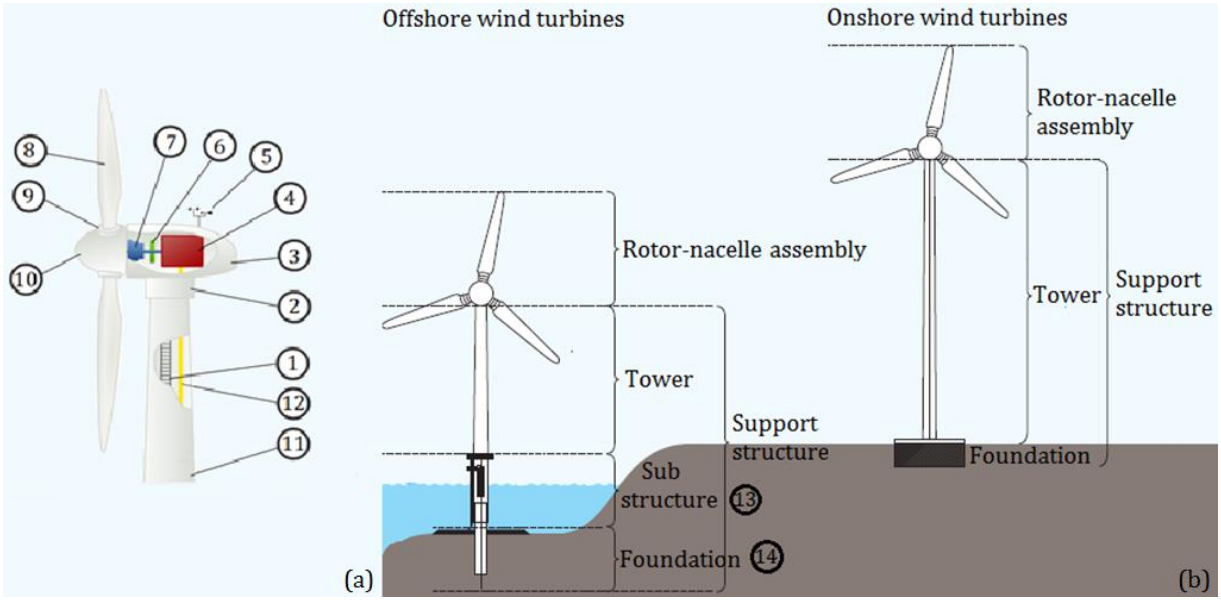

FIGURE 2-5: Components of the rotor-nacelle assembly (a) [16] and support structure components (b) [17]

As mentioned before, OWTs have larger dimensions and capacity than onshore ones. As a result, the foundations have larger sizes to withstand the increasing self-weight of the structure and above all, the high horizontal and overturning moment loads compared to the gravity loads. A significant cyclic component coming from waves, wind, and underwater seismic and landslides activity is introduced when working offshore. These harsh marine environmental conditions may also lead to expensive site investigations and design modifications during installation, and uncommon ground conditions are often encountered. All these specific features of offshore engineering help to explain the major influence of the support structure on the design phase as well as on the development and on the costs of the OWT projects [20].

2.4. Support structures for offshore wind turbines

The type and the design of foundation solutions for OWT projects depend on the size of the turbine, on the water depth, and on the local seabed conditions. Considering these site specific constraints, the challenge is to develop the most cost-effective solution for the support structure and for the installation process on site [21]. As mentioned previously, the support structure of an OWT comprises the substructure on top of the foundation system. On the one hand, the substructure is chosen based on the mean sea level, and on the other hand, the foundation type is bond to the dimensions of the OWT, to the transfer of the applied loads to the soil, and the geotechnical properties of the ground.

In shallow to moderate water ranging from $\sim 10m$ to $\sim 70m$, use is made of bottom-mounted substructures that are firmly fixed to the seabed by underwater foundations. Three main lay-

outs are commonly used for shallow OWT applications, namely the monopod, the multipod and the jacket structure, and there are three practical options for the foundation system, comprising gravity base foundations (GBF's), piled foundations, and skirt or bucket foundations, also known as suction caissons foundations [21].

In deep to ultra-deep water reaching more than $\sim 70m$, moored floating structures are usually adopted for which the lower segment of the substructure is replaced by a mooring system and the anchoring system plays the role of the foundation [20][21]. This new concept is currently under research and design stages but constitutes a promising alternative for the future in order to competitively exploit the large and stable wind potential of deep water spots in the Atlantic Ocean, Mediterranean and North Seas, that are characterized by a too deep water level for bottom-mounted structures. Three main alternative solutions of floating substructures emerging from the gas and oil offshore market are under development and differ in the way the structural stability is ensured: ballast stabilized, mooring line stabilized and buoyancy stabilized concepts [22]. The line connection between these substructures and the anchoring system acts in tension and can be out of three main types: vertical, catenary or taut mooring.

On the basis of the data provided by the EWEA, it appears in Figure 2-6 (a) that 88% of all 560 installed substructure-foundation systems in 2016 in Europe were monopiles, whereas the remaining 12% corresponded to jacket structures. The cumulative market in Europe is also substantially dominated by monopiles with 80,8% of all 4152 fully installed units. The rest of the market is divided among gravity based, jaket, tripod and tripile substructures respectively, while floating structures are still in a development phase as illustrated in Figure 2-6 (b) [10].

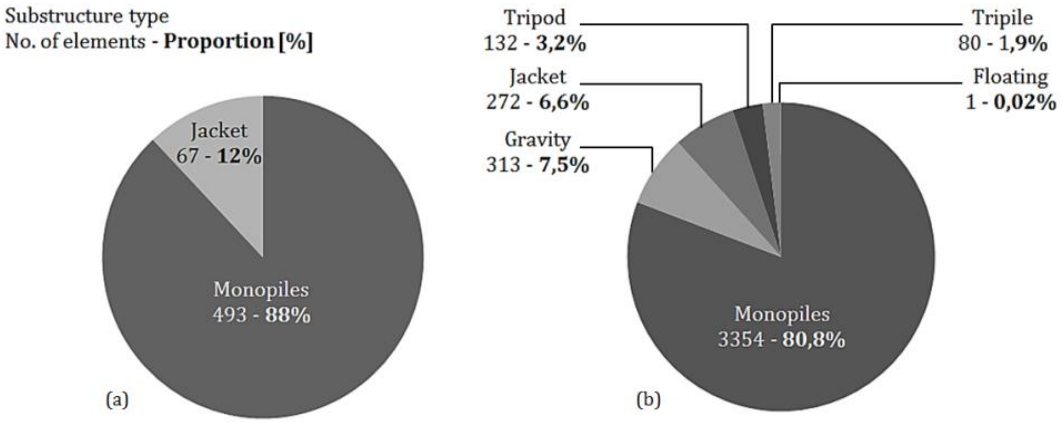

FIGURE 2-6: Share of the support structure for OWT in Europe : In 2016 (a) and cumulative (b)[10]

2.4.1. Bottom-mounted OWT structures

2.4.1.1. Substructure

The monopod concept refers to substructures that consist of one single foundation member to create contact with the soil and to transfer the overturning moment and the applied horizontal loads. In case of monopod arrangements, three types of foundation are used as a function of the water level. As presented in Figure 2-7 (a)(b)(c), gravity-based and suction caisson foundations are commonly employed between 15m and 20m, whereas pile foundations are more suitable in shallow water depths ranging between 20m and 30m [21][23].

The multipod concept refers to braced substructures that consist of three circular steel tubes disposed in triangle in case of a tripod configuration and of four circular steel tubes arranged in a square in case of a quadruped configuration. These configurations are combined with gravity-based, pile or suction caisson foundations. The multiple contacts with the soil lead to the distribution of the loads from the OWT tower onto the different legs and to the conversion of the moment loading into a combination of vertical tension and compression loads. The axial resistance enables to stabilize structures in transitional water depths, reaching about 40m to 50m, as displayed in Figure 2-7 (d)(e)(f) [22][23].

The jacket concept refers to lattice-type steel substructures, with three-legged triangulated or four-legged squared structures, similar to the multipod arrangement. These braced support structures transfer the loads to the surrounding soil by piled or suction bucket foundations embedded at each jacket leg, and are adapted to deeper sea levels and heavier OWTs (Figure 2-7 (g)(h)). [17][21][23].

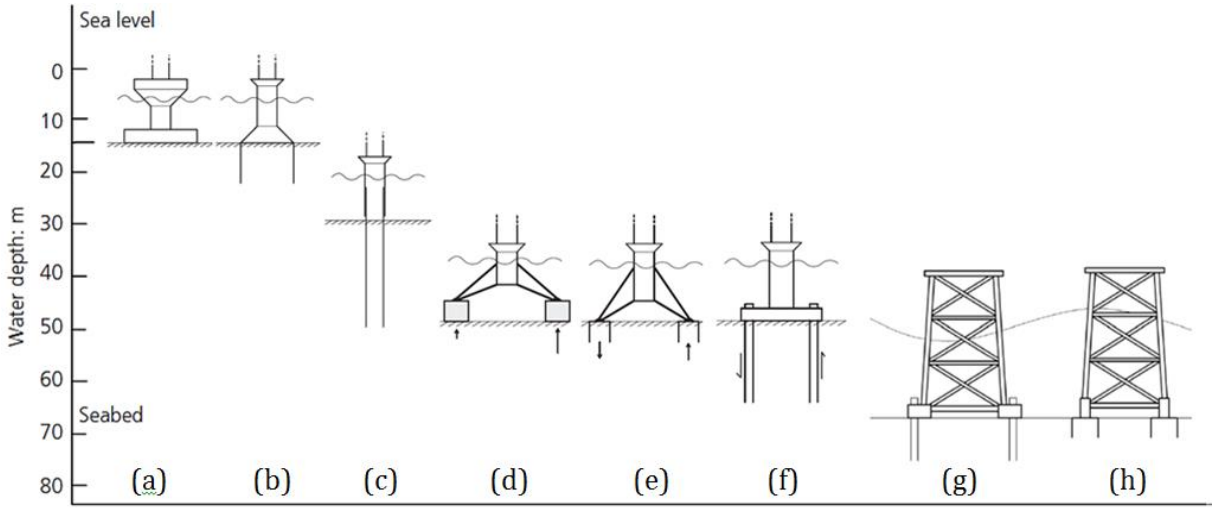

FIGURE 2-7: Monopod substructure : (a) gravity base monopod, (b) suction caisson monopod, (c) monopile – Multipod substructure : (d) gravity base multipod, (e) suction caisson multipod, (f) multipile – jacket substructure : (g) piled, (h) suction caisson anchored [23]

2.4.1.2. Gravity base foundations

Gravity base foundations (GBF's) are massive systems that make use of their own self-weight and footprint on the seafloor to counterbalance the applied moment and the lateral loading, and to ensure the structural stability [20]. Different geometries (squared, circular or polygonal configurations), arrangements (mono- or multipod disposition) and construction material types (reinforced or prestressed concrete, steel, or a combination of both) can be employed but the most common design turns out to be the hollow concrete members [23][24]. Depending on the site soil conditions, skirts can be added to enter into the top soft layer, and supply extra support, and bearing capacity.

The installation of GBF's summarized in Figure 2-8 starts with a dual step. During the inland erection of the main structure, the offshore construction site is dredged over a few meters, partially backfilled with filter and gravel layers and levelled to shape a perfectly horizontal foundation bed, with sufficient bearing capacity. In a second time, the GBF structure is carried into

place and lowered by a heavy lift vessel. Once in position on the ground, inside cells are filled with additional ballast such as sand, concrete, rock or iron, which enlarges the weight and the resistance of the structure. Finally the surrounding sandy soil is put back in place and scour protections are arranged around the foundation [24][25][26].

The use of empty structures has the advantage of reducing the amount of building materials and hence the construction costs. However, this is offset by the logistic complexity of transportation and handling which contributes to rise the installation fees, and therefore restricts the positioning to shallow waters [24]. As the footing is simply laid on the seabed, there is no need of hammering piles, which constitutes a suitable alternative in soils where pile driving is impossible. However, in case of saturated sand layers, there is a risk of liquefaction under cyclic loading. This major issue of offshore engineering is further detailed in section 3.4.

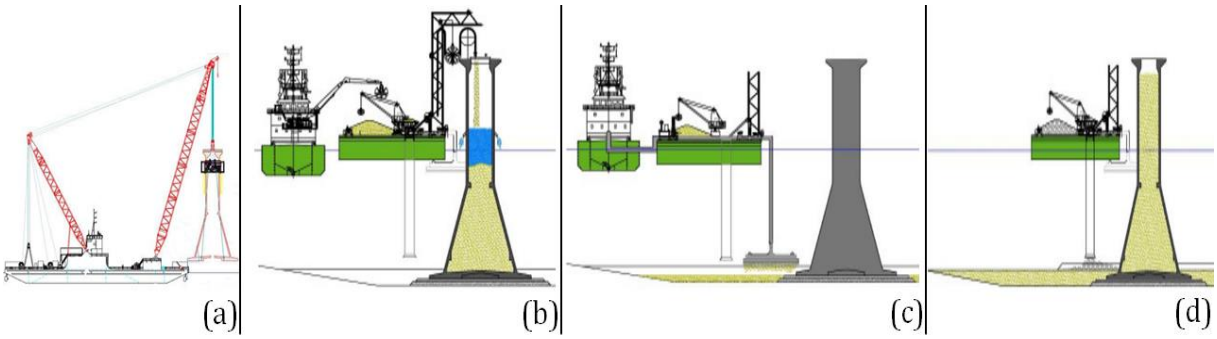

FIGURE 2-8: Installation of gravity based foundations [26]

2.4.1.3. Piled foundations

Piled foundations consist of a large diameter steel pipe that extends into the soil from the seafloor level. The soil characteristics and the magnitude of the design loads govern the dimension of each pile independently. The maximum applied moment fixes the order of magnitude of the embedded length, usually between 25m and 35m. The diameter closely depends on the soil resistance and on the interaction between the soil and the pile behaviour at failure, and is expected to range between 4m-6m, with the most recent projects showing up to 7.5m diameter. The thickness is finally determined on the basis of fatigue or buckling considerations [20][27]. Piles are introduced as foundations in many OWT applications, either alone in case of monopile, or in group in order to support multi-pile and jacket substructures, or to be used as anchor for floating structures.

The vertical load components on piled foundations, depicted in blue in Figure 2-9, are withstood through lateral and tip friction. As far as the eccentric horizontal load components and the ensuing applied moment are concerned, they are transferred through lateral soil stiffness in case of monopile or through a couple of tensile and compressive loads in case of multipile or jacket substructures [20]. This is represented in red in Figure 2-9.

There exist two main installation methods, for pile elements in offshore sites, as a function of the surrounding soil conditions. Driven steel piles are used in the majority of cases, and are put in their operational position by vibration or impact of an underwater hydraulic hammer. Drilled and grouted piles are favoured either with a hard layer such as emerging bedrock that

prevents pile driving or in case of crushable sediments layers such as calcareous sand in order to ensure sufficient shaft resistance. A tubular pipe is initially embedded through uncemented layers to support the edges during excavation which is undertaken by a drilling rig until the target depth. Finally, the pile is inserted into the oversized hole that is subsequently plugged by grout [20]. However, due to its low time and cost effectiveness and due to its high environmental impact especially in terms of noise during installation phase, this process is hardly ever implemented. Once in place, the piled foundation and the substructure are connected to the tower by a transition component, and scour protections consisting of layers of size-classified gravels are placed to prevent water flows from eroding the soil cover around the pile base [28].

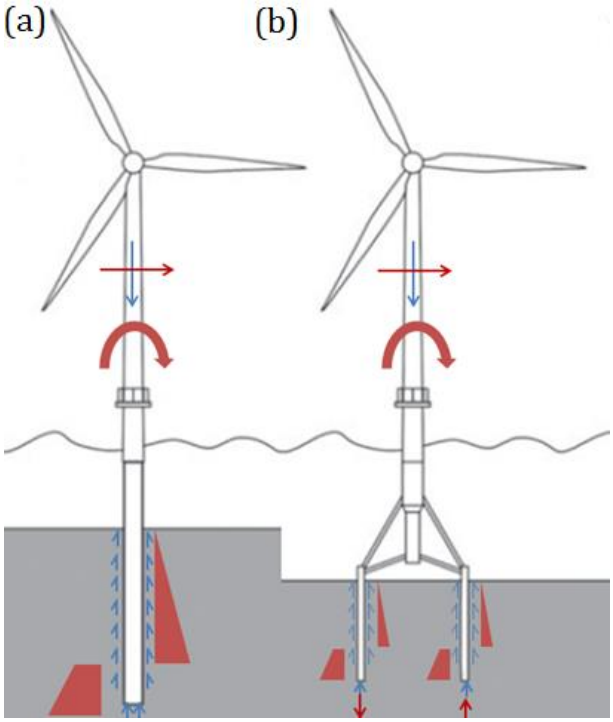

FIGURE 2-9: Load components applied on: (a) monopile, (b) multipile [27]

The piles foundation concept is at the moment the best-known solution for OWT foundations, and directly comes from the mature piling method that is used onshore. This expertise has led to a mass production thanks to both the simple conception and fabrication processes and thanks to the robust installation in most of the soil conditions. Nowadays, the piled foundation arises as the most advanced and cost-effective technology, and is therefore logically the most common type of OWT support structure installed on a global scale.

2.4.1.4. Suction caisson foundations

Suction caisson foundations, also referred as suction skirt or suction bucket foundations, consist of large cylinder-shaped steel structures, closed at the top and open at the bottom like upturned buckets [20]. This concept exploits the suction phenomenon to penetrate deeper into the seabed, and takes advantage of the weight of the soil plug enclosed in the skirt to provide structural stability, in a similar way as GBF's. This support structure can be implemented alone in case of a monopod substructure, or in an assembly of three or four in case of jacket and multipod substructures. Since this master dissertation is dedicated particularly to suction

caissons foundations, they will be treated in further details in chapter 3 “Suction caissons for offshore wind turbines”.

2.4.2. Moored floating OWT structures

2.4.2.1. Substructure

The ballast stabilized configuration (Figure 2-10 (a)) refers to spar-type buoy that consists of a slender vertical and cylindrical element, split into two main parts. An upper empty tank is used to support the OWT platform, and to ensure flotation by raising the centre of buoyancy. A lower container is on the contrary filled with heavy ballast weight to offset the external loads applied on the topside turbine, by lowering the centre of gravity of the floating support structure below the sea level and the centre of buoyancy. These two components create a restoring force that brings the structure back to its upright position. Together with mooring lines, this system provides the required inertial resistance to stabilize the OWT platform [24][29][30]. The simple design of spar-type buoy has the advantages of limiting the mooring installation costs, as well as the critical oscillations induced by waves, but requires a higher water depth to operate [31].

The mooring line stabilized configuration (Figure 2-10 (b)) refers to a tension leg platform (TLP) which consists of a slender vertical and cylindrical buoy, with an ended node connecting three or four floating supports. Out of each individual leg, leaves a group of axially stiff tethers that forms together a tension leg. The other extremity of the mooring system is anchored at the foundation level, and therefore, the structural stability of the OWT platform comes from the balance between the excess buoyancy of the TLP and the tension in the vertical mooring lines. As a result, this kind of support structure has a high stiffness in the vertical plane and a significant flexibility in the horizontal plane. It is interesting to note that the TLP is intentionally maintained underwater to restrain the cross-section subjected to wave impacts [30][32]. TLP’s have the advantages of being lightweight structures with limited wave-induced motion and of being assembled onshore. However the mooring installation costs are relatively high, and the transport and the installation are made complicated by the relative instability of this type of substructure [31].

The buoyancy stabilized configuration (Figure 2-10 (c)(d)) refers either to a semi-submersible barge including a water tank or tri-floater tanks connected by an open space truss, which combines the design features of the two other types of substructure. The stability of the structure is ensured through the tank flooding management, which provides sufficient weight to maintain the OWT platform in an upright position, and adequate buoyancy to allow the platform to float [29][33]. The buoyancy stabilized configuration has the advantages of combining onshore construction, simple transportation on site, and low mooring installation costs. However the fabrication is quite tricky and requires more materials with respect to the two other concepts [31].

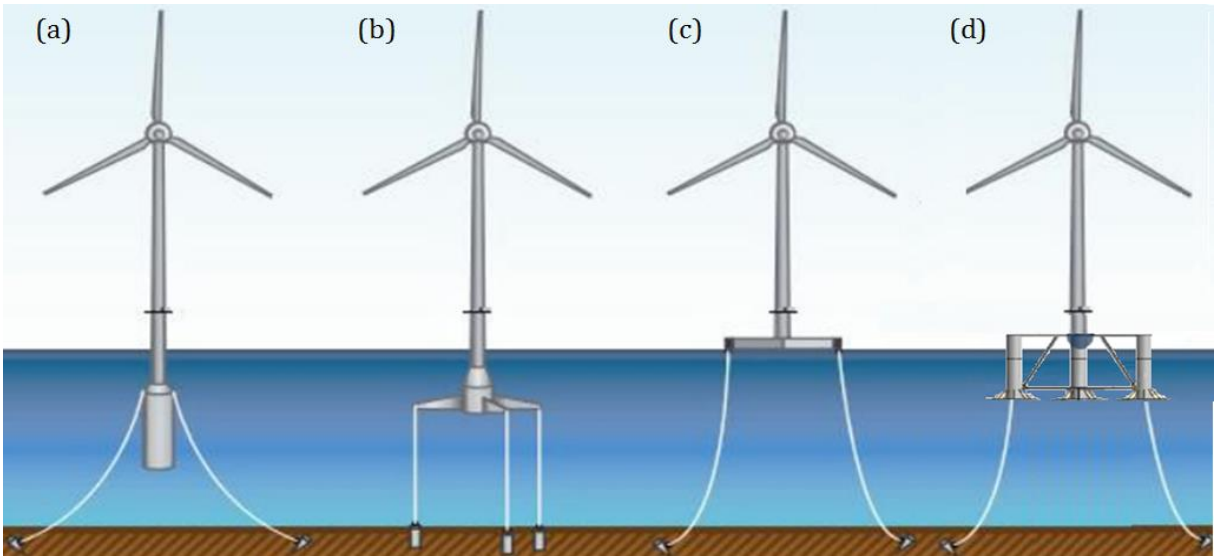

FIGURE 2-10: Moored floating substructures : (a) Ballast stabilized configuration, (b) Mooring line stabilized configuration; Buoyancy stabilized configuration : (c) semi-submersible barge including water tank,(d) tri-floater tanks connected by an open space truss [34]

2.4.2.2. Mooring system

The catenary mooring system (Figure 2-11 (a)) takes a catenary curve between the OWT platform and the seafloor, and has an important segment of its line lying on the seafloor. This system consists of steel wire ropes or chains to withstand the predominant horizontal load in moderate to deep waters [35].

The taut mooring system (Figure 2-11 (b)) takes a straight inclined line between the OWT platform and the seabed. This angle creates both horizontal and vertical loading components in the line. Since this mooring system is developed to be used in deep to ultra-deep waters, the self-weight of the line plays a negative role on the design which has led to the use of synthetic ropes in place of steel wire ropes [35].

The vertical mooring system (Figure 2-11 (c)) takes a vertical line between the OWT platform and the seafloor. Due to this right angle, there is no segment of the line lying on the bed and therefore, the system is nearly only subjected to a vertical tensile load. This mooring system is formed from steel wire ropes and mainly employed with TLP in not too deep waters [35][20].

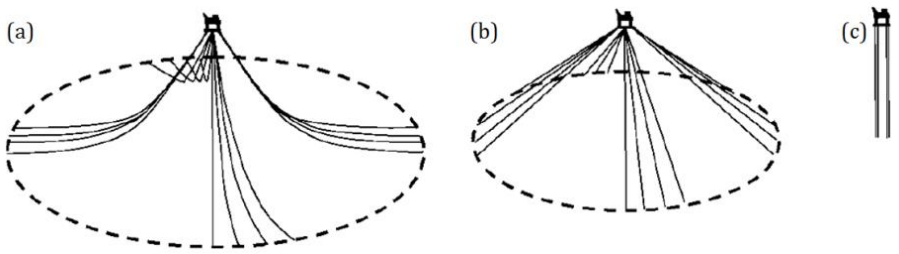

FIGURE 2-11: Mooring systems : (a) Catenary mooring system, (b) Taut mooring system, (c) Vertical mooring system [20]

2.4.2.3. Surface gravity anchor

The surface gravity anchor is a type of anchoring for moored OWTs that is made of a structural component filled with bulk granular and that monopolizes this self-weight together with the resulting friction at the anchor-soil interface to fix the mooring line into the seabed. Bulk fill consists of rock, concrete or heavier materials such as iron ores. The rigid structure of surface gravity anchors can be either an empty steel box with underside shearing ribs in case of a box anchor or a buried grillage installed underneath a heavy berm, as shown in Figure 2-12 (a) and (b) respectively. This anchoring system is exclusively used to secure the catenary mooring lines in not too deep waters. Failure occurs by horizontal sliding or by limited bearing capacity for the first kind of structure and also by pull-out of the grillage, by erosion or by slope instability for the second type of surface gravity anchor [26][36].

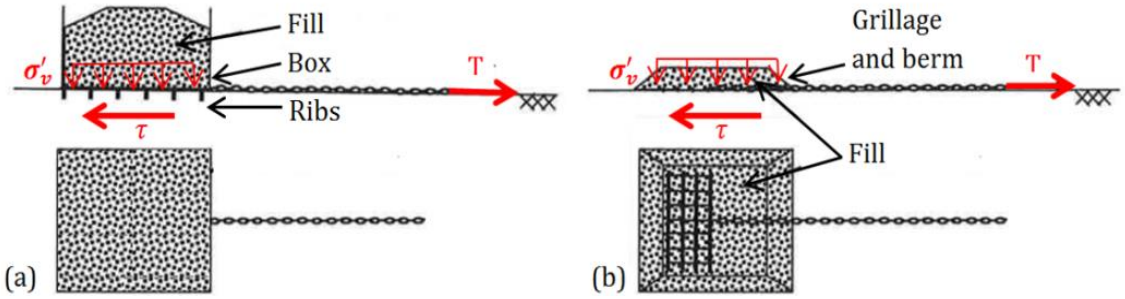

FIGURE 2-12: Surface gravity anchor: (a) box anchor, (b) grillage and berm anchor [36]

2.4.2.4. Pile anchor

The pile anchor refers to the same type of embedded system as for bottom mounted OWTs (cfr Figure 2-13), which consists of either driven or drilled and grouted steel piles with the mooring line attached to the tube at a certain level below the mudline (Figure 2-13 (a)). The mooring line is attached at a padeye and consists of either a catenary or a taut, since the pile anchor are able to resist both horizontal and vertical loads. For this kind of anchoring technique, the holding capacity is developed through the friction at the interface between the anchor and the surrounding soil, in the same way as traditional piled foundations [20][37].

The dynamically penetrating anchor (DPA) is a third type of pile anchors (Figure 2-13 (b)) specific to moored floating structures, which comprises a rocket-shaped tip and a cylindrical steel shaft, filled with heavy ballast. The DPA is released from a specific height above the seabed, in order to reach a high velocity by freefall and to penetrate and get fixation deep into the seabed under its massive self-weight. The final holding capacity is a function of the embedded depth and thus of the subsoil conditions and the drop height of the DPA [20][37]. This concept comes from a simple and trustable design, and is also easy and cheap to build and to install as no ROV is required. An accurate positioning can be achieved despite uncertainty about the verticality. This recent technology is still under development and suffers from a lack of maturity [38].

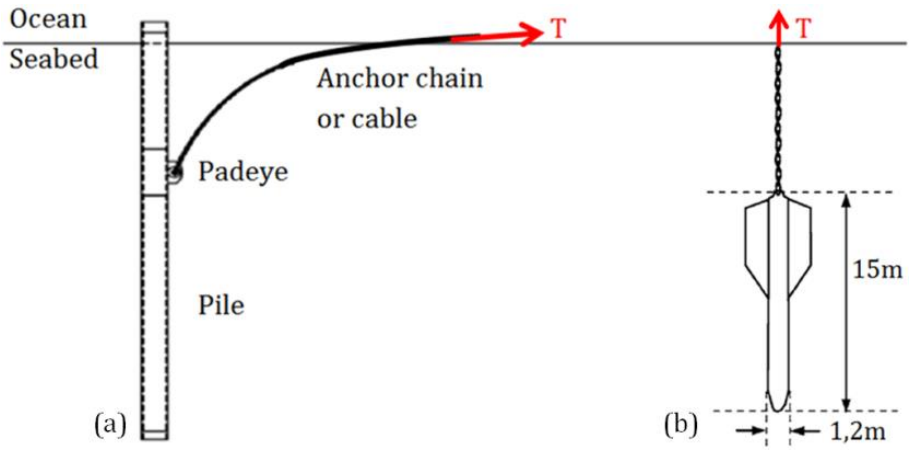

FIGURE 2-13: Pile anchor: (a) Driven or drilled pile [35], (b) DPA [20]

2.4.2.5. Embedded anchor

Embedded anchors are used in situations where more holding capacity is required. The traditional drag anchor presented in Figure 2-14 (a) is made of a broad fluke rigidly attached to a shank, which allows combining the bearing capacity of the plate with the friction capacity along the shank. This anchoring system is initially installed into the seabed with the aid of ROV, and then orientated in the working position by tensioning the mooring line to an appropriate load. It is practically applicable with a catenary mooring line in not too deep waters, and is therefore not suitable for large vertical loads.

The vertically loaded anchor (VLA) displayed in Figure 2-14 (b) is an alternative concept to the traditional drag anchor, suitable for taut mooring lines, and thus for both horizontal and vertical loads and higher water depths. The design consists of a thinner plate and anchor bridles in place of the shank [20][37]. This concept takes benefit from a smaller size and from a lighter weight to ease the transport to the site. The accumulation of experience has also led to robust design and installation techniques. This installation is thought expensive since it requires a certain number of specific vessels as well as ROV. Another drawback arises from the difficulty to reach the design depth and orientation of the VLA [38].

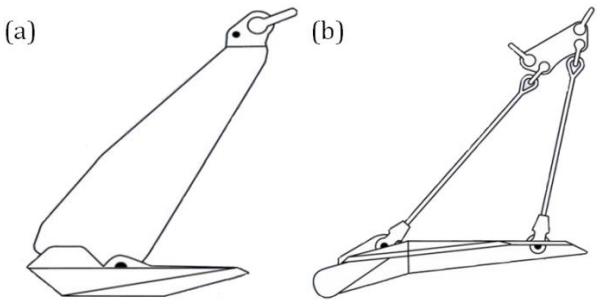

FIGURE 2-14: Embedded anchor: (a) traditional drag anchor, (b) vertically loaded anchor [20]

2.4.2.6. Suction caisson anchor

Suction caisson anchors refer to a similar concept of embedded system as for bottom mounted OWTs (cfr 2.4.1), namely a large tubular steel structure used as jacket in the seabed with the aid of suction. In addition, the padeye which holds the anchoring line is attached at a side posi-

tion of the suction caisson anchor as shown in Figure 2-15 (a) that optimizes the holding capacity. The concept of suction caissons will be treated in further details in chapter 3 "Suction caissons for offshore wind turbines".

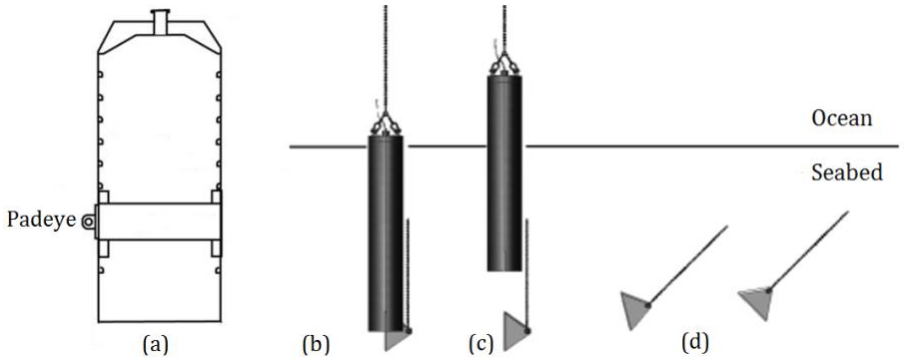

FIGURE 2-15 : (a) Suction caisson anchor and installation of SEPLA's: (b) installation of suction caisson, (c) suction caisson retrieval, (d) plate anchor keying [39]

The suction embedded plate anchor (SEPLA) consists of a rectangular plate anchor slotted at the base of a suction caisson, which has been developed to combine the low cost of the first technique with the precise installation of the second one. The deployment of SEPLA's is achieved through three stages: in a first time the suction caisson is embedded into the seabed, then the anchor plate is left in place at the required location, while the suction caisson is retrieved by using the reserve pumping, and finally the keying process of the plate is performed by tensioning the mooring line. This way of working, presented in Figure 2-15 (b)(c) and (d), helps to maximize the holding capacity of the SEPLA [20][37][39], but suffers from a low time-efficiency compared to the traditional suction caisson anchors [39].

2.4.3. Summary of supports for OWTs

The flow chart reported in appendix A gives an overview of all the various combinations of substructures and foundation types that can be put in place to serve as OWTs support.

Chapter 3
Suction caissons for offshore wind turbines

3.1. Introduction

This chapter aims at investigating more thoroughly the suction caisson type of foundation for the application of OWTs. Firstly a general description of the suction caisson technology is proposed, as initiation. Then the advantages and disadvantages of this type of foundation are discussed, and the characteristic loads to consider in an offshore environment are briefly defined. Subsequently, the installation process in clay and sand is explained and basic analytical rules are given. Further on, the design principles for the in-service performances of the suction caisson are broached.

3.2. General description

The first large scale application of suction caisson foundations – also suction skirt, suction bucket foundations - in the offshore industry dates back to the early 1980's. The suction concept was developed a temporary mooring anchor system for floating petroleum platforms, and was followed a few years later by the very first permanent structure. These worldwide accumulated experience and expertise in the oil and gas field have been transposed to the offshore energy sector, which is looking for innovative foundation systems to deal with the rising number of OWTs installed further from the shore [40][41]. Though key differences between the two sectors require adjustments in the original suction caisson design. In particular, offshore wind farms encompass multiples small and shallow turbine foundations that involve mass production for time and installation efficiency, whereas offshore oil rigs deal with large and one-off projects with their own foundation design. Suction foundations for OWTs must also withstand a reduced vertical load component, and larger horizontal and overturning moment loadings [42][43]. Anyway, Suction caisson foundations arise as an attractive, cost-effective and low-noise alternative to driven pile foundations for the future.

Applications of suction caisson foundations in the offshore energy market have already been implemented in Europe. Between 2003 and 2008, a full scale 3.0 MW offshore wind turbine supported by a suction caisson prototype was installed in a testing basin in the north of Denmark, in order to monitor the operational performances of this concept [44]. In 2014, monobucket foundations were built in three offshore wind farms in the UK portion of the North Sea,

as part of a trial installation programme. In the same year, the first suction caissons for a three-legged jacket substructure were installed at 25m water depth in the Borkum Riffgrund 1 offshore wind park, about thirty kilometres away from the North West coast of Germany. It is intended to serve as a support for a 3.6MW turbine. In the coming years, this technology is expected to expand in the European waters: twenty 8MW offshore wind turbines mounted on jackets with suction caissons are planned to be erected in the neighbouring wind farm of Borkum Riffgrund 1, and another eleven OWTs set down on suction caissons are commissioned for the first half of 2018 for the Scottish Aberdeen Bay wind farm [45][46].

By definition, a suction caisson refers to large and rigid cylinder-shaped steel structures, sealed at the top and open at the bottom like upturned buckets [20]. The ring wall of the caisson known as the skirt is defined by its length L and thickness t and is welded together to the head part, called the lid which has a stiffened plate or dome shape of diameter D, and which includes a pump or vent system in order to apply a differential pressure across this upper face during the installation process. All this component terminology is sketched in Figure 3-1 which gives a general overview of a conventional suction caisson for OWTs [47]. The concept exploits the suction phenomenon to penetrate deeper into the seabed and offers an alternative to GBF's and pile foundations for future offshore wind projects.

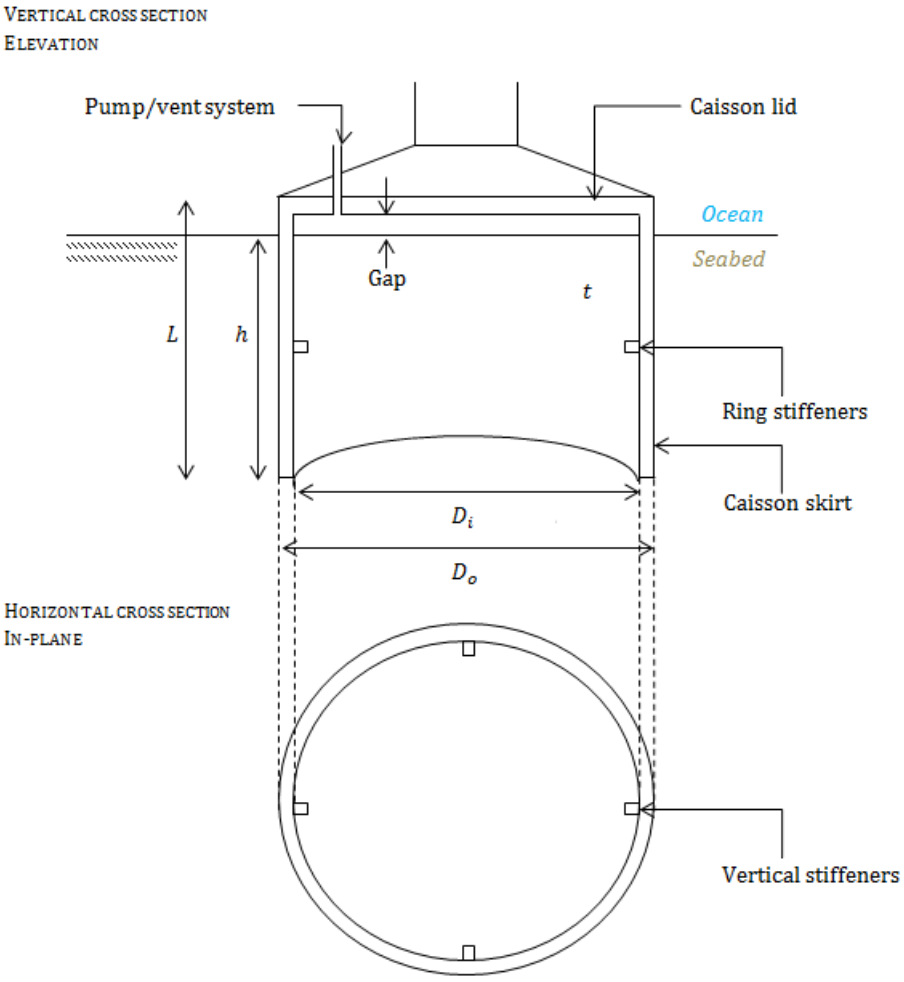

FIGURE 3-1 : Suction caisson component terminology based on vertical and horizontal cross sections

This support structure can be implemented alone in case of monopod substructure, or in an assembly of three or four in case of jacket and multipod substructures. Single monopods are suitable for shallow water depths around 15m – 20m, and are mainly subjected to horizontal (H) and moment (M) loadings. On the countrary, multiple leg options are favoured in intermediate sea level deeper than 30m, and are primarily loaded in the vertical (V) direction given that the overturning moment is converted into a push and pull mechanism. A set of individual suction caissons can also be used to firmly anchor the floating offshore platforms in case of very deep water, and have to withstand really different loading cases[23][43][47].

The global geometry of the caisson is governed by its slenderness ratio $\frac{D}{L}$. A large ratio, namely $\frac{D}{L} > 1$ is associated to shallow foundations that make use of the weight of the soil plug enclosed in the skirt to provide structural stability to the OWT, in a similar way as GBF's. Small ratios, namely $\frac{D}{L}$ in the range $[0{,}5\ ;\ 1]$ refer more particularly to slender foundation units, whose behaviour is closer to that of driven piles in greater water depths. The array of conventional diameters for suction caisson foundations starts around a few meters for small monopod or multipod structures, and reaches more than ten meters in large-scale projects (12m diameter for the mono caisson prototype in Frederikshavn). As far as skirt length is concerned, it is a direct function of the diameter, and of the growing penetration resistance with the embedded depth (13m skirt length for coming suction caissons in Aberdeen Bay). The skirt thickness to diameter ratio $\frac{t}{D}$ is very small, in the range $[0{,}3\% - 0{,}6\%]$ which makes suction caissons belong to the class of thin shell structures. The high sensitivity to shell buckling in the installation phase and under large vertical load requires the placing of ring and vertical stiffeners, especially in clay where the slenderness ratio is higher [23][41][48].

3.3. Pros and cons

The extensive use of suction caissons in the oil and gas industry has already highlighted the versatile capacity of the suction caisson technology, and the large number of advantages in comparison with the few drawbacks.

Suction caissons benefit from a real cost-effectiveness in relation to conventional foundation techniques for bottom-mounted OWTs. This cost competitiveness comes on the one hand from the low cost of the raw material and on the other hand from the reduced impact of the installation process on the total budget [49].

The suction caisson is indeed a lightweight structure which requires less steel than piles at the manufacturing stage. Nevertheless, the labour expenses are far more significant since this foundation type incorporates a lot of complex welding details in its design [48][50].

The installation of suction caissons is the stage of the project where most of the savings are achieved. Firstly, it is a very rapid procedure, which can be completed within one single working day [21]. Secondly, there is no need for sophisticated installation equipments such as underwater hammers used for pile embedding. The insertion of the caisson into the seafloor only requires a pump whose functioning is not altered by the water depth. Moreover, the low noise emission during the positioning of the caisson is a real attractive feature regarding environmen-

tal issues. As the structure can be floated to the installation site, the number of transportation and crane vessels is reduced. This implies to have a sufficient water level on the route of the suction caisson, which may lead to problems particularly in harbour zone and near the coastline [48][50].

The suction caisson technology also takes advantage of ahigh flexibility and accuracy during the implantation phase compared to the other foundation types. By applying the reverse installation procedure, and injecting water in the caisson, it is possible and easy to entirely remove the caisson in order to decommission old generation OWTs, to reuse the caissons in another area, or to prevent failure if something goes wrong during the installation process[48][50].

The steps preceding and following the embedment of the foundation are also greatly shortened since only little seabed preparation, and fewer needs for scour protection are required [50].

To date, the main disadvantage arises from the uncertainty linked to the behaviour of the structure in some soil conditions, which makes their use unsuitable so far [43].

3.4. Conditions in marine environment

3.4.1. Soil conditions

The seabed is commonly made of thick sediments near the coast line and thin-sized particles in mid-oceanic ridges. Fine-grained sediments are indeed more susceptible of being transported away from the shore than coarse sediments. Depending on the hydrodynamic site conditions, some areas with strong bottom currents can be devoid of sediments, whereas others can be characterized by a continual sediment accumulation. Moreover, the stress state of the seabed sediments may be defined as normally consolidated if the sediments have not been altered yet since their slow deposition, as overconsolidated if events such as a gradual erosion or submarine landslides occur, or as incompletely consolidated if the excess pore water pressures (PWP) does not have the opportunity to dissipate [20].

The soil classification is based on the particle size. Cohesionless soils are detailed as materials with really limited internal bonds, and include either large-size grains such as gravels, intermediate-size grains such as sands and small-size particles such as silts. Cohesive soils such as clay refer to very small flake-shaped minerals of the order of one μm. The failure behaviour of suction caissons in this particular type of soil is studied in this dissertation. In such cohesive soils, particles stick to each other with the help of water, because of their negatively charged surface which attracts the positive charge of water [35].

The total vertical stress in the soil σ_{tot} is given by Equation 3-1 of Terzaghi as the sum of the effective stress σ' and the pore water pressure u. When a load is applied, the variations of these terms are considered [20].

$$\sigma_{tot} = \sigma' + u$$
$$\Delta\sigma_{tot} = \Delta\sigma' + \Delta u \qquad \text{EQUATION 3-1}$$

In sandy soils having high permeability, a drained response is initiated. Under loading, the soil has a tendency to compress and the pore water is immediately drained away to zones of low

pressure ($u = 0$) while the total load is entirely carried by the soil skeleton ($\sigma_{tot} = \sigma'$). If the applied loads are shortly repeated or cyclic as it is usually the case for OWTs, a singular soil failure mechanism, known as liquefaction can occur. Between two successive loads, the pore water does not have the time to drain, and increases in pressure until exceeding the effective contact stress that keeps the grain in contact. As a consequence, the soil looses its strength and imposes large and irregular settlements to the foundation [20].

In clay soils having low permeability, an undrained response is faced. Under loading, the load is first carried wholly by the pore fluid, without instantaneous volume change. Then as time is running, the pore fluid is progressively drained from the soil skeleton, allowing it to undergo compression. This time-dependent reduction of the void ratio e associated with the transition from undrained to drained conditions is best known as consolidation process [20].

3.4.2. Loading conditions

Foundations are designed to transfer the monotonic and cyclic loads applied on the superstructure into the soil, in a way that ensures structural stability. The typical loading conditions of the support structures for OWTs combine reduced vertical components due to moderate gravity loads and significant components of lateral loading and overturning moment which arise from the harsh maritime environment [51]. Since the loading consists of cyclic events of different magnitudes and durations, such as vibrations, wind, waves and buoyancy, the behaviour of suction caissons is dynamic. If the support structure is a multipod, the overturning moment is converted into a push-pull loading case of the suction caisson. The light self-weight of structures for OWTs exposed to large overturning moments during storm period requires to consider the behaviour of the foundation under tensile load as one of the main concerns. The wave characteristics of storms with a 50-year return period, meaning an annual probability of occurrence of $\frac{1}{n} = \frac{1}{50}$, are commonly employed for the design of offshore wind turbines[52].

Each of the design loads involved in the working conditions of the turbine refers to one specific type namely, permanent, variable, environmental, accidental or deformation loads.

3.4.2.1. Permanent loading

The permanent loading of an OWT, denoted as G, refers to the self-weight or the dead weight of the structure. In particular, it covers all loads having a constant point of application, direction and intensity, such as the mass of all structural elements and permanent equipments, and the persistent hydrostatic pressure on the submerged components [52].

3.4.3.2. Variable loading

The variable loading of an OWT, denoted as Q, refers to the time-dependent or live loads applied during the operational conditions of the turbine. In particular, it covers all loads having a variable point of application, direction and intensity. The relevant types of variable loads for an OWT structure include activation loads, accidental loads, deformation loads, loads related to the fabrication, crane manoeuvres and installation process, and loads on the access platform and on the internal equipment. The characteristic value is obtained by considering the extremum value induced by the most unfavourable load case [52].

The activation loads are forces of a dynamic nature that follow from the working procedure and the periodic maintenance operations performed on the wind turbine. The activation loads are most of the time assimilated to environmental loads in the design strategy since they are evaluated from an analysis of the wind turbine under wind load. The accidental loads correspond to impacts on the structure that are related to mechanical and operating irregularities or failures. It comes principally from exceptional loading cases such as explosions, fires, impacts during maintenance works, collisions with vessels or helicopter, or unusual impacts from large breaking waves. The deformation loads characterises phenomena that impose a structural strain, such as air and sea temperature variations, or settlement of the foundation system[51][52].

3.4.2.3. Environmental loading

The environmental loading of an OWT, denoted as E, refers also to live loads that have a variable point of application, direction and intensity during the operational use of the structure. Therefore, they deal with a high degree of uncertainty and are really site and time specific, with time periods extending from a fraction of a second to many hours. The environmental loads work on the OWT through very site dependent load cases, and play a major role in the optimization of the design costs. Examples belonging to environmental loading category include wind loads, hydrodynamic loads induced by waves and current, seismic loads and snow and ice loads [51][52]. Among those, wind and wave loads accountable for cyclic tensile loading during extreme storm events are particularly important within this dissertation, and their features will be discussed in further details.

Wind

The origin of wind-induced loads on the components of an OWT above the waterline is twofold. Primary loads are generated by direct wind inflows on the exposed structure, and correspond mainly to aerodynamic blade loads and aerodynamic drag forces on the turbine tower and on the nacelle [58]. Secondary loads arise from the indirect motions and vibration of the operating installation generated by wind turbulences. This mainly relates to centrifugal and Coriolis forces as well as gyroscopic forces and breaking forces [51][52].

The derivation of the wind-generated loads required for the design of OWTs is based on area-specific wind speed measurements gathered over a sufficient period of time. Statistical data of the design wind are commonly defined by a 10-minute mean wind speed U_{10} and a standard deviation σ_U. The DNV [52] has proposed a relevant formulation (Equation 3-2) of the mean wind speed U for a return period below 50 years, representative of the usual weather conditions that are encountered in the North Sea.

$$U(T,z) = U_{10}\left(1 + 0{,}137\ln\frac{z}{h} - 0{,}047\ln\frac{T}{T_{10}}\right) \qquad \text{EQUATION 3-2}$$

Where

T, T_{10}	Averaging period and 10-min mean wind period
U, U_{10}	Mean wind speed and 10-min mean wind speed
z	Height above sea level

The derived wind velocity is height-dependent and can subsequently be translated into a wind-generated force F_{wind} on the OWT. This force is basically estimated by considering the mass of air with speed U that passes through the circumference delimitating the considered component area A, and by allocating a shape factor specific to the geometrical element. It follows the Equation 3-3 below [53]. The point of application of this force is assumed to be located at the centre of the stressed component.

$$F_{wind} = \frac{w}{2g} U^2 C_g A \qquad \text{EQUATION 3-3}$$

Where

w	Weight density of the air
g	Gravitational acceleration of the earth
C_g	Geometrical factor of the OWT component
A	Area of the OWT component

Waves

Wave-induced loads on the submerged parts of an OWT are correlated to the wind loads owing to the fact that waves originate from the wind pressure exerted on the sea surface. Wave conditions at a specific site combine locally generated wind waves and swell waves caused by distant weather system [52].

The derivation of the waves-generated loads required for the design of OWTs is based on area-specific wave measurements collected over a sufficiently long period of time. These full scale data recording together with model tests provide the most relevant parameters involved in the analysis, among which the (significant) wave height $H_{(S)}$, the spectral peak period T_p , the wave velocity and hydrodynamic coefficients. In particular, the significant wave height which measures the variability in the arbitrary wave heights, and the spectral peak period linked to the mean wave period – the time between the zero-crossings of two successive waves – are of great importance in order to define the wave climate. This knowledge of the wave climate enables to assess the relative importance of inertia, drag and diffraction in the total wave force [52][53].

Large volume structures are characterized by dimensions of the same order of magnitude as the wave lengths λ exciting the installation, and therefore interfere with the wave kinematics. Wave-induced forces are then evaluated under a wave diffraction analysis.

In case of slender structural members, such as the submerged part of an OWT tower, having cross-sectional dimensions sufficiently small, wave-induced forces are derived from Morison's equation (Equation 3-4). In this formulation, the horizontal wave force on a vertical element dz at level z consists of the summation of the drag and inertia contributions [54]. The point of application of this wave load is assumed to be located at the mean wave height that is the distance between the trough of the wave and its crest.

$$F_{waves} = \underbrace{C_D \frac{\gamma_w}{2g} D_{tower} \frac{\partial u}{\partial t} \left|\frac{\partial u}{\partial t}\right|}_{Drag\ term} + \underbrace{C_M \frac{\gamma_w}{g} \frac{D_{tower}^2 \pi}{4} \frac{\partial^2 u}{\partial t^2}}_{Inertia\ term} dz \qquad \text{EQUATION 3-4}$$

Where

F_{waves}	Unitary wave force vector normally acting on the member axis
$C_{D/M}$	Drag/Inertia coefficient
γ_w	Unit weight of water
D_{tower}	Effective diameter or width of the submerged part
$\frac{\partial u}{\partial t}$	Horizontal wave-induced velocity of water
$\frac{\partial^2 u}{\partial t^2}$	Horizontal wave-induced acceleration of water

Other environmental loads

Current loads on OWT arise from varying mechanisms including subsurface currents due to wind and atmospheric pressure variations through a storm, and tidal currents. In shallow to moderate water levels coinciding with bottom-mounted structures, currents are stronger and intervene in the environmental load to a greater extent than in deep offshore sites. In offshore wind farms near the shoreline, currents are susceptible to provoke erosion of soil particles around OWT foundations and to cause the wave height and the period to fluctuate [52][54].

Ice loads on OWTs must be considered in the design especially in offshore parks located in the arctic areas of the North and Baltic Seas. Ice-induced loads are relatively difficult to assess, mainly on account of the uncertainties on the geometry, on the nature and on the properties of drifting ice [51][54].

Earthquake loads are included in the design of OWTs that are intended to be installed in seismic regions. It is achieved by performing vertical and horizontal analyses under the 2D earthquake acceleration. In the vertical direction, buckling calculations are conducted for loads applied on the tower under the maximum vertical acceleration, whereas in the horizontal direction, the analysis is carried out for a concentrated mass on top of the tower to take the inertia of the nacelle, of the rotor and of the hub into account [52].

3.4.3. Typical loading magnitudes acting on OWTs

Typical loading magnitudes acting on a 3.5 – 5 MW turbine, installed on suction caissons in water depths ranging from 20 to 50m are mentioned in the literature [55][56]. This example deals with an installation characterized by a rotor amplitude in between $[120\text{m} - 160\text{m}]$ and a turbine level comprised in the range $[110\text{m} - 160\text{m}]$ above the seabed, as shown in Figure 3-2 (a). Net horizontal loading under extreme conditions amounts to 60% of the vertical dead weight of the superstructure included in the region of $[6\text{MN} - 10\text{MN}]$. Wave loading intervenes for $[3\text{MN} - 6\text{MN}]$ in the horizontal load and acts at a height of about $[10\text{m} - 50\text{m}]$ above the seabed. As far as wind loading is concerned, a $[1\text{MN} - 2\text{MN}]$ contribution is added to the total horizontal load and is assumed to act at the turbine level. Average values of the previous intervals are used for the calculations, and in these conditions, the maximum overturning moments

are expected to be as high as **320MNm** and **300MNm** under wind and wave loads respectively [56].

As previously mentioned the sources of the horizontal cyclic loading comprise wave and wind actions as well as the loads induced by seism or the rotation of the blades. Here only the main wind component is investigated. In the vertical direction, cyclic loading comes from variable buoyancy but is sufficiently small to be neglected [56].

The superstructure supported by either a monopod or a tripod configuration is taken into account. Wind is assumed to impose a constant reduced horizontal load of **0,5MN** during a storm. Wind speeds encountered in such events are indeed much higher than the maximum allowable wind speeds to produce power and therefore, the blades are slightly angled which reduces the wind resistance. Maximum wind and waves loading are thus never applied at the same time on the OWT. Waves are assumed to exert a lateral load of **1,5MN** $\pm$ **3MN** and to be aligned with the wind force in the course of a storm [56].

3.4.3.1. Maximum loading on a monopod foundation

When a monopod substructure is used as displayed in Figure 3-2 (b), the static vertical loading and the cyclic horizontal and moment loading are resisted by one individual caisson at the same time. Table 3-1 stores the assessed average, maximum and minimum values of the overturning moment, as well as the horizontal and the vertical loads imposed on the OWT at the peak of the storm. Equation 3-5 gives the axial eccentricity h at which the resultant vertical and horizontal loads are applied, where M is the extremum overturning moment on the caisson and H involves the contribution of wind and wave actions.

$$h = \frac{M}{H} = 25{,}75\ m \qquad \text{EQUATION 3-5}$$

TABLE 3-1 : Indicative loading magnitudes for a 3,5-5MW OWT supported by one single suction caisson during a storm

	WEIGHT	WAVES		WIND	MAX	MIN
		AVERAGE	CYCLIC			
VERTICAL [MN]	8	–	–	–	10	6
HORIZONTAL [MN]	–	1,5	± 3	0,5	5	-1
MOMENT [MNm]	–	26,25	52,5	50	128,75	23,75
Level arm[m]	–	35/2	35/2	100	25,75	$-23{,}75$

3.4.3.2. Maximum loading on a tripod foundation

When a multipod structure is used as displayed in Figure 3-2(c), the static vertical and cyclic horizontal loading are equally apportioned over the number of installed caissons, whereas the moment loading is converted into an additional push and pull contribution on the foundation. In case of a tripod structure, this moment is substituted by an additional tensile force on the windward caissons and a compressive force on the leeward caisson. As a result, the moment loading on each single caisson becomes negligible with respect to the vertical and horizontal components. Table 3-2 stores the horizontal and the vertical loads imposed on the OWT at the peak of the storm.

Equation 3-6 encountered in the literature [56] is used to calculate the necessary spacing w between one individual caisson of the tripod arrangement and the centre of gravity in case the wind turbine rotates around the windward foundation. It results from the moment equilibrium around the rotation point, with assumptions that no tensile load can be taken in the upwind foundation and that the restoring moment is supplied by the vertical load V.

$$w = \begin{cases} \dfrac{H\,h}{V} & \text{for a quadripod structure} \\ \sqrt{3}\dfrac{H\,h}{V} & \text{for a tripod structure} \end{cases} \qquad \text{EQUATION 3-6}$$

Taking into account the axial eccentricity $h = 25{,}75m$ from the above case of one individual caisson under maximal loading, the required distance w between the middle point of the caisson and the foundation centre amounts to $16{,}54m$ for a quadruped substructure and $23{,}8m$ for tripod substructure.

TABLE 3-2 : Indicative loading magnitudes for the leeward caisson of a tripod substructure supporting a 3.5-5MW OWT during a storm.

	WEIGHT	WAVES		WIND	MAX	MIN
		AVERAGE	CYCLIC			
VERTICAL [MN]	$\frac{8}{3} = 2{,}6$	-	$\frac{3}{3} = 1$	$\frac{3}{3} = 1$	$\frac{14}{3} = 4{,}6$	$\frac{8}{3} = 2{,}6$
HORIZONTAL [MN]	-	$\frac{1{,}5}{3} = 0{,}5$	$\frac{3}{3} = 1$	$\frac{0{,}5}{3} = 0{,}17$	$\frac{5}{3} = 1{,}67$	$-\frac{1}{3} = 0{,}33$

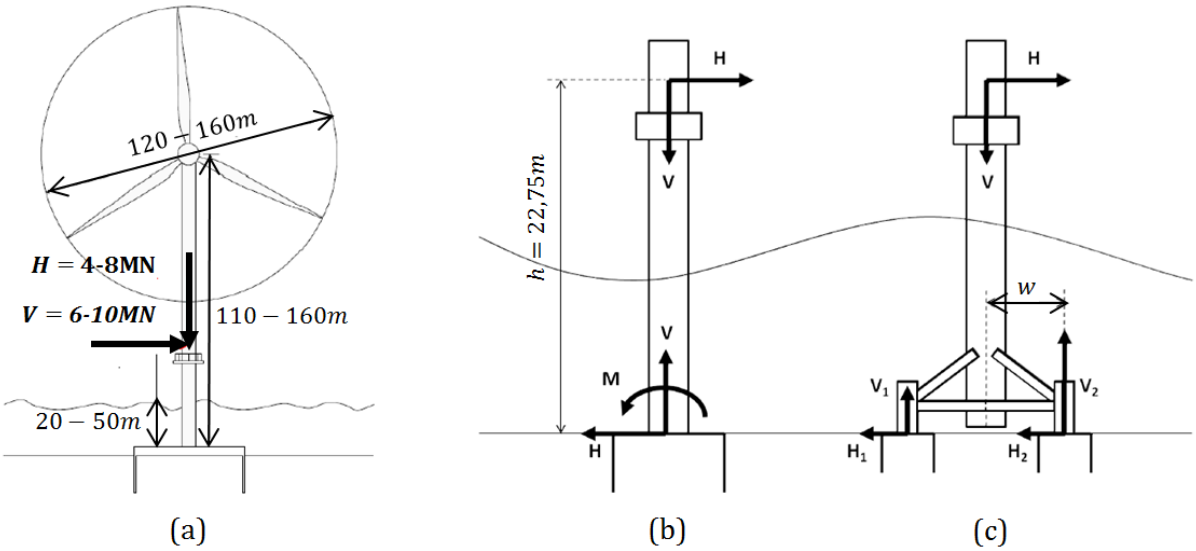

FIGURE 3-2 : (a) Typical loading on a 3,5-5MW OWT under extreme conditions, Equivalent loading acting on the OWT and reaction forces on the suction caisson in case of: (a) monopod, (b) multipod arrangement

3.5. Installation procedure

3.5.1. Basic principles

Suction caissons are the most appropriate type of offshore foundations in case the overlying structure has an insufficient vertical self-weight under extreme environmental loadings. This concerns in particular OWTs. The installation process of suction caissons is therefore carried out in two major straightforward steps. The initial stage is the partial penetration of the skirt under the effective self-weight of the caisson. Afterwards, a pressure difference is applied by suction on the top of the caisson, to obtain a complete penetration. The upper bound of the pumping rate will be reached when a critical suction related to zero effective stresses is obtained [58]. As it is advised to start the suction assist penetration at a sufficient embedded depth to have sufficient watertightness, a ballast load is commonly added on top of the caisson in the preliminary phase [58]. If a top structure is installed together with the support structure, additional weight can be obtained by flooding the inner tanks incorporated in the legs of the structure.

3.5.2. Installation in sandy soil conditions

The installation principle in sandy soil conditions illustrated in Figure 3-3 (a) refers to suction caisson penetration in coarse grained and high permeable sediments. This high permeability allows the development of a seepage flow field in the surrounding soil. The step by step installation process in sand is summarized here below [48][58].

1. Initially, the suction caisson foundation is lowered by gravity until touchdown with the seafloor.
2. Then, the self-weight penetration phase is achieved and an opened valve in the lid allows the evacuation of free-water that is enclosed inside the caisson.
3. During the transitional sub-phase, the trapped water under the suction lid is pumped out. The pressure deficiency inside the caisson generates a differential pressure with the outside that sucks up the pore water of the underlying sand layers.
4. An upward seepage flow is initiated within the soil plug, which consequently decreases the friction resistance and eases the penetration.
5. During the suction-assisted sub-phase, the pore pressure and the rate of pumping-out water progressively become constant which help to maintain the underpressure in the caisson. This way, the remainder of the caisson is gradually pressed into the seabed until the target embedment depth is reached. In sandy soils, the occurrence of liquefaction within the soil usually indicates that the critical suction has been reached.
6. Once the suction caisson has been properly installed, the pump is removed from the lid.
7. A small gap is usually maintained between the seabed and the bucket lid in order to deal with seafloor irregularities. This remaining space can be grouted under pressure to improve the moment capacity and the resistance to vertical settlements, when subjected to cyclic loading [59].

3.5.3. Installation in clay soil conditions

The installation principle in clay soil conditions that is illustrated in Figure 3-3 (b) refers to suction caisson penetration in fine grained and low permeable sediments. The lower permeability prevents seepage flows from developing on a large scale. The step by step installation process in clay is summarized here below [48][58].

1. Initially, the suction caisson foundation is lowered by gravity until touchdown with the seafloor.
2. Then, the self-weight penetration phase is achieved and an opened valve in the lid allows the evacuation of the free-water that is enclosed inside the caisson.
3. During the suction assisted penetration, the opening in the lid is sealed and water is pumped out of the caisson. The lowering of the inside pressure gives birth to a downward pressure gradient onto the lid which constrains the skirt to penetrate deeper in the seabed until the target embedment depth is reached. In clay soils, a global uplift of the soil plug is expected once the critical suction is exceeded.
4. Once the suction caisson has been properly installed, the pump is removed from the lid.
5. A small gap is usually maintained between the seabed and the bucket lid in order to deal with seafloor irregularities. This remaining space can be grouted under high pressure to improve the moment capacity and the resistance to vertical settlements, when subjected to cyclic loading [59].

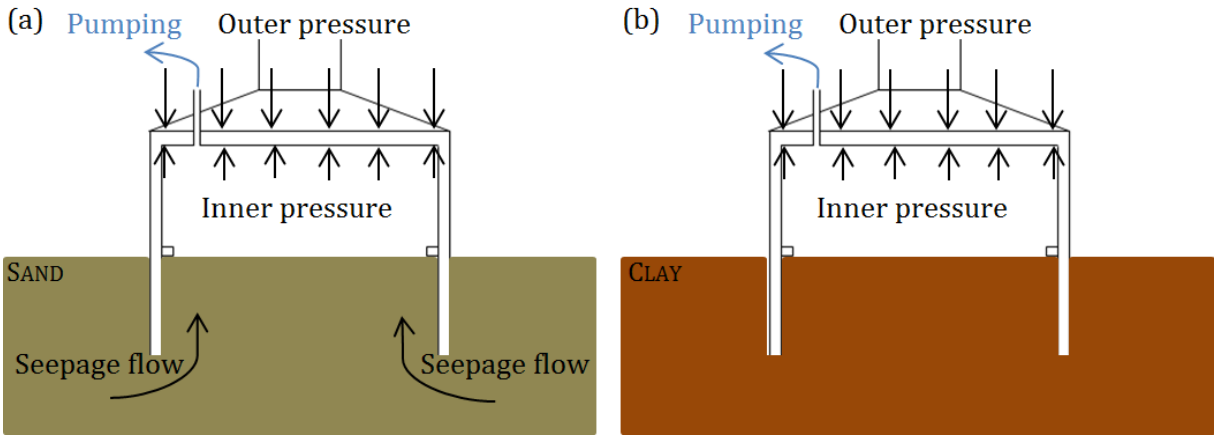

FIGURE 3-3 : Installation of a suction caisson in: (a) sand and (b) clay

3.5.4. Analytical approach

The analytical approach for the suction caisson installation offers a way to assess the penetration depth h that is reached in each of the two phases of the procedure, namely the self-weight penetration and the suction-assisted penetration respectively. It is based on an effective stress-approach whose principle is to calculate all the components involved in the penetration resistance as a function of the effective stresses [58].

For the initial stage, the self-weight penetration depth h is calculated by solving the relation between the driving force consisting of the self-weight of the submerged caisson, and the resistance forces including the inside and outside skirt frictions and the end bearing and overburden pressures on the annular tip, as expressed in Equation 3-7 and displayed in Figure 3-4 (a). There is intrusion of the caisson into the seabed as soon as the downward penetration force surpasses the counteracting resultant force [58][60]. The effects of stiffeners are not considered here.

$$Q_{phase\,1} = Q_i + Q_o + Q_{tip} \qquad \text{EQUATION 3-7}$$

Where

$Q_{phase\,1}$	Vertical capacity during the self-weight installation
Q_i, Q_o, Q_{tip}	Friction acting respectivelyon the inside and outside surfaces of the caisson, and end bearing capacity and overburden pressure on the skirt tip

In homogeneous clay, the unknown parameter h_c is assessed by making the assumptions that the submerged self-weight is equal to the penetration resistance, and that the strength of the clay is undrained and linearly increasing with depth [61]. Equation 3-7 can then be rewritten as Equation 3-8.

$$W' = \underbrace{A_i \alpha_i \bar{s_u} h_c}_{\substack{Friction\ resistance \\ on\ the\ inside}} + \underbrace{A_o \alpha_o \bar{s_u} h_c}_{\substack{Friction\ resistance \\ on\ the\ outside}} + \underbrace{\left(s_u N_c + \gamma_c' h_c N_q\right) A_{tip}}_{End\ bearing\ on\ the\ skirt\ tip} \qquad \text{EQUATION 3-8}$$

Where

W'	Submerged self-weight of the caisson
$A_i = \pi D_i$	Inside surface area of the skirt (per linear meter of penetration)
$A_o = \pi D_o$	Outside surface area of the skirt (per linear meter of penetration)
$A_{tip} = \pi D t$	Tip area
$\alpha_i = \alpha_o$	Adhesion factor assumed to be equal on the inner and outer surfaces
$\bar{s_u} = s_{u0} + \frac{\rho h_c}{2}$	Average undrained shear strength over the penetration depth
$s_u = s_{u0} + \rho h_c$	Undrained shear strength at the skirt tip level
N_c	End bearing parameter (cohesion) equal to 6.2 for shallow penetration and 9 for deep penetration
N_q	End bearing parameter (overburden) assumed to be equal to 1 for the undrained analysis

In homogeneous sand, the unknown parameter $\mathrm{h_s}$ is derived from the same principle, by using Equation 3-7 restated as Equation 3-9. Here the sand material is assumed to have a drained behaviour. The skirt friction terms are therefore function of the horizontal effective stress which can be calculated by multiplying the lateral earth pressure coefficient K times the vertical effective stress [62].

$$W' = \underbrace{\frac{1}{2}A_i K \tan(\emptyset_e)\gamma_s' h_s^2}_{\substack{Friction\ resistance \\ on\ the\ inside}} + \underbrace{\frac{1}{2}A_o K \tan(\emptyset_e)\gamma_s' h_s^2}_{\substack{Friction\ resistance \\ on\ the\ outside}} + \underbrace{\left(\gamma_s' \frac{t}{2} N_\gamma + \gamma_s' h_s N_q\right) A_{tip}}_{End\ bearing\ on\ the\ skirt\ tip} \qquad \text{EQUATION 3-9}$$

Where

$\emptyset_e = 0{,}9\emptyset_i$	External friction angle obtained from the internal friction angle whose value results from a drained triaxial test
K	Lateral earth pressure coefficient
N_γ	Bearing capacity factor (self-weight)

For the second stage, the suction-assisted penetration depth h is calculated by solving the same kind of vertical equilibrium, and by considering that an additional term of suction is acting as driving force within the caisson. This required suction S_{req} is applied as soon as the penetration under the submerged self-weight W' equals to the penetration resistance of the caisson in the initial phase $Q_{phase\,1}$ and will help mobilizing a greater penetration resistance $Q_{phase\,2}$. The additional vertical load $\mathrm{Q_{suct}}$ originates from the pressure differential across the tip of the caisson given by the applied suction times the internal cross-section area. This is formulated by general Equation 3-10 and illustrated in Figure 3-4 (b) [52][60].

$$S_{req} = \frac{Q_{phase2} - W'}{A_{base,i}} \qquad \text{EQUATION 3-10}$$

Where

S_{req}	Required suction for the installation of the suction caisson
Q_{phase2}	Vertical capacity during the suction-assisted penetration
$A_{base,i}$	Internal cross-section area of the caisson base

In homogeneous clay, the unknown parameter h_c is derived in a similar way as for the initial phase, by considering the additional effect of the suction and reorganizing Equation 3-10. This leads to final Equation 3-11 [61].

$$Q_{phase1} + S_{req}\, A_{base,i} = Q_{phase2}$$

$$W' + S_{req}\left(\frac{\pi D_i^2}{4}\right) = A_i \alpha_i \bar{s_u} h_c + A_o \alpha_o \bar{s_u} h_c + \left(s_u N_c + \gamma_c' h_c N_q - s\right) A_{tip}$$

$$\Leftrightarrow \quad W' + S_{req}\left(\frac{\pi D_0^2}{4}\right) = A_i \alpha_i \bar{s_u} h_c + A_o \alpha_o \bar{s_u} h_c + \left(s_u N_c + \gamma_c' h_c N_q\right) A_{tip} \qquad \text{EQUATION 3-11}$$

In homogeneous sand, the unknown parameter h_s is derived in a similar way as for the initial phase, by considering the additional effect of the suction and the resulting seepage flows that lower the tip resistance. According to HOULSBY and BYRNE [62], this capacity reduction can be taken into acount by applying to each term a weighting factor that varies with the embedment depth. This leads to final Equation 3-12 [56][58][62].

$$W' + S_{req}\left(\frac{\pi D_0^2}{4}\right) = \alpha_{in}(z) \times \underbrace{Q_i}_{\frac{1}{2}A_i K \tan(\emptyset_e)\gamma_s' h_s^2} + \alpha_{out}(z) \times \underbrace{Q_o}_{\frac{1}{2}A_o K \tan(\emptyset_e)\gamma_s' h_s^2} + \alpha_{tip}(z) \times \underbrace{Q_{tip}}_{\left(\gamma_s'\frac{t}{2}N_\gamma + \gamma_s' h_s N_q\right)A_{tip}}$$

EQUATION 3-12

Where

$\alpha_{in}(z) = f(z, A_i, a)$ Reduction factor applied to the inside resistance that depends on the penetration depth z, on the inner surface of the skirt A_i, and on a dimensionless factor a considering the excess PWP

$\alpha_{out}(z) = f(z, A_o, a)$ Reduction factor applied to the outside resistance

$\alpha_{tip}(z) = f(\alpha_{in}, \alpha_{out})$ Reduction factor applied to the tip resistance

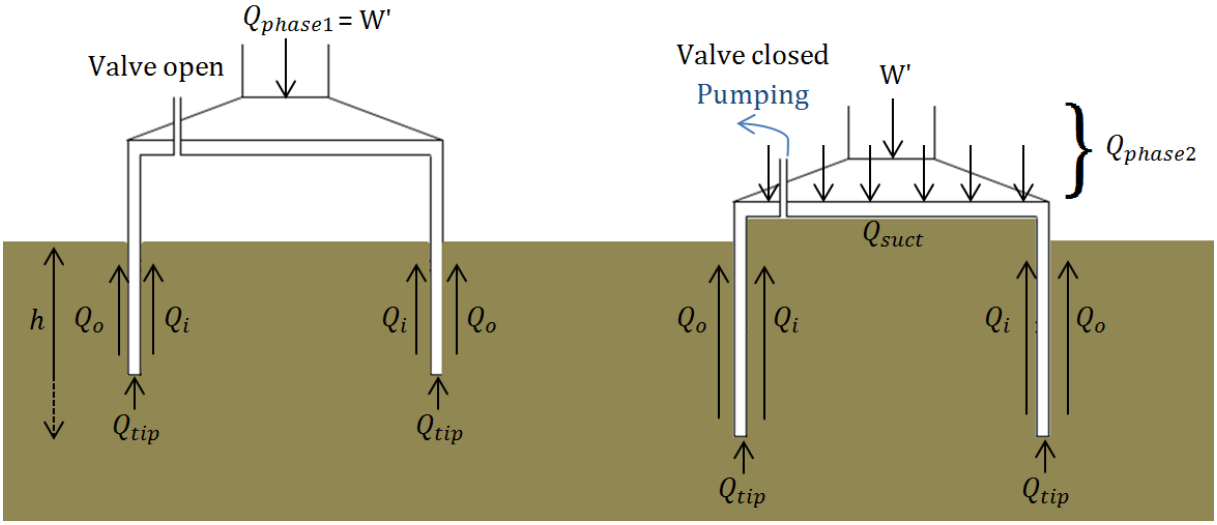

FIGURE 3-4 : Forces during installation: (a) Self-weight penetration, (b) suction-assisted penetration

3.5.5. Issues during installation

Clay soil conditions require the installation of a suction caisson with a relatively small ratio $\frac{D}{L}$. In this case, the slenderness of the foundation unit, the lateral resistance of the soil and the pressure differential between the inner and outer skirt surfaces are all the parameters potentially leading to buckling of the thin circular wall of the caisson. The skirt thickening, for example with concrete, and the caisson reinforcement by having recourse to stiffeners are two potential options that may avoid a local plastic failure, while adding an extra resistance against penetration [40][61].

In sandy soil conditions, the application of suction introduces a pore water pressure gradient in the soil plug, which makes the penetration easier. However, this pressure differential is restricted to a critical gradient in such a way as to avoid the development of negative effective stresses. Otherwise, the sand grains partly liquefy and which might induce the development of channels due to erosion along the skirt, leading to piping failure together with significant water inflows inside the caisson. This local liquefaction mechanism may interrupt the caisson installation by seriously degrading the on-site behaviour of the foundation. This phenomenon may also be en-

countered in clay, and manifests itself through a global uplift of the whole clay plug. This soil heave subsequently prevents the caisson from reaching the target penetration depth. This major issue may be mitigated by a careful control of the pumping [40][61].

3.6. Design principles of suction caisson foundations

In this section, the baseline rules for the design of loaded OWTs are outlined. Since design issues faced during the installation process have already been tackled in section 3.5.5, this section rather deals with the working conditions, such as the caisson capacity. The structural integrity of suction caissons at the ULS is basically assessed in an analytical way by limit equilibrium methods. These are based on the soil – foundation interactions and on the potential soil failure mechanisms. A numerical analysis using finite element methods may also be implemented.

As a result from section 3.4, it is now established that the suction caissons are devised to withstand axial loads, lateral loads and a combination of both. Horizontal capacity is often of a critical nature for the floating OWT structures secured by mooring lines laterally fixed at the side of a suction caisson. On the other hand, the vertical capacity is proved to be the critical design criterion in case of monopod or tripod foundation structures. In particular, given that suction caissons for OWTs deal with relatively small dead-weight loads and may therefore be considered as a so-called reversible technique, the pull-out failure mechanisms are more likely to occur apart from the traditional push failure mechanisms. Since it refers to the main subject of this dissertation, a special attention will be dedicated to this concern.

Also the constraint imposed by the offshore environment requires investigating the drained, partially drained and undrained behaviours of the seabed soil. In a drained configuration, a complete drainage of the pore water pressure (PWP) from the soil plug to the surrounding soil usually occurs under long-term and slow rate loading. In a partially drained configuration, the rate of loading is speeded up. In an undrained configuration, there is no migration of the pore water from the soil plug to the surrounding soil under short-term and rapid rate loading [63].

3.6.1. Vertical bearing capacity

3.6.1.1. Drained response

The ultimate bearing capacity of the suction caissons in drained homogeneous soils $V_{ult,d,I}$ is derived from the equilibrium between the downwards vertical load applied on the upper part of the lid of the caisson and the upwards reaction components, as translated in Equation 3-13. Since the exerted load is slowly increased, it firstly mobilizes the friction over the entire outer skirt surface of the caisson. Another fraction of the load is transferred to the soil plug inside the caisson by the lid. It follows an enhancement of the soil confinement and the development of inner skirt friction. A final part of the compressive load is withstood by a skirt tip component. All these considerations are illustrated in Figure 3-5 (a) [62][63].

$$V_{ult,d,I} = Q_i + Q_0 + \underbrace{Q_{tip} + Q_{lid}}_{W'} \qquad \text{EQUATION 3-13}$$

Where

$V_{ult,d,\mathrm{I}}$	Vertical ultimate bearing capacity in drained conditions
Q_{lid}	Bearing capacity of the lower part of the lid of the caisson
Q_{tip}	Bearing capacity of the skirt tip
Q_i	Friction on the inside of the caisson
Q_o	Friction on the outside of the caisson
W'	Submerged self-weight of the caisson

3.6.1.2. Partially drained response

The ultimate bearing capacity of suction caissons in partially drained homogeneous soils $V_{ult,pd,\mathrm{I}}$ is also derived from the equilibrium between the downwards vertical load applied on the upper part of the lid of the caisson and the upwards reaction components, as formulated in Equation 3-14. Under a compressive loading, the outer skirt friction still accounts in the total resistance. Due to the partially drained behaviour of the soil plug, PWP variations appear between the inner confined environment and the outside of the caisson. As a result the soil trapped in the skirt constitutes an almost monolithic block with the caisson reducing significantly the contribution of the lid, of the skirt tip and of the inner friction components. This mechanism showed in Figure 3-5 (b) provides a greater resistance of the caisson in comparison with the drained scenario [62][63].

$$V_{ult,pd,\mathrm{I}} = Q_i + Q_0 + \underbrace{Q_{tip} + Q_{lid}}_{W'} + Q_{pw} \qquad \text{EQUATION 3-14}$$

Where

$V_{ult,pd,\mathrm{I}}$	Vertical ultimate bearing capacity in partially drained conditions
Q_{pw}	PWP distribution on the lower part of the lid of the caisson

3.6.1.3. Undrained response

Undrained homogeneous soil conditions are characterized by a really low permeability and PWP accumulations that cause the soil plug to settle uniformly with the caisson. This monolithic mass can therefore be analysed as a gravity foundation with its based at the skirt tip level which is described by the conventional three-term Equation 3-15 from the theory of Terzaghi [66].

$$q = \underbrace{s_q\,\delta_q d_q\,p\,N_q}_{depth\ or\ overburden\ term} + \underbrace{s_\gamma\,\delta_\gamma d_\gamma\,\gamma\frac{B}{2}N_\gamma}_{Surface\ term} + \underbrace{s_c\,\delta_c\,d_c\,c\,N_c}_{cohesion\ term} \qquad \text{EQUATION 3-15}$$

Where

$p = \gamma L$	Overburden pressure at skirt tip level
$B = D$	Foundation embedment equal to the caisson diameter
L	Embedded skirt length
$s_q = 1\,;\ s_\gamma = 0{,}6\,;\ s_c = 1{,}3$	Shape factor for circular foundations [19]

$\delta_q = \delta_c = \left(1 - \frac{\theta}{90°}\right)^2 = 1$ $\delta_\gamma = \left(1 - \frac{\theta}{\phi}\right)^2$	Load inclination factors [19]
$d_q = d_c = d_\gamma = 1$	Depth factors conservatively taken equal to 1
γ	soil weight
c	Cohesion of the soil
ϕ	Soil friction angle
$N_q = e^{\pi \tan\phi} \tan^2\left(45° + \frac{\phi}{2}\right)$	Bearing capacity factor (Prandtl) [67]
$N_\gamma = 1{,}5(N_q - 1)\tan\phi$	Bearing capacity factor (Caquot & Kerisel) [68]
$N_c = (N_q - 1)\ \cot\phi$	Bearing capacity factor (Prandtl) [67]

In saturated undrained soil conditions encountered in the offshore environment, it is common practice to consider the effective soil weight (γ'), and to set the cohesion c equal to the undrained shear strength s_u and ϕ to 0°[63], leading to adapted Equation 3-16 for the end bearing capacity.

$$q = \underbrace{s_q\, \delta_q d_q\, \gamma' L\, N_q}_{\text{depth or overburden term}} + \underbrace{s_\gamma\, \delta_\gamma d_\gamma\, \gamma' \frac{B}{2} N_\gamma}_{\substack{\text{Surface term} \\ =0}} + \underbrace{s_c\, \delta_c\, d_c\, c\, N_c}_{\text{cohesion term}} \qquad \text{EQUATION 3-16}$$

The ultimate bearing capacity of the suction caissons in undrained homogeneous soils $V_{ult,u,I}$ is calculated by the equilibrium between the downwards vertical load applied on the upper part of the lid of the caisson and the sum of the contributions of the end bearing resistance q and the outer skin friction resistance. It is expressed in Equation 3-17 and represented in Figure 3-5 (c). It should be noticed that the overburden pressure term, corresponding to the gravity force of the soil column adjacent to the suction caisson is cancelled from the formula by the equal and opposite weight of the soil plug inside the caisson. The failure behaviour in this mechanism is divided into three zones. The soil wedge I under the foundation is assumed to be elastic and to shift jointly with the foundation. The soil zones II are transitional between elastic and plastic ground conditions. The soil zones III refer to plastic passive blocks pushed back upwards at failure [19].

$$V_{ult,u,I} = Q_0 + q\, A_{base,o} \qquad \text{EQUATION 3-17}$$

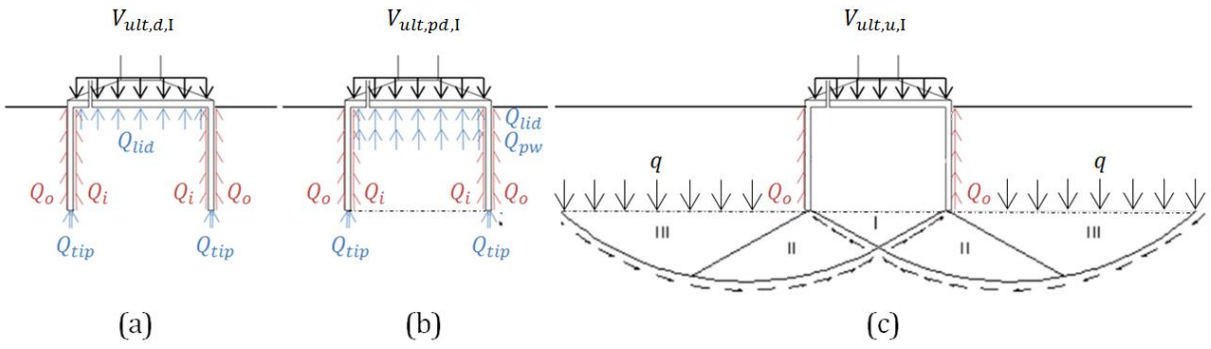

FIGURE 3-5 : vertical bearing capacity in : (a) drained, (b) partially drained, (c) undrained conditions

3.6.2. Vertical pull-out (tensile) capacity

3.6.2.1. Drained response

The ultimate pull-out capacity of suction caissons in drained homogeneous soils $V_{ult,d,II}$ is derived from equilibrium between the upwards vertical load applied on the upper part of the lid of the caisson and the downwards reaction components, as translated in Equation 3-18 and represented in Figure 3-6 (a). Since the tensile load is slowly increased, the long-term drained conditions lead to a complete dissipation of PWP and no generation of passive suction inside the soil plug which will remain in place. The soil – caisson contact is lost at the level of the lid, and there is a sliding of the skirt in the soil. Therefore, only the inner and outer skin friction components are actively mobilized in the total capacity, with the weight of the submerged caisson playing a negligible role [15][61][62][63].

$$V_{ult,d,\mathrm{II}} = Q_i + Q_0 + W' \qquad \text{EQUATION 3-18}$$

Where

$V_{ult,d,\mathrm{II}}$ Vertical ultimate pull-out capacity in drained conditions

Figure 3-7(a) proposes the failure mechanism associated with the fully drained tensile configuration.

3.6.2.2. Partially drained response

The ultimate pull-out capacity of suction caissons in partially drained homogeneous soils $V_{ult,pd,\mathrm{II}}$ is derived from the equilibrium between the upwards vertical load applied on the upper part of the lid of the caisson and the downwards reaction components, as translated in Equation 3-19 and illustrated in Figure 3-6 (b). The application of a tensile load in not fully drained soil conditions generates negative variations of PWP in the soil plug, known as passive suction, that remains trapped inside the skirt during the uplift movement. An increase of the pull-out resistance is then noticed by mobilizing the passive suction, the submerged weights of the caisson and the soil plug and skin friction on the outer skirt surface [15][61][62][63].

$$V_{ult,pd,\mathrm{II}} = Q_0 + Q_{pw} + W' + W'_{plug} \qquad \text{EQUATION 3-19}$$

Where

$V_{ult,pd,\mathrm{II}}$ Vertical ultimate pull-out capacity in partially drained conditions
W'_{plug} Effective submerged weight of the soil plug

Figure 3-7(b) proposes the failure mechanism associated with the partially drained uplift.

3.6.2.3. Undrained response

The ultimate pull-out capacity of suction caissons in undrained homogeneous soils $V_{ult,u,\mathrm{II}}$ is derived from equilibrium between the upwards vertical load applied on the upper part of the lid of the caisson and downwards reaction components, as translated in Equation 3-20 and illustrated in Figure 3-6 (c). The application of a short-term rapid tensile loading in a low per-

meability medium has the consequence to develop passive suction in the soil plug. As a function of the degree of consolidation, the suction caisson and the soil plug will behave as a monolithic mass, and mobilize a reverse end bearing mechanism in the surrounding soil at the skirt tip level. This bearing resistance q together with the skin friction on the outer skirt surface and the submerged weight of the caisson contribute to the two-term pull-out capacity. Here again, the overburden pressure term included in the bearing resistance and the weight of the soil plug within the caisson cancel each other out [15][61][62][63].

$$V_{ult,u,\mathrm{II}} = Q_0 + qA_o + W' \qquad \text{EQUATION 3-20}$$

The vertical tensile capacity is generally lower than the vertical compression capacity. This may come from the reverse end bearing mechanism in tension which mobilizes less resistance in comparison with the end bearing mechanism in compression. A partial dissipation of the negative excess PWPs during the swelling of the soil during soil swelling may explain this reduction [67]. The development of cavitation during large pull-out rates further to very negative variations of PWP is another phenomenon susceptible to reduce the ultimate pull-out capacity of the suction caissons [61][62][67].

Figure 3-7(c) proposes the failure mechanism associated with the fully undrained uplift.

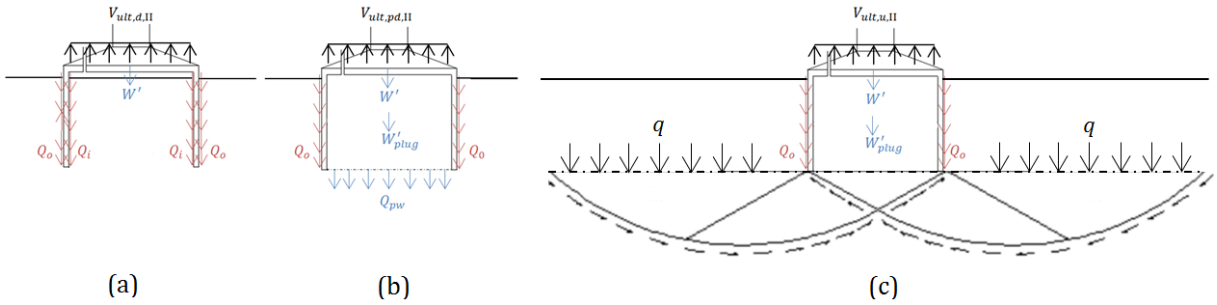

FIGURE 3-6 : vertical pull-out capacity in: (a) drained, (b) partially drained, (c) undrained conditions

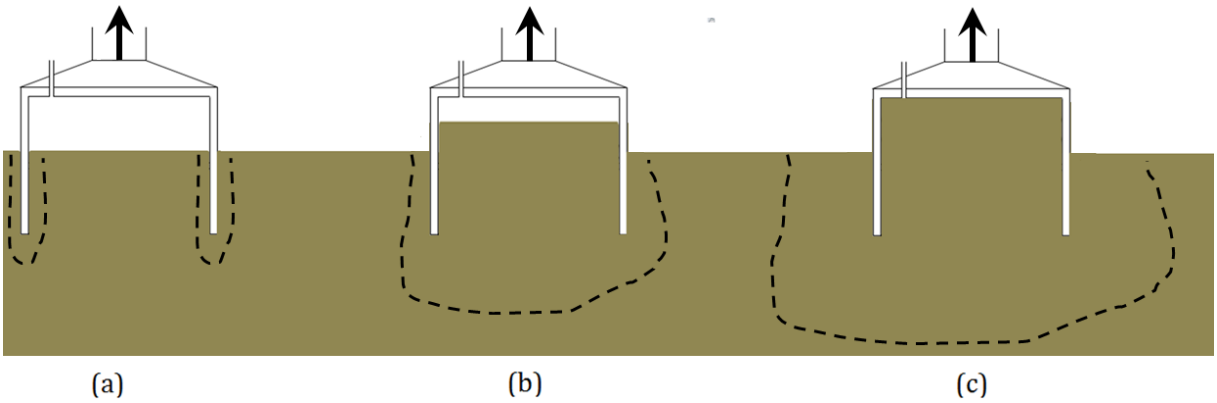

FIGURE 3-7 : failure mechanisms during fully drained, partly drained and fully undrained uplift

3.6.3. Horizontal capacity

The ultimate horizontal capacity of suction caissons H_{ult} is greatly dependent on the point of application of the horizontal load.

In case of a suction caisson used as an anchor for a floating OWT, the ultimate lateral resistance of the caisson can be maximized by selecting an optimum attachment depth for the padeye z_a, in such a way that the failure mechanism only involves a pure horizontal translation without forward and backward rotations. This attachment point is generally located at around 70 percents of the embedded skirt length, which allows to obtain the maximum possible value for the lateral bearing capacity factor.

This way, the ultimate horizontal capacity can be formulated as Equation 3-21 [20]. In such a case, the soil failure mode around the suction caisson comes from laterally loaded pile analysis and is twofold. It includes a conical wedge extending from the side of the caisson in its upper part and a flow field in the skirt tip area below the wedge. It is illustrated in Figure 3-8 (a).

$$H_{ult} = N_p \, L \, D_o \, \bar{s_u} \qquad \text{EQUATION 3-21}$$

Where

H_{ult}	Ultimate lateral capacity of the caisson
$N_p = f\left(\frac{L}{D}\right)$	Lateral bearing capacity factor varying with the slenderness ratio
L	Embedded skirt length
D_o	Outer caisson diameter
$\bar{s_u}$	Average undrained shear strength over the penetration depth

For suction caissons incorporated in monopod and tripod substructures, the point of application of the horizontal load is located above the optimal depth, which prevents from monopolizing the full horizontal capacity and allows the rotation of the foundation. Since the centre of rotation of the foundation goes up within the caisson, in addition to the conical wedge mechanism, a scoop failure mechanism develops in place of a flow field in the lower part of the skirt, as depicted in Figure 3-8 (b).

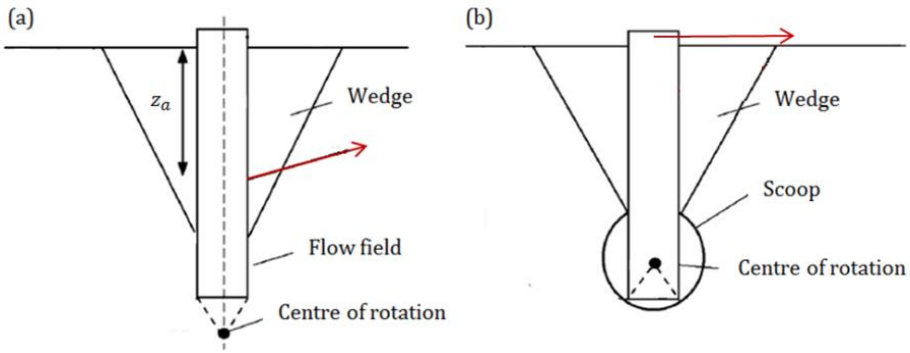

FIGURE 3-8 : Soil failure mechanism under horizontal loading : (a) caisson anchor with optimal attachment depth, (b) monopod suction caisson [15]

It is still important to note that the suction caisson failure under a horizontal load is common in monopod configurations but is less likely to occur in multi-pod configurations. Indeed, the latter arrangement has a much greater rigidity, so that if the structure tends to rotate under the applied horizontal loads, it gives birth to a counteracting bending moment on the top of the caisson that sets the total angular rotation to zero. On the contrary, the former foundation

arrangement allows free rotation which results in a 50-percent reduction of the possible maximum horizontal capacity [20][65].

3.6.4. Inclined capacity

In practice, the general loading case on the OWT foundation system consists of a combination of axial and lateral loads. Under these circumstances, the maximum capacities of a suction caisson under the uniaxial vertical or lateral loads are degraded by the presence of forces in the orthogonal direction. This interaction between the orthogonal loads is modelled through a failure envelope in the (V, H) loading plane. For the suction caissons, the failure envelope is shaped by an elliptical relationship, which is formulated by Equation 3-22 [20][63].

$$\left(\frac{H}{H_{ult}}\right)^{a} + \left(\frac{V}{V_{ult}}\right)^{b} = 1 \qquad \text{EQUATION 3-22}$$

Where

H_{ult}, V_{ult}	Ultimate lateral and vertical capacities of the caisson
H, V	Horizontal and vertical loads
a, b	Exponents varying with the slenderness ratio $\frac{L}{D}$

Under an inclined uplift loading, one of the conceivable failure mechanisms is rather similar to the failure mode under horizontal loading. It involves a two-sided conical wedge, pushed laterally and upwards by the inclined translational and possibly rotating motion of the caisson. Below the caisson, a soil flow field is here again assumed to develop, as sketched in Figure 3-9 [65][69].

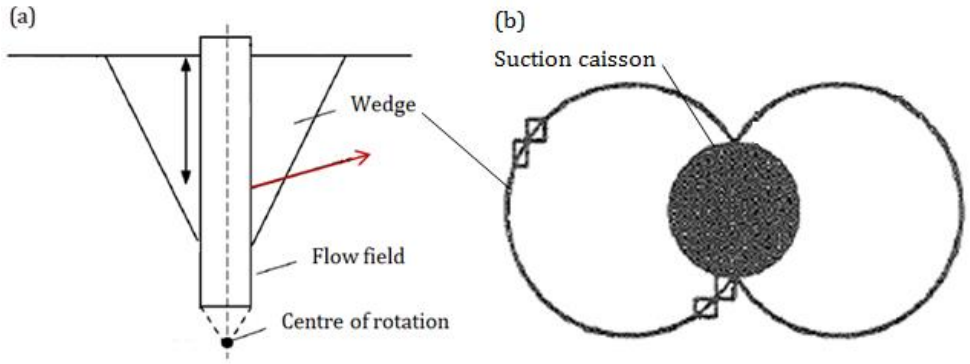

FIGURE 3-9 : Soil failure mechanism under inclined loading: (a) elevation, (b) in-plane views [67]

Chapter 4
2D Finite Element Analysis

4.1. Introduction

This chapter aims at apprehending the finite-element software packages LAGAMINE employed for the simulations and to present the numerical results. Firstly, the initial 2D model used as reference for the simulations is defined, and its initial rest state is properly characterized in order to highlight all the key components involved in the extraction resistance of the caisson (section 4.2). After that, the numerical analysis of the caisson under a tensile load is carried out for a primary scenario, dealing with drained conditions and with an elastic soil behaviour (section 4.3). The investigation is subsequently extended to a second partially drained scenario (section 4.4). For both configurations, two sub-cases are treated: in a first phase, the soil is held in place during the extraction and in a second phase it is free to move. In each case, the FE model and the potential related assumptions are outlined, the numerical results are displayed, discussed, and then compared to analytical calculations, proposed in the literature.

4.2. Definition of the reference FE model

4.2.1. Problem statement

The real life example that will be investigated by means of the finite element software is one single caisson under an uniaxial tensile load that is part of a multipod substructure for an OWT. In the specific case of Figure 4-1 (a), a triopod foundation is sketched. As discussed in chapter 3, such support structures cope with large overturning moments coming from the environmental loading, and which are transferred to the foundation level through a push and pull mechanism. From then on, the caisson is only submitted to a prevailing vertical force and a minor horizontal component, allowing to reduce the system to a 2-degree of freedom loading.

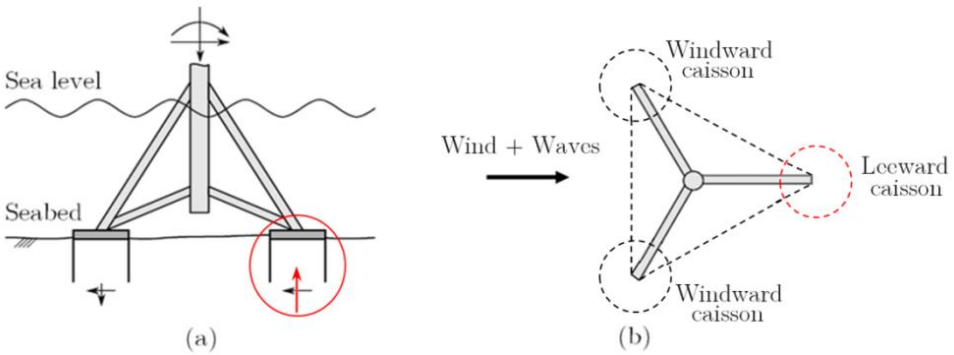

FIGURE 4-1: typical tripod foundation: (a) Elevation view, (b) Plane view with the modelled part (red)[56]

In the problem under discussion, the wave and wind-induced horizontal loads are supposed to be applied in the same single direction on the leeward side of the foundation system, as coloured in red in Figure 4-1 (b). Only this part of the substructure will be modelled, and the group effect is neglected as a first assumption.

Moreover, a non-linear analysis of the problem is required. Indeed, soils can undergo high deformations through their behaviour. Apart from this material non-linearity, contact non linearities can also arise at the interface between the two dissimilar materials, namely the soil and the caisson. The area of contact is a function of the deformation and the relative motion along a joint surface, i.e. the debonding, makes the joint segment non-linear. This leads to a nonlinear relation between the force F and the displacement fields u, as depicted in Figure 4-2. The tangent to this curve represents the integration matrix K, that varies with the imposed displacements, and that gives the general formulation of Equation 4-1.

$$\{u\} = [K\ u\ ]^{-1}\{F\} \qquad \text{EQUATION 4-1}$$

To solve this problem, an iterative process must be performed to progressively reduce the out-of-balance nodal forces (i.e. the difference between the external solicitations and the internal forces) and to converge to a more accurate solution. It is done in LAGAMINE by applying a linearization process on the basis of a Taylor series expansion of the out-of-balance nodal forces, around the last known approximation of the displacement. The solution is obtained once the increment of displacement becomes negligible and the results between the iterations does not evolve anymore .

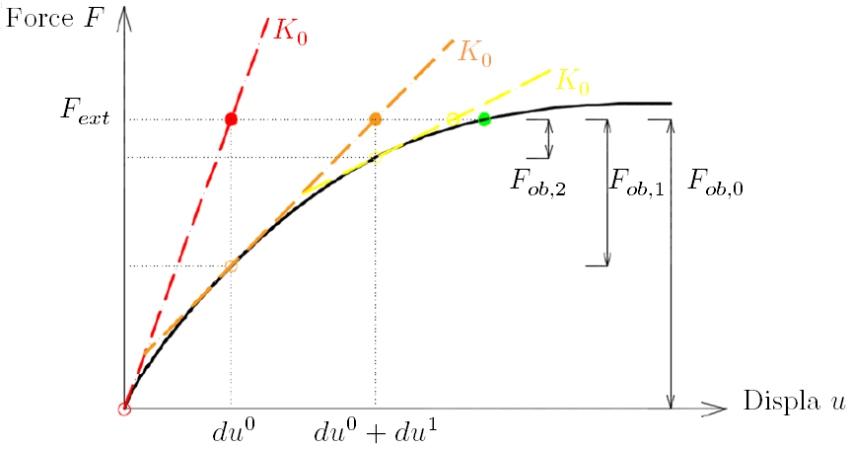

FIGURE 4-2 : Iterative resolution of the non-linear force-displacement relationship

In the LAGAMINE environment, it is allowed to select its own consistent system of units for the analysis. The International System of units (SI) recalled in Table 4-1 will be adopted as set of basic units.

TABLE 4-1 : System of units used in the LAGAMINE program

QUANTITY	Length	Mass	Time	Force	Stress	Density
SI	m	kg	s	N	$Pa\ (N/m^2)$	kg/m^3

4.2.2. Numerical model implementation

4.2.2.1. Initial geometry

At the start of the input of the reference geometry, it is decided to implement a two-dimensional (2D) model considering that the main loads only act in two well-defined directions. In such a case, a unique and representative vertical cross-section of the situation is analysed. Two types of model are susceptible to be used, either an axisymmetric or a plane-strain model. Plane-strain models, as illustrated in Figure 4-3 (a), are more common in case of geometries with a regular cross-section, and with a uniform stress state and loading along a length perpendicular to the $z-axis$. In a state of strain-plane, displacements and strains only take place in the $xy-plane$ ($\varepsilon_z = 0$), whereas normal stresses are accounted for along the $z-axis$. As for the axisymmetric models displayed in Figure 4-3 (b), they are suitable for circular structures with a uniform radial cross-section as well as a uniform loading around the central $y-axis$. The stress state and deformations are here considered equal in any radial direction, ly $\varepsilon_x = \varepsilon_z$. Since the geometry of the suction caisson is circular and symmetrical with respect to the $y-axis$, this second model appears to be the most suitable solution for the case under study. Moreover, the second assumption implying to neglect the low horizontal load is raised to justify the use of an axisymmetric analysis for the caisson and its surrounding soil.

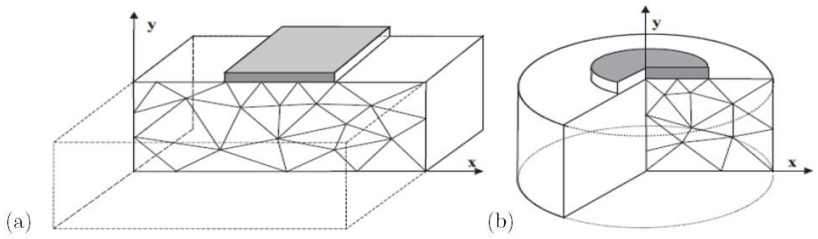

FIGURE 4-3: (a) Plane-strain model and (b) axisymmetric model [80]

The geometry of the caisson is represented as a simplified hollow cylinder, without stiffeners along the inner face of the skirt, despites these reinforcements play a role in the behaviour of the caisson. This simplification must be kept in mind since it has an influence on the results. The diameter D, the skirt length L, and the thickness of the skirt tip t are the geometric parameters that fully define the caisson.

As a first step, the suction caisson is assumed to belong to shallow foundations which are specifically defined by Terzaghi [66] for $\frac{D}{L} \leq 1$, and thus the initial geometry is implemented for a slenderness ratio $\frac{D}{L} = 1$. Further on, other aspect ratios of 0,5 - 0.75 - 1.5 and 2 will be imposed in order to investigate the influence of the penetration depth and the size of the soil plug in the mobilization of the extraction resistance. The thickness of the skirt defined by the aspect ratio $\frac{t}{D}$ is slightly oversized compared to the usual values previously mentioned, in order to get rid of numerical issues. The ratio adopted for the reference geometry is given by Equation 4-2.

$$t = 0{,}012 \times D \qquad \text{EQUATION 4-2}$$

The geometry of this reference case is sketched in Figure 4-5, with the dimensions summarized in Table 4-2.

4.2.2.2. Mesh

The whole of the caisson and the surrounding soil is implemented as a 2D axisymmetric model in the finite element code. Prior initialisation procedures have revealed that a domain depth of three times the caisson diameter under the skirt length, namely $L + 3D = 32m$, and a domain width of three times the caisson diameter D, namely $3D = 24m$, were sufficient to eliminate the impacts and the impositions of the boundary conditions on the results. The study focuses on the soil behaviour and its interactions with the foundation, and so the caisson is assumed to be in place and neither the installation phase nor the superstructure are modelled. The FE mesh is presented in Figure 4-5.

Around the caisson skirt, which is especially the zone to be analysed, a refinement of the mesh is applied, whereas near the boundaries, the mesh is let coarser. In total, the 24×32 domain comes to 10803 nodes and 3566 finite elements, as mentioned in Table 4-2. It should finally be noted that the origin of the axes is located in the bottom left-hand corner of the domain.

TABLE 4-2: Geometrical parameters of the reference FE model

Diameter D [m]		Skirt length L [m]	Thickness t [m]	No. nodes [-]	No. elements [-]
Inner	*Outer*				
7.8	8	8	0.096 - 0.1	10803	3566

Similar eight-noded hydro-mechanical elements are employed to mesh the soil and the caisson. These quadratic elements are based on a parabolic interpolation of the degrees of freedom. Two mechanical degrees of freedom, that is the displacement in the $x-$ and in the $y-$ directions, and one hydraulical degree of freedom that is the water pressure, are assigned to each node.

The soil-caisson contact zones [64] are defined by bi-dimensional interface elements having their own mechanical and flow constitutive laws, and using a two-point Gaussian integration scheme. The other side of the contact zone is discretized by using foundation elements. As the two surfaces of the interface never match perfectly, the global behaviour of this zone is characterized by the normal effective contact pressure $p_N{}'$ and the shear stress τ. The first component is responsible for the interpenetration in the contact zone. If the interface is open, i.e. there exists a gap between both sides, no contact pressure will develop. On the contrary, in case the interface is closed, i.e. the contact holds between both sides, the normal pressure progressively appears at the interface. Mathematically the penalty Equation 4-3 is used for the detection of the contact.

$$p'_N = K_N \, \varepsilon_N \qquad \text{EQUATION 4-3}$$

Where

p'_N	Normal effective contact pressure
K_N	Normal penalty coefficient taken as large as possible
ε_N	Normal strain rate

The second component τ describes the shear behaviour of the interface. The shearing or sliding at the interface level is defined by a similar penalty Equation 4-4.

$$\tau = K_T \, \varepsilon_T \qquad \text{EQUATION 4-4}$$

Where

τ	Shear stress
K_T	Tangential penalty coefficient taken as large as possible
ε_T	Tangential strain rate

A Coulomb's criterion (Equation 4-5) is assumed to govern the maximum shear stress.

$$\tau_{max} = \mu \; p'_N \qquad \text{EQUATION 4-5}$$

Where

μ	Friction coefficient of the interface

To fully characterize the hydro-mechanical behaviour of the contact elements, fluid flows through $(f_{w,N})$ and along $(f_{w,L})$ the interface should also be considered since these zones constitute a preferred path for the groundwater. The transversal fluid flow is characterized by a first flow from the interface element to the inside and a second one from the inside to the foundation element, described by Equation 4-6.

$$f_{w,N} = \rho_w T_w \Delta p_w \qquad \text{EQUATION 4-6}$$

Where

$f_{w,N}$	Normal fluid flow
ρ_w	Density of water
T_w	Transmissivity
Δp_w	Variation of water pressure

To be consistent with reality, the foundation is supposed to be impermeable, cancelling the second transversal flow, while the first one is initiated by a transmissivity T_w initialized to $10^{-3}\,\frac{m}{Pa\;s}$. As for the longitudinal flow, it is in most cases characterized by the well-known hydrogeology Equation 4-7, where the minus sign stands for a flow from high to low pressures.

$$f_{w,L} = -\rho_w \frac{k_l}{\mu_w} \; \nabla p_w + \; \rho_w g \nabla \mathrm{z} \qquad \text{EQUATION 4-7}$$

Where

$f_{w,L}$	Longitudinal fluid flow
$k_l = \frac{\varepsilon_N^2}{12}$	Longitudinal intrinsic permeability assumed to fluctuate conforming to a cubic law while the gap between the soil and the foundation is progressively widening and is thus filled in with water
∇p_w	Gradient of water pressure (longitudinal)
$\rho_w g \nabla \mathrm{z}$	Gradient of static pressure (longitudinal)

In the present work, the longitudinal fluid flow is set equal to the transverse one. All these information regarding the definition of the contact zones can be retrieved in Figure 4-4.

Based on this contact zone characterization, an hydro-mechanical coupling, described by Terzaghi's postulate (Equation 4-8) arises at the interfaces to give the total normal pressure p_N.

$$p_N = p'_N + p_w \qquad \text{EQUATION 4-8}$$

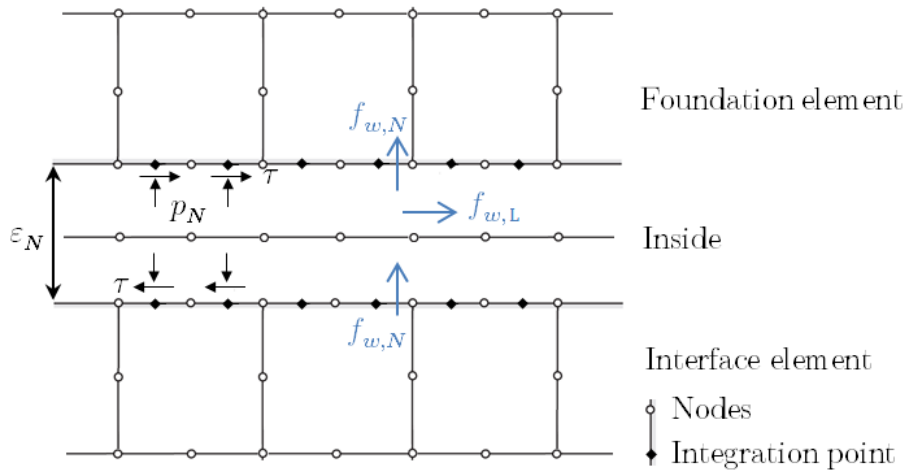

FIGURE 4-4 : Discretization of the interface finite element [64]

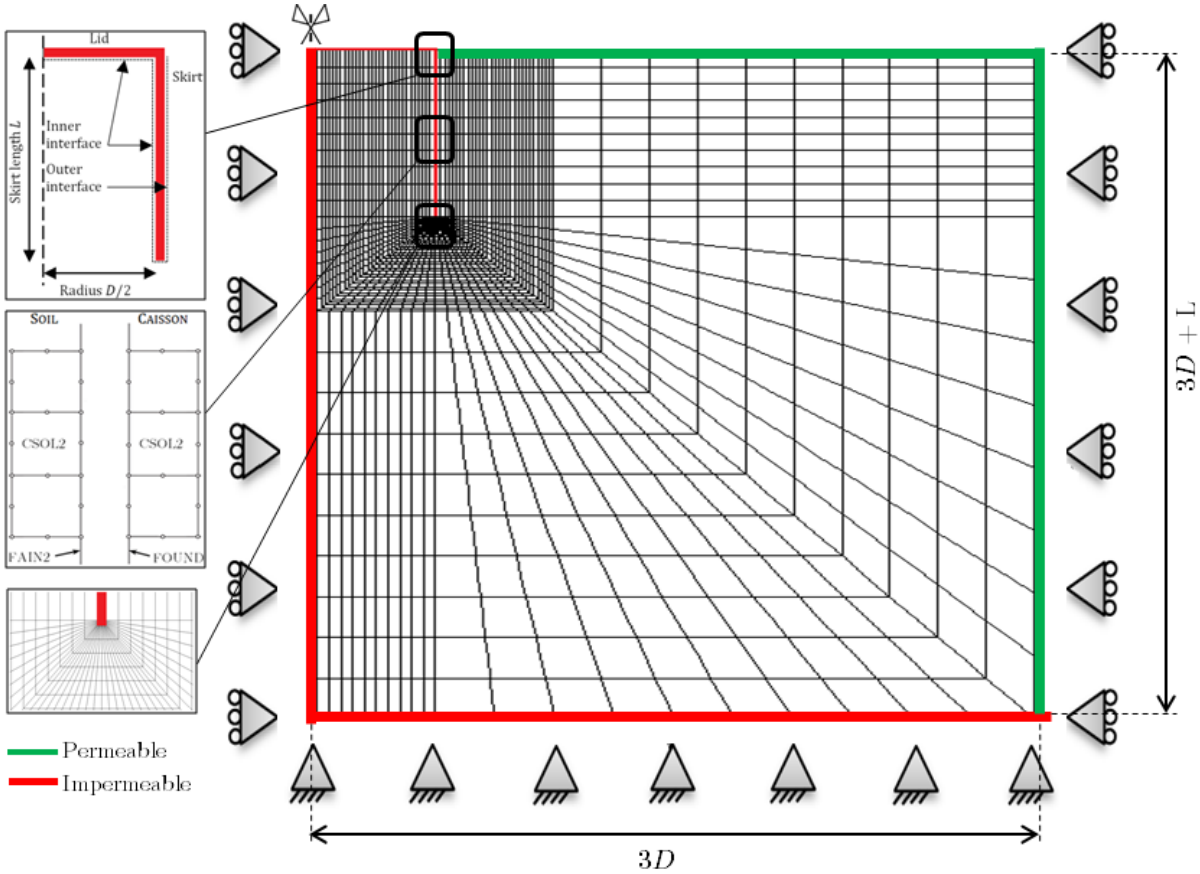

FIGURE 4-5 : Meshed geometry of the axisymmetric FE model with the mechanical and the hydraulic boundary conditions, as well as some details of the caisson lid and of the interfaces

4.2.2.3. Boundary conditions

Specific boundary conditions are imposed to the domain, as presented in Figure 4-5. Regarding the mechanical ones, no displacement is allowed in the out-of-plane tangential direction by definition. In addition, the horizontal displacements along the $x-axis$ are fixed on the two lateral sides, while the lower limit of the mesh is confined in both the horizontal $x-$ and the vertical $y-$directions.

As far as the hydraulic boundary conditions are concerned, the symmetry axis of the axisymmetric model is supposed to be an impermeable boundary and the bottom edge of the model can be seen as a layer of consolidated clay having a so low permeability that it is set to zero. Through these sides of the domain, no water flows can be transmitted. Also no water flows can go through the surfaces of the caisson to be consistent with the physical properties of steel. On the contrary, the upper boundary, that is in contact with free water from the sea and the right boundary that corresponds to the continuity of the clay soil are both assumed to be drained. Along these sides, the water pressure is maintained constant and some fluid flows are initiated.

For the definition of this reference FE model, all the nodes that compose the caisson have been fixed horizontally to ensure numerical stability in the zone where the tensile load is applied.

4.2.2.4. Initial material parameters

The suction caisson is made of steel with a bulk density ρ_s of $7800\frac{kg}{m^3}$. This material is assumed to have a linear elastic behaviour, characterized by a Young's - or elastic - modulus E_s of 210 GPa and a Poisson's ratio υ_s of 0,2. The acceleration due to the gravity in the $y-$direction is assigned a value of $10\frac{m}{s^2}$.

Concerning the soil conditions, the caisson is set up in normally consolidated clay (NC) conditions, that is broadly defined in the literature [70][71][72], and that is representative for various sites in European seas. The Poisson's ratio takes a constant value in the range [0.3 ;0.5] in case of saturated clay. For this particular type of soil conditions, it is also common practise to consider a frictionless material with both the friction and the dilation angles equal to zero ($\phi = \psi = 0$) and to set the cohesion equal to the undrained shear strength ($c = s_u$). The average undrained shear strength is often assumed to increase linearly with depth, as formulated in Equation 4-9.

$$s_u = s_{u0} + kz \qquad \text{EQUATION 4-9}$$

Where

z	Soil depth below the seafloor
s_{u0}	Undrained shear strength at the seafloor level, e.g. 5 kPa
k	Gradient of the undrained shear strength with depth, e.g. 1,5 kPa/m

Despites its variation throughout the soil profile, the Young modulus is assumed to have a constant value around $10MPa$. The value of the particle density of the saturated clay is assigned to $\rho_{s,clay} = 2650\ \frac{kg}{m^3}$. Assuming a fully saturated soil material with a porosity of 50 percent (for a sandy clay [72]), respectively $S_r = 1$ and $n = 0.5$, and knowing that the density of water

ρ_w is approximately equal to 1000 $\frac{kg}{m^3}$, then it is possible to assess the saturated unit weight and the effective unit weight of the clayey soil, thanks to Equation 4-10 and Equation 4-11. Finally, the soil permeability is set at $10^{-7}\,\frac{m}{s}$ for the considered sandy clay [70].

$$\gamma_{sat,clay} = \ 1-n\ \gamma_{s,clay} + n\ S_r\ \gamma_w = \ 18.25\ kN/m^3 \qquad \text{EQUATION 4-10}$$

$$\gamma'_{clay} = \gamma_{sat,clay} - \gamma_w = 8.25\ kN/m^3 \qquad \text{EQUATION 4-11}$$

All material parameters and properties are summarized in Table 4-3.

TABLE 4-3 : Parameters of: reference geometry, steel caisson, elastic clay soil and contact elements

COMPONENT	PROPERTY	SYMBOL	VALUE	UNIT
Steel caisson	Elastic modulus	E_s	210	[GPa]
	Poisson's ratio	υ_s	0.2	[-]
	Bulk density	ρ_s	7800	$[kg/m^3]$
NC clay	Elastic modulus	E_c	10	[MPa]
	Poisson's ratio	υ_c	0.3	[-]
	Bulk density	$\rho_{s,clay}$	2650	$[kg/m^3]$
	Porosity	n	50	[%]
	Horizontal earth pressure coefficient at rest	K_0	1	[-]
	Friction angle	ϕ	0	[°]
	Dilatation angle	ψ	0	[°]
	Coefficient of permeability	k	1×10^{-7}	[m/s]
	Coefficient of consolidation	c_v	0.3	$[mm^2/s]$
	Average effective unit weight	γ'_{clay}	8.25	$[kN/m^3]$
Interfaces	Transmissivity	T_w	10^{-3}	$[m/(Pa.\,s)]$
	Friction coefficient of the interface	μ	0.5	[-]
	Normal penalty coefficient	K_N	4×10^9	$[N/m^3]$
	Tangential penalty coefficient	K_T	4×10^8	$[N/m^3]$

4.2.3. Initial stress state in the soil

Throughout the domain, an effective stress component arises from the self-weight of the soil. At the bottom edge of the domain, the overlying soil depth gives rise to initial effective stresses $\sigma'_{v,0}$ of $\gamma'_{clay}h = 264\ kPa$ with an effective stress variation $\Delta\sigma'_{v,o}$ of $-8.250\ \frac{kPa}{m}$. An average water depth of 20m is considered for the simulations which results in the imposition of a vertical water presure p_w of $\gamma_w z = 200\ kPa$ at the mudline level. A horizontal water pressure, linearly increasing between $z = 19.9m$ and $z = 20m$ is also applied on the small vertical surface of the caisson lid outside the soil and is approximated by a constant pressure of 200 kPa as well. These two water pressures are implemented in the model through a mechanical constitutive law defining an uniformly distributed load on a line element [75].

The loading of the caisson is carried out by means of a displacement-controlled process imposed to the upper part of the lid. Initially, the vertical movement of the caisson is prevented. Then the caisson is progressively extracted from the ground at a constant rate, until an imposed displacement is reached. By working in this way, it should be taken into account that the total

reaction assessed by the software encompasses both the downward weight of water and the upward force required to assign the displacement (Figure 4-6).

Considering saturated soil conditions, the pore water pressure u is initiated hydrostatically on the basis of the water level, and the initial stress field in the vertical direction can then be calculated by Terzaghi's Equation 4-12.

$$\sigma_{v,0} = \sigma'_{v,0} + u_0 \qquad \text{EQUATION 4-12}$$

Where

$\sigma_{v,0}$	Initial total stress in the vertical direction
$\sigma'_{v,0}$	Initial effective stress in the vertical direction
u_0	Initial pore water pressures in the vertical direction

Lateral stress state in the soil (Equation 4-13) and around the interfaces is assessed by the pore water pressures and the lateral earth pressure coefficient at rest K_0 that is the ratio of the vertical and the horizontal effective stresses.

$$\sigma_{h,0} = \sigma'_{h,0} + u_0 \qquad \text{EQUATION 4-13}$$

Where

$\sigma_{h,0}$	Initial total stress in the horizontal direction
$\sigma'_{h,0} = K_0\ \sigma'_{v,0}$	Initial effective stress in the horizontal direction
u_0	Initial pore water pressures in the horizontal direction

The empirical Jacky's formula, given in Equation 4-14, is often used to estimate the coefficient of earth pressure at rest, as a function of the friction angle ϕ.

$$K_0 = 1 - sin\,\phi \qquad \text{EQUATION 4-14}$$

In the situation under study, the initial state of the soil is supposed to be isostatic, which gives $K_0 = 1$. Moreover, it is assumed that the caisson installation process does not cause any disruption of the initial stress field in the soil.

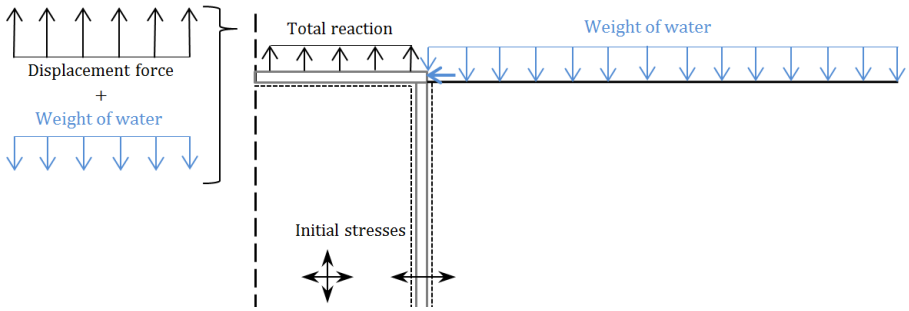

FIGURE 4-6 : Loading applied to the caisson and initial stresses at the beginning of the extraction phase

4.2.4. Initial loading state of the caisson

At the initial stage (initial time step Δt) no displacement d of the caisson is expected (initial displacement step $\Delta y = 0m$). This means that a state of equilibrium should exist between the different components of the reaction when a zero-displacement is considered. All the components included in the uplift resistance of the caisson are listed in the present section.

4.2.4.1. Downward-acting components

Among these components, the weight of the steel caisson W_{cais} as well as the hydrostatic weight of water W_w both belong to the downward acting forces, and are expressed by Equation 4-15 and Equation 4-16 respectively.

Comp 1
$$W_{cais} = \gamma_{sat,clay} \frac{(A_{base,o}\ t + (A_{base,0} - A_{base,i})\ L)}{10^{-6}} = 0{,}4565\ MN \qquad \text{EQUATION 4-15}$$

Comp 2
$$W_w = \gamma_w \frac{A_{base,o}\left(h_{w,lid}(t) - d\ t\ \right)}{10^{-6}} = 10{,}0028\ MN \qquad \text{EQUATION 4-16}$$

Where

$h_{w,lid}(t)$	Height of the water column above the lid (as a function of the time)
$d(t)$	Imposed displacement on the lid (as a function of the time)

The integral of the shear stresses along the inner and outer interfaces of the caisson skirt, denoted Φ_{in} and Φ_{out} respectively constitutes the two other components directing downward at the initial point of the simulation. Numerically, these friction forces are reconstituted by a Gaussian quadrature, i.e. a numerical integration based on the values of the shear stresses known at two integration points (IP) for each element of the skirt. This results in the generic formula of Equation 4-17. The factor 2π allow to convert the 2D problem into the initial circular geometry of the caisson.

Comp 3*a* & 3*b*
$$\Phi = \sum_{ELEM} (\overline{\Phi_{IP1}} x_{IP1}\ |J_{IP1}| + \overline{\Phi_{IP2}}\ x_{IP2}\ |J_{IP2}|) \times\ 2\pi) = 0MN \qquad \text{EQUATION 4-17}$$

Where

$\overline{\Phi}$	Value of the shear stresses at the integration point
x	Abscise coordinate of the integration point
J	Jacobian of the integration point

Naturally, as there is no motion of the caisson at the beginning of the displacement controlled process, friction on the inner and outer faces of the skirt is not mobilized yet. However, it is already possible to obtain an analytical estimation of the maximum friction resistance that can be activated at the soil-caisson interface along the skirt. It is expressed by Equation 4-18 taking into account the horizontal soil pressure distribution and the friction coefficient at the interface.

$$\Phi^{max} = 2\pi \frac{D}{2} L\ \left(K_0 \gamma'_{clay} \frac{L}{2}\right) \tan\phi \qquad \text{EQUATION 4-18}$$

Where

$D = D_i\ or\ D_o$	Inner or outer caisson diameter
L	Skirt length
$\tan\phi = \mu$	Coulomb's friction coefficient (along the interfaces)

This gives maximum values of $\Phi_{in}^{max} = 3{,}2784\ MN$ and $\Phi_{out}^{max} = 3{,}3625\ MN$.

The integral of the pore water pressure distribution P_{pwp} on the lower part of the lid of the caisson is one additional component orientating downwards. It can be quantified numerically by the following Equation 4-19, and will be taken into account as a variation term to the initial quantity. Initially, as the caisson is kept at rest, there is no generation of negative excess pore pressures (i.e. suction) relative to the ambient water pressure below the caisson lid, and thus the variation of this 4th component is null: $\Delta P_{pwp}^{0} = 0\ MN$.

Comp 4 $$\mathrm{P_{pwp}} = \sum_{ELEM} (\overline{\mathrm{P_{pwp,IP1}}}\ \mathrm{x_{IP1}}\ |\mathrm{J_{IP1}}| + \overline{\mathrm{P_{pwp,IP2}}}\ \mathrm{x_{IP2}}\ |\mathrm{J_{IP2}}|) \times\ 2\pi$$ EQUATION 4-19

Where

$\overline{\mathrm{P_{pwp}}}$	Value of the pore water pressures at the integration point
x	Abscise coordinate of the integration point
J	Jacobian of the integration point

Finally, the soil encapsulated inside the skirt of the caisson and the soil below the skirt tip level will contribute to the general uplift resistance of the foundation, as a function of the applied suction effect. In the presence of a partially drained soil, the suction is prone to develop and to make a certain amount of soil be pulled out with the foundation, while for an undrained soil, an extra contribution from the soil at the bottom of the caisson is taken into account in the same way as a reverse end bearing mechanism. In this particular case, it is common practise to account for the total bearing pressure by dividing it into its independent contributions above and below the skirt tip level [81]. However, since performing real undrained simulations is not as easy as it sounds, the emphasis will be solely on the contribution of the soil plug in the scope of this study. The last component oriented upwards thus encompasses the effects of the soil plug within the skirt and will be denoted ΔW_{plug}.
The weight of the soil plug at the initial rest phase is given by Equation 4-20. As this component directly depends on the appearance of suction underneath the lid of the caisson, it will also be formulated as a variation term from the initial state. Initially, the contribution of this term is naturally equal to zero : $\Delta W_{plug}^{0} = 0\ MN$.

Comp 5 $$W_{plug} = \frac{A_{base,i} \times L \times \gamma'_{clay}}{10^6} =\ 3.175\ MN$$ EQUATION 4-20

Where

$A_{base,i}$	Inner cross section area of the caisson base
L	Skirt length
γ'_{clay}	Effective unit weight of the clay

4.2.4.2. Upward-acting components

The upward-acting force group mainly includes the resistance due to the buoyancy force P_w and the effective stresses of the in-situ soil Σ' under the caisson lid and at the skirt tip

level. These components are here again evaluated on the basis of a quadrature rule at two specified integration points, as stated in Equation 4-21 and Equation 4-22.

Comp 6*a* & 6*b*
$$\mathrm{P}_w = \sum_{ELEM} (\overline{P_{w\,IP1}}\; x_{IP1}\; |J_{IP1}| + \overline{P_{w\,IP2}}\; x_{IP2}\; |J_{IP2}|) \times\; 2\pi \qquad \text{EQUATION 4-21}$$

Comp 7*a* & 7*b*
$$\Sigma' = \sum_{ELEM} (\overline{\Sigma'_{IP1}}\; x_{IP1}\; |J_{IP1}| + \overline{\Sigma'_{IP2}}\; x_{IP2}\; |J_{IP2}|) \times\; 2\pi \qquad \text{EQUATION 4-22}$$

Where

$\overline{P_w}$	Value of the buoyancy force at the integration point
$\overline{\Sigma'}$	Value of soil pressure at the integration point
x	Abscise coordinate of the integration point
J	Jacobian of the integration point

The derived values of these forces acting on the lid are the following: $\mathrm{P}_{w,lid} = 9{,}5567\ MN$ and $\Sigma'_{lid} = 0{,}00095\ MN$. Under the skirt tip, the following results are got: $\mathrm{P}_{w,tip} = 0{,}6963\ MN$ and $\Sigma'_{tip} = 0{,}1649\ MN$.

Finally the total reaction R_{tot} corresponding to the external load that needs to be applied to the caisson in order to obtain the imposed displacement, also points upwards since extraction of the caisson is simulated. Originally, the value of this resultant should be zero given that the caisson is embedded at rest in the soil. All the reaction contributions at the nodes that constitute the foundation can be extracted from the FE code and then sum up to obtain the global reaction R_{tot} on the caisson.

Comp 8
$$R_{tot} = \sum_{NODES} R \qquad \text{EQUATION 4-23}$$

4.2.4.3. Equilibrium

Now that all the components involved in the initial loading state of the caisson have been defined, the starting equilibrium can be expressed by Equation 4-24. The corresponding initial error is given by Equation 4-25 and might point out that a negligible tension must be kept initially in order to satisfy the forces equilibrium and to keep the caisson in a zero displacement state. Figure 4-7 specifies the initial orientation of all these components and illustrates the colour code that will be used throughout this work, whereas the upward or downward contributions of each reaction component in the initial state are sketched on the bar diagrams of Figure 4-8.

$$\underbrace{\textit{Comp}\ 1 + \textit{Comp}\ 2 + \textit{Comp}\ 3a + \textit{Comp}\ 3b + \textit{Comp}\ 4 + \textit{Comp}\ 5}_{\text{Downward-acting components } \Sigma_{\text{down}}}$$

$$= \underbrace{\textit{Comp}\ 6a + \textit{Comp}\ 6b + \textit{Comp}\ 7a + \textit{Comp}\ 7b + \textit{Comp}\ 8}_{\text{Upward-acting components } \Sigma_{\text{up}}}$$

$$\iff \quad W_{cais} + W_w + \Phi_{\text{in}} + \Phi_{\text{out}} + \Delta P_{pwp} + \Delta W_{plug} = \mathrm{P}_{w,lid} + \mathrm{P}_{w,tip} + \Sigma'_{lid} + \Sigma'_{tip} + R \qquad \text{EQUATION 4-24}$$

$$\Longleftrightarrow \qquad \varepsilon = \left|\Sigma_{\text{down}} - \Sigma_{\text{up}}\right| = 4.0653 \times 10^{-4}\ MN \approx 0,41kN \qquad \text{EQUATION 4-25}$$

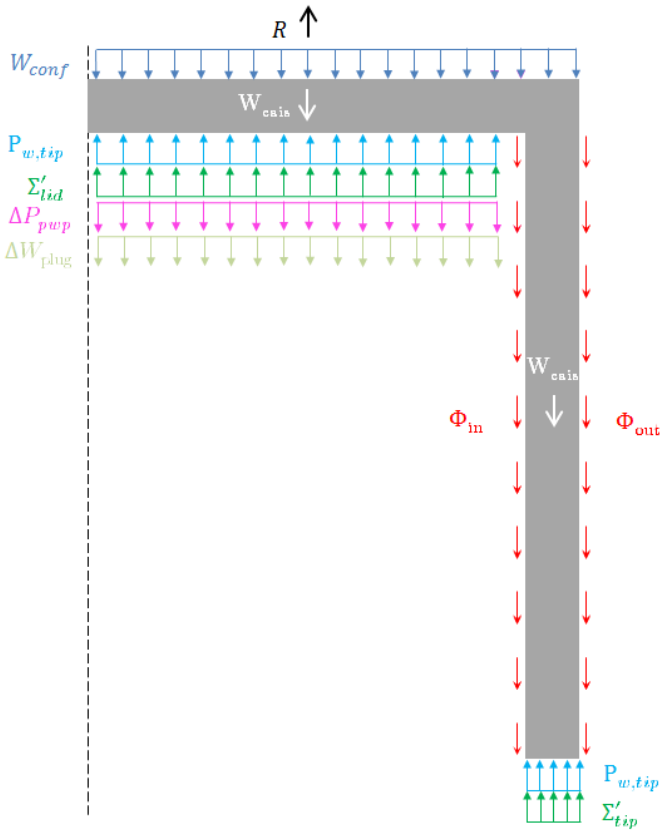

FIGURE 4-7 : Orientation and colour code of the reaction components in the initial state

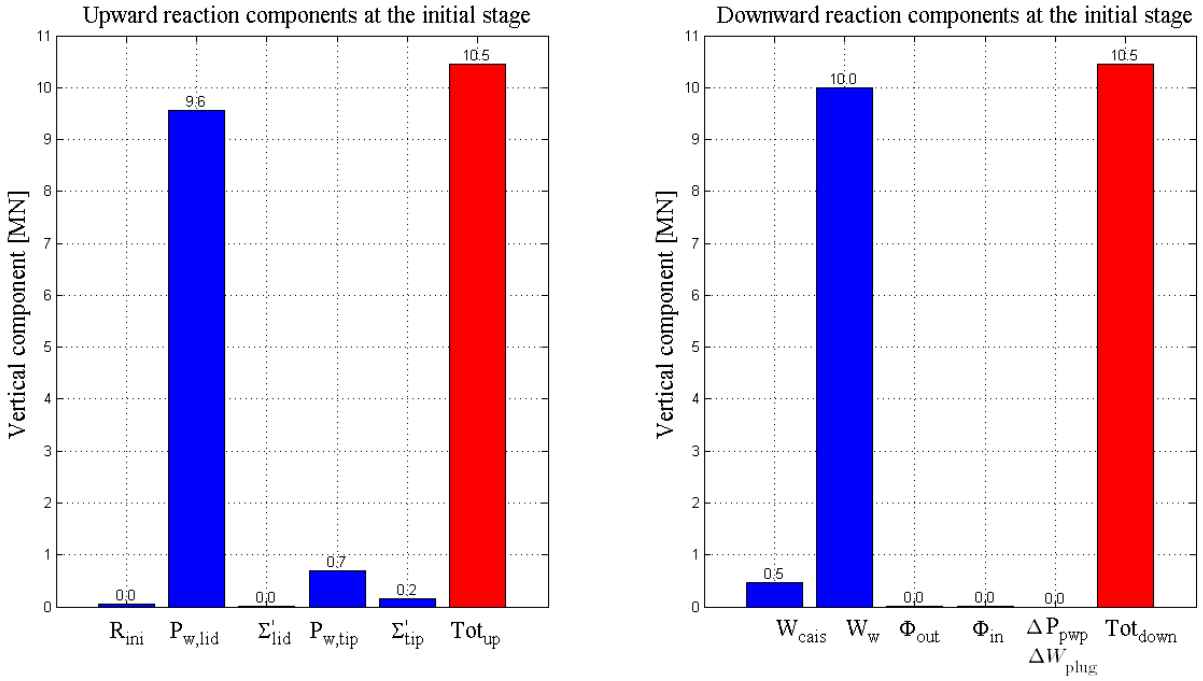

FIGURE 4-8 : Contribution of each component (blue) to the total upward or downward reaction (red)

As it might be expected, the absence of movement of the caisson during the first time step avoids the development of shear stresses and thus of friction forces along the inner and the outer skirt interfaces. Similarly, since the caisson remains motionless, the state of initial stresses within the soil stays unchanged which inhibits the appearance of excess pore water pressures. The same goes for the resistance component due to the weight of the soil plug, that is not taken into account in the absence of uplift of the caisson. As it can be seen from Figure 4-8, the prevailing contributions that act upon the caisson come from the selfweight and the hydrostatic pressure and buyoancy. A small contribution of the effective stresses in the soil arises at the skirt tip level Σ'_{tip}, whereas under the lid, these effective contact stresses are really close to zero, making this component Σ'_{lid} negligible.

4.3. 1st Scenario - Drained conditions and linear-elastic soil

4.3.1. Assumptions

Numerical simulations of the reference model are first performed for an idealised system that makes the assumption of an elastic soil behaviour. By definition, this means that the stress is directly proportional to the strain according to Hooke's law. This linear relationship makes the principle of superposition valid, by which the stresses from two applied loads can simply be added up. Two main parameters are associated with the linear-elastic theory, namely the Young's modulus E and the Poisson's ratio ν providing an estimation of the expansion of the material in the two directions perpendicular to the direction of the applied load. It is obvious that real soils do not cope with Hooke's law, given that an enhancement of the load will actually go hand in hand with a reduction of the stiffness and thus with an increase of the (plastic) deformations. However, such basic theory furnishes a first useful estimation of the problem despite its roughness and may help to understand which mechanisms develop in the soil under a tensile load. As the stress-strain response of a soil under loading often starts with a constant elastic modulus, Hooke's law is supposed to be valid at the very beginning of the loading process. For the executed simulations, the elastic modulus and the Poisson's ratio are kept constant over the entire domain, and typical values for the clay under study can be as high as $E_c = 1 \times 10^7\ Pa$ and $\nu_c = 0.3$ respectively [73][74].

In addition to its linear elastic behaviour, the soil is also assumed to be drained. This means that the water pressure degree of freedom is not activated for all the nodes of the geometry, leaving a purely mechanical system.

About the 2D interface elements, these are characterized by unilateral contacts between the soil and the caisson which is implemented by a Mohr-Coulomb dry friction law. The nonlinearitiss that are likely to manifest during the idealized case under study come therefore from the behaviour of these contact elements, where shearing is progressively mobilised.

4.3.2. The FE model

The Finite Element model is based on the one defined as reference in the previous section. Investigations will also be carried out for smaller ($\frac{D}{L} = 0.5$ and 0.75) and larger ($\frac{D}{L} = 1.5$ and 2) aspect ratio's, while keeping the skirt length constant and preserving the set of imposed

conditions at the boundaries. To ensure a permanent drainage across the domain, the water pressure degree of freedom is imposed at each individual node, thus preventing any variation of water pressure during the extraction of the caisson. The main mechanical parameters of the linear-elastic soil model and the Mohr-Coulomb interface model are summarized in Table 4-4. The parameters of the steel of the caisson are the same as in the reference model.

Since the maximum tensile capacity is rapidly reached in the idealized case being studied, simulations will be run in small displacements, for a total imposed displacement d of 0.03m or 0.05m (according to the case). These numerical simulations are executed using an automatic strategy. It consists in defining the general parameters of the strategy, as well as the characteristics of the first calculation step. Afterwards, the program manages to converge automatically based on the implemented parameters, and using the default implicit integration scheme. Table 4-4 summarizes the main execution data for the present simulation.

TABLE 4-4: Set of simulation input values: parameters of the mechanical constitutive law of the interface elements, of the soil and the caisson materials and execution data

MATERIAL	LAW	PARAMETERS	SYMBOL	VALUE	UNIT
Interface	Mohr-Coulomb	Penalty coefficient on the contact pressure	K_p	4×10^9	[-]
		Penalty coefficient on the shear friction stress	K_τ	4×10^8	[-]
		Coulomb's friction coefficient	μ	0.5	[-]
Soil	Elastic-Linear	Cohesion	c	0	[kPa]
		Poisson's ratio	υ_c	0,3	[-]
		Young's modulus	E_c	1×10^7	[MPa]
Steel	Elastic-Linear	Poisson's ratio	υ_s	0.2	[-]
		Young's modulus	E_s	210	[MPa]
		Imposed displacement	d	0.03-0.05	[m]
Simulation parameters		Time increment (initial value)	DELTAT	0.001	[s]
		Final value of the imposed displacement multiplier	ALAMBF	1.0	[-]
		Min value of the increment of the imposed displacement multiplier	DMINMU	1×10^{-6}	[-]
		Max value of the increment of the imposed displacement multiplier	DMAXMU	0.05	[-]
		Maximum number of steps to perform during the present execution	ISAME	9999	[-]
		Maximum number of iterations per step	MAXIT	15	[-]

Within these first simulations, four sub-cases will be considered to apprehend as well as possible the behaviour of the caisson in the presence of a linear-elastic soil and drained conditions. At first, a rigid body motion is examined for which all the nodes of the caisson are fixed in the $x-direction$, and all the nodes of the soil at the interfaces with the caisson are fixed along $x-$ and $y-directions$. The displacement of the caisson is imposed for each individual node of the foundation. In a second phase, the same configuration is used but only the top of the caisson will be assigned the required displacement. In the third configuration, soil nodes at the interface will be released in both $x-$ and $y-directions$, and in the fourth configuration, the

caisson nodes will also be made free in order to take into consideration a possible Poisson's effect. A characterization of these specific sub-cases is proposed in Figure 4-9.

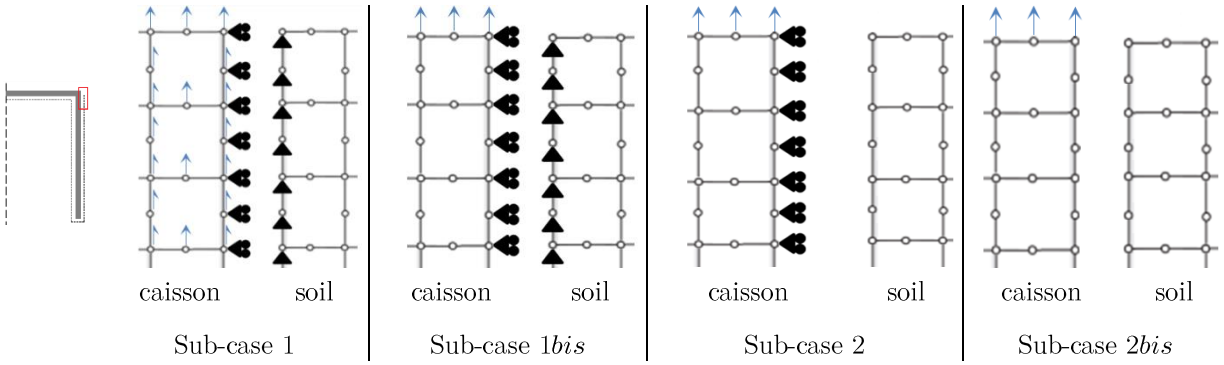

FIGURE 4-9: Definition of the four sub-cases examined in the 1st scenario

4.3.3. Results

First of all, one can have an idea of the scale of the problem on the basis of the main attributes of the performances of the FE program for the different sub-cases, summarized in Table 4-5. It appears logically that the magnitude of the problem is in correlation with the number of free degrees of freedom.

TABLE 4-5: Linear elastic soil behaviour & drained configuration: simulation attributes

SUB-CASE	NO. NODES [-]	NO. ELEMENTS [-]	RUNNING TIME [S]	NO. STEPS [-]	NO. ITERATIONS[-]
1	10803	3566	27	34	69
1*bis*			37	34	73
2			78	34	96
2*bis*			127	51	118

Now that the simulations are executed for specific displacement-controlled cases, the various contributions to the extraction resistance will be progressively mobilised to a certain extent. Therefore, the different components of the reaction can be denoted as positive or negative variation terms from the initial state, that balance the variation of the total vertical tensile load ΔR_{tot} applied to the lid of the caisson. From Equation 4-24, it can be derived the general equilibrium equation in terms of variation of each component for a vertical uplift motion of the caisson $d(t) \neq 0$, given by Equation 4-26 and sketched in Figure 4-10 (b). As this equation is expressed in terms of variation components, the total contribution of the water pressure can be cancelled out since the downward acting and the upward acting water components are applied to an exactly identical surface. This point is illustrated in Figure 4-10 (a). Also the variation of the weight of the caisson is set to zero and the term of negative excess pore water pressures can be omitted since drainage is initiated for the current simulations. The ensuing suction effect will thus not occur, leaving the soil within the caisson in place and eleminating the component ΔW_{plug} from Equation 4-26. It will be exhibited further in this section that the soil plug is still subjected to a slight uplift motion because of other physical phenomena. Anyway, this contribution will be assumed to be low enough to be neglected in this first scenario.

$$\Delta R_{tot} = \underbrace{\Delta W_{cais}}_{=0} + \underbrace{\Delta W_w}_{<0} + \underbrace{\Delta \Phi_{\text{in}}}_{>0} + \underbrace{\Delta \Phi_{\text{out}}}_{>0} + \underbrace{\Delta P_{pwp}}_{=0} + \underbrace{\Delta W_{plug}}_{\approx 0} - \underbrace{(\Delta \text{P}_{w,lid} + \Delta \Sigma'_{lid})}_{<0} - \underbrace{(\Delta \text{P}_{w,tip} + \Delta \Sigma'_{tip})}_{<0}$$

$$\Leftrightarrow \quad \Delta R_{tot} = \Delta \Phi_{\text{in}} + \Delta \Phi_{\text{out}} - \Delta \Sigma'_{lid} - \Delta \Sigma'_{tip} \qquad \text{EQUATION 4-26}$$

Where

$\Delta W_{cais}/\Delta W_w$	Resultant of the variation of the weight of the caisson/ water column above the lid of the caisson
$\Delta \Phi_{\text{in}}/\Delta \Phi_{\text{out}}$	Resultant of the variation of the total shear stresses along the skirt interface inside/ outside the caisson
ΔP_{pwp}	Resultant on the lower part of the lid of the variation of the pore water pressure distribution inside the caisson
ΔW_{plug}	Resultant of the variation of the uplift movement of the soil plug confined within the skirt
$\Delta \text{P}_{w,lid}/\Delta \text{P}_{w,tip}$	Resultant of the variation of the buoyancy pressure on the lower part of the lid / on the skirt tip
$\Delta \Sigma'_{lid}/\ \Delta \Sigma'_{tip}$	Resultant of the variation of the total effective contact stresses of the soil on the lower part of the lid/ on the skirt tip

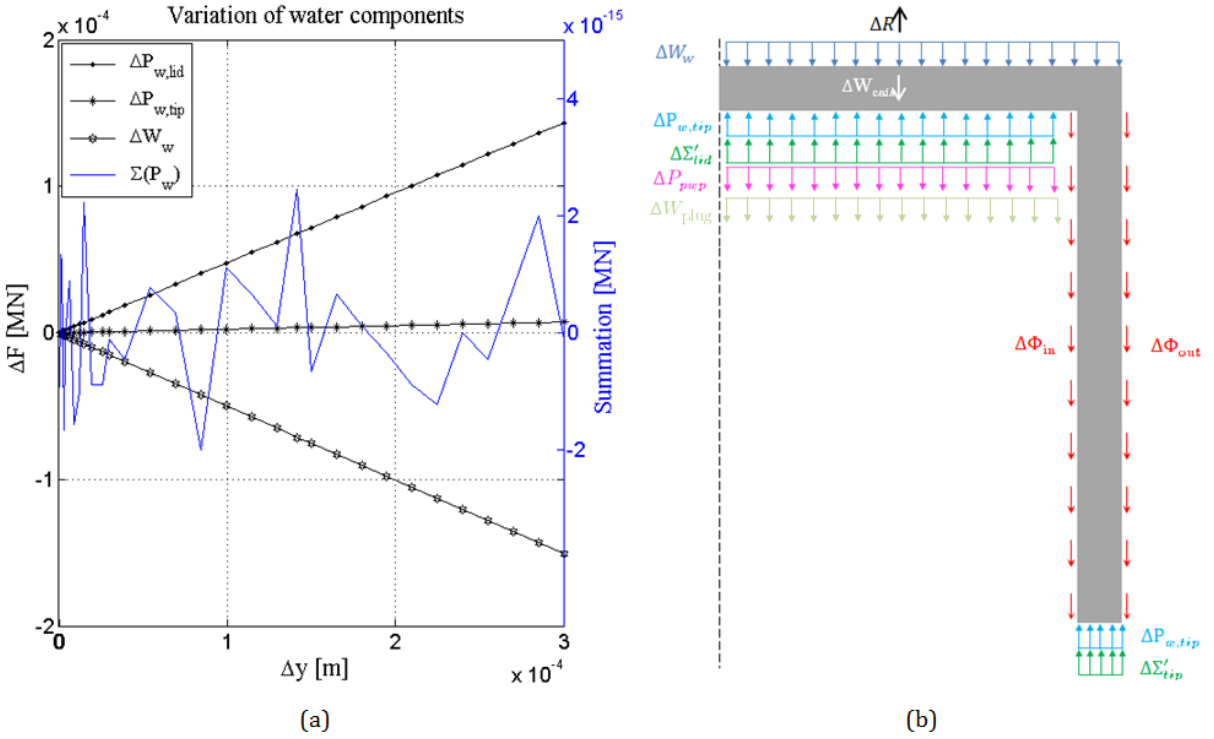

FIGURE 4-10: (a) Cancellation of the variation of water components, (b) variation of the reaction components during an imposed displacement

The displacement-load curves of both the total and the normalised variation of the reaction components for the drained traction simulations are illustrated in Figure 4-11(a) in case of a

rigid body movement (sub-case 1*bis*) and in Figure 4-11(b) in case of free soil and caisson nodes (sub-case 2*bis*). The same charts for the two other intermediate sub-cases are attached in Appendix B. The normalisation is done according to the variation of global load ΔR_{tot} at the considered step, which gives an overview of the influence of each reaction component over the total tensile capacity.

The progressive mobilisation of the reaction components appears distinctly [77]. For both cases, the trend shows that the main part of the variation of the total reaction ΔR_{tot} is almost only counterbalanced by friction components $\Delta\Phi_{in}$ and $\Delta\Phi_{\text{out}}$ throughout the simulation. As previously noticed in the initial loading of the caisson, the effective stresses in the soil under the lid are so low that the related soil pressure component can be cancelled $\Delta\Sigma'_{lid} = 0$. At the skirt tip level, the contact is progressively lost between the skirt annulus and the soil as soon as a motion of the caisson is initiated, which gives rise to a small contribution $\Delta\Sigma'_{tip}$ to the total resistance. From Figure 4-11 (a) and (b), the soil and the skirt tip are totally unstuck almost instantly $(\Delta y = 0.5 \times 10^{-4} m)$ for a rigid body motion and for a greater uplift movement $(\Delta y = 0.01 m)$ when the soil is free to move. However, this component does not play a significant role in the resistance since it accounts for about 5% and 10% of the resistance at the beginning of the process (for subcases 1*bis* and 2*bis* respectively) and then rapidly decreases to less than 5%. By contrast, at the starting point of sub-case 2*bis*, the shares of the inner and outer friction components weight respectively 20% and 70% of the total resistance and then converge each towards the value of 50% as friction is completely mobilised over the inner and outer skirt surfaces under the imposed displacement. As for sub-case 1*bis*, both the inner and the outer frictions amount to nearly 50% of the total resistance. This underlines the fact that shears along the inner and outer skirt interfaces of the caisson $\Delta\Phi_{in}$ and $\Delta\Phi_{\text{out}}$ are the prevailing resistance mode during a drained extraction of the foundation, as given by Equation 4-27.

$$\Delta R_{tot} \approx \Delta\Phi_{in} + \Delta\Phi_{\text{out}} \ . \qquad \text{EQUATION 4-27}$$

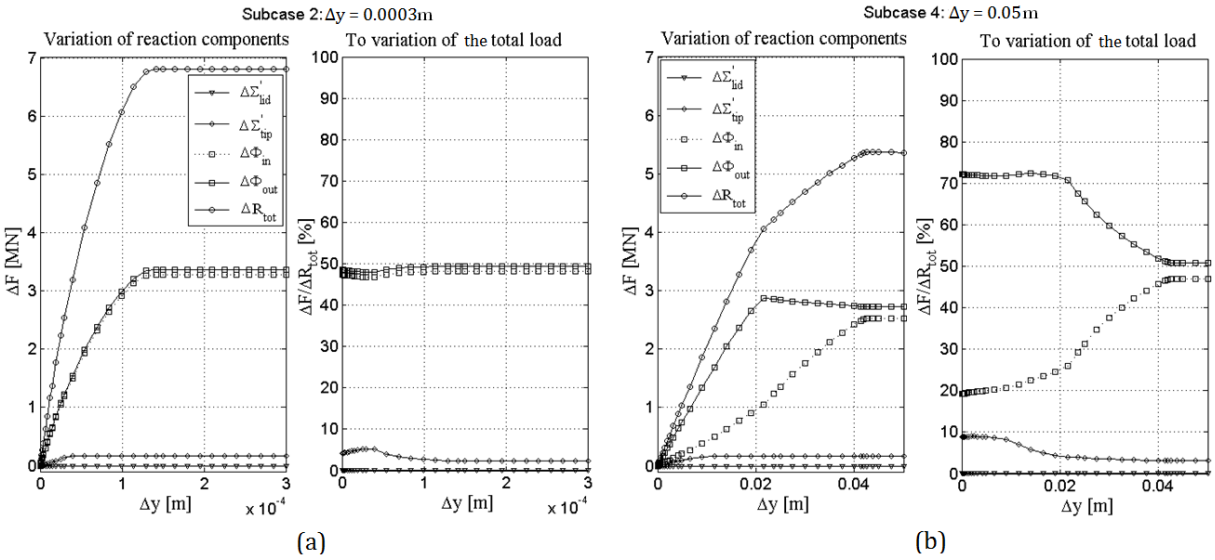

FIGURE 4-11: Drained traction simulations: variations of the reaction components and variations of the reaction components to variation of the total load for (a) subcase 1*bis* and (b) subcase 2*bis*

By analysing more in details the shape of mobilisation of the friction components depicted in Figure 4-12 (a) and (b) for the different sub-cases, it can be first noticed that the stiffness (the slope) tends to decrease while the system is progressively released (from sub-case $1bis$ to sub-case $2bis$). Thus, the maximum available friction over the inner and the outer skirt is mobilized almost instantly with rigid body movement, namely after $\Delta y = 0.85 \times 10^{-4}\ m$ and $\Delta y = 1.4 \times 10^{-4}\ m$ for the first two sub-cases, whereas it is more progressive in the case of a soil free to move, namely after $\Delta y = 0.042\ m$ for the last two sub-cases.

As the inner friction is mobilised over a smaller surface than the outer friction, a small offset between the two related curves arises in both cases of Figure 4-12 (a). This difference of stiffness is much more pronounced in Figure 4-12 (b). Since the soil is enclosed inside the caisson, it is not able to spread the stresses laterally, and keeps the contact with the skirt, leading to an upward displacement of this soil plug. Consequently, the activation of the shear stresses along the inner skirt surface is shifted as the relative displacement between the soil and the caisson is reduced. Once the maximum friction is reached on the outside of the caisson, a plateau develops and the value of $\Delta\Phi_{out}$ remains almost constant. At that particular time, any further increase in loading can only be withstand by the development of extra inner friction, which is reflected by an enhancement of the angle of inclination of the solid curve, displayed in yellow in Figure 4-12 (b).

A slight decrease in the outer friction in the case of a released soil is also observed and highlighted in orange in Figure 4-12 (b), after the maximum available resistance is reached, which reflects the partial loss of contact at the top right interface of the caisson due to the lateral diffusion of stresses, previously outlined. At the top left of the caisson, this phenomenon is not visible because the soil remains confined by the enclosing caisson. These considerations are apparent in Figure 4-13 showing the soil-caisson behaviour under a controlled-displacement of 0.05m in both the rigid body motion and the released soil cases. As expected, in the case of an extraction of a rigid body (Figure 4-13 (b)), no vertical displacement field develops around the caisson. On the contrary, when the soil particles are free to move (Figure 4-13 (c)) an overall upward displacement of the soil inside the caisson is distinctly observed. The confinement state of the soil within the skirt leads to a vertical drive of the particles with the caisson that is about two times higher than outside the caisson where the stresses can freely spread through the domain. It is obvious that this soil mass forced to move will play a role in the resistance to the extraction of the caisson, analogous to ΔW_{plug}. As this contribution remains significantly low and is moreover rather difficult to quantify, the effect of the pulling out of the soil will be neglected in the assessment of the total resistance, as stated in Equation 4-27.

Figure 4-14 characterizes both the shear stresses and the normal stresses along the inner and the outer interfaces of the skirt for the sub-cases $1bis$ and $2bis$. Logically, when a rigid motion of the caisson is considered, there is no notable variation of the stress distributions among all simulations since maximum shear stresses are mobilised almost instantaneously and there is no soil disruption to alter the normal stress distribution, as indicated in Figure 4-14 (a) and (b). However, when the soil is free to move, different stress profiles develop on both sides of the caisson due to the stress state disruption under an external loading. On the outside of the caisson, the loss of soil-caisson contact over about 2m appears clearly between the initial and final steps, whereas on the inside, this detachment is reduced because of the constraint on the stress

diffusion. This dissimilarity in the relative upward displacement between the soil and the caisson explains why the mobilized friction resistance is lower on the inside than on the outside of the caisson. Furthermore, the normal stress distribution takes a triangular shape with depth and has an influence on the shear stress distribution once the maximum available friction resistance is activated. In such a case, the shear stress profile along the skirt simply results from a uniform change of scale of the normal stress profile, as previously mentioned in Equation 4-5 and described in Figure 4-14 (e) and (f).

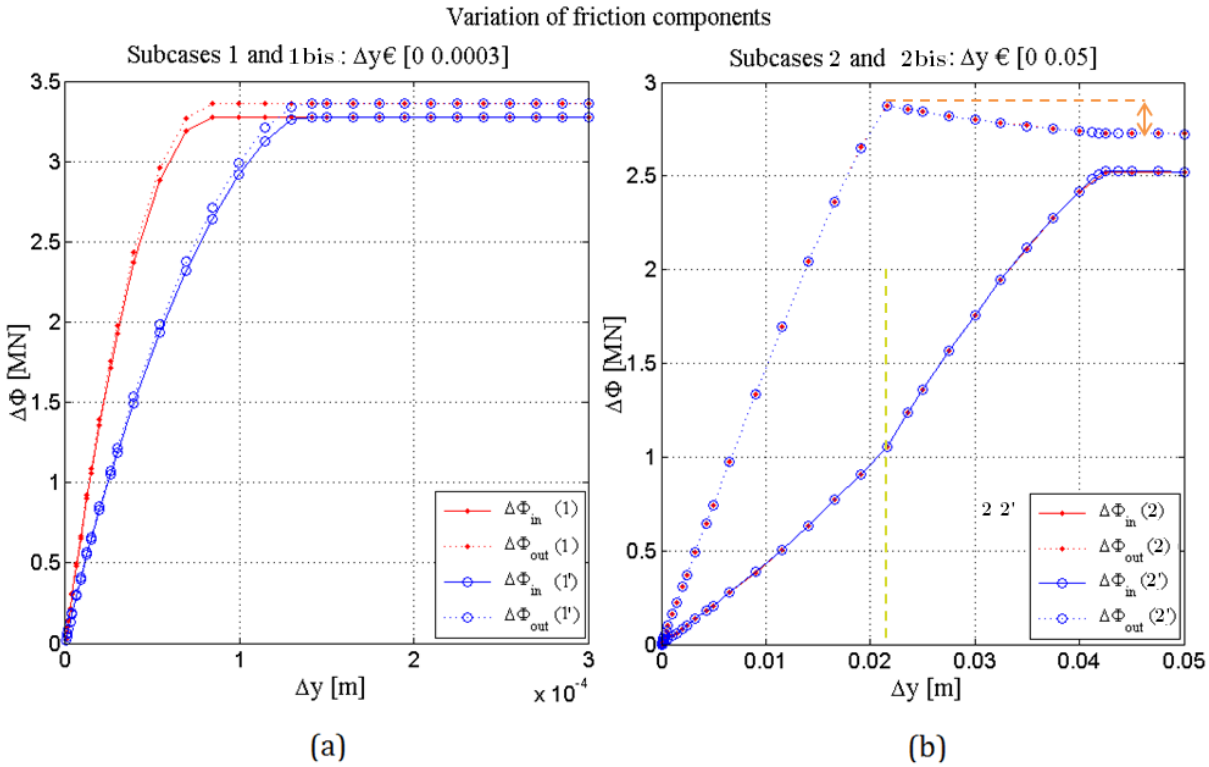

FIGURE 4-12 : Comparison of the mobilisation of friction components in the case of (a) a rigid body motion and (b) a soil free to move

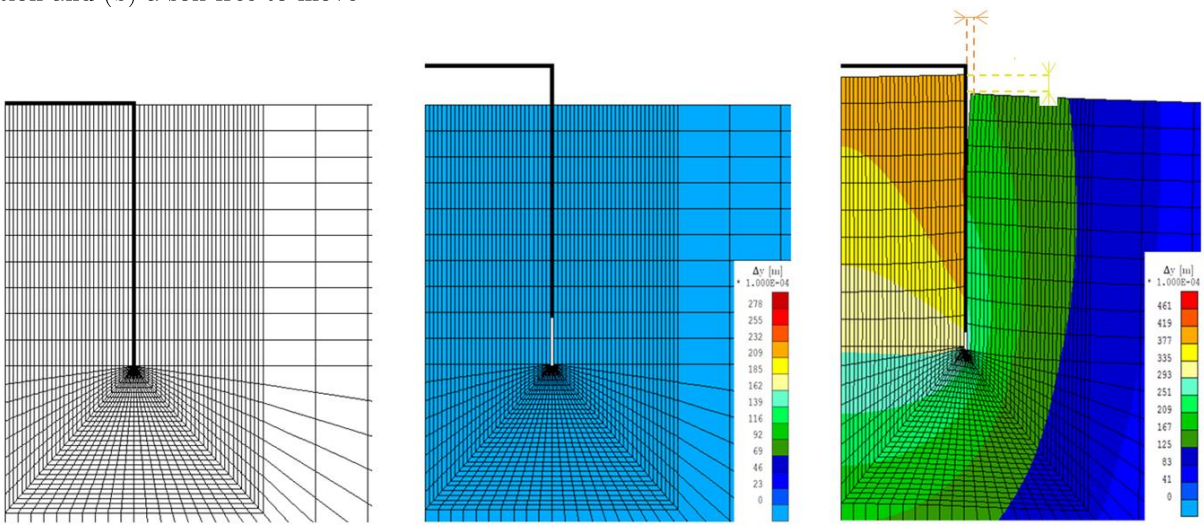

FIGURE 4-13: Soil-caisson behaviour in the initial phase (a, black) and variation of vertical displacement in both rigid body movement (b) and released soil cases (c), Amplification Factor = 25%

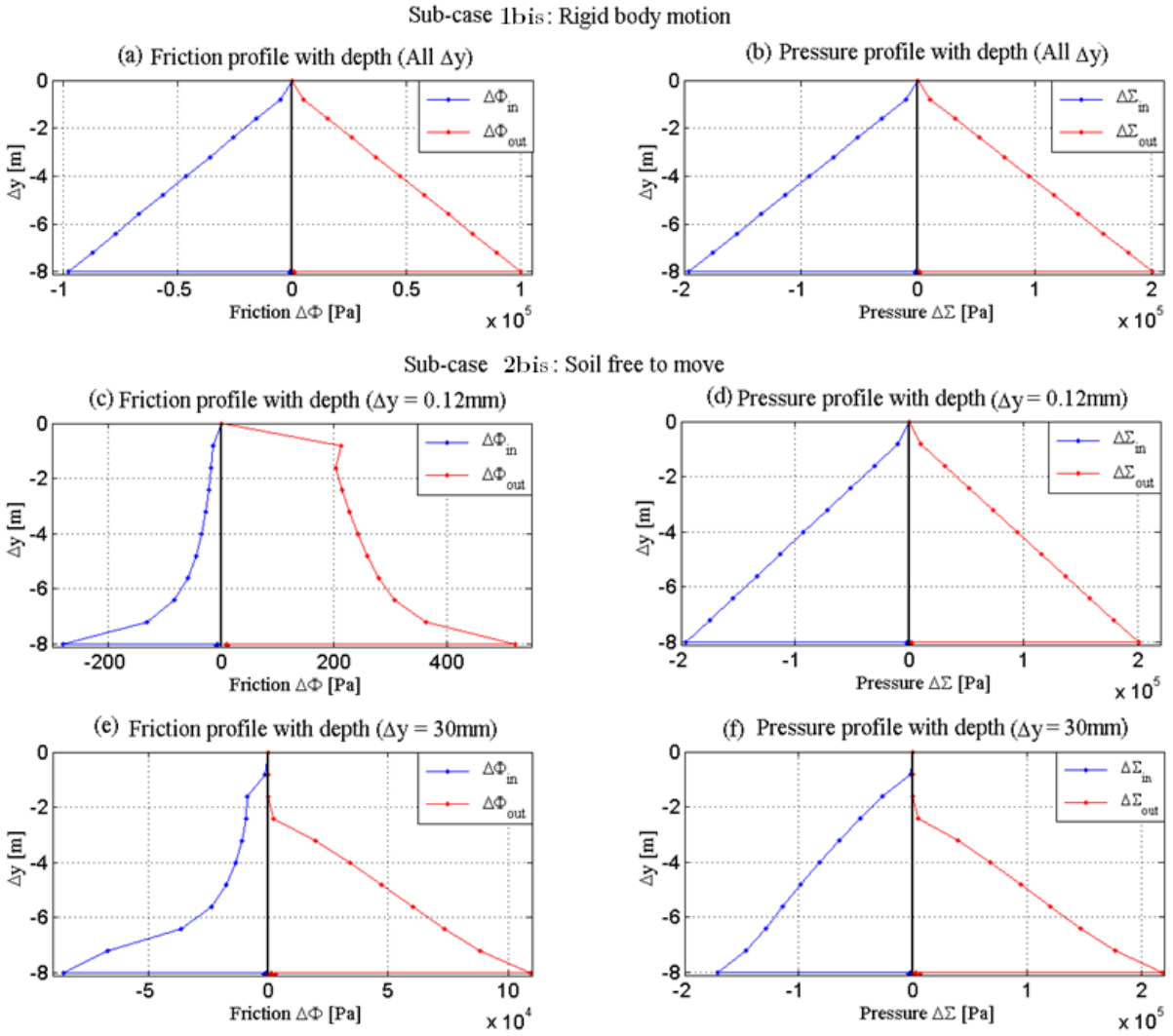

FIGURE 4-14: Distribution of the shear and normal stresses along the caisson skirt in the cases of a rigid body motion (a)-(b) and of a soil free to move (c)-(d)-(e)-(f), 1st scenario

4.3.4. Influence of the main parameters

This section aims at highlighting the principal parameters that play a key role in the response of the soil-caisson system. Performing such a study is crucial to understand how the tensile capacity of the caisson will be affected by either soil parameters or geometrical parameters of the model. Parameters will be analysed for the sub-case $2bis$, dealing with a soil free to move.

Figure 4-15 (a) presents the influence of the aspect ratio $\frac{D}{L}$ of the caisson on the outer and the inner friction components. An extraction of $0.05m$ of the caisson is tested for five slenderness ratio having a constant skirt length $L = 8m$. Not surprisingly, the wider the suction caisson, the higher the resistance components. This comes basically from the larger inner and outer surfaces on which friction can be developed. It can also be noticed that for high values of $\frac{D}{L}$, the maximum friction is almost equal on the inside and on the outside of the caisson because of the limited confinement of the soil plug inside the caisson. All these curves are governed by a homothetic ratio in such a way that if the ratio $\frac{D}{L} = 1$ is taken as reference, then the curves generated for the other ratio's $\frac{D}{L}$ can be computed as a fraction of the reference curve of $\frac{D}{L} = 1$.

Figure 4-15(b) illustrates the influence of the Poisson's ratio ν_c of the soil on the outer and the inner friction components. An extraction of $0.045m$ of the caisson is tested for three values of $\nu_c = 0.2, 0.3, 0.4$ respectively. It appears that the friction is mobilized in a similar way for the different values of ν_c both inside and outside. Distinctive behaviours arise at the mobilization of the maximum friction. On the outer surface, it can be seen that a similar maximum value is reached but then the post-peak decrease is all the more marked that a low value of ν_c is considered, owing to the more important loss of contact. On the inside surface, a high value of ν_c will help to keep the contact between the soil and the caisson, leading to a reduced friction.

Figure 4-15(c) displays the influence of the Young's modulus E_c of the soil on the outer and the inner friction components. Simulations are carried out for an imposed displacement of $0.1m$ and three orders of magnitude of the elastic modulus. Generally speaking, it appears that the parameter E_c controls the speed at which maximum friction is reached. The higher the value of E_c, the steeper the slope of the $\Delta\Phi - \Delta y$ curve, and the sooner the peak is got to.

Figure 4-15(d) gives an overview of the influence of the shear constant K_τ on the friction components. It seems that this parameter does not impact the extraction resistance that much since really slight variations are noted when three orders of magnitude of K_τ are considered.

In Figure 4-15(e), the influence of the horizontal earth pressure at rest K_0 is assessed. According to the displayed curves, the parameter K_0 does not play a role in the progressive mobilization of friction but governs the maximum friction that can be reached. Thus the higher the value of K_0, the more important the effective stress in the $x-$direction and the greater the extraction resistance.

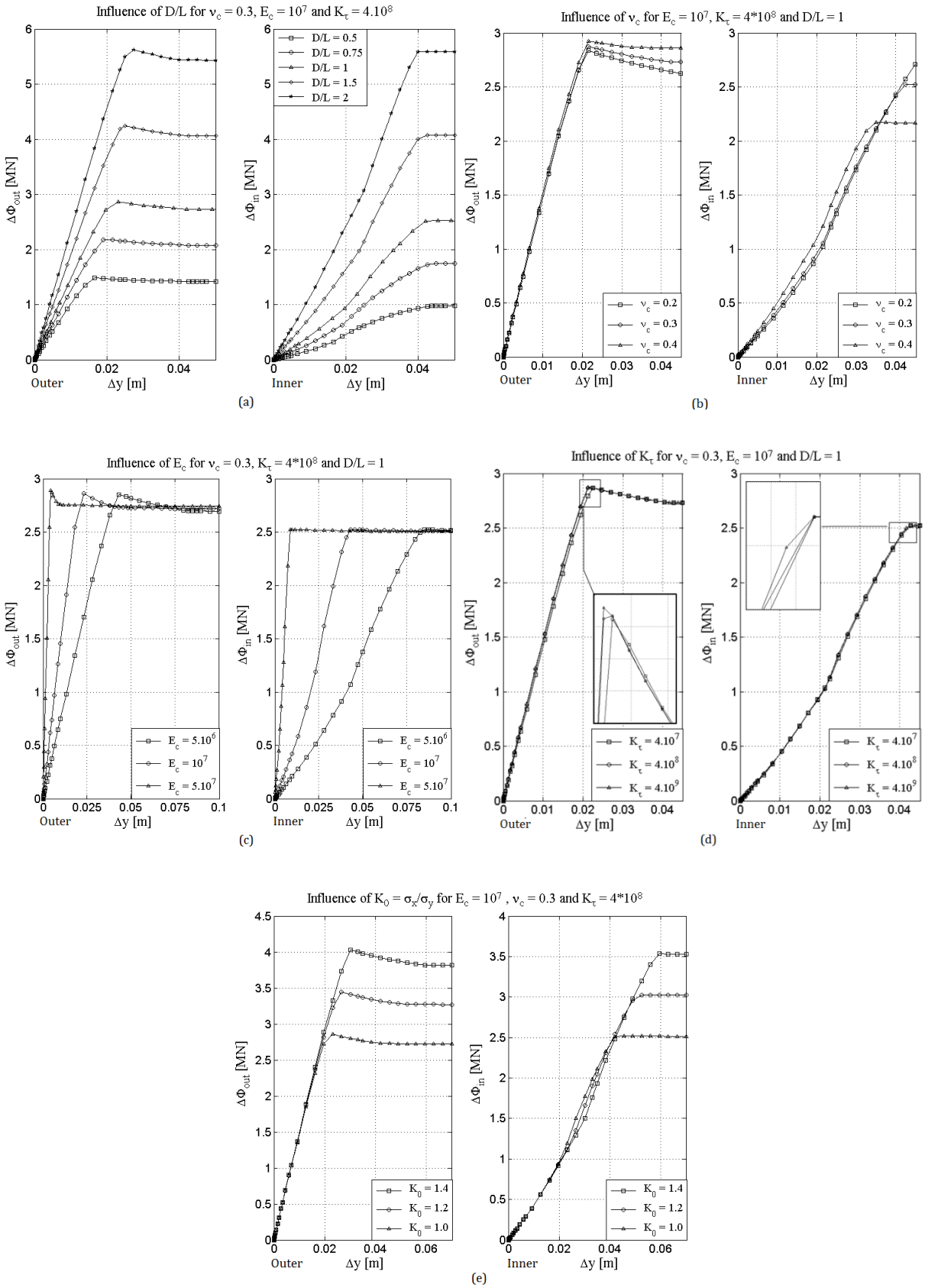

FIGURE 4-15: Influence of the main parameters on the friction components

4.3.5. Comparison between numerical and analytical results

Now that the numerical results have been generated and interpreted for a drained and linear-elastic soil configuration, the next step consists in formulating and validating analytical equations that reproduce as closely as possible the numerical solutions. From the previous section, it can be assumed that the predominant components contributing to the total uplift resistance in the studied scenario are the shear stresses acting upon the inside and the outside of the skirt. Therefore, the analytical calculations will focus on the prediction of the inner and the outer friction involved in the drained tensile capacity under the hypotheses of a rigid body movement and of a released soil at the interfaces respectively.

4.3.5.1. Rigid body motion (sub-cases 1 and 1*bis*)

Regarding the case of a purely rigid body motion with a displacement imposed to all the caisson nodes (sub-case 1), the manual computation method to assess friction is simply based on the integration of the shear distribution along the skirt interface. The value of the shear stresses along the profile $\tau = K_\tau \Delta y$ is directly related to the tangential penalty coefficient K_τ and the imposed displacement step Δy. However this shear stress state is assumed to be bounded to the maximum mobilisable friction $\tau_{max} = \mu K_0 \Delta\sigma'_{v,o} z$ which is a linear function of the depth z as shown in Figure 4-16. This means that the total friction force is obtained by integrating a triangular shear stress profile between 0 and z_0, and then a rectangular shear stress profile between z_0 and the total length L, all integrated over the cylindrical surface, as stated in the final Equation 4-28. To attest of this evolution of the shear profiles with depth, it is put into perspective with the profiles obtained numerically, and provided in Figure 4-16 (c). All the computation steps are detailed in Appendix C.1. The expression for the maximum available friction derived previously in section 4.2, is recalled in Equation 4-29.

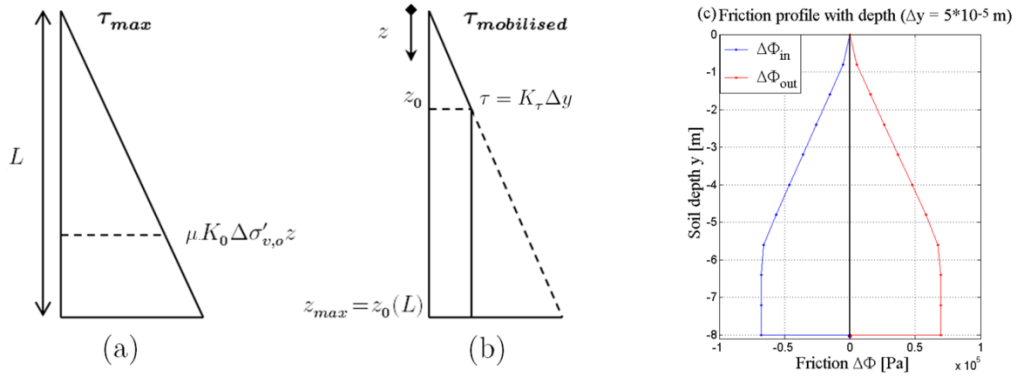

FIGURE 4-16: (a) Linearly increasing shear stress profile with depth and (b) real shear stress profile bounded to the maximum available shear stress τ_{max}

$$\tau\ \Delta y = \underbrace{\int_0^{z_0} \mu K_0 \Delta\sigma'_{v,o} z\ dz}_{\text{triangular profile}} + \underbrace{\int_{z_0}^{L} K_\tau \Delta y}_{\text{rectangular profile}}$$

$$\hookrightarrow \quad \Phi_{mob} = 2\pi R\ \tau\ \Delta y$$

$$= 2\pi R \left(K_\tau \Delta y L - \frac{1}{2} \frac{K_\tau^2 \Delta y^2}{\mu K_0 \Delta \sigma'_{v,o}} \right) \qquad \text{EQUATION 4-28}$$

$$\Phi_{max} = 2\pi \frac{D}{2} L \left(K_0 \gamma'_{clay} \frac{L}{2} \right) \mu \qquad \text{EQUATION 4-29}$$

An enlargement of the first point of the numerical and the analytical load-displacement curves for both the inner and the outer friction components is proposed in Figure 4-17 (a) and (b). The good concordance between the results derived by both methods can be directly observed from the graphs. This correlation can also be highlighted by using an indicator to quantify the error, namely the relative error defined by Equation 4-30. The relative error in the sub-case 1 amounts to less than 1% over the entire friction mobilisation profile, which attests of the reliability of the proposed analytical method in the case of a purely rigid body motion.

$$\mathrm{E_r} = \frac{|\Delta\Phi_{\mathrm{ana}} - \Delta\Phi_{\mathrm{num}}|}{|\Delta\Phi_{\mathrm{ana}}|} \quad [\%] \qquad \text{EQUATION 4-30}$$

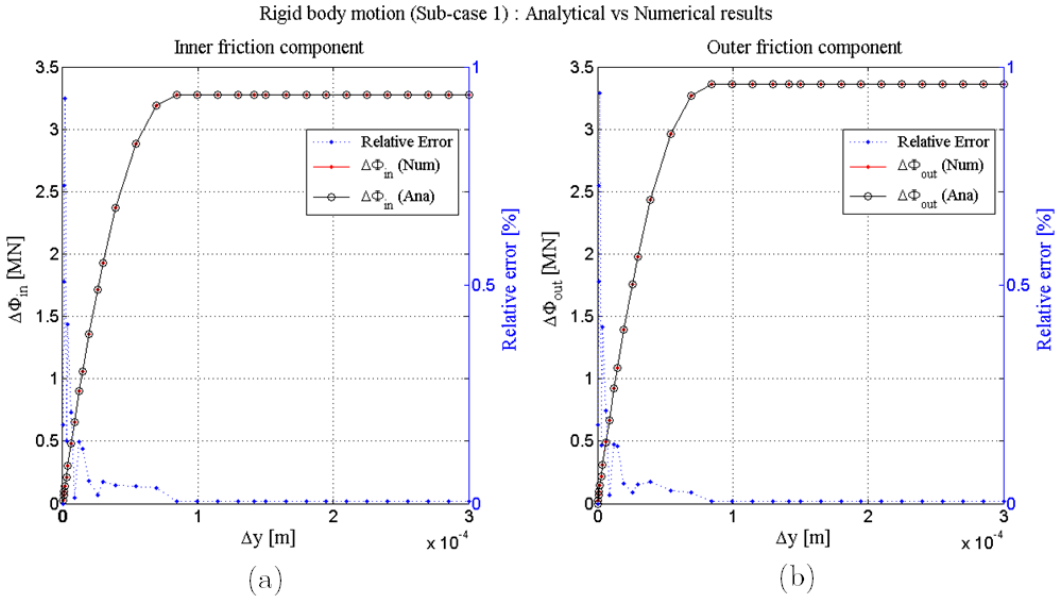

FIGURE 4-17: Comparison between the numerical and the analytical computations of friction components for a purely rigid body movement (sub-case 1): Inner available friction (a) and outer available friction (b)

Regarding the sub-case 1*bis*, for which only the top nodes of the caisson are assigned a displacement, Figure 4-18 (a) and (b) gives the plot of the inner and the outer friction components. It is shown that the slope of the numerical curves is gentler than that of the analytical ones, and that the maximum available friction is thus mobilized under a slightly larger displacement. In terms of relative error, this is expressed by a deviation of 40% that progressively decreases until almost 0% once both curves have reached the maximum mobilisable friction. Physically, when a displacement is imposed at the top, the whole capacity of each element will be consumed one after the others from the top to the bottom of the caisson skirt, which will require a greater relative displacement to mobilise the maximum friction than in the case of an overall motion of all the caisson nodes.

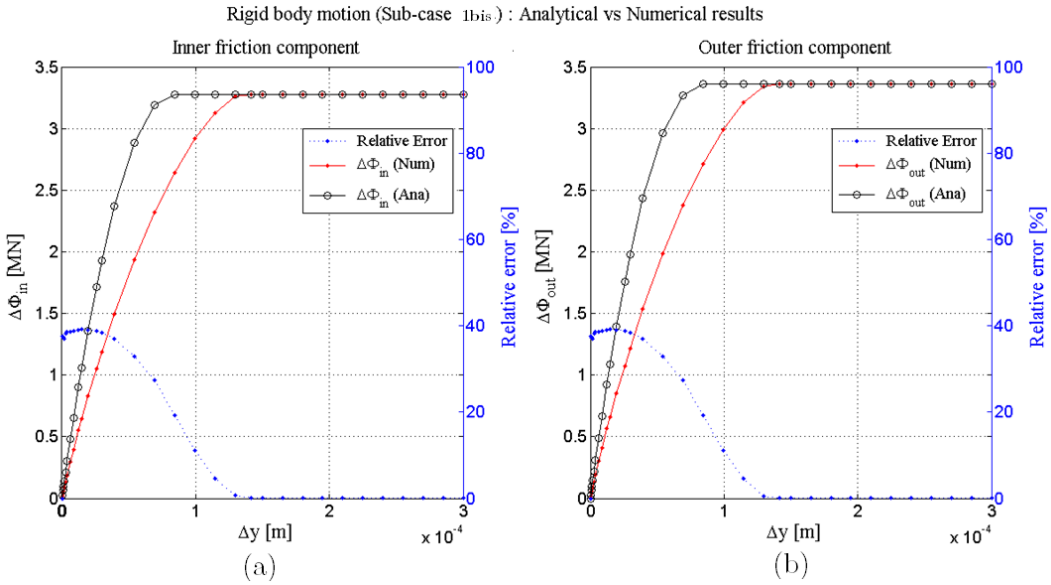

FIGURE 4-18: Comparison between numerical and analytical computation of friction components for a rigid body movement (sub-case 1*bis*): Inner available friction (a) and outer available friction (b)

4.3.5.2. Soil free to move (Sub-cases 2 and 2*bis*)

Regarding the configurations of a soil free to move, the friction components are assessed on the basis of the analytical expression derived by Randolph & Wroth [75] to analyse the deformation of vertically loaded piles. This expression formulated in Equation 4-31 furnishes an explicit value for the shear constant K_s which links the shear stresses to the displacement of the foundation. The details of all the intermediate calculation steps leading to this final equation are proposed in Appendix C.2. This approach is based on the hypothesis of a homogeneous linearly elastic soil that does not take the effects of the installation of the foundation into account. The application of this method to suction caissons is all the more valid as the slenderness ratio $\frac{D}{L}$ of the caisson is high which is related to a behaviour close to the one of piles.

$$\tau(\Delta y) = K_s\ \Delta y$$

$$\Longleftrightarrow \qquad \tau(\Delta y) \quad = \boxed{\frac{1}{\frac{r}{G}ln\left(\frac{r_m}{r}\right)}}\ \Delta y \qquad \text{EQUATION 4-31}$$

Where

$r = D/2$	Radius of the suction caisson
G	Shear modulus
$r_m = 2.5L(1-\nu_c)$	Parameter defined as the radius at which the shear stress becomes negligible in [75]
K_s	Shear constant

The expression for the shear constant K_s is then substituted instead of K_τ in Equation 4-28, in order to obtain the relationship between the variation of the total friction force and the vertical displacement, given by Equation 4-32.

$$\Delta\Phi = 2\pi R \left(K_s \Delta y L - \frac{1}{2}\frac{K_s^2 \Delta y^2}{\mu K_0 \Delta\sigma'_{v,o}}\right) \qquad \text{EQUATION 4-32}$$

Outer friction component

Using this Equation 4-32 to estimate the friction on the external interface of the caisson for the setting parameters ($E_c = 10^7\ MPa, K_\tau = 4.10^8\ MPa, \upsilon_c = 0.3$) furnishes the analytical curve in Figure 4-19 (a). Compared to the numerical curve, a progressive divergence occurs for increased displacements, leaving a significant underestimation of the mobilised outer friction.

In response to this, a first calibration parameter $\zeta_{out,d}$ is included in the expression of r_m (and thus in K_s) as expressed in Equation 4-33. This parameter is adjusted by means of a first robust condition that the maximum analytical friction is activated at the same imposed displacement as numerically. Mathematically, this requirement is formulated as Equation 4-35.

$$r_m = 2.5L \boxed{\zeta_{out,d}} \quad 1 - \nu_c \qquad \text{EQUATION 4-33}$$

It gives rise to the analytical curve displayed in Figure 4-19 (b). If the overall trend of this manual approach looks quite good, the relative error between the two lines is rather high, especially due to the overestimation in the phase of mobilisation of friction. To refine the superposition between the analytical and the numerical results, a second calibration parameter $\xi_{out,d}$ is introduced in Equation 4-34 in such a way that the relative error is reduced by about 10 and becomes negligible, as stated in Figure 4-19 (c). Here again, the parameter $\xi_{out,d}$ requires a second robust condition to reach a suitable value. This will be done by supposing that the initial slope of the analytical curve, i.e. the 1st derivative of the function, is set equal to the initial declivity of the numerical curve, as expressed mathematically by Equation 4-36.

$$\Delta\Phi_{out} = 2\pi R_o \left(\boxed{\xi_{out,d}} \; K_s \Delta y L - \frac{1}{2}\frac{K_s^2 \Delta y^2}{\mu K_0 \Delta\sigma'_{v,o}} \right) \qquad \text{EQUATION 4-34}$$

$$\underbrace{\Phi_{ana}(y_{peak}) = \Phi_{max}}_{1st\ condition} \iff 2\pi R_o \left(\xi_{out,d} K_s \Delta y_{peak} L - \frac{1}{2}\frac{K_s^2 \Delta y_{peak}^2}{\mu K_0 \Delta\sigma'_{v,o}}\right) = \Phi_{max} \qquad \text{EQUATION 4-35}$$

$$\underbrace{\left.\frac{\partial\Phi_{ana}(y)}{\partial y}\right|_0 = \left.\frac{\partial\Phi_{num}(y)}{\partial y}\right|_0}_{2nd\ condition} \iff 2\pi R_o \left(\xi_{out,d} K_s L\right) = \left.\frac{\partial\Phi_{num}(y)}{\partial y}\right|_0 \qquad \text{EQUATION 4-36}$$

Inner friction component

An accurate estimation of the friction on the inside of the caisson is pretty much tricky compared to the outer friction. Indeed, it has been showed in section 4.3.3 that the inner friction is mobilised in two stages. From then on, a precise analytical reconstruction of this curve will require a lot of calibration parameters. However, during the first stage, the activation of the inner friction is governed by the mobilisation of the outer friction that mainly contributes to the tensile capacity. Once the maximum available friction is reached on the outside of the caisson, only then the mobilisation of the inner friction becomes the main mechanism. Since this

work aims at developing a simplified calculation method, the analytical curved of $\Delta\Phi_{in}$ will be assessed using only one calibration parameter $\zeta_{\mathrm{in,d}}$ included in the expression of r_m based on the second part of the numerical curve, where the inner friction becomes predominant. Equation 4-37 furnishes the analytical expression for the friction on the inside of the caisson. As for the parameter $\zeta_{\mathrm{out,d}}$, it is rather logical to use the 1st condition of Equation 4-35 to calibrate the parameter $\zeta_{\mathrm{in,d}}$. Figure 4-20 gives an overview of the superposition between the numerical and the analytical curves of the inner friction. A general evidence is that the trend of the analytical curve is rather good despites it does not match the real curved shape of the numerical results.

$$\Delta\Phi_{in} = 2\pi R_i \left(K_s \Delta y L - \frac{1}{2}\frac{K_s^2 \Delta y^2}{\mu K_0 \Delta\sigma'_{v,o}}\right) \qquad \text{EQUATION 4-37}$$

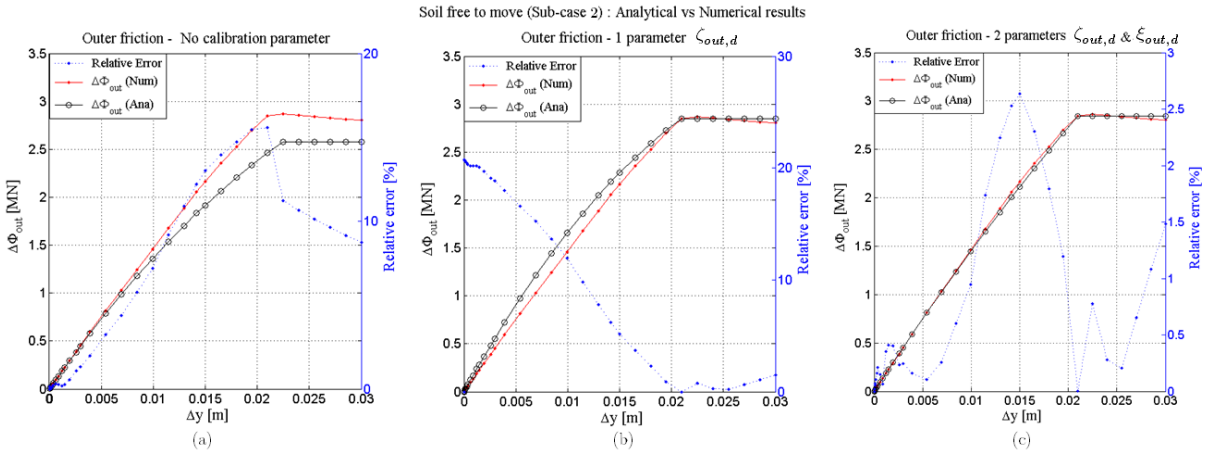

FIGURE 4-19: Superposition of the numerical and analytical curves when (a) no parameter, (b) 1 parameter and (c) 2 parameters are considered in the analytical formula (Outer friction component)

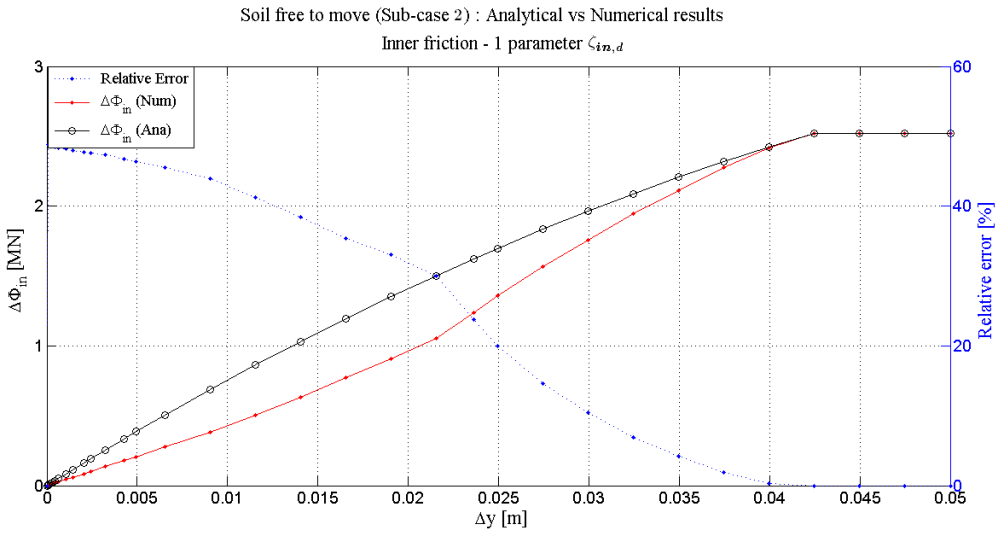

FIGURE 4-20: Superposition of numerical and analytical curves considering 1 parameter in the analytical expression (Inner friction component)

4.4. 2nd Scenario - Partially drained conditions and elastic soil

4.4.1. Assumptions

In this second scenario, the numerical simulations of the reference model are carried out for the same linear-elastic soil configuration as in the first scenario. The initial representative values for the elastic modulus and the Poisson's ratio are defined identically as in the drained scenario, namely $E_c = 1 \times 10^7\ Pa$ and $\nu_c = 0.3$ respectively.

In addition to its linear elastic behaviour, the soil is assumed to be made of small-sized clay particles establishing an undrained or at least a partly drained soil behaviour, giving rise to an hydro-mechanical system. In accordance with the implementation of the reference model, the clayey material is assigned a porosity n of 0.5 and a coefficient of permeability k of $10^{-7}\,\frac{\mathrm{m}}{\mathrm{s}}$. The associated intrinsic permeability k_{int} which regulates water movements across the domain is assessed according to Equation 4-38.

$$k_{int} = k\frac{\mu_w}{g\ \rho_w} = 10^{-14}\ [m^2] \qquad \text{EQUATION 4-38}$$

Where

$\mu_w = 10^{-3}\ [Pa\ s]$ Fluid dynamic viscosity for water at 20°C

As specified in the reference model, the contact zones are governed by a mechanical law, which is a Mohr-Coulomb dry friction, and also a flow law which characterizes the way in which water flows are distributed at the soil-caisson interfaces. These laws have their own associated parameters tabulated in Table 4-6.

4.4.2. The FE model

The Finite Element model is still based on the one defined as reference with an aspect ratio $\frac{L}{D} = 1$. In contrast to the previous scenario, the water pressure degree of freedom is here free to vary by means of the fluid flows across the domain, except at the left and bottom edges and around the caisson. These zones are supposed to be impermeable and thus to prevent water flows. The main initial parameters of the soil, the caisson and the interfaces for this second scenario are summarized in Table 4-6.

In the present partly drained configuration, the value of the imposed displacement will have a direct impact on the duration of the simulation. Consequently, the displacement at the top of the caisson is assigned a value of $d = 0.3\ mm$ for the 1st sub-case and a value of $d = 0.05m$ for the second sub-case. Since the loading of the caisson is performed by means of displacement-ontrolled simulations, a first reference value of $1 \times 10^{-6}\,\frac{m}{s}$ for the loading rate is considered. Such a small value is required in order to ensure the convergence of the code. If a greater rate of loading was applied, it would become essential to envisage a refinement of the mesh inside the caisson to cancel out the numerical oscillations under the lid. The simulations will be executed by an automatic strategy making use of the same parameters as for the 1st scenario.

In line with the numerical simulations conducted in the 1st scenario, the four sub-cases will be here reduced to two main ones. First a rigid body motion with all the nodes of the caisson fixed in the x −direction, all the soil nodes at the interfaces with the caisson fixed in both $x-$ and $y-$ directions, and a displacement imposed to all caisson nodes (sub-case 3). Then a soil free to move around and inside the caisson is assumed with a vertical upward displacement applied at the top of the caisson (sub-case 4), as depicted in Figure 4-21.

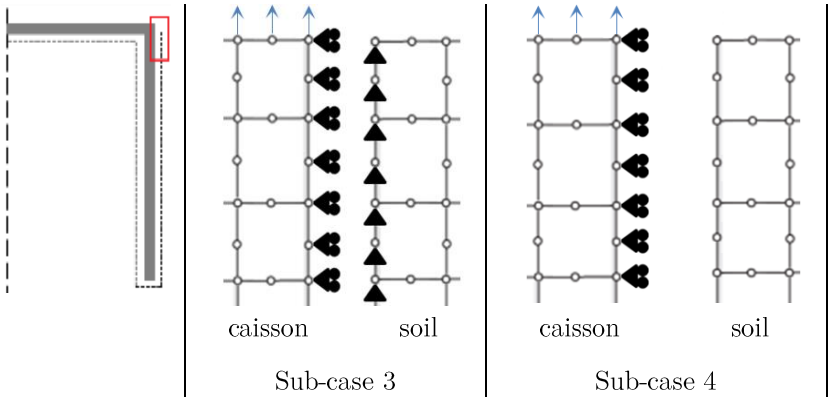

FIGURE 4-21: Definition of the two sub-cases examined in the second scenario

TABLE 4-6: Set of the simulation input values: parameters of the mechanical constitutive law of the interface elements, of the soil and caisson materials and execution data

MATERIAL	LAW	PARAMETERS	SYMBOL	VALUE	UNIT
Interface	Mohr-Coulomb	Penalty coefficient on the contact pressure	K_p	4×10^9	[-]
		Penalty coefficient on the shear friction stress	K_τ	4×10^8	[-]
		Coulomb's friction coefficient	μ	0.5	[-]
		Transmissivity	T_w	10^{-3}	$\left[\frac{m}{Pa.\,s}\right]$
Soil	Elastic-Linear	Cohesion	c	0	[kPa]
		Poisson's ratio	υ_c	0,3	[-]
		Young's modulus	E_c	1×10^7	$[MPa]$
		Intrinsic permeability	k_{int}	10^{-14}	$[m^2]$
Steel	Elastic-Linear	Poisson's ratio	υ_c	0.2	[-]
		Young's modulus	E_s	210	$[MPa]$
		Loading rate	LR	1×10^{-6}	[m/s]
		Imposed displacement	d	0.05	[m]
				0.0003	
Simulation parameters		Identical to the 1st scenario (see Table 4-4)			

4.4.3. Results

As a first step, the scale of the problem can be visualized on the basis of the main FE model features for the two sub-cases which are given in Table 4-7.

TABLE 4-7: Linear elastic soil behaviour & drained configuration: simulation attributes

SUB-CASE	NO. NODES [-]	NO. ELEMENTS [-]	RUNNING TIME [S]	NO. STEPS [-]	NO. ITERATIONS[-]
3	10803	3566	67	22	64
4			187	22	94

As for the fully drained configuration, the various contributions to the variation of the total extraction resistance ΔR_{tot} can be highlighted. The general equilibrium Equation 4-39 in terms of variation components for a vertical uplift motion of the caisson $d(t) \neq 0$ in a partially drained configuration, is derived from Equation 4-24. Here again the total contribution of the water pressure involving ΔW_w acting downwards and $\Delta P_{w,lid}$ and $\Delta P_{w,tip}$ acting upwards, as well as the variation of the weight of the caisson ΔW_{cais} can be cancelled out. This leaves a system with the main components depicts in Figure 4-22.

$$\Delta R_{tot} = \underbrace{\Delta W_{cais}}_{=0} + \underbrace{\Delta W_w}_{<0} + \underbrace{\Delta \Phi_{in}}_{>0} + \underbrace{\Delta \Phi_{out}}_{>0} + \underbrace{\Delta P_{pwp}}_{>0} + \underbrace{\Delta W_{plug}}_{>0} - \underbrace{(\Delta P_{w,lid} + \Delta \Sigma'_{lid})}_{<0} - \underbrace{(\Delta P_{w,tip} + \Delta \Sigma'_{tip})}_{<0}$$

$$\Leftrightarrow \quad \Delta R_{tot} = \Delta \Phi_{in} + \Delta \Phi_{out} + \Delta P_{pwp} + \Delta W_{plug} - \Delta \Sigma'_{lid} - \Delta \Sigma'_{tip} \qquad \text{EQUATION 4-39}$$

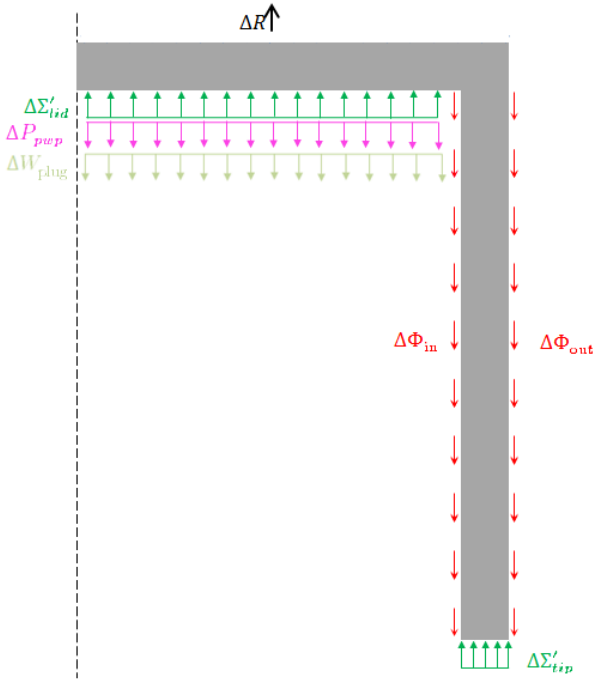

FIGURE 4-22: Variation of the reaction components during an imposed displacement, 2nd scenario

To be able to discern to what extent the remaining compoents are applied, the displacement-load curves of both the total and the normalised variations of the reaction components for partially drained traction simulations are illustrated in Figure 4-23 (a) in the case of a rigid body movement (sub-case 3) and in Figure 4-23 (b) in the case of free soil and caisson nodes (sub-case 4). The normalisation is still done according to the variation of the global load ΔR_{tot} at the considered step, which gives an overview of the influence of each reaction component over the total tensile capacity in percent.

The progressive mobilisation of the reaction components appears distinctly, with features already noted for the drained elastic scenario [77]. The shares of the soil pressure components under the lid $\Delta \Sigma'_{lid}$ and at the skirt tip level $\Delta \Sigma'_{tip}$ are still really limited, as already discussed

in the drained configuration. Similarly to the 1st scenario, the contributions of these components to the total reaction are assumed to be small enough (at most equal to 5%, Figure 4-23 (a) and (b)) to be neglected. Concerning the weight of the soil that is driven with the caisson ΔW_{plug}, it is logical to note from Figure 4-23(a) and (b) that this component is zero when the soil is held in place. This means that the tensile load is almost only sustained by the three remaining components for the extraction of the rigid body, namely the friction components $\Delta\Phi_{in}$ and $\Delta\Phi_{out}$ and the variation of PWPs inside the caisson ΔP_{pwp}, as stated in Equation 4-40. When the soil is released, the contribution of the soil plug ΔW_{plug} takes a really low value (because the study is conducted in small displacements) that slightly increases with the imposed displacement. Contrary to the effects of the contact pressure $\Delta\Sigma'_{lid}$ and $\Delta\Sigma'_{tip}$, this term will not be neglected in the general equilibrium equation, despites its low weight, because it will directly influence the way in which the inner friction will be mobilised. Indeed, the higher the uplift movement of the soil plug, the smaller the relative displacement between the confined soil and the caisson, and thus the lower the amount of inner shear stresses. This way, the general equilibrium equation includes one more term, as stated in Equation 4-41.The magnitude of the soil heave will rely on the accumulation of negative excess PWPs underneath the lid, which is a function of the permeability of the soil and the drainage paths. For low permeable clayey soils, the suction effect will develop faster under tensile loading.

Sub-case 3

$$\Delta R_{tot} \approx \Delta\Phi_{in} + \Delta\Phi_{out} + \Delta P_{pwp} \qquad \text{EQUATION 4-40}$$

Sub-case 4

$$\Delta R_{tot} \approx \Delta\Phi_{in} + \Delta\Phi_{out} + \Delta P_{pwp} + \Delta W_{plug} \qquad \text{EQUATION 4-41}$$

Compared to the drained scenario, an increase in the total resistance of the caisson is noticed (Figure 4-24 (a) for the held in place soil, subcase 3), which is a consequence of the appearance of the suction effect mobilised over the entire cross-sectional area and produced by the variation of fluid pressures. When considering a partly drained configuration, this total resistance becomes transient and is dependent on the loading rate and the permeability. This will be investigated further on in section 4.4.4, influence of the main parameters.

The outer friction along the skirt $\Delta\Phi_{out}$ is mobilised identically to the fully drained configuration. Outer shear stresses increases progressively until the maximum available friction is reached symbolised by an almost constant limit. At this time, any increase in loading should be withstood by the other reaction components since sliding arises at the outer soil-caisson interface. If no quantitative variation of the outer friction component appears when the soil remains in place (sub-case 3), a slight increase in this component is noticed when the soil is free to move, as reported in Figure 4-24 (c). This mainly comes from the enhancement of the outer surrounding effective stresses under the hydrodynamic flows that gradually set up.

The inner friction along the skirt $\Delta\Phi_{in}$ is mobilised in the same way as the outer friction when a rigid body motion is considered, as illustrated in Figure 4-23 (a). It is not a surprise since the soil remains in place in such a configuration. When the soil is released, the results differ from those obtained in the 1st scenario for a drained configuration, as highlighted in Figure 4-24 (b). Indeed, the development of the suction effect under water pressure variations tends to stick the soil plug to the caisson. This way, the relative soil-caisson displacement, and the related inner friction component, is reduced to such a degree that will depend on the variation of the pore

water pressures inside the caisson and thus on the loading rate and the permeability. The reduced effect of the inner friction is visible in Figure 4-23 (b) where it accounts for about 10% of the total resistance. An increase in the slope of the inner friction component is still apparent from the moment when the outer friction has been completely mobilised.

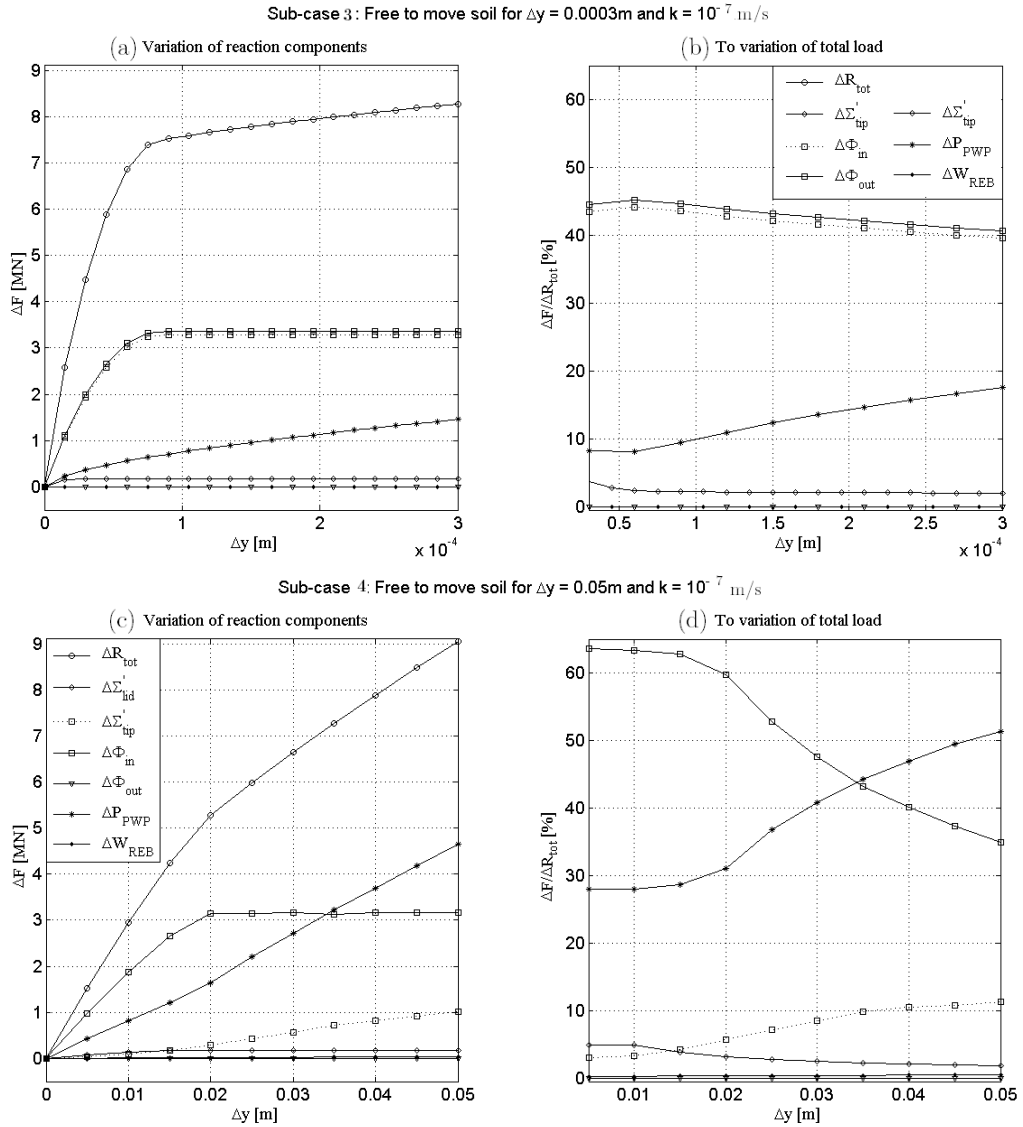

FIGURE 4-23: Partially drained traction simulation : variations of the reaction components and variations of the reaction components to variation of the total load for (a,b) sub-case 3 and (c,d) sub-case 4

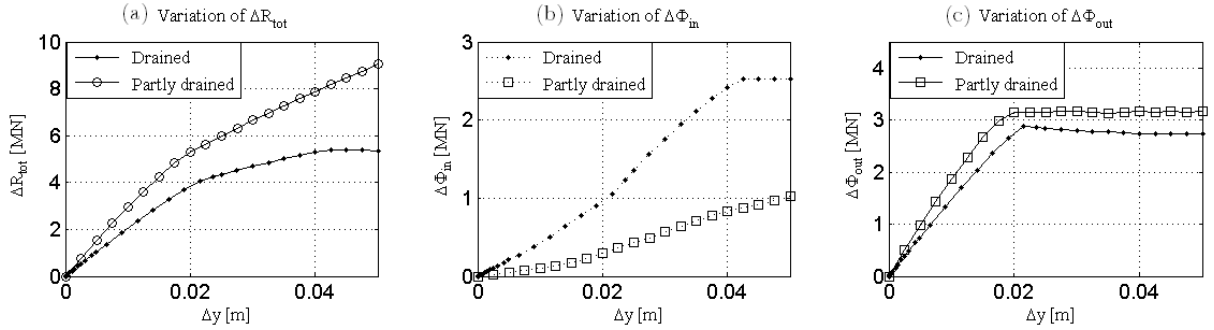

FIGURE 4-24: Comparison of the (a) total reaction component, (b) inner friction component and (c) outer friction component between drained and partly drained conditions

The variation of the PWPs inside the caisson is a new component of the reaction that occurs when an undrained or a partially drained state of the system is considered. It is the vector of an increased resistance of the caisson with respect to the drained configuration. For a loading rate of $1 \times 10^{-6} \frac{m}{s}$ and considering a displacement of 0.0003m in the sub-case 3 and a displacement of 0.05m in the sub-case 4, it can be seen in Figure 4-23 (a) and (b) that the contribution of the PWPs to the total resistance amounts to nearly 20% and a bit more than 50% respectively. Compared to the results obtained for the drained scenario (see Figure 4-11), this leads to an enhancement of the tensile capacity from 6.8MN to 8.3MN in the case of a rigid body motion, and from 5.4MN to 9MN in the case of a soil free to move. As previously mentioned, the magnitude of the PWP contribution and thus of the total tensile load sustained for a given displacement will be directly dependent on the system parameters, namely the displacement, the soil permeability, the loading rate, and the aspect ratio $\frac{D}{L}$. The influence of the main system parameters will be investigated in the next section. From Figure 4-23 (a) and (b), it appears that the share of the PWP component first declines during the activation of the outer friction, reaches its minimum value once the maximum available outer friction is mobilized and then starts to increase from this point. When the soil is fixed in place, the evolution of the PWP contribution takes a curved shape, while for a released soil the trend is more linear including a slope break at the point where the outer friction component is fully mobilized.

Figure 4-25 shows the distribution of the PWPs in the form of contour lines for a displacement of the lid of the caisson of 0.0003m (sub-case 3, (a)) and of 0.05m (sub-case 4, (b)). For both cases, a negative pore pressure field develops inside the skirt of the caisson during the pull simulation and rapidly dissipates beyond the skirt periphery. This is responsible for the appearance of the suction effect in sub-case 4, i.e. the negative variations of PWPs cause the rise of the effective normal stresses along the inner skirt interface, and with them the increase of the maximum available inner friction. This way, the soil plug has a tendency to follow the movement of the caisson, impeding the extraction of the caisson and explaining why the variation component of the inner friction ΔF_{in} is greatly reduced in a configuration of a soil free to move. In the case of a rigid body motion, a gap opens under the lid that is progressively filled with water flows from the soil and along the interstices at the soil-caisson interfaces, giving birth to underpressures.

The consistency between the curves of pressure obtained in Figure 4-23 (a) and (b) and the distribution of PWPs from Figure 4-25 (a) and (b) can be easily assessed by the following calculations from Table 4-8.

TABLE 4-8: Check of the consistency of the results

SUB-CASE	FIGURE 4-23		FIGURE 4-25
3	$\Delta P_{pwp} \approx \lvert -29500 \rvert \times \pi \times \left(\frac{D_i}{2}\right)^2 = 1.41\ MN$	$\leftrightarrow$	$1.45\ MN$
4	$\Delta P_{pwp} \approx \lvert -90\ 700 \rvert \times \pi \times \left(\frac{D_i}{2}\right)^2 = 4.33\ MN$	$\leftrightarrow$	$4.65\ MN$

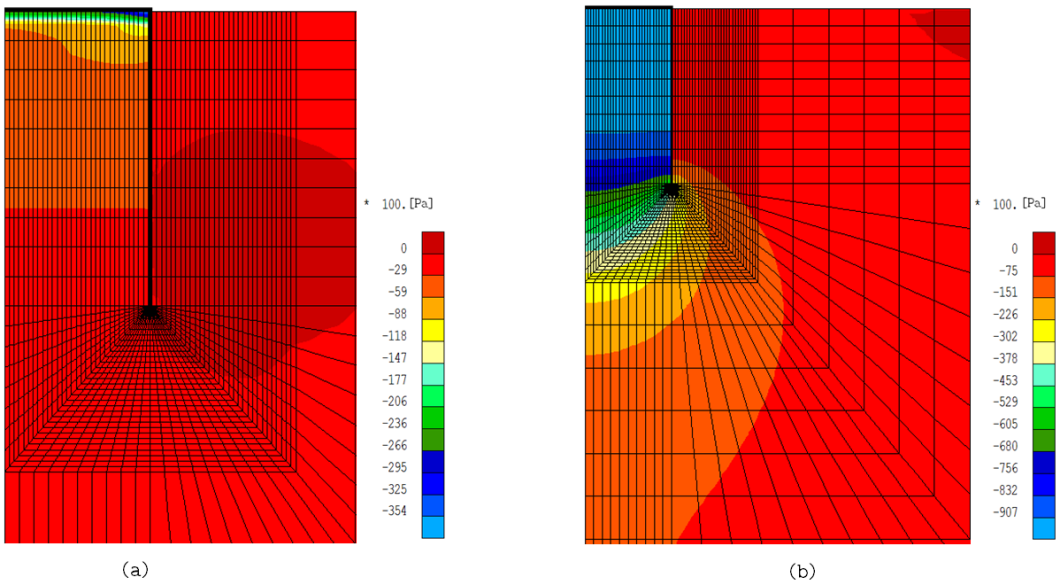

FIGURE 4-25: Distribution of pore water pressures around the caisson for (a) a rigid body motion and (b) a soil free to move, rate of loading $= 1 \times 10^{-6} \frac{\mathrm{m}}{\mathrm{s}}$ and $\mathrm{k} = 10^{-7}$ m/s

Wishing to highlight the failure modes occurring during a partly drained uplift of the caisson, the simulations of sub-case 4 are carried out for a coefficient of permeability of 5.10^{-5} m^2 and of $5.10^{-8} m^2$, with the results presented in Figure 4-26 and Figure 4-27 respectively.

When the caisson is extracted from a higher permeable soil, drainage is more susceptible to establish under the loading and thence only small variations of the water pressure appear inside the caisson. The total load is mainly sustained by the inner and the outer friction, similarly to a fully drained configuration. Several failure modes follow one another, as made explicit in Figure 4-26 (a). First the contact is lost between the caisson lid and the soil, while at the same time, the outer shear stresses are mobilized up to the limit of maximum available outer friction. When the soil starts to slide on the outside of the caisson, any increase in loading is transferred to the inner friction component which rises up until it is also fully mobilized. When sliding occurs on the two interfaces, then the variation of PWPs becomes the only component that can sustain additional loading increments. As displayed in the color scheme of Figure 4-26 (b), the same model of vertical soil deformations under uniaxial tensile load can be ascertained as in the literature [47] for a partially drained configuration tending to a drained one.

When the caisson is extracted from a low permeability soil, drainage has no time to properly establish under the loading, and the variations of PWPs become a dominant contribution to the pull-out resistance, together with the outer friction, as stated in Figure 4-27 (a). The effect of suction owing to the under-pressures keeps the soil and the caisson in contact, thereby nearly cancelling out the contribution of the inner friction and the variation of the soil pressure under the lid. As soon as the outer friction reaches its limit of resistance, any extra load applied will almost only be sustained by the increase in the PWP contribution. Here again, it is possible to match the obtained pattern for the variations of vertical displacements, with what is already defined in the literature [47], Figure 4-27 (b).

The plug uplift mechanism is directly dependent upon the suction effect that exerts an upward attraction force on top of the soil plug. For a first infinitesimal extraction step of the caisson,

small gaps will be created at the micro-scale under the lid. Instantaneously, the PWPs will decrease in this zone, and this negative variation of pressure (suction) will force the soil plug to move upwards, in such a way that the corresponding volume reduction above the plug brings the underpressures back to its initial equilibrium. The uplift of the soil plug goes hand in hand with the seepage flows through the confined soil from the surrounding soil and free water. Basic diagrams of Figure 4-28 give a qualitative overview of the coupling between the two phenomena. An undrained soil configuration is characterized by low permeable soil conditions or by a so fast loading rate that it does not allow the seepage flows to re-establish the initial water pressure under the lid. Under these conditions, significant negative excess PWPs will cause important soil heaves to occur inside and below the caisson in a so-called reverse end bearing failure mode, as illustrated in Figure 4-27 (b). When the drainage is more incline to set up, the combination of higher permeability with slower extraction rate exploits much more the seepage flow mechanism, which limits the development of negative excess PWPs and this way lowers the plug uplift mechanism, as exemplified in Figure 4-26 (b). In these conditions, the more the partially drained configuration tend towards a drained behaviour, the more the soil plug remains in place, leading to a sliding failure mode.

When the caisson is rigidly extracted from the ground held in place, the balancing of pressures in the gap between the soil and the lid comes solely from the seepage flows through the soil.
As the soil is assumed to be linear elastic in the present analysis, elastic deformations will occur in the soil during plug uplift by suction. Whatever the drainage conditions, it can be seen from Figure 4-26 (b) and Figure 4-27 (b) that the main soil deformations are concentrated at the base of the caisson where the displacement contours are the closest.

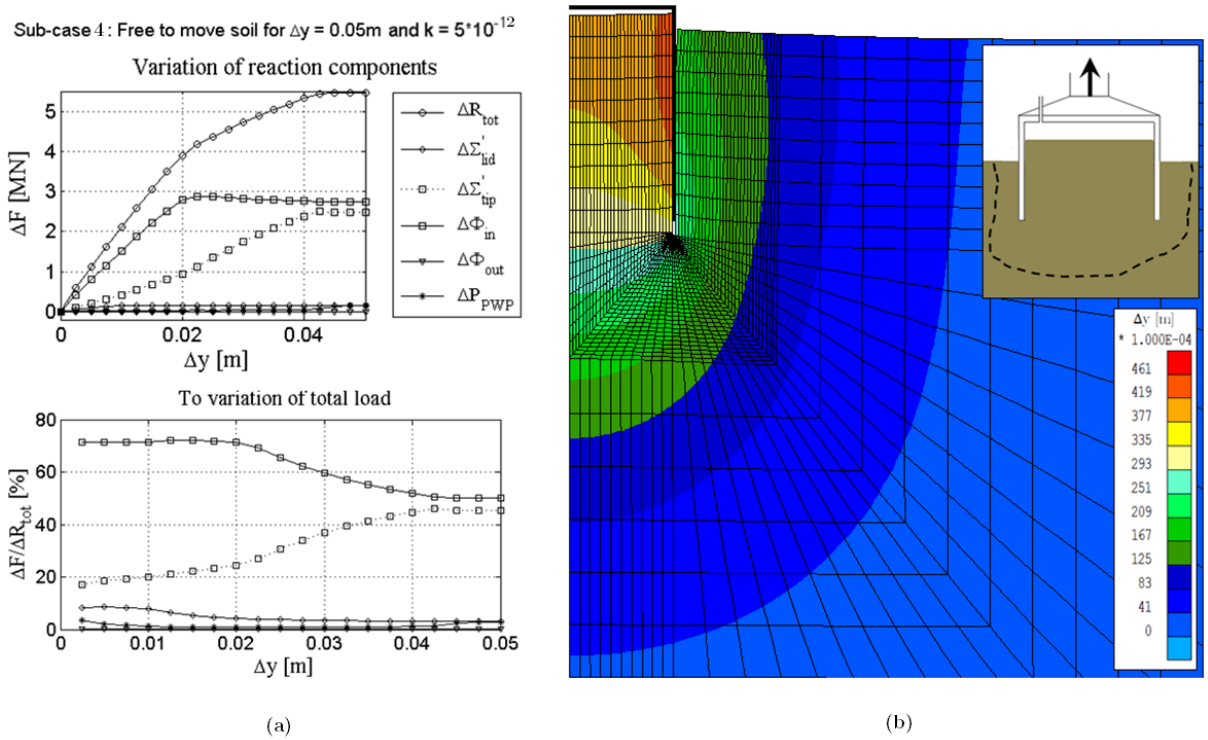

FIGURE 4-26: Results of the sub-case 4 for $k = 5.10^{-12}$: (a) Load-displacement curves and (b) variations of vertical displacement, Amplification factor = 25%

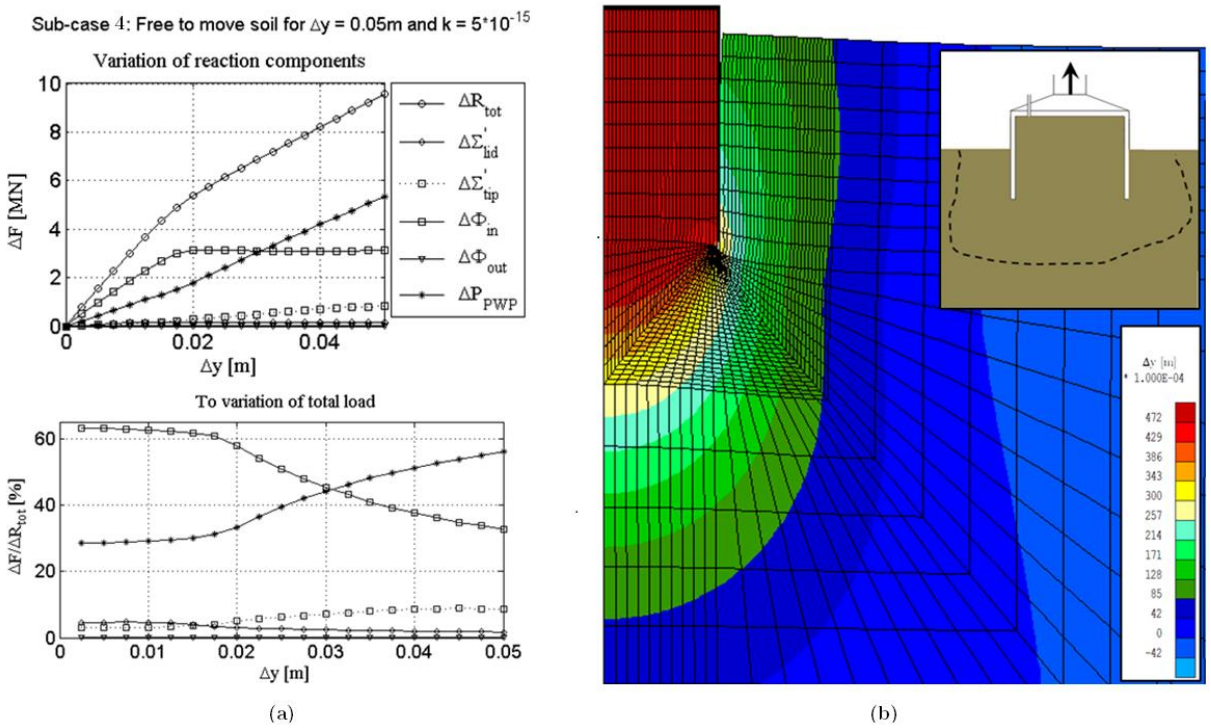

FIGURE 4-27: Results of the sub-case 4 for $k = 5.10^{-15}$: (a) Load-displacement curves and (b) variations of vertical displacement, Amplification factor = 25%

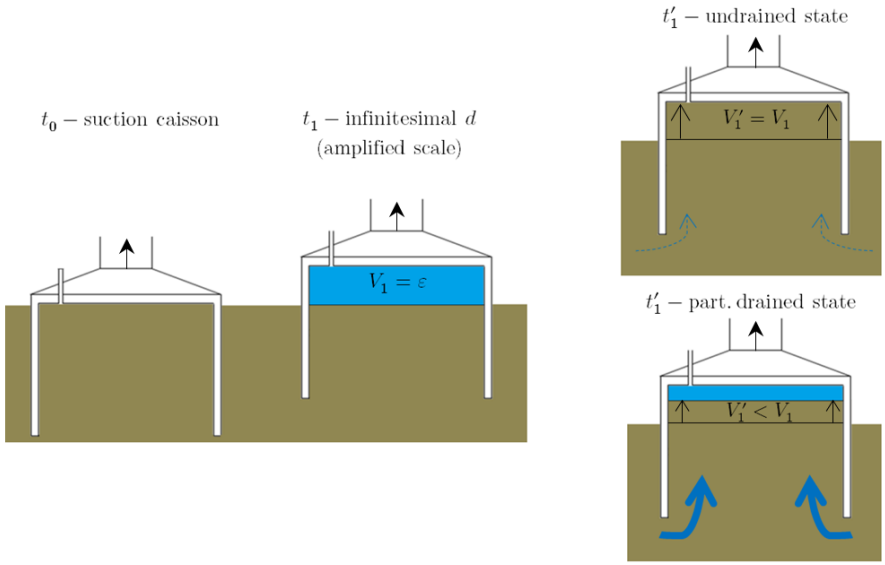

FIGURE 4-28: Coupling between the plug uplift and the seepage flow mechanism

Figure 4-29 characterizes both the shear stresses and the normal stresses along the inner and the outer skirt interfaces in the case of a partly drained scenario. Consistently to the results of the 1st drained scenario for a rigid body motion, the maximum friction is mobilized almost instantaneously, which explains that the shear stresses at the initial stage ($\Delta y = 0.015mm$) already encompass a significant part of the friction resistance at the last stage (Δy = 0.3mm), see Figure 4-29(a). The absence of soil disturbance in this configuration is responsible for the uniformity of the normal stress diagrams during the pull test (for all Δy), see Figure 4-29(b) When the soil is free to move, different normal stress profiles develop on both sides of the cais-

son due to the stress state disruption under external loading, as displayed in Figure 4-29(d) and (f). At the outer interface, the results are rather identical to those of the first drained scenario, with a distribution of the shear stresses at the last stage of the pull test that is homothetic to the distribution of the normal stresses. At the inner interface, the shear stresses are slightly negative on the upper part of the caisson which corresponds to stresses pointing upwards, and helping to extract the caisson, visible in Figure 4-29(c) and (e).

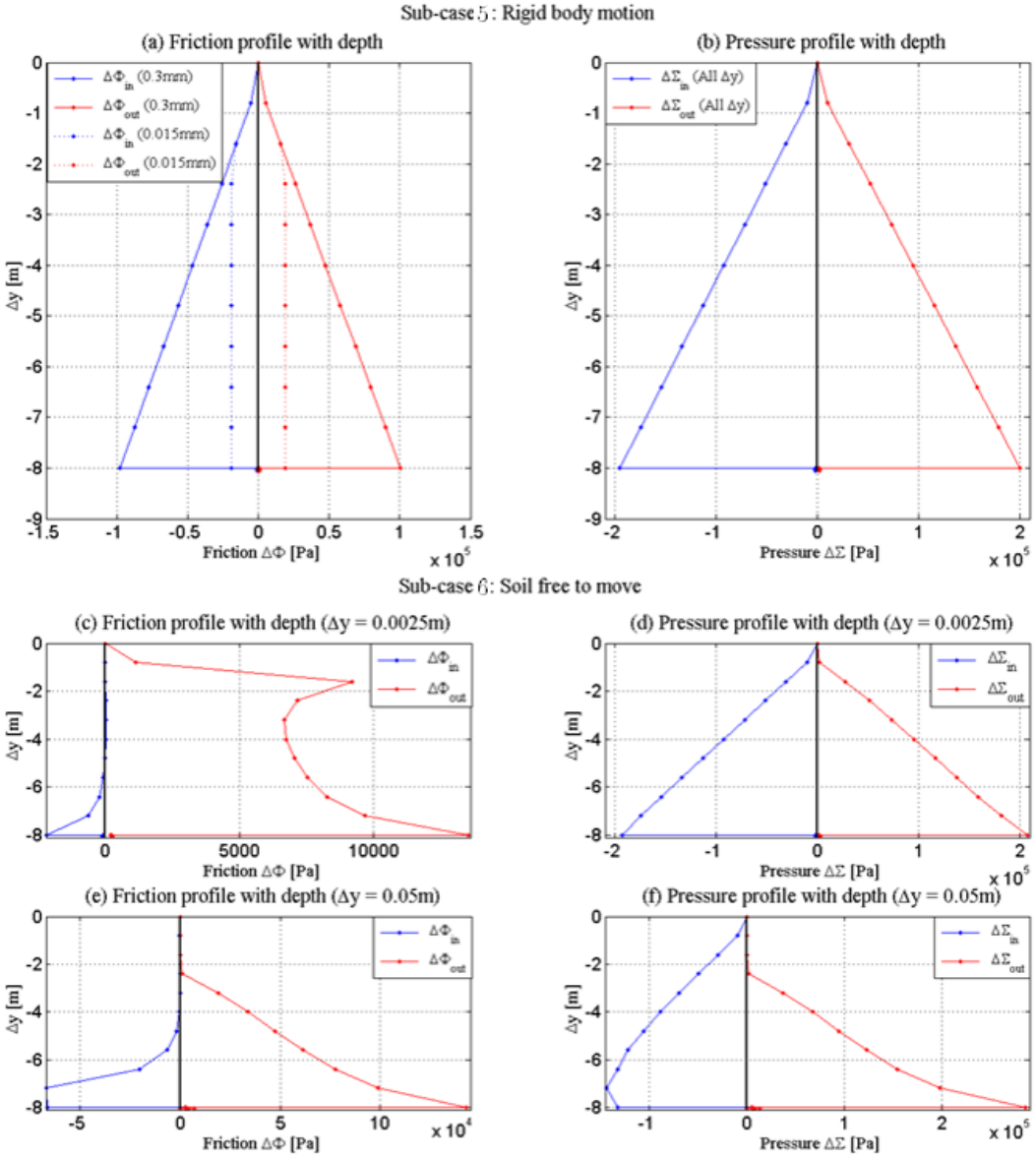

FIGURE 4-29: Distribution of the shear and the normal stresses along the caisson skirt in the case of a rigid body motion (a)-(b) and of a soil free to move (c)-(d)-(e)-(f), 2nd scenario

4.4.4. Influence of the main parameters

As for the drained scenario, this section aims to emphasize the principal parameters that affect the response of the soil-caisson system, in the present case of a partially drained soil. The parameters will be investigated by considering first a soil held in place, and then switching to the configuration of a soil free to move.

Figure 4-30 (a) and (b) gives a preview of the influence of the permeability k on the behaviour of the caisson when the sub-case 3 and 4 are respectively considered. Four orders of magnitude of the coefficient of permeability are tested upon traction. From these graphs, it is apparent that the lower the permeability of the soil, the higher the applied tension to obtain a given uniaxial uplift Δy of the caisson. It seems to be logical since a higher coefficient of permeability enables a more important dissipation rate of the under-pressures that accumulate below the lid of the caisson, and thus the development of variations in pressure ΔP_{pwp} is lower as illustrated in Figure 4-30 (a) and (b), right. The bifurcation point in the displacement Δy - load ΔR_{tot} curves of Figure 4-30 (a, left) and (b, left) stands for the fully mobilisation of friction on the outer interface in the case of a soil free to move and on both faces of the caisson in the case of a soil held in place. This change of slope associated to sliding is much more pronounced in Figure 4-30 (a) where only the contribution of the PWPs can withstand the load than in Figure 4-30 (b) where the contribution of inner friction can also be mobilised to resist the load increments. As a conclusion, a system with a high permeability should converge towards a fully drained configuration where the friction is prevailing and the excess PWPs are dissipated whereas in the presence of a low permeability, the system tends to become undrained with a significant contribution of the variation of fluid pressure ΔP_{pwp}.

Figure 4-30 (c) and (d) displays the effect of the loading rate LR on the displacement - load curves as well as on the pore pressure component, in sub-cases 3 and 4 respectively. It is obvious that the impacts of the variations of the pullout rate are strongly correlated to those of the coefficient of permeability. Similar conclusions can then be drawn as for the permeability. A fast loading restricts the drainage and the dissipation of the under-pressures, resulting in a large PWP contribution, while a slow loading speed will enable the progressive drainage of excess PWPs similarly to a high coefficient of permeability.

The geometric parameters of the caisson also directly affect the extraction resistance as well as the variations of the pore water pressure inside the caisson. The influence of the aspect ratio $\frac{D}{L}$ is illustrated in Figure 4-30 (e) and (f) and the effects of increasing the skirt length L are shown in Figure 4-30 (g) and (h). Not surprisingly, the wider the suction caisson, the larger the amounts of PWP variations that can arise inside the caisson and the greater the total pull-out resistance. In a quantitative manner, if the aspect ratio is doubled, the total resistance is increased almost by 3, and the contribution of PWP variations amounts to more than 50% in this total. The same principle is observed in Figure 4-30 (g) and (h), i.e. when the length of the skirt is increased for the same imposed displacement, a greater contribution of the PWPs emanates from the system but to a lesser extent in comparison to the influence of the aspect ratio.

Rigid body motion (Sub-case 3) : Influence of k [m^2] for Lr = 10^{-6}, T_w = 10^{-3} and D/L = 1

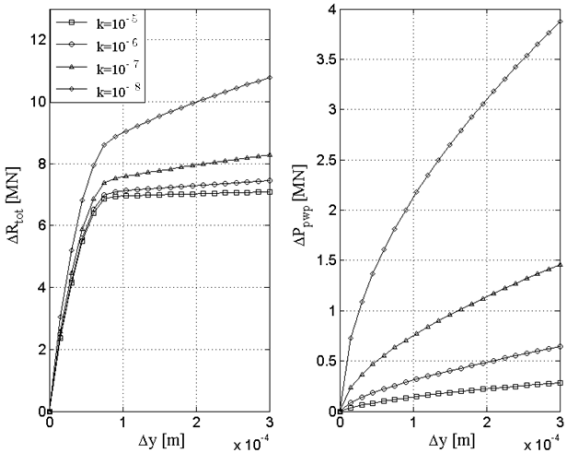

(a)

Free to move soil (Sub-case 4) : Influence of k [m^2] for Lr = 10^{-6}, T_w = 10^{-3} and D/L = 1

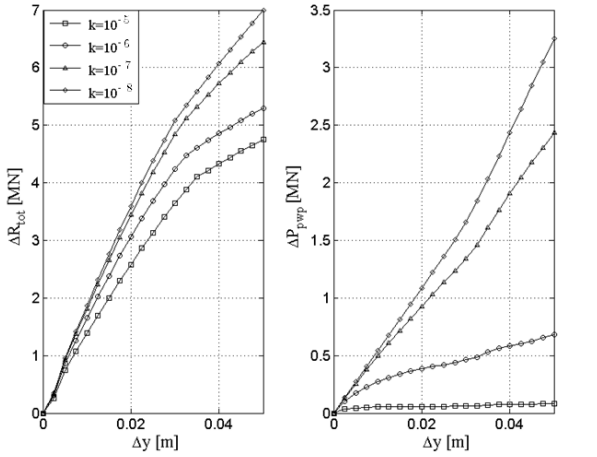

(b)

Rigid body motion (Sub-case 3) : Influence of the loading rate [m/s] for k = 10^{-7} , and D/L = 1

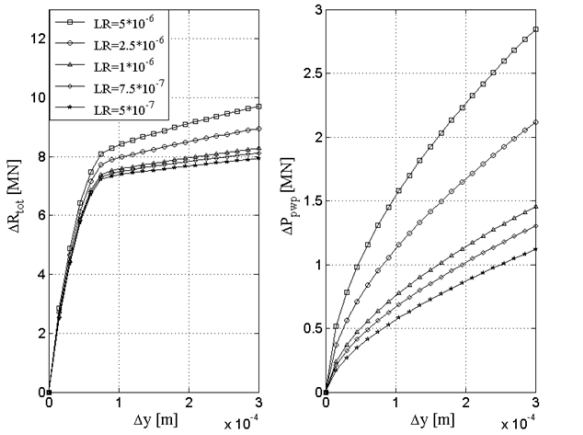

(c)

Free to move soil (Sub-case 4) : Influence of the loading rate [m/s] for k = 10^{-7} , and D/L = 1

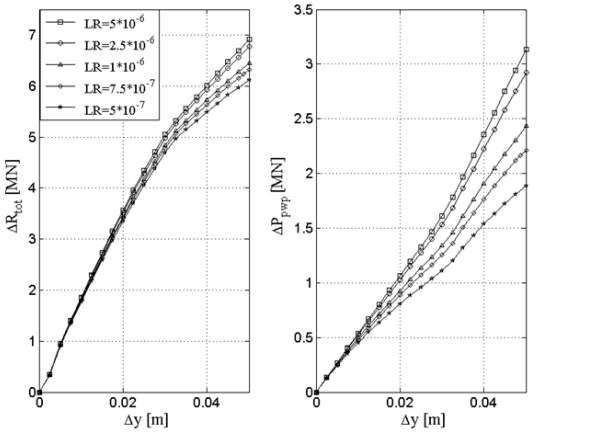

(d)

Rigid body motion (Sub-case 3) : Influence of the aspect ratio [-] for LR = 10^{-6}, k = 10^{-7}

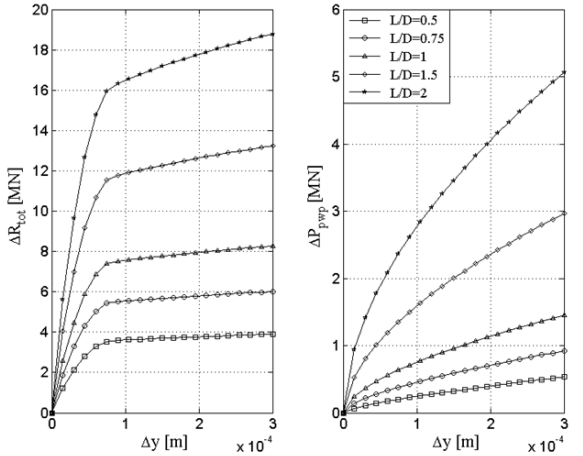

(e)

Free to move soil (Sub-case 4) : Influence of the aspect ratio [-] for LR = 10^{-6}, k = 10^{-7}

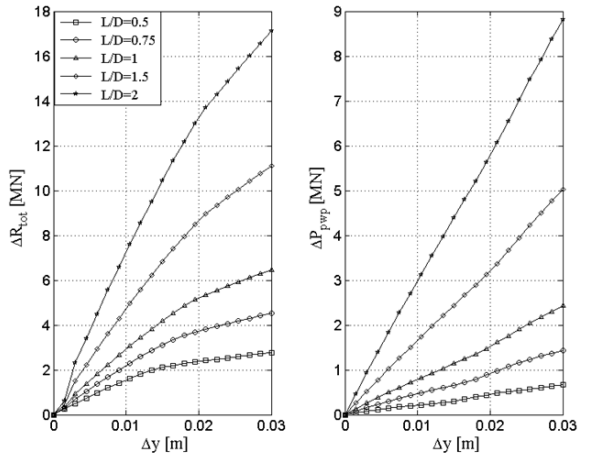

(f)

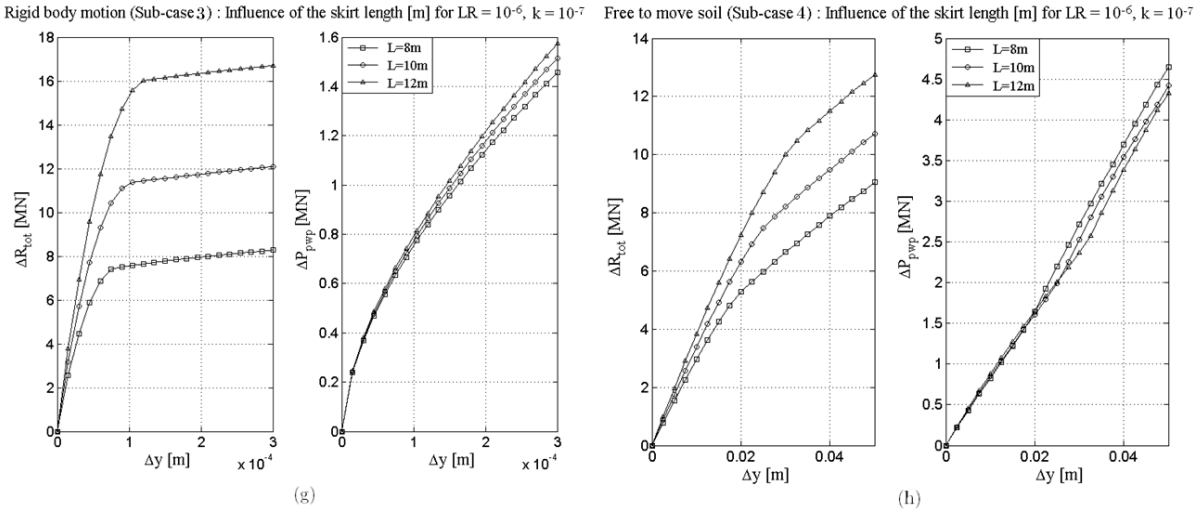

FIGURE 4-30: Influence of the main parameters on the friction components

4.4.5. Comparison between numerical and analytical results

In line with what was achieved for the 1st scenario, the analysis of the numerical results for a partially drained and a linear elastic soil configuration will be used to formulate and validate the analytical equations that replicate as accurately as possible the behaviour of the caisson. From the previous section, it is apparent that the prevailing components to the total uplift resistance are the shear stresses on the inner and the outer soil-skirt interfaces, as well as the variations of the pore water pressures under the lid and in a lesser extent the uplift movement of the soil plug. Depending on whether the sub-case 3 (rigid body motion) or the sub-case 4 (soil free to move) is studied, the resistance components will be mobilised in a different way, requiring the adaptation of the analytical computation methods. This will be used to develop a simplified design method in the next chapter.

4.4.5.1. Rigid body motion (Sub-case 3)

The case of a purely rigid body motion with a displacement imposed to all the caisson nodes is first considered. As the soil is held in place, there is no movement of the soil particles within the skirt and thus no effect on the total resistance. The friction components are assessed similarly to the drained scenario by integrating the shear distribution along the soil-skirt interface between 0 and τ_{max}. This gives Equation 4-42, which is identical to Equation 4-27 derived for the 1st scenario. All the calculation steps are listed in appendix C.1. The superposition of the inner and the outer friction curves obtained analytically and numerically is proposed in Figure 4-31 (a) and (b). The perfect concordance between the two sets of results can be attested through the relative error plotted in blue in Figure 4-31, and which remains less than 1% for all Δy.

$$\Phi_{mob} = 2\pi R \left(K_\tau \Delta y L - \frac{1}{2} \frac{K_\tau^2 \Delta y^2}{\mu K_0 \Delta \sigma'_{v,o}} \right) \qquad \text{EQUATION 4-42}$$

The suction component that arises from the variation of the negative excess PWPs between the underside of the caisson lid and the soil plug is responsible for the emergence of seepage flows through the confined soil from the surrounding soil and free water. These internal hydraulic

gradients will help to progressively fill the gap that appears under the lid. The analytical assessment of the suction component will thus first be based on the well-known Darcy's law furnishing an expression for the seepage velocity, as reminded in Equation 4-43 [78].

$$v = \frac{\Delta y}{\Delta t} = k \times i \qquad \text{EQUATION 4-43}$$

Where

$v\ [m/s]$	Seepage velocity
$k\ [m/s]$	Coefficient of permeability
$i\ [-]$	Hydraulic gradient

The hydraulic gradient may be expressed as Equation 4-44 [78].

$$i = \frac{q}{L_s\ \gamma_w} \qquad \text{EQUATION 4-44}$$

Where

$q = s\ [Pa]$	Applied load per unit area (here the suction)
L_s [m]	Seepage length
$\gamma_w\ [kN/m^3]$	Unit weight of water

The critical hydraulic gradient occurs when the seepage flows become equal to the effective weight of the soil, cancelling the contact forces between the grains. It is mathematically formulated as Equation 4-47. The corresponding critical suction pressure is then assessed by Equation 4-46.

$$i_{cr} = \frac{\gamma'}{\gamma_w} = 0.8250 \qquad \text{EQUATION 4-45}$$

$$s_{crit} = i_{cr} L_s \gamma_w = L_s \gamma' \qquad \text{EQUATION 4-46}$$

Where

$\gamma'\ [kN/m^3]$	Effective unit weight of the soil

In Equation 4-44, an accurate estimation of the average seepage length for the range of aspect ratio $\frac{D}{L}$ of practical interest is provided in the literature [79], and defined as Equation 4-47. In order to fit the non-linear PWP-displacement response obtained numerically, the expression of L_s will be slightly adapted to incorporate a dimensionless factor F and can then be rewritten as Equation 4-48. The factor F is given as a function of a calibration parameter $\xi_{pwp,u,I}$ and the displacement step Δy normilized by the imposed displacement d. The parameter $\xi_{pwp,u,I}$ is adjusted by means of a robust condition previously encountered, i.e. the maximum analytical contribution of the PWPs is activated at the same imposed displacement as numerically.

$$L_s = 1 + 0.2 \left(\frac{L}{D}\right)^{-0.9} \qquad \text{EQUATION 4-47}$$

$$\underbrace{L_s = 1 + 0.2\left(\frac{L}{D}\right)^{-0.9}}_{Expression\ from\ [79]} \boxed{\underbrace{\xi_{pwp,u,I}\left(\frac{\Delta y}{d}\right)^{0.5}}_{F}} \qquad \text{EQUATION 4-48}$$

By combining Equation 4-43, Equation 4-44 and Equation 4-48, it is possible to get the relationship between the resultant force applied on the lower part of the lid by the variations of the PWP distribution inside the caisson ΔP_{pwp} and the displacement step Δy, as formulated in Equation 4-49. This second order formula, derived thanks to the adjustements made on the expression of the seepage length, captures rather well the partially drained behaviour of the caisson under a rigid body motion, as illustrated in Figure 4-31 (c). Taking the relative error as indicator, it appears indeed that the deviation between numerical and analytical curves remains below 1%.

$$\Delta P_{pwp} = A_{base,i} \times [\frac{L_s\ \gamma_w}{k}\frac{\Delta y}{\Delta t}] \qquad \text{EQUATION 4-49}$$

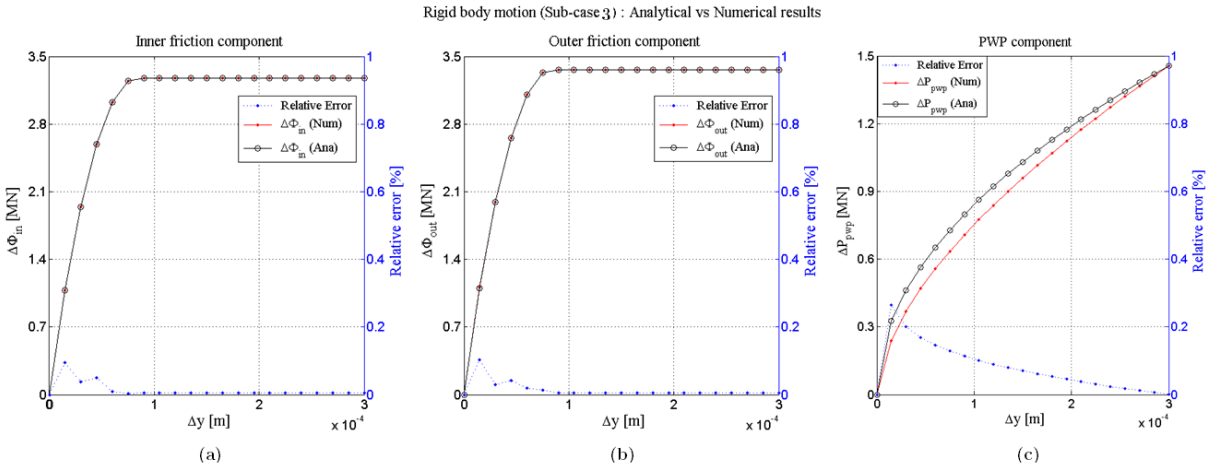

FIGURE 4-31: Comparison between the numerical and the analytical computations of the friction components for a purely rigid body movement (sub-case 3): Inner available friction (a) outer available friction (b) and PWP component (c), 2nd scenario

4.4.5.2. Soil free to move (Sub-case 4)

With respect to the configuration of a soil free to move, the resistance depends on the three same components as for the rigid body extraction ($\Delta\Phi_{\text{in}} - \Delta\Phi_{\text{out}} - \Delta\text{P}_{\text{pwp}}$) to which must be added the component emerging from the uplift movement of the soil particles ΔW_{plug}. This latter contribution appears as a result of the negative variation of the water pressures underneath the lid, and will significantly impact the mobilisation of the inner friction.

Outer friction component

Regarding the outer friction, it is still assessed on the basis of the analytical expression used in the first scenario [75], which gives the second order relationship between the variation of the total outer friction force and the vertical displacement, recalled in Equation 4-50.

$$\Delta\Phi = 2\pi R \left(K_s \Delta y L - \frac{1}{2}\frac{K_s^2 \Delta y^2}{\mu K_0 \Delta\sigma'_{v,o}}\right) \quad \text{EQUATION 4-50}$$

$$K_s = \frac{1}{\frac{r}{G} ln\left(\frac{r_m}{r}\right)} = \frac{1}{\frac{r}{G} ln\left(\frac{2.5\ L\ \boxed{\zeta_{out,u}}\ 1-\nu_c}{r}\right)} \quad \text{EQUATION 4-51}$$

$$\Delta\Phi_{out} = 2\pi R_o \boxed{\xi_{out,u}} \left(K_s \Delta y L - \frac{1}{2}\frac{K_s^2 \Delta y^2}{\mu K_0 \Delta\sigma'_{v,o}}\right) \quad \text{EQUATION 4-52}$$

Applying this equation in a partially drained configuration for the setting parameters ($k = 10^{-7}\frac{m}{s}$, loading rate of $10^{-6}\frac{m}{s}$) leads to the results depicted in Figure 4-32 (a). Clearly the basic analytical formula has a tendency to underestimae the contribution of the outer friction to the total resistance. Similarly to the procedure performed for the 1st scenario, a first calibration parameter $\zeta_{out,u}$ is introduced in the analytical expression of K_s by means of the first robust condition (cfr. 4-35) in order to straighten up the initial slope of the curve. It is reminded in Equation 4-51. The load-displacement curve obtained in this case offers a rather good estimation of the development of shear stresses on the outside. Only a low overestimation of the numerical results persists during the mobilisation of friction, as indicated in Figure 4-32 (b). Depending upon the level of accuracy desired, this first approximation could of course be implemented as it is in the macro-element. However, in a perspective of minimizing the difference between the two approaches, a second calibration parameter $\xi_{out,u}$ can be employed, so that the relative error becomes nearly negligible, as reported in Figure 4-32 (c).

Inner friction component

Regarding the inner friction component during partly drained conditions, the analytical reconstruction of the curve is conducted similarly to the drained scenario based on the expression detailed in the literature [75] and recalled in Equation 4-53. When the soil is free to move, the development of the negative excess PWPs under the suction caisson lid will tend to move the confined soil upwards and this way, will affect and restraint the mobilisation of the inner friction. As proposed in the literature [76], a linear reduction of the inner friction can be assumed between the fully drained conditions (no suction effect) and the point at which the critical suction pressure s_{crit} is reached. The ratio between the applied suction s and the critical suction s_{crit} is thus implemented in Equation 4-54 in order to make it possible to distinguish between the sliding mechanism and the plug uplift mechanism in the component response.

One fitting parameter $\xi_{in,u}$ is included in this expression, and is calibrated according to the suction pressure. As long as this applied suction s remains below the critical suction $s < s_{crit}$, the condition for setting the value of $\xi_{in,u}$ will be that the maximum analytical friction is activated at the same imposed displacement as numerically (Figure 4-33 (a)). When the applied suction reaches the critical one $\mathrm{s = s_{crit}}$, the parameter is calibrated on the basis of the displacement for which s_{crit} is obtained (Figure 4-33 (b)). It appears from these figures that the matches between analytical and numerical curves are basically not quite perfect, but the offsets are assumed to be sufficiently small to accept these results. After this point, the failure of the soil should normally occur in normal (elasto-)plastic soil conditions. However in the case of an

elastic soil, the rupture mechanisms are not expected to arise since the deformations are infinitely reversible.

$$\Delta\Phi_{\text{in}} = 2\pi R \left(K_s \Delta y L - \frac{1}{2} \frac{K_s^2 \Delta y^2}{\mu K_0 \Delta\sigma'_{v,o}} \right) \qquad \text{EQUATION 4-53}$$

$$\Delta\Phi_{\text{in}} = 2\pi R_i \xi_{in,u} \left(K_s \Delta y L - \frac{1}{2} \frac{K_s^2 \Delta y^2}{\mu K_0 \Delta\sigma'_{v,o}} \right) \boxed{\left(1 - \frac{s}{s_{crit}} \right)} \qquad \text{EQUATION 4-54}$$

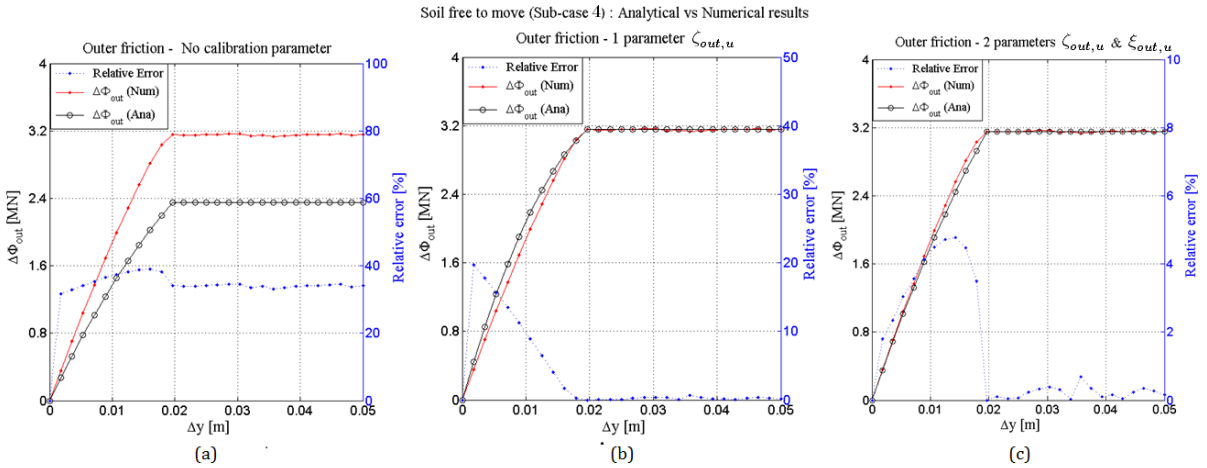

FIGURE 4-32: Superposition of the numerical and the analytical curves considering (a) no calibration parameter, (b) 1 parameter and (c) 2 parameters in the analytical formula

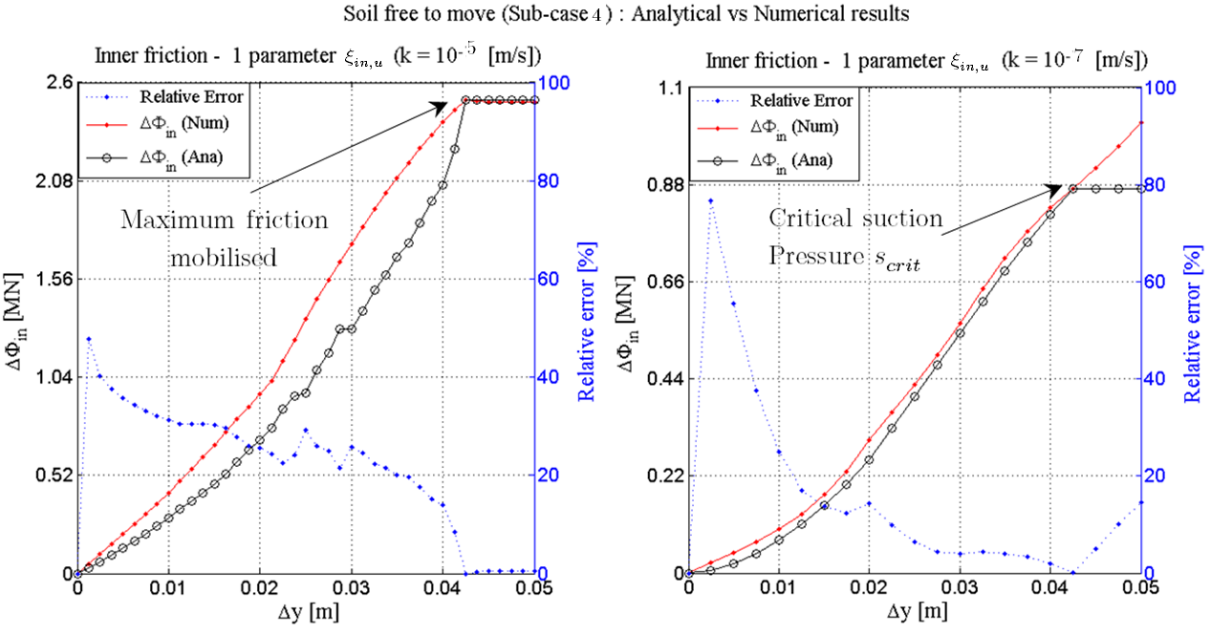

FIGURE 4-33: Superposition of the numerical and the analytical curves considering 1 parameter in the analytical expression: (a) the friction is fully mobilised and (b) the critical suction is reached

PWP component

The suction component that arises from the development of the negative excess PWPs under the lid of the caisson is assessed analytically on the basis of the same expression as the one

used for a rigid body motion. As a reminder, this Equation 4-55 has been derived from the definition of the velocity v, of the seepage flows through the soil plug, and of the expression of the hydraulic gradient i. It incorporates the factor L_s, referred to as the seepage length in the literature [79] and which expression will be slightly adjusted in order to optimize the curve fitting on the numerical results. Equation 4-56 gives the adapted expression of the seepage length including the dimensionless factor F that still depends on the normalized displacement step and on a calibration parameter $\xi_{pwp,u,II}$. The power of this factor is here changed from 0.5 to 0.75, since a more linear response of the PWP component has been noticed in comparison to the rigid body motion. If no calibration parameter is taken into account, the analytical results drastically underestimate the real influence of the PWP component as depicted in Figure 4-34 (a), whereas a rather good estimation of the numerical results is provided when one fitting parameter is considered, as illustrated in Figure 4-34 (b). The recourse to a calibration parameter makes it possible to reduce the relative error by more than half.

$$\Delta P_{pwp} = A_{base,i} \times [\frac{L_s\ \gamma_w}{k} \frac{\Delta y}{\Delta t}] \qquad \text{EQUATION 4-55}$$

$$\underbrace{L_s = 1 + 0.2 \left(\frac{L}{D}\right)^{-0.9}}_{Expression\ from\ [79]} \boxed{\underbrace{\xi_{pwp,u,II} \left(\frac{\Delta y}{d}\right)^{0.75}}_{F}} \qquad \text{EQUATION 4-56}$$

The adjustment of this parameter is performed by applying the robust condition that the maximum of the analytical contribution of the PWPs coincides with the maximum of the numerical curve. The critical hydraulic gradient i_{cr} and the related critical suction pressure s_{crit} defined in Equation 4-45 and in Equation 4-46 respectively remain identical with refernce to sub-case 3.

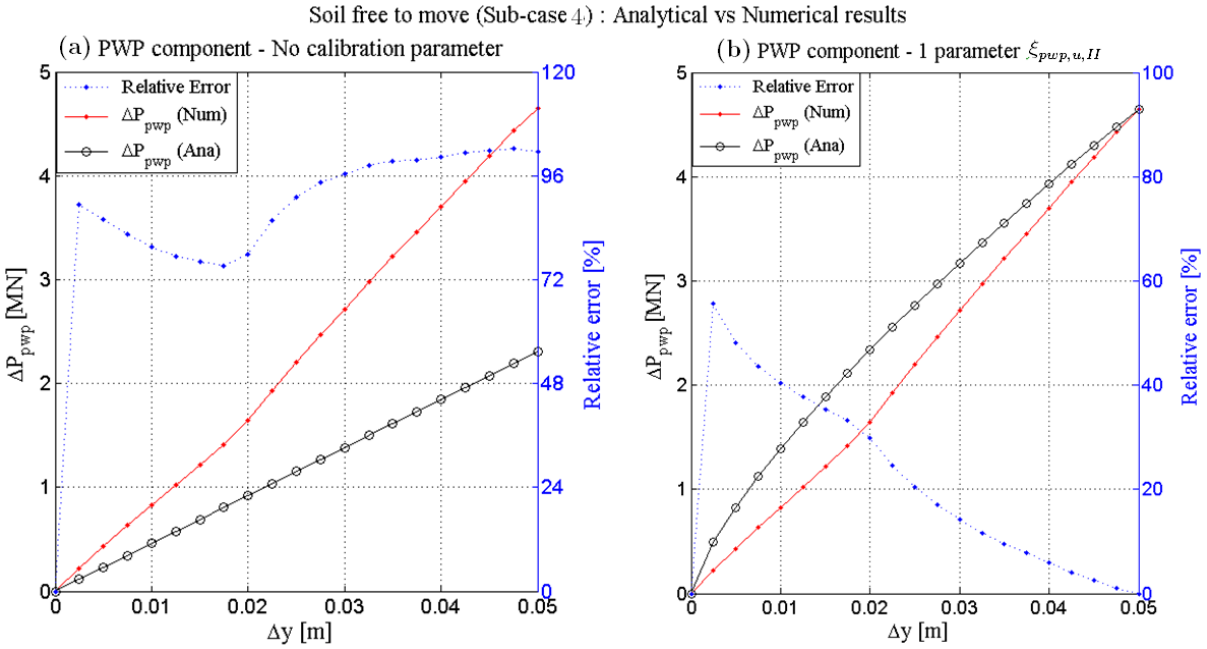

FIGURE 4-34: Superposition of the numerical and the analytical curves considering (a) no calibration parameter and (b) one parameter $\xi_{pwp,u,II}$ in the analytical formula

Plug uplift component

The resistance component coming from the uplift of the soil plug is analytically assessed on the basis of the procedure specified in [58] for the installation of a caisson in non-standard soil conditions. In this report, the principle of the mechanical work is used to solve the iterative process of the plug uplift mechanism under suction only. By definition, a force is said to do work when it acts on a body so that there is a displacement of the point of application of the force. For the case of a suction caisson subject to an imposed vertical displacement, the force refers to the applied suction s multiplied by the inner cross-section area of the lid $A_{base,i}$, while the displacement of the point of application corresponds to the unknown, namely the uplift length of the plug L_{plug}, as reported in Equation 4-57.

$$\Delta W(t) = s(t) A_{base,i} \times \Delta L_{plug} \qquad \text{EQUATION 4-57}$$

Where

$\Delta W(t)$	Increment of mechanical work at the time-step t
$s(t)$	Applied suction at the time-step t
ΔL_{plug}	Increment of the uplift length of the plug during the time step t

In this equation, the generated work $W\ t$ for an increment of imposed displacement $\Delta d\ t$ occurring during a time-step Δt is calculated as the product of the increments of the suction and of the volume with respect to the previous time-step, as stated in Equation 4-58.

$$\Delta W\ t\ = \Delta s\ t_{-1}\ \times \Delta V_{plug}\ t_{-1} \qquad \text{EQUATION 4-58}$$

Where

$\Delta s\ t_{-1}$	Variation of applied suction between the time steps t and t_{-1}
$\Delta V_{plug}\ t_{-1}$	Variation of uplift volume of the plug between t and t_{-1}

Combinig Equation 4-57 and Equation 4-58 directly provides an expression for the increment of the uplift length of the soil plug, under an imposed displacement applied during a time-step Δt (Equation 4-59). This value is then used in Equation 4-60 in order to determine the total plug uplift component. Appendix E gives a flow chart of the iterative process to assess the plug uplif mechanism.

$$\Delta L_{plug} = \frac{\Delta s\ t_{-1}\ \times \Delta V_{plug}\ t_{-1}}{s\ t\ A_{base,i}} \qquad \text{EQUATION 4-59}$$

$$\Delta W_{plug} = \xi_{plug,u}\ \times (A_{base,i} \gamma'_{clay} L_{plug}) \qquad \text{EQUATION 4-60}$$

It can be seen from Figure 4-35 (a) that the analytical results based on Equation 4-60 minimize quite strongly the numerical results. One possible track of interpretation of this underestimation would be that a non-negligible part of the total plug heave is not due to the suction but to the confinement state of the soil that is encompsulated within the skirt. This phenomenon restrains the lateral diffusion of stresses and maintains the contact between the

soil and the inner interface of the caisson. The calibration parameter $\xi_{plug,u}$ will be used to account for this mechanism, which allows to greatly reduce the offset between the curves, as depicted in Figure 4-35 (b).

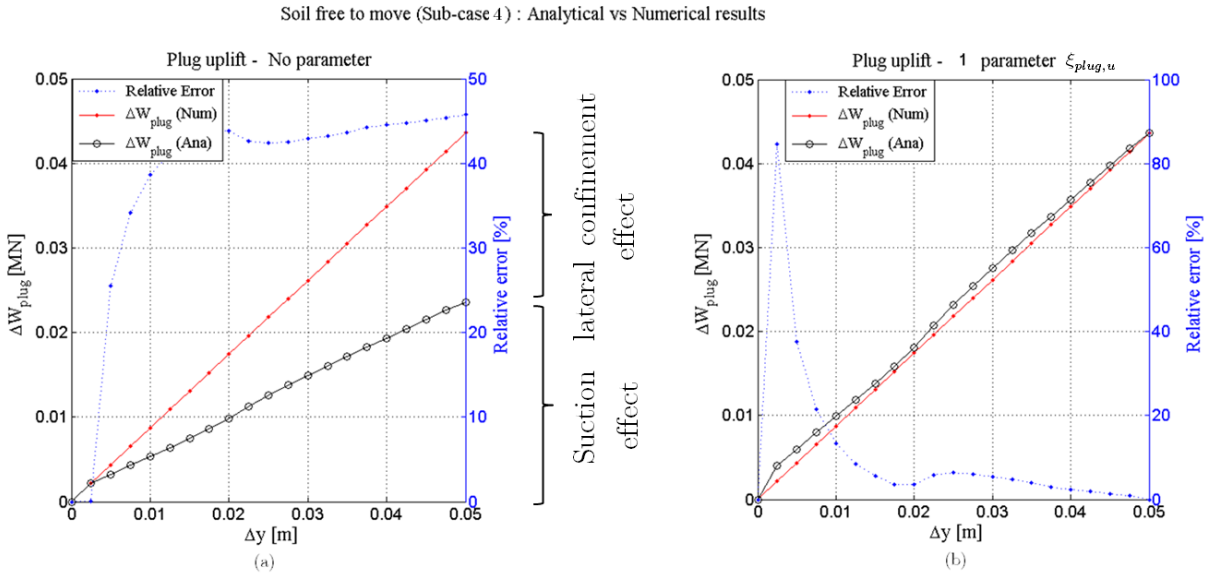

FIGURE 4-35: Superposition of numerical and analytical curves considering (a) no calibration parameter or (b) one parameter $\xi_{plug,u}$ in the analytical formula (plug uplift component)

Chapter 5
Macro-element

5.1 Introduction

The purpose of this chapter is to provide a simplified design method for computing the Load - Displacement $V-d$ response of a suction caisson under an uniaxial tensile load. The elaboration of this calculation method is conducted in parallel to the previous chapter, starting with a basic fully drained case and going afterwards more and more into complexity. To that end, the specific soil-caisson behaviour as well as the key physical factors highlighted by the 2D numerical analysis are used to formulate a macro-element of the suction caisson foundation. This mechanical model aims at reproducing the tensile behaviour of the caisson by combining various rheological elements such as springs, sliders or dampers, so that for a specific implemented configuration of the caisson, it would be possible to predict the extraction resistance R_{tot} (resp. the imposed displacement) for any imposed displacement d (resp. extraction resistance).

A standardisation of the results is adopted in order to provide the representative quantities for both the displacement and the resistance that can be straightforward compared with the values obtained in other configurations. The imposed displacement will be expressed as a dimensionless coefficient by normalising it to the caisson diameter, whereas the extraction resistance will be given in terms of stresses by reducing it to the circular outer cross section area of the lid. Table 5-1 summarizes this normalisation of the main study parameters.

TABLE 5-1 : Normalisation of the main study parameters

PARAMETER	SYMBOL	UNIT	NORMALISATION
Imposed displacement	d	[m]	d/D
Global resistance	R_{tot}	[N]	$R_{tot}/A_{base,o}$

5.2 1st Simulation - Drained conditions and linear-elastic soil

5.2.1. Model

From section 4.3, it appears that for a drained configuration and a soil behaviour that is linear elatic, then the uplift resistance of the caisson is mainly governed by the variation of friction on the inner $\Delta\Phi_{in}$ and the outer $\Delta\Phi_{out}$ surfaces of the caisson, as expressed in Equation 4-24, and recalled below in Equation 5-1 .

$$\Delta R_{tot} \approx \Delta\Phi_{in} + \Delta\Phi_{out} \ . \qquad \text{EQUATION 5-1}$$

The progressive mobilisation of friction along the caisson skirt when the foundation undergoes a tensile loading can be modelled by a spring of stiffness κ, according to the constitutive relationship $\Delta F = \kappa \times \Delta y$. In practise, the interfaces display a non-linear behaviour meaning that the response of the springs will be modelled by a curve and not by a straight line, and that the spring stiffness also depends upon the displacement increment, i.e. $\kappa = \kappa(\Delta y)$. The physical significance of this coefficient of proportionality is that the higher its value, the more difficult it is to initiate displacement between the contact surfaces of solid bodies. So far, the concept of time is not taken into account. Since friction is not infinitely available, a slider ς is put in series with the spring to limit the elongation of the spring once the maximum available friction is reached, as illustrated in Figure 5-1(a) and mathematically formulated in Equation 5-2 and Equation 5-3. This characterizes the perfectly plastic behaviour of the caisson once the maximum load threshold is reached.

Under a tensile load, the friction components will arise simultaneously on both the internal and the exernal interfaces of the caisson skirt, and thus the mechanical model will include two sets of serial spring-slider as depicted in Figure 5-1 (b) [76]. Mathematically, the spring-slider coupling for the inner and the outer friction is translated into Equation 5-5, after having rearranged Equation 5-2 and Equation 5-3 on the basis of the displacement and load relationships expressed in Equation 5-4.

$$L_{out} = \frac{\Delta\Phi_{out}}{\kappa_{out}} + \begin{cases} 0 & \Delta\Phi_{out} < \Delta\Phi_{out,max} \\ L_{slider,out} & \Delta\Phi_{out} \geq \Delta\Phi_{out,max} \end{cases}$$

EQUATION 5-2

$$L_{in} = \frac{\Delta\Phi_{in}}{\kappa_{in}} + \begin{cases} 0 & \Delta\Phi_{in} < \Delta\Phi_{in,max} \\ L_{slider,in} & \Delta\Phi_{in} \geq \Delta\Phi_{in,max} \end{cases}$$

EQUATION 5-3

Considering

$$\begin{aligned} &\mathrm{R_{tot}} = \Delta\Phi_{out} + \Delta\Phi_{in} \\ &L = L_{out} = L_{in} = \Delta y \\ &L_{slider} = \Delta y - \Delta y_{max} \end{aligned}$$

EQUATION 5-4

$$\mathrm{R_{tot}} = \begin{cases} (\kappa_{out} + \kappa_{in})\Delta y & \Delta\Phi_{out} < \Delta\Phi_{out,max} \\ & \Delta\Phi_{in} < \Delta\Phi_{in,max} \\ \kappa_{out} + \kappa_{in}\ \Delta y - \underbrace{\kappa_{out}(\Delta y - \ \Delta y_{max})}_{\varsigma_{out}} & \Delta\Phi_{out} \geq \Delta\Phi_{out,max} \\ & \Delta\Phi_{in} < \Delta\Phi_{in,max} \\ \kappa_{out} + \kappa_{in}\ \Delta y - \underbrace{\kappa_{out}\ \Delta y - \ \Delta y_{max}}_{\varsigma_{out}} - \underbrace{\kappa_{in}\ \Delta y - \ \Delta y_{max}}_{\varsigma_{in}} & \Delta\Phi_{out} \geq \Delta\Phi_{out,max} \\ & \Delta\Phi_{in} \geq \Delta\Phi_{in,max} \end{cases}$$

EQUATION 5-5

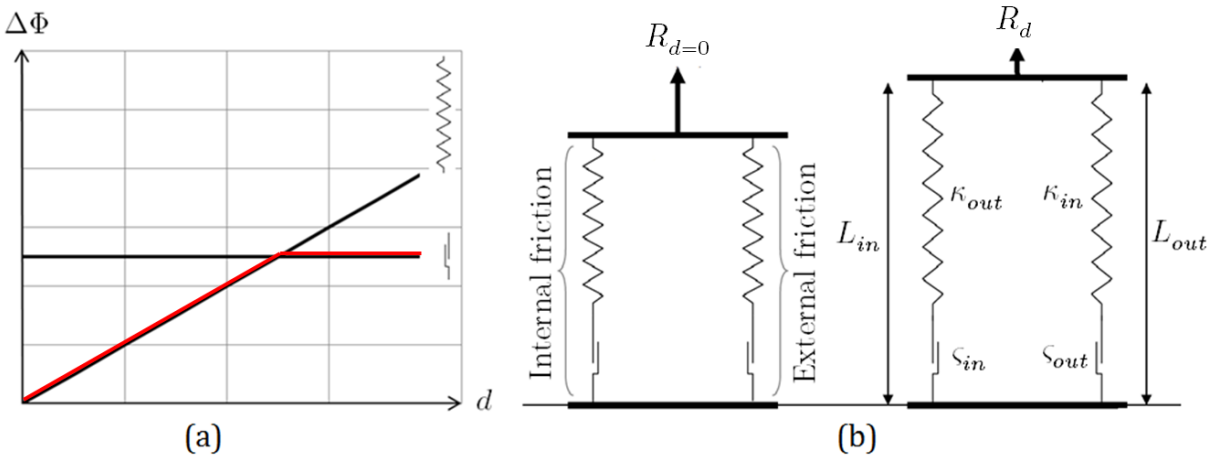

FIGURE 5-1: (a) Mechanical behaviour of a spring and a slider - (b) Rheological model for the 1st fully drained scenario [76]

5.2.1.1. Rigid body motion

Regarding the case of a purely rigid body motion with a displacement imposed to all the nodes of the caisson (sub-case 1), the implementation of the behaviour of the springs, i.e. the progressive mobilisation of friction along the skirt, is performed by means of the second degree Equation 4-28 derived in section 4.3 and recalled hereafter in Equation 5-6.

$$\Delta\Phi = \underbrace{2\pi R \left(K_\tau L - \frac{1}{2}\frac{K_\tau^2 \Delta y}{\mu K_0 \Delta\sigma'_{v,o}} \right)}_{\kappa\ \Delta y} \times \Delta y \qquad \text{EQUATION 5-6}$$

The expression for the sliders that is the maximum inner and outer friction resistance has been derived in section 4.3. This Equation 4-18, recalled below in Equation 5-7, is directly dependant on the geometrical parameters ($\therefore$), the friction angle ($\vdots$) and the horizontal soil pressure distribution ($\cdots$).

$$\Delta\Phi^{max} = \varsigma = \underbrace{2\pi \frac{D}{2} L}_{(\therefore)} \left(\underbrace{K_0 \gamma'_{clay} \frac{L}{2}}_{(\cdots)} \right) \underbrace{\tan\frac{2}{3}\phi}_{(\vdots)} \qquad \text{EQUATION 5-7}$$

5.2.1.2. Soil free to move

Regarding the configurations with a soil free to move (sub-cases 2 and 2*bis*), distinct responses between the inner and the outer interfaces of the caisson have been highlighted in section 4.3.3. Expressions employed to model the springs adjustments are thus slightly different from each other, as recalled in Equation 5-8 and Equation 5-9.

Outside

$$\Delta\Phi_{\text{out}} = \underbrace{2\pi R_o \left(\xi_{out,d} K_s L - \frac{1}{2}\frac{K_s^2 \Delta y}{\mu K_0 \Delta\sigma'_{v,o}} \right)}_{\kappa_{out}\ \Delta y} \times \Delta y \qquad \text{EQUATION 5-8}$$

Inside

$$\Delta\Phi_{\text{in}} = \underbrace{2\pi R_i \left(K_s \Delta y L - \frac{1}{2}\frac{K_s^2 \Delta y}{\mu K_0 \Delta\sigma'_{v,o}}\right)}_{\kappa_{in}\ \Delta y} \times \Delta y$$

EQUATION 5-9

One fitting parameter $\xi_{out,d}$ is directly present in the first expression and a second parameter ζ_d is incorporated into the expression of K_s for both the inner and the outer friction components, as shown in Equation 5-10 just below. It should be noted that it was also possible to do it well with only two calibration parameters ($\zeta_{out,d}$ outside and $\zeta_{in,d}$ inside the caisson) if one is satisfied with a slightly larger error.

$$K_s = \frac{1}{\frac{r}{G}\ln\left(\frac{r_m}{r}\right)} = \frac{1}{\frac{r}{G}\ln\left(\frac{2.5L\ \boldsymbol{\zeta_d}\ 1-\nu_c}{r}\right)} = \frac{1}{\frac{r}{\frac{E_c}{2(1+\nu_c)}}\ln\left(\frac{2.5L\ \boldsymbol{\zeta_d}\ 1-\nu_c}{r}\right)}$$

EQUATION 5-10

This way, the variations of the inner and the outer friction, idealized by spring elements explicitly incorporate the parameters ν_c and E_c and are also implicitly dependant on the tangential penalty coefficient K_τ.

With regards to the behaviour of the sliders, it has been noted in section 4.3.3 that in the present specific case, the soil has a tendency of keeping some physical contact with the foundation, leading to a reduction of the maximum friction resistance. In the present investigated scenario of a suction caisson extracted of 30 cm from the ground, the drop in the total mobilisable resistance is taken into account by a factor $\xi_{max,d}$ which is given as a function of the aspect ratio $\frac{D}{L}$ for the inner and the outer friction in Figure 5-2(a) and in Figure 5-2 (b) respectively. Based on this parameter and on Equation 4-18, the slider behaviour in case of surrounding soil free to move will simply be implemented as Equation 5-11.

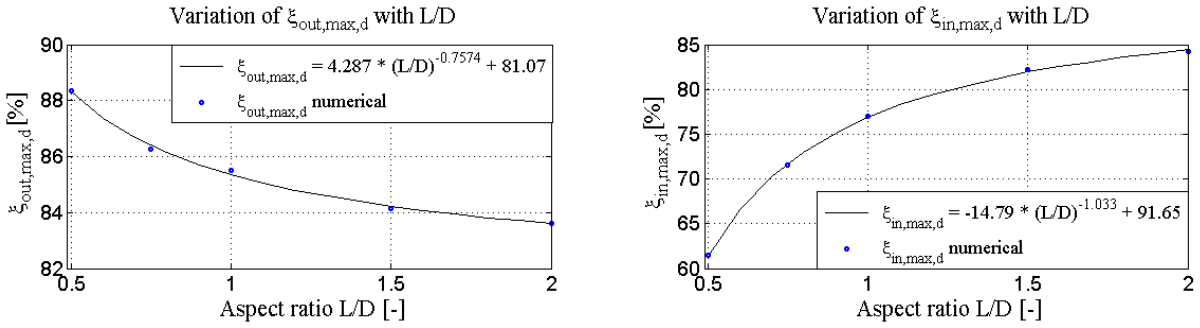

FIGURE 5-2: Variation of the calibration parameter of the slider with the aspect ratio: (a) outer friction and (b) inner friction

$$\Delta\Phi^{max} = \xi_{max,d} \times \underbrace{2\pi\frac{D}{2}L\left(K_0\gamma'_{clay}\frac{L}{2}\right)\mu}_{\Delta\Phi^{max}\ (rigid\ body\ motion)}$$

EQUATION 5-11

5.2.2. Parametric study in the case of a soil free to move

To reproduce as accurately as possible the response of the soil-caisson system under loading, the main parameter ν_c, E_c and K_τ having an influence on the calibration factors $\xi_{out,d}, \zeta_{out,d}$, $\zeta_{in,d}$ involved in the analytical reconstruction of the friction curves are investigated through a parametric study. The purpose is to be able to approximate the values of the calibration parameters for different aspect ratio's $\frac{D}{L}$ and for one parameter differing from the reference values of the system parameters.

First a variation of the Poisson's ratio υ_c in the range $[0.2 - 0.4][-]$ and for five slenderness ratio's ($\frac{D}{L} = 0.5 - 0.75 - 1 - 1.5 - 2$) is conducted. The curves showing the evolution of the calibration parameters for an imposed displacement of $0.03m$ are presented in Figure 5-3. A first finding is that the calibration parameters for the friction on the outside are decreasing for an increased value of the Poisson's ratio. The higher the slenderness ratio, the bigger the value of $\xi_{out,d}$ and $\zeta_{out,d}$ and the steeper the falling-off of these values. For the friction on the inside on the contrary, the higher the value of ν_c , the greater the value of $\zeta_{in,d}$, except for $\frac{D}{L} = 0.5$. Trend lines are then fitted on each of these curves to enable an estimation of the calibration parameters for any given value of the Poisson's ratio, as described in Appendix D.1.

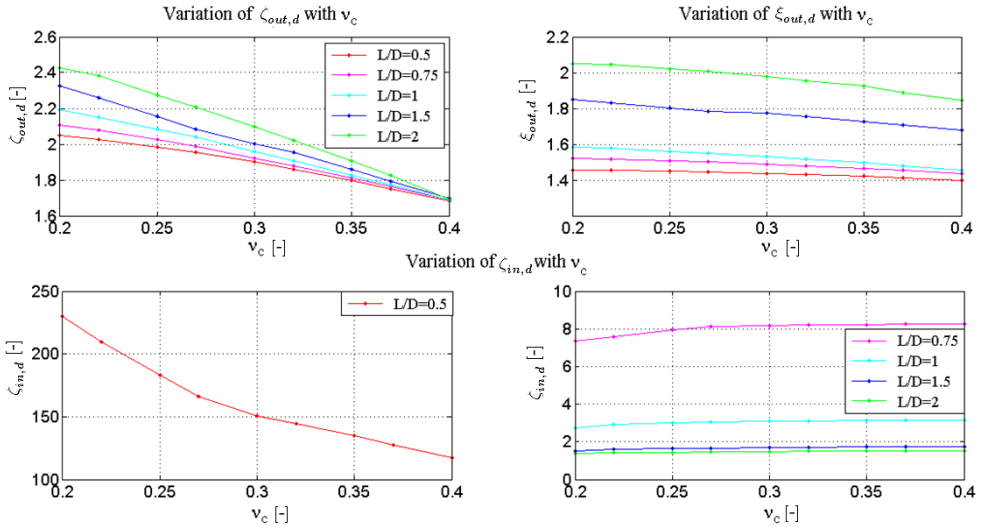

FIGURE 5-3 : Variations of the calibration parameters $\xi_{out,d}, \zeta_{out,d}$ and $\zeta_{in,d}$ with ν_c for 5 aspect ratio's

In a second phase, the same procedure is undertaken to assess the variability of the calibration parameters with the shear constant K_τ, considering the same five slenderness ratio as before. Three orders of magnitude for K_τ are investigated, in the range $[4.10^7 - 4.10^9]$. The curves showing the evolution of the calibration parameters for an imposed displacement of 0.03m are presented in Figure 5-4. A common tendency is emerging from these graphs, namely that all the parameters decrease progressively while increasing K_τ and that the variation of the parameters remains really limited compared to the variation of K_τ. The values of $\zeta_{out,d}$ and $\xi_{out,d}$ diminish with a growing ratio $\frac{\mathrm{D}}{\mathrm{L}}$ while considering $\zeta_{in,d}$ it is the other way around. Trend lines, collected in Appendix D.2, are then fitted on each of these numerical curves to enable an estimation of the calibration parameters for any given value of K_τ.

Finally, the variability of the calibration parameters relative to the Elastic modulus E_c is examined for the same aspect ratio's. The Young's modulus is taken in the range $[5.10^6 - 10^8][\frac{N}{m^3}]$ and the curves showing the evolution of calibration parameters with E_c are displayed in Figure 5-5. Basically, the calibration parameters have a tendency to grow with E_c. The parameters for the outside friction $\zeta_{out,d}$ and $\xi_{out,d}$ slightly increase with the slenderness ratio $\frac{D}{L}$ whereas the parameter for the inside friction $\zeta_{in,d}$ progressively diminishes with $\frac{D}{L}$. Trend lines, collected Appendix D.3, are then fitted on each of these curves to enable an estimation of the calibration parameters for any given value of E_c.

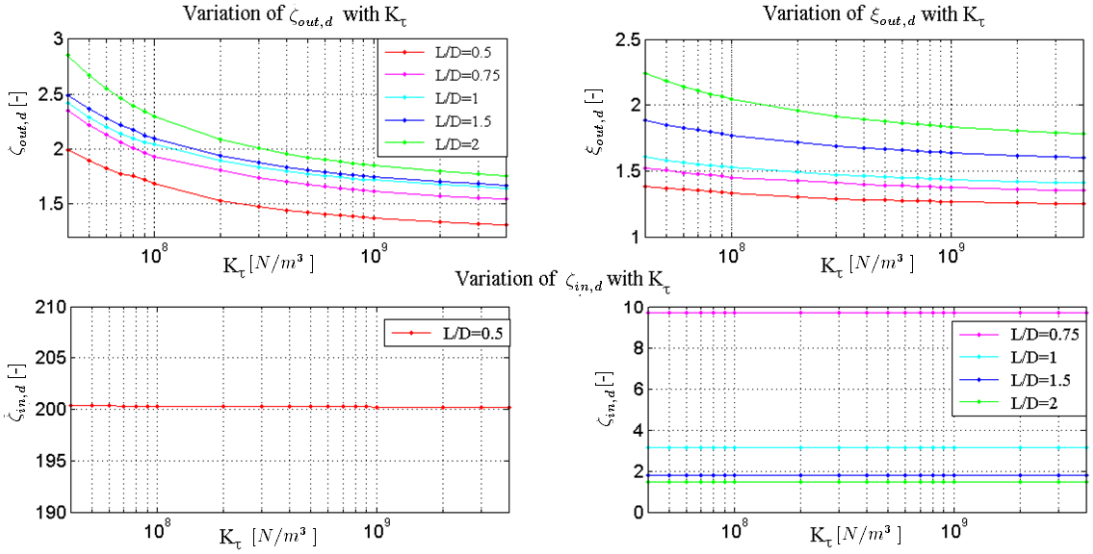

FIGURE 5-4 : Variations of the calibration parameters $\xi_{out,d}, \zeta_{out,d}$ and $\zeta_{in,d}$ with K_τ for 5 aspect ratio's

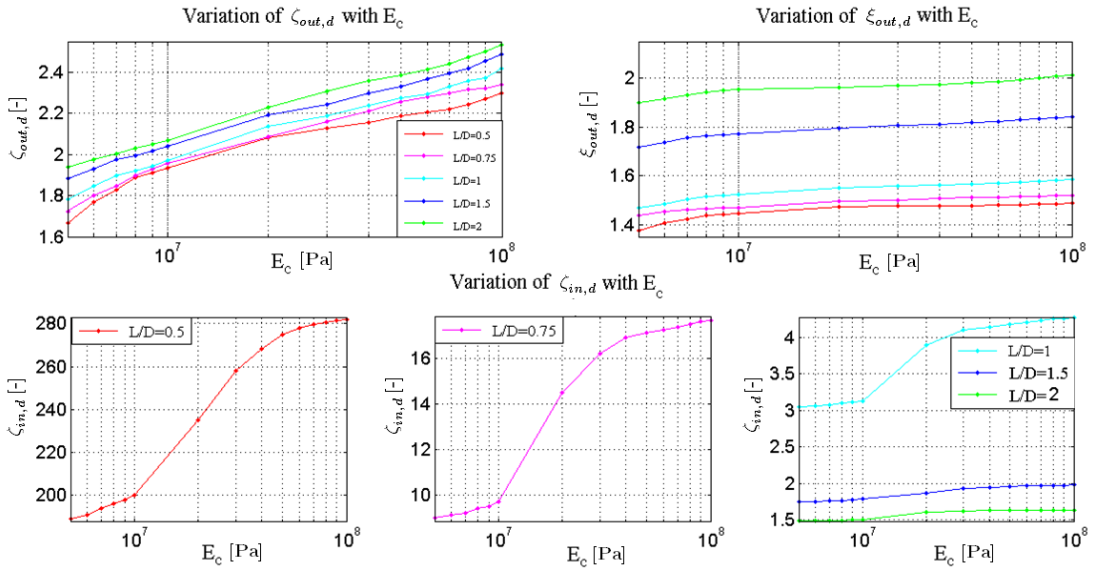

FIGURE 5-5 : Variations of the calibration parameters $\xi_{out,d}, \zeta_{out,d}$ and $\zeta_{\mathrm{in,d}}$ with E_c for 5 aspect ratio's

All the generated trend lines will be implemented in the macro-element, so that for any given values of the system parameters ν_c , K_τ and E_c, it will be possible to obtain an estimation of the calibration parameters, and thus to derive the equation of the friction components.

5.3. 2nd Scenario - Partially drained conditions and elastic soil

5.3.1. Model

5.3.1.1. Rigid body motion (Sub-case 3)

From section 4.4, it appears that for a partially drained configuration and a soil behaviour that is linear elatic and held in place, then the uplift resistance of the caisson is mainly governed by the variations of friction on the inner $\Delta\Phi_{in}$ and the outer $\Delta\Phi_{out}$ surfaces of the caisson, and the generation of negative excess PWPs under the lid of the caisson as expressed in Equation 4-30, and recalled in Equation 5-12.

$$\Delta R_{tot} \approx \Delta\Phi_{in} + \Delta\Phi_{out} + \Delta P_{pwp} \qquad \text{EQUATION 5-12}$$

Outer friction component

Outside the foundation, the resistance to the uplift of the caisson under an imposed displacement comes solely from the progressive mobilisation of friction along the outer soil-caisson interface. Similarly to the drained configuration of scenario 1, the sequence of a non-linear behaviour and a plateau will be modelled by a spring of displacement-dependent stiffness $\kappa_{out}(\Delta y)$ put in series together with a slider ς_{out} that establishes the activation of the maximum available friction and the initiation of the sliding along the external interface.

Based on the findings from section 4.4.5.1, the behaviour of the spring that represents the progressive mobilisation of friction along the skirt is performed by means of the second degree Equation 5-13.

$$\Delta\Phi_{out} = \underbrace{2\pi R_o \left(K_\tau L - \frac{1}{2}\frac{K_\tau^2 \Delta y}{\mu K_0 \Delta\sigma'_{v,o}}\right)}_{\kappa\ \Delta y} \times \Delta y \qquad \text{EQUATION 5-13}$$

Still on the basis of the results from section 4.3, an analytical expression for the maximum available friction is known, which is recalled in Equation 5-17.

$$\Delta\Phi_{out}^{max} = \varsigma = 2\pi\frac{D_o}{2}L\left(K_0\gamma'_{clay}\frac{L}{2}\right)\mu \qquad \text{EQUATION 5-14}$$

Inner friction component

Simultaneously, the extraction of the caisson is controlled inside by the two other resistance components. The modelling of the activation of inner shear stresses along the skirt is strictly similar to that of the outer friction that is to say a spring of stiffness $\kappa_{in}(\Delta y)$ to represent the rising development of shear stresses and a slider ς_{in} to take over from the spring when the inner friction is fully mobilised.

From the previous formula's, it is easy to realise that the difference between the development of the inner and the outer friction will solely come from the geometrical parameter ($D = \frac{R}{2}$).

And thus the response of the spring and the slider for the inner friction component can be also assessed from Equation 5-16 and Equation 5-17 respectively.

PWP component

Regarding the partly drained scenario, another part of the resistance to uplift is attributable to the water seepages that occur during a certain time step Δt and gradually update the underpressures underneath the lid, as a function of the seepage length and the permeability. This time dependent behaviour can be captured by means of a non-linear damper with a coefficient of viscosity η, according to the constitutive relationship $\Delta \mathrm{F} = \eta \times \Delta y^{\frac{1}{N}}$ between the load and the displacement rate. Physically, the viscosity characterizes the flow resistance that will further restrict the fluid flow as its value is great.

To estimate the transient behaviour of the damper, one has to refer to the analytical developments performed in section 4.4, where an expression for the variation of the negative excess PWPs has been derived and is recalled in Equation 5-15. It is formulated as a function of the coefficient of viscosity η which depends upon geometrical parameters $(\ddots)$, the ratio of the unit weight of water to the coefficient of permeability $(\therefore)$ and a dimensionless factor $(*)$. This factor F includes a calibration parameter $\xi_{pwp,u,II}$ which variation in relation to the main system parameters is analysed in the next section 5.3.2.

$$\Delta P_{pwp} = \underbrace{\underbrace{A_{base,i}\ L_s}_{(\ddots)} \times \underbrace{\frac{\gamma_w}{k}}_{(\therefore)} \times \underbrace{F}_{(*)}}_{\eta} \times \underbrace{\frac{\Delta y}{\Delta t}}_{\Delta y^{\frac{1}{N}}} \qquad \text{EQUATION 5-15}$$

Where

$L_s = L\left(1 + 0.2\left(\frac{L}{D}\right)^{-0.9}\right)$ Seepage length

$F = \xi_{pwp,u,II}\left(\frac{\Delta y}{L}\right)^{0.5}$ Factor to account for the non-linear behaviour of the damper

$\xi_{pwp,u,II}$ Calibration parameter

Combination of the components

Since the evolution of the seepage flow over a time lapse Δt will happen concurrently to the rise of the inner friction with a displacement increment Δy, these two resistance components from inside will be put in parallel in the mechanical model. Furthermore, considering the case of a soil held in place with a rigid body subjected to tensile load, the friction components will develop simultaneously on both the internal and the external interfaces of the caisson skirt. Thence, the mechanical model will be made up of two sets of serial spring-slider and one non-linear damper, all three assembled in parallel as depicted in Figure 5-6 [76]. Mathematically, the coupling between the two sets of spring-slider and one damper is translated by Equation 5-20, after having rearranged Equation 5-16, Equation 5-17 and Equation 5-18 on the basis of the displacement and load relationships of Equation 5-19.

$$L_{out} = \frac{\Delta\Phi_{out}}{\kappa_{out}} + \begin{cases} 0 & \Delta\Phi_{out} < \Delta\Phi_{out,max} \\ L_{slider,out} & \Delta\Phi_{out} \geq \Delta\Phi_{out,max} \end{cases}$$

EQUATION 5-16

$$L_{in} = \frac{\Delta\Phi_{in}}{\kappa_{in}} + \begin{cases} 0 & \Delta\Phi_{in} < \Delta\Phi_{in,max} \\ L_{slider,in} & \Delta\Phi_{in} \geq \Delta\Phi_{in,max} \end{cases}$$

EQUATION 5-17

$$L_{pwp} = \sqrt[1/N]{\frac{\Delta P_{pwp}}{\eta}} \times \Delta t$$

EQUATION 5-18

Considering $R_{tot} = \Delta\Phi_{out} + \Delta\Phi_{in} + \Delta P_{pwp}$

$L = L_{out} = L_{in} = L_{pwp} = \Delta y$

$L_{slider} = \Delta y - \Delta y_{max}$

EQUATION 5-19

$$\mathrm{R_{tot}} = \begin{cases} \kappa_{out} + \kappa_{in}\ \Delta y + \eta \times \Delta y^{\frac{1}{N}} & \Delta\Phi_{out} < \Delta\Phi_{out,max} \\ & \Delta\Phi_{in} < \Delta\Phi_{in,max} \\ \kappa_{out} + \kappa_{in}\ \Delta y - \underbrace{\kappa_{out}\ \Delta y - \ \Delta y_{max}}_{\varsigma_{out}} + \eta \times \Delta y^{\frac{1}{N}} & \Delta\Phi_{out} \geq \Delta\Phi_{out,max} \\ & \Delta\Phi_{in} < \Delta\Phi_{in,max} \\ \kappa_{out} + \kappa_{in}\ \Delta y - \underbrace{\kappa_{out}\ \Delta y - \ \Delta y_{max}}_{\varsigma_{out}} - \underbrace{\kappa_{in}\ \Delta y - \ \Delta y_{max}}_{\varsigma_{in}} + \eta \times \Delta y^{\frac{1}{N}} & \Delta\Phi_{out} \geq \Delta\Phi_{out,max} \\ & \Delta\Phi_{in} \geq \Delta\Phi_{in,max} \end{cases}$$

EQUATION 5-20

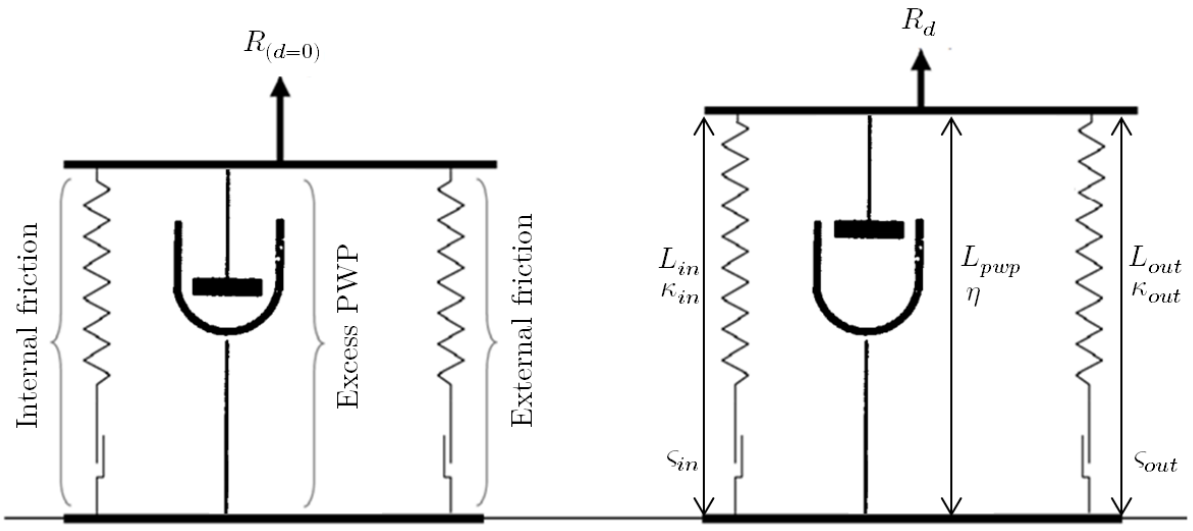

FIGURE 5-6: Rheological model for the 2nd partly drained scenario in the case of a rigid body motion [76]

5.3.1.2. Soil free to move

From section 4.4, it has been demonstrated that for a partially drained configuration and a soil behaviour that is linear elastic and free to move, then the uplift resistance of the caisson is mainly governed by the variation of friction on the outer surface of the caisson $\Delta\Phi_{out}$ and the

generation of negative excess PWPs under the lid of the caisson ΔP_{pwp}. The latter component directly influences the way in which the two other contributions to resitance are activated, namely the friction on the inner surface of the caisson $\Delta\Phi_{in}$ and the plug uplift ΔW_{plug}. Basically, the global extraction resistance includes four major terms, as expressed in Equation 4-41 and recalled in Equation 5-21.

$$\Delta R_{tot} \approx \Delta\Phi_{in} + \Delta\Phi_{out} + \Delta P_{pwp} + \Delta W_{plug} \qquad \text{EQUATION 5-21}$$

Outer friction component

Outside the foudation, the resistance to the uplift of the caisson under an imposed displacement comes solely from the progressive mobilisation of friction along the outer soil-caisson interface. Despite the slightly higher shear stress values in relation to the drained conditions, the outer friction response is still made up of a first non-linear behaviour, followed and bounded by a plateau. As described in such previous cases, this sequence is modelled by a spring of displacement-dependent stiffness $\kappa_{out}\ \Delta y$ serially combined with a slider ς_{out} denoting the limit of maximum mobilizable friction.

Based on the findings from section 4.4.5.2, the assessment of the response of the spring schematizing the outer friction mobilisation is performed by means of the second degree Equation 5-22. This analytical formulation incorporates explicitly a first fitting parameter $\xi_{out,\mathrm{u}}$ and a second parameter $\zeta_{out,\mathrm{u}}$ is included in the expression of K_s. As previously mentioned, the recourse to this single second parameter $\zeta_{out,\mathrm{u}}$ already provides satisfactory analytical results. The variation of this parameter with respect to the main system parameters is examined in depth in the next section 5.3.2.

$$\Delta\Phi_{out} = \underbrace{\xi_{out,u} \times 2\pi R_o \left(K_s L - \frac{1}{2}\frac{K_s^2 \Delta y}{\mu K_0 \Delta\sigma'_{v,o}} \right)}_{\kappa_{out}\ \Delta y} \times \Delta y \qquad \text{EQUATION 5-22}$$

With regards to the slider behaviour, a reduction of the maximum friction resistance has been noticed compared to the case of a pull-out of a rigid body. It is due to the tendency of the soil to keep some physical contact with the foundation when the latter is progressively extracted from the ground. Thus the value of the slider for the outer friction when the soil is released will be expressed as a percentage $\xi_{out,max,u}$ of the corresponding slider in the case of a rigid body motion, as mentioned in Equation 5-11. The parameter $\xi_{out,max,u}$ depends on the geometrical dimensions of the caisson, and varies according to a 2-terms power equation as illustrated in Figure 5-7 (a).

$$\Delta\Phi_{out}^{max} = \xi_{out,max,u} \times \underbrace{2\pi \frac{D_o}{2} L \left(K_0 \gamma'_{clay} \frac{L}{2} \right) \mu}_{\Delta\Phi_{out}^{max}\ (rigid\ body\ motion)} \qquad \text{EQUATION 5-23}$$

PWP component

Inside the caisson, the resistance to the uplift of the caisson under an imposed displacement is threefold. A first part of the tensile capacity arises from the water seepage that sets up during a certain time step Δt and gradually fills the gaps between the soil plug and the lid, lowering thereby the underpressures that have been generated underneath the lid. As for the rigid body motion modelling, this time-dependent behaviour can be schematized by a non-linear dashpot with a coefficient of viscosity η. The relationship between the load and the displacement rate will be assessed according to the constitutive law $\Delta \mathrm{F} = \eta \times \Delta y$.

The transient behaviour of the damper can be schematized on the basis of the analytical developments performed in section 4.4.5.2, where an expression for the variation of the negative excess PWPs has been derived and is recalled in Equation 5-29. This expression is similar to the one used for the partially drained rigid body motion, except for the formula of the dimensionless factor F which differs slightly. This formula includes a calibration parameter $\xi_{pwp,u,II}$ which variation in relation to the main system parameters is analysed in the next section 5.3.2.

$$\Delta P_{pwp} = \underbrace{A_{base,i} \times F \times [\frac{L_s\ \gamma_w}{k}]}_{\eta} \times \underbrace{\frac{\Delta y}{\Delta t}}_{\Delta y^{\frac{1}{N}}} \qquad \text{EQUATION 5-24}$$

Where

$L_s = L\left(1 + 0.2\left(\frac{L}{D}\right)^{-0.9}\right)$ — Seepage length

$F = \xi_{pwp,u,II}\left(\frac{\Delta y}{L}\right)^{0.75}$ — Factor to account for the non-linear behaviour of the damper

$\xi_{pwp,u,II}$ — Calibration parameter

Plug uplift component

Depending on the magnitude of the tensile force (i.e. the suction pressure) acting on top of the confined soil, a plug uplift mechanism will be initiated. As highlighted in section 4.4.3, the more the partially drained conditions tend towards a drained behaviour (higher permeability, slower loading speed), the more the soil plug remains in place, leading to a sliding failure mode. On the contrary, in case of a more undrained soil behaviour (lower permeability, faster loading speed), the soil plug as well as soil accumulations from below the skirt tip level are gathered together and pulled out with the caisson, establishing a so-called reverse end bearing mechanism. In the present work, the focus is on an intermediate failure mode, for which only a certain portion of the soil plug moves upwards with the suction caisson. This plug uplift component is assumed to be directly and linearly proportional to the applied suction pressure, and is thus modelled on the basis of a spring of stiffness κ_{plug}. The soil plug behaves as an Hookean body, meaning that potential energy is stored in the spring for the elastic deformations of the soil under uplift.

The behaviour of the spring that idealises the response of the soil plug can be approximated by the empirical Equation 4-60 established in section 4.4.5.2. It is formulated as a linear density

(°) transposed vertically by a distance L_{plug} that is directly dependent on the applied suction. One fitting parameter $\xi_{plug,u}$ is implemented to capture the plug uplift due to the confinement state, and its dependency to the main system parameters will be treated in the next section 5.3.2.

$$\Delta W_{plug} = \underbrace{\xi_{plug,u} \times \underbrace{(A_{base,i}\gamma'_{clay})}_{(^\circ)}}_{\kappa_{plug}} \times L_{plug} \qquad \text{EQUATION 5-25}$$

In normal soil conditions, a tensile strength failure is expected to happen all the more quickly as the permeability is low or the loading rate is high, which would be characterized by a slider. Since the present case deals with an elastic soil behaviour, large reversible deformations are prone to occur without failure, and thus the slider would correspond to the complete extraction of the caisson which is does not need to be considered in a analysis in small displacements.

Inner friction component

The suction pressure and the related plug uplift highly influence the way the inner friction is mobilised. The inner shear stresses will develop as long as sliding occurs at the soil-caisson interface, which is not the case when the soil plug is moving upwards with the suction caisson. To account for this specific response along the inner interface, the inner friction will be schematised by means of a spring of displacement-dependent stiffness $\kappa_{in}(\Delta y)$, slightly adapted compared to the drained behaviour. Here again, a slider ς_{in} is implemented in series of the spring to materialize the maximum mobilizable friction.

Based on the findings from section 4.4.5.2, the assessment of the response of the spring representing the inner friction mobilisation is performed by means of the second degree Equation 4-54. This expression is similar to the one employed in the drained configuration (<), with the exception of an additional factor (>) pointing out the reliance on the applied suction. The calibration parameter $\xi_{in,u,II}$ will be investigated in the next section 5.3.2.

$$\Delta\Phi_{\text{in}} = \underbrace{\underbrace{\xi_{in,u,II} \times 2\pi R_i \left(K_s L - \frac{1}{2}\frac{K_s^2 \Delta y}{\mu K_0 \Delta\sigma'_{v,o}}\right)}_{(<)} \underbrace{\left(1 - \frac{s}{s_{crit}}\right)}_{(>)}}_{\kappa_{in}(\Delta y)} \times \Delta y \qquad \text{EQUATION 5-26}$$

With regards to the slider behaviour, a reduction of the maximum inner friction resistance has been noticed compared to the case of a pull-out of a rigid body, and thus the expression of the slider will be given as a fraction $\xi_{in,max,u}$ of the corresponding slider in the case of a rigid body motion, as mentioned in Equation 5-27. The parameter $\xi_{in,max,u}$ depends on the geometrical dimensions of the caisson, and varies according to a 2-terms power equation, according to a trend contrary to $\xi_{out,max,u}$, as reported in Figure 5-7 (b).

$$\Delta\Phi_{in}^{max} = \xi_{in,max,u} \times \underbrace{2\pi \frac{D_i}{2} L \left(K_0 \gamma'_{clay} \frac{L}{2}\right) \mu}_{\Delta\Phi_{in}^{max}\ (rigid\ body\ motion)} \qquad \text{EQUATION 5-27}$$

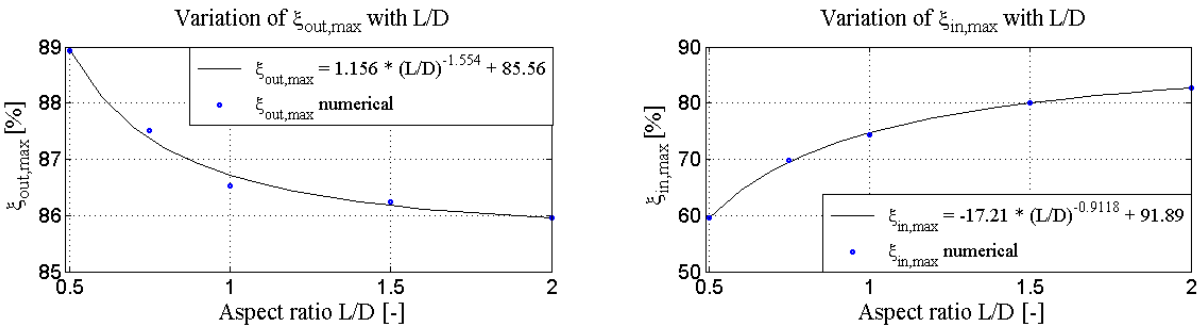

FIGURE 5-7: Variations of the calibration parameters of the sliders with the aspect ratio: (a) outer friction and (b) inner friction

Combination of the components

Inside the caisson, the evolution of the seepage flow over a time lapse Δt governs the extent of the plug uplift mechanism. Logically, these two components will operate in series, to materialise this balance between the soil heave and the size of the gap between the top of the soil plug and the underside of the lid. The rise in the inner friction for a displacement increment Δy coincides with the updating of the seepage over a time step Δt, and is also restricted by the magnitude of the plug uplift. Therefore the mechanical model will be made up of a set of spring-slider put in parallel with a non-linear dashpot and this assemblage will be connected in series with another spring, in order to fully characterize the extraction resistance part arising from inside.
Outside the caisson, the fraction of the total resistance comes solely from the friction that develops simultaneously on the external interface of the skirt. This spring-slider set is thus arranged in parallel to the whole inner component of the model, as depicted in Figure 5-8[76].

Mathematically, the coupling between the two sets of spring-slider, one single spring and one damper is translated by Equation 5-33, after having rearranged Equation 5-28, Equation 5-29, Equation 5-30 and Equation 5-31 on the basis of the displacement and load relationships of Equation 5-32.

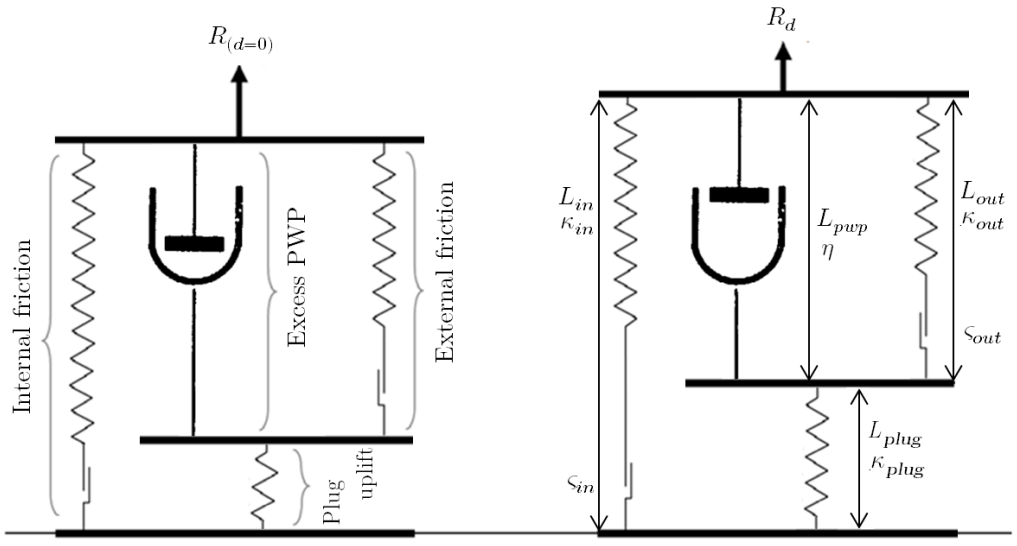

FIGURE 5-8: Rheological model for the 2nd partially drained scenario in the case of a soil free to move [76]

$$L_{out} = \frac{\Delta\Phi_{out}}{\kappa_{out}} + \begin{cases} 0 & \Delta\Phi_{out} < \Delta\Phi_{out,max} \\ L_{slider,out} & \Delta\Phi_{out} \geq \Delta\Phi_{out,max} \end{cases}$$ EQUATION 5-28

$$L_{in} = \frac{\Delta\Phi_{in}}{\kappa_{in}} + \begin{cases} 0 & \Delta\Phi_{in} < \Delta\Phi_{in,max} \\ L_{slider,in} & \Delta\Phi_{in} \geq \Delta\Phi_{in,max} \end{cases}$$ EQUATION 5-29

$$L_{pwp} = \sqrt[1/N]{\frac{\Delta P_{pwp}}{\eta}} \times \Delta t$$ EQUATION 5-30

$$L_{plug} = \frac{\Delta W_{plug}}{\kappa_{plug}}$$ EQUATION 5-31

Considering

$$\begin{aligned} &\mathrm{R_{tot}} = \Delta\Phi_{out} + \Delta\Phi_{in} + \Delta P_{pwp} + \Delta W_{plug} \\ &L = L_{out} = (L_{in} + L_{plug}) = (L_{pwp} + \mathrm{L_{plug}}) = \Delta y \\ &L_{pwp} = L_{in} \\ &L_{slider} = \Delta y - \Delta y_{max} \end{aligned}$$ EQUATION 5-32

$$\mathrm{R_{tot}} = \begin{cases} \kappa_{out}\Delta y + (\Delta y - L_{plug})\ \kappa_{in} + \frac{\eta}{\Delta t}\ + L_{plug}\kappa_{plug} & \Delta\Phi_{out} < \Delta\Phi_{out,max} \\ & \Delta\Phi_{in} < \Delta\Phi_{in,max} \\ \kappa_{out}\Delta y - \underbrace{\kappa_{out}\ \Delta y - \ \Delta y_{max}}_{\varsigma_{out}} + (\Delta y - L_{plug})\ \kappa_{in} + \frac{\eta}{\Delta t}\ + L_{plug}\kappa_{plug} & \Delta\Phi_{out} \geq \Delta\Phi_{out,max} \\ & \Delta\Phi_{in} < \Delta\Phi_{in,max} \\ \kappa_{out}\Delta y - \underbrace{\kappa_{out}\ \Delta y - \ \Delta y_{max}}_{\varsigma_{out}} + (\Delta y - L_{plug})\left(\kappa_{in} + \frac{\eta}{\Delta t}\right) & \Delta\Phi_{out} \geq \Delta\Phi_{out,max} \\ & \Delta\Phi_{in} \geq \Delta\Phi_{in,max} \\ \qquad - \underbrace{\kappa_{in}\ \Delta y - \ \Delta y_{max}}_{\varsigma_{in}} + L_{plug}\kappa_{plug} & \end{cases}$$ EQUATION 5-33

As previously exposed, the implementation of the mechanical model gives an approximation of the components that govern the uniaxial tensile behaviour of the suction caisson. Depending on the way these components are mobilised, the different drainage conditions can be schematized.

In the case of a fully drained uplift (Figure 5-9 (a)), the seepage flow counterbalances exactly the negative excess PWP emerging from the upward movement of the caisson, which means that the shift of the damper is equal to the total displacement ($\mathrm{L_{pwp}} = \Delta\mathrm{y}$). Since the plug uplift component is controlled by the development of differential pressures, the related spring does not contribute to the total displacement ($\mathrm{L_{plug}} = 0$). From this, it results in a purely shearing failure mode, for which the sum of the inner and the outer friction components gives the total tensile strength.

In the case of a partially drained uplift (Figure 5-9 (b)), the setting up of the seepage flow is limited, which will induce the activation of the plug uplift mechanism. The summation of the displacements of the related damper and spring is equal to the total displacement of the caisson ($\mathrm{L_{pwp}} + \mathrm{L_{plug}} = \Delta\mathrm{y}$). In parallel, there is a full mobilisation of outer friction $\mathrm{L_{out}} = \Delta\mathrm{y}$ while

the upward movement of the soil lowers the contribution of the inner friction $L_{in} < \Delta y$. The activation of all rheological elements will give the total load-displacement response.

In the case of an undrained uplift (Figure 5-9 (c)), the seepage flow is severely restricted, and thus the displacement of the damper is almost zero ($L_{pwp} \approx 0$) and equal to the displacement of the slider characterizing the inner friction. This latter component is indeed nearly cancelled out by the large uplift of the soil plug, which completely describe the reverse end bearing failure mode in combination with the outer friction component ($\Delta y = L_{plug} = L_{out}$).

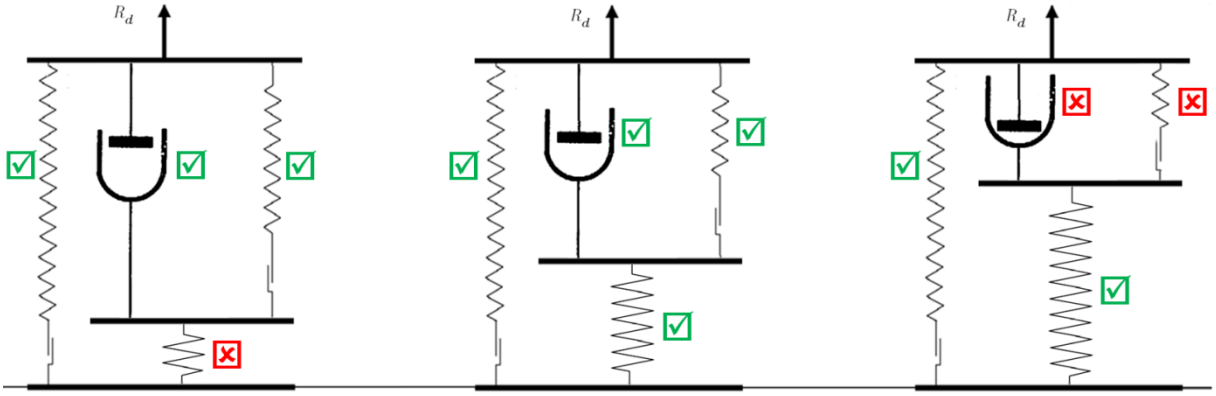

FIGURE 5-9: Activation of the rheological elements for (a) fully drained, (b) partly drained and (c) undrained conditions

5.3.2. Parametric study

To reproduce as accurately as possible the response of the soil-caisson system under loading, the main parameters having an influence on the calibration factors involved in the analytical reconstruction of the curves of the components are investigated through a parametric study. In particular, attention is paid to the effects of the coefficient of permeability, the loading rate and the aspect ratio.

5.3.2.1. Rigid body motion

In the case of an extraction of a rigid body from the soil, it is only a question of estimating how the calibration parameter of the excess PWP component $\xi_{pwp,u,I}$ evolves with the system parameters.

First the variability of $\xi_{pwp,u,I}$ relative to the permeability k is tested. The simulations are carried out for values of the coefficient of permeability in the range $[10^{-7} - 10^{-4}][\frac{m}{s}]$ and for five specific slenderness ratio's $\frac{D}{L} = 0.5 - 0.75 - 1 - 1.5 - 2$. The curves showing the evolution of the calibration parameter for an imposed displacement d of $0.0003m$ are given in Figure 5-10 (a). A global exponential increase of the parameter is noted, and for a defined permeability, lower values of the parameter are obtained when higher aspect ratio's are considered. To be able to estimate the calibration parameter as accurately as possible for any given value of the permeability, trend lines are fitted to the set of data of Figure 5-10 (a). The results are collected in Appendix D.4.

Then the variability of $\xi_{pwp,u,I}$ as a function of the loading rate LR is examined. In this case, the simulations are performed for values of the extraction rate in the range $[5.10^{-7} - 5.10^{-6}][\frac{m}{s}]$ and for the same five aspect ratio's $\frac{\mathrm{D}}{\mathrm{L}}$. In Figure 5-10 (b), the curves showing the variation of the parameter under an imposed uplift d of $0.0003m$ are presented. Similarly to the evolution of $\xi_{pwp,u,I}$ with k, a decreasing exponential tendency is noticed, which seems to be logical since reducing the loading rate has more or less the same effects on the PWP generation as an increase in the permeability. Again the values of the calibration parameter are inversely related to the aspect ratio $\frac{\mathrm{D}}{\mathrm{L}}$. Trend lines that fit the set of data of Figure 5-10 (b) are attached in Appendix D.4.

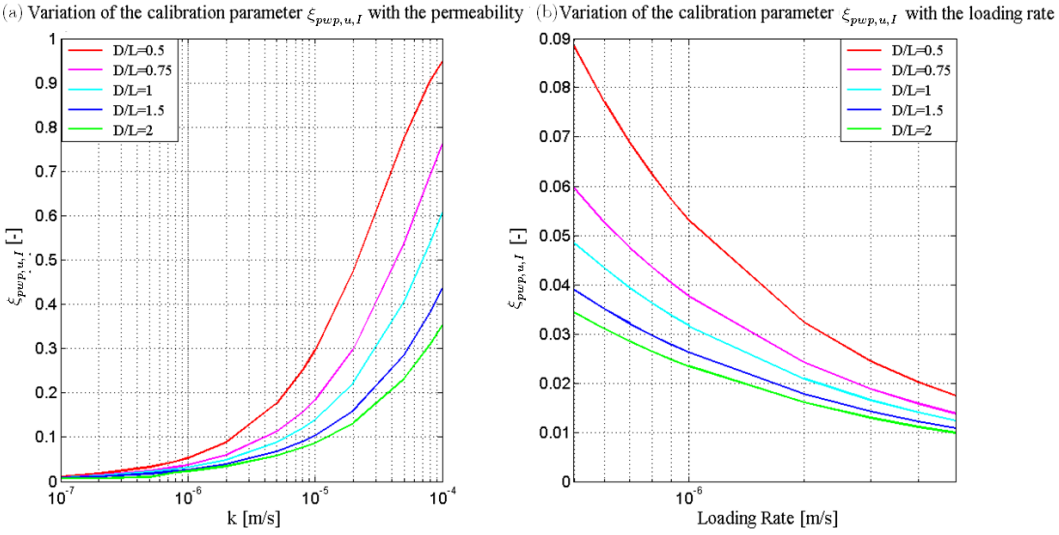

FIGURE 5-10: Variation of the calibration parameter $\xi_{pwp,u,I}$ with (a) the permeability and (b) the loading rate, for 5 distinct slenderness ratio's

5.3.2.2. Soil free to move

When the extraction of a suction caisson from a soil free to move is considered, the variation of multiple calibration parameters according to the main system parameters needs to be analysed.

First the parameter $\xi_{pwp,u,II}$ that calibrates the excess PWP component is investigated. The variability of this parameter relative to the permeability k is tested by varying the value of the coefficient of permeability in the range $[10^{-7} - 10^{-4}][\frac{m}{s}]$ and by considering five specific slenderness ratio's $\frac{D}{L} = 0.5 - 0.75 - 1 - 1.5 - 2$, while leaving the other system parameters to their initial values. Figure 5-11 (a) gives the evolution of the parameter for an imposed displacement d of $0.05m$. A growing exponential trend is noticed with higher values of $\xi_{pwp,u,II}$ for lower aspect ratio's. To be able to estimate the calibration parameter as accurately as possible for any given permeability, trend lines are fitted to the set of data of Figure 5-11 (a). The results are collected in Appendix D.5. The variability of $\xi_{pwp,u,II}$ as a function of the loading rate is also examined for extraction speeds in the range $[5.10^{-7} - 5.10^{-6}][\frac{\mathrm{m}}{\mathrm{s}}]$ and for the same five aspect ratio's $\frac{\mathrm{D}}{\mathrm{L}}$. Figure 5-11 (b) gives the evolution of the parameter for an imposed displacement d of $0.05m$. Compared to the evolution of $\xi_{pwp,u,II}$ with k, here a decreasing exponential trend is obtained with still higher values related to lower aspect ratio's. Trend lines that fit the set of data of Figure 5-11 (b) are attached in Appendix D.5.

Secondly, the parameter $\xi_{out,u}$ governing the outer friction component is considered. The variability of this parameter relative to the permeability k is depicted in Figure 5-12 (a) for an imposed displacement $d = 0.05m$ and evaluating five slenderness ratio's. It appears that the value of $\xi_{out,u}$ first slightly decreases until $k = 10^{-7}\frac{m}{s}$ and then starts to go up. Moreover, the higher the aspect ratio $\frac{D}{L}$, the higher the value of the parameter. The estimation of the parameter $\xi_{out,u}$ for any given permeability is done through the equations of trend lines that are fitted to the present set of data, and collected in Appendix D.6. The same procedure is applied to the variation of $\xi_{out,u}$ with the loading rate. Here, the trend seems to be more constant, showing a very slight increase in the value of the parameter, as illustrated in Figure 5-12 (b). Thus, linear straight trend lines are fitted to these curves, as reported in Appendix D.6.

Thirdly, the parameter $\xi_{in,u}$ governing the inner friction component is considered. The variability of this parameter relative to the permeability k is depicted in Figure 5-12 (a) for an imposed displacement $d = 0.05m$ and evaluating five slenderness ratio's. It appears that the value of $\xi_{in,u}$ is highly dependent on k and grows exponentially while increasing the coefficient of permeability. The higher the aspect ratio $\frac{D}{L}$, the lower the value of the parameter. Here again, the evolution of the parameter $\xi_{in,u}$ is approached by trend lines presented in Appendix D.7. The dependence of $\xi_{in,u}$ on the loading rate shows a decreasing tendency, as exhibited in Figure 5-12 (b) and that can be approximated by specific trend lines given in Appendix D.7.

Finally, the parameter $\xi_{plug,u}$ implemented in the plug uplift component is assessed. The variability of this parameter as a function of k is displayed in Figure D- 16 (a) for five aspect ratio's. The values of $\xi_{plug,u}$ reach an explicit peak for a coefficient of permeability in the range $[10^{-7} - 10^{-6}][\frac{m}{s}]$ and then decrease steeply. Higher values go hand in hand with higher aspect ratio's. These observations are used to assess trend lines that capture the evolution of the parameter for any given permeability, cf. Appendix D.8. By applying the same procedure to the variability of $\xi_{plug,u}$ with the loading rate, the exponential decreasing curves of Figure 5-14 (b) are obtained which can be approximated by the fitting lines given in Appendix D.8.

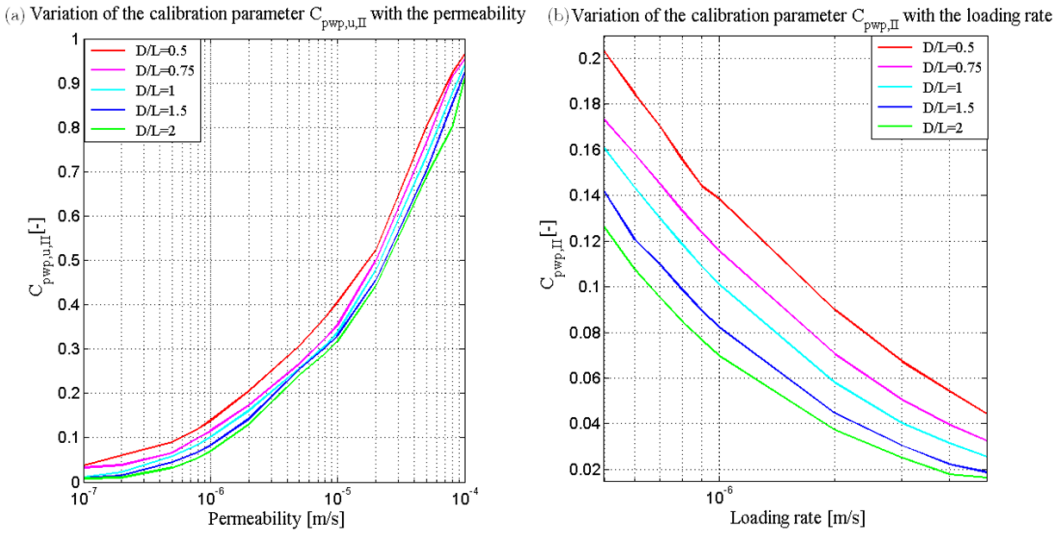

FIGURE 5-11: Variations of the calibration parameter $\xi_{pwp,u,II}$ with (a) the permeability and (b) the loading rate, for 5 distinct slenderness ratio's

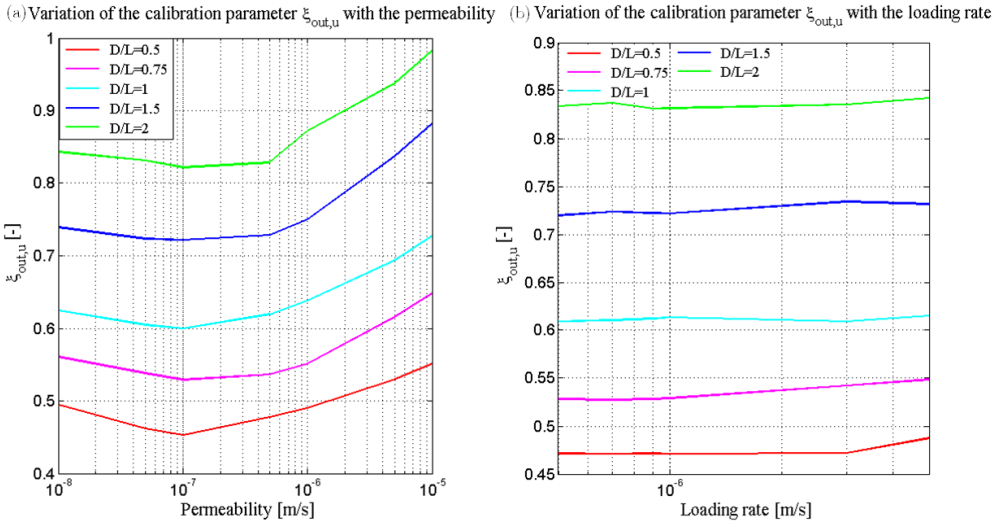

FIGURE 5-12: Variations of the calibration parameter $\xi_{out,u}$ with (a) the permeability and (b) the loading rate, for 5 distinct slenderness ratio's

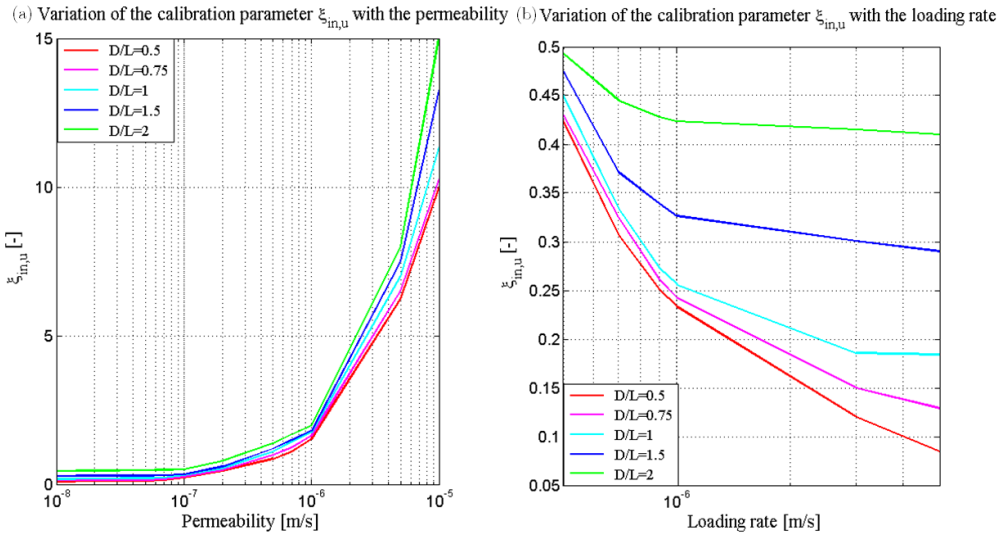

FIGURE 5-13: Variations of the calibration parameter $\xi_{in,u}$ with (a) the permeability and (b) the loading rate, for 5 distinct slenderness ratio's

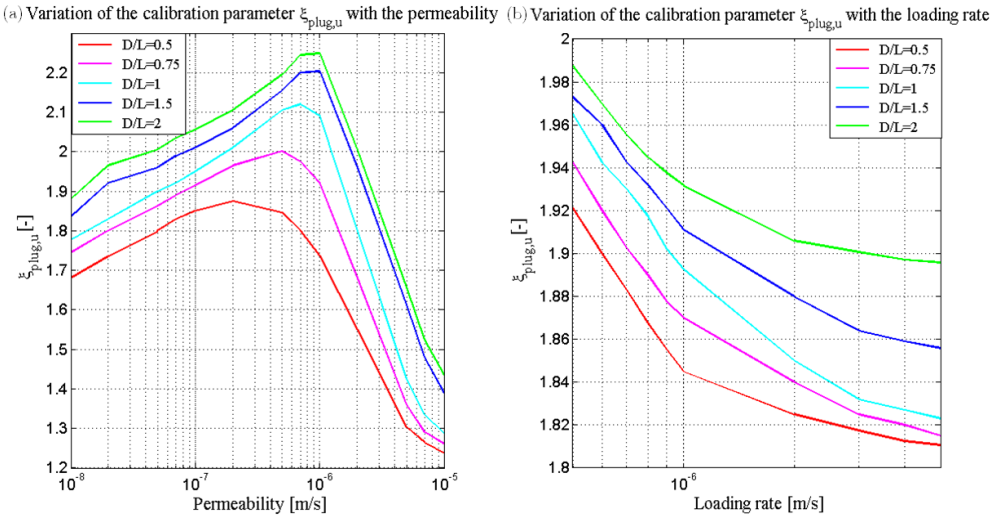

FIGURE 5-14: Variations of the calibration parameter $\xi_{plug,u}$ with (a) the permeability and (b) the loading rate, for 5 distinct slenderness ratio's

Chapter 6
Conclusion

6.1. Summary and conclusions

In conclusion, this master thesis aimed at investigating the behaviour of suction caisson foundations embedded in an elastic soil and subjected to a monotonic axial tensile load in order to formulate a practical prediction method of the uplift resistance in the form of a macro-element. To pursue this objective and to bring this work to an end, the following three-step procedure was carried out:

- The deepening of the knowledge of the topic through a scientist literature review;
- The implementation of the 2D axisymmetric FE model, the simulations for different soil-foundation configurations, the analysis of the numerical results and their comparison to some analytical formulations;
- The development of a macro-element on the basis of the previous findings with the aim of establishing the tensile behaviour of the caisson;

In the first instance, a purely mechanical system assuming fully drained conditions was studied, while in a second phase, the hypothesis of partially drained conditions gives rise to an hydro-mechanical system. From this, four specific cases were investigated as recalled in Table 6-1.

TABLE 6-1: Summary of the different specific cases and their features

SCENARIO	SUB-CASE	DRAINAGE CONDITION	SOIL CONDITION	RESISTANCE
1	1-1*bis*	Drained	Rigid body motion	$\Phi_{out} - \Phi_{in}$
	2-2*bis*	Drained	Free to move	$\Phi_{out} - \Phi_{in} - (W_{plug})$
2	3	Partly drained	Rigid body motion	$\Phi_{out} - \Phi_{in} - P_{pwp}$
	4	Partly drained	Free to move	$\Phi_{out} - \Phi_{in} - P_{pwp} - W_{plug}$

The examination of the sub-case 1-1*bis* has revealed a purely frictional mode of reaction. In particular, the shear stresses are progressively and concurrently mobilised to the same extent along the inner and the outer skirt interface of the caisson. The response of the system is thus straightaway computed by integrating the shear stress profiles along the skirt up to the full mobilisation. This results in a model made up of two parallel springs bounded by a slider.

If the soil is made free to move (sub-cases 2-2*bis*), the friction represents still the predominant share of the reaction but two major distinctions from the previous case are observed.

- On the one hand, the internal and the external friction mechanisms are no longer synchronous since the inner friction component is shifted towards greater displacements;
- On the other hand, the confined state of the soil encapsulated within the skirt limits the free lateral diffusion of the stresses in the soil upon traction. As a result, the soil plug keeps physical contacts with the surrounding foundation and there is a reduction of the total mobilisable inner friction which is all the more pronounced that the aspect ratio $\frac{D}{L}$ is low and the confinement is large. Outside the caisson, a partial loss of contact between the soil and the caisson occurs just under the mudline and has the consequence of partially reducing the maximum outer friction that is mobilisable.

The mechanical model still consists of two parallel springs followed by a slider. The analytical formulation from [75] has been successfully implement to schematize the non-linear springs' behaviour using one or two calibration parameters to improve the consistency with the numerical results. As for the sliders, they capture the drop of resistance with the help of an additional reduction parameter compared to the 1st case.

From the study of the sub-case 3, it appears that the mobilisation of the friction components remains exactly similar to the drained configuration and can be described by the same spring-slider assembly. However, it has been noted that the combination of a reduced permeability with a higher rate of loading leads to the generation of underpressures below the lid of the caisson. The effect of suction arises from the emergence of this differential of pressure with the outside, and insures a rise in the tensile capacity. The evolution of this phenomenon takes place on a transient basis with the development of seepage flows. It is modelled by a dashpot put in parallel with the two frictional springs and assessed by coupling Darcy's law, the hydraulic gradient, the definition of the seepage length given in [79], and one calibration parameter.

Finally, from the investigation of the sub-case 4, it has been established that an extra contribution to the tensile resistance is due to the plug uplift mechanism. This component is governed by the applied suction and is thus coupled with the components of PWP generation and of inner friction by an inversely proportional relationship. The lower the seepage flow initiation, the greater the negative variations of PWPs under the lid and therefore the higher the upward movement of the soil. This reduces the relative displacement between the soil and the caisson and the development of friction. As a result, the plug uplift component is modelled as a spring that is placed in series with the other two contributions to the extraction resistance and that can be analytically derived by the principle of the mechanical work according to [58]. Along the external interface of the caisson, the friction is modelled similarly to the sub-case 2.

Table 6-2 summarizes the different components activated in each configurations as well as the related mechanical elements and calibration parameters, highlighted in this work.

6.2. Perspectives

The writing of a master thesis is a long-run process which implies that some of the initial objectives have inevitably been redefined, refined or prioritized at the expense of some others throughout the life of the project to finally come up with the present work.

This being said, a non-exhaustive list of six paths that would have been interesting to explore is provided here below, and can be seen as possible future contributions to enlarge the scope of the present study.

1. Performing an analysis of the FE model closer to reality by including a plastic soil behaviour, and testing the influence of various constitutive laws. This should be the very first step to treat as a continuation of the present work;
2. Extending the study to the case of non-standard soil conditions such as layered soil consisting of clay and sand;
3. Integrating the unloading stage of the caisson as well as the compressive loading into the numerical modelling and inferring the adjustments of the mechanical elements included in the macro-element;
4. Switching to a cyclic loading of the caisson in place of a monotonic one since it is more in line with the kind of solicitations encountered in an offshore environment;
5. Performing a refined parametric analysis by investigating the variation of two or more parameters from the setting values at once time;
6. Improving the accuracy of the macro-element by implementing some neglected contributions such as the soil pressure at the skirt tip level or the development of differential pressure due to the expansion of water in the voids above the soil plug (gap, valves,...).

TABLE 6-2: Summary of the different components of the resistance and their related mechanical elements

	COMPONENTS OF THE RESISTANCE							
SUB-CASES	*Inner friction*		*Outer friction*		*PWP*		*Plug uplift*	
1-1*bis*	Spring	–	Spring	–	–	–	–	–
	Slider	–	Slider	–				
2-2*bis*	Spring	$\zeta_{in,d}$	Spring	$\zeta_{out,d}$	–	–	Not modelled	
	Slider	$\xi_{max,in,d}$	Slider	$\xi_{max,out,d}$				
3	Spring	–	Spring	–	Damper	$\xi_{pwp,u,I}$	Spring	$\xi_{plug,u,I}$
	Slider	$\xi_{max,in,d}$	Slider	$\xi_{max,out,d}$				
4	Spring	$\zeta_{in,d}$	Spring	$\zeta_{out,d} - \xi_{out,u}$	Damper	$\xi_{pwp,u,II}$	Spring	$\xi_{plug,u,II}$
	Slider	$\xi_{max,in,u}$	Slider	$\xi_{max,in,u}$				

Appendix A
Combinations of solutions for the OWT supports

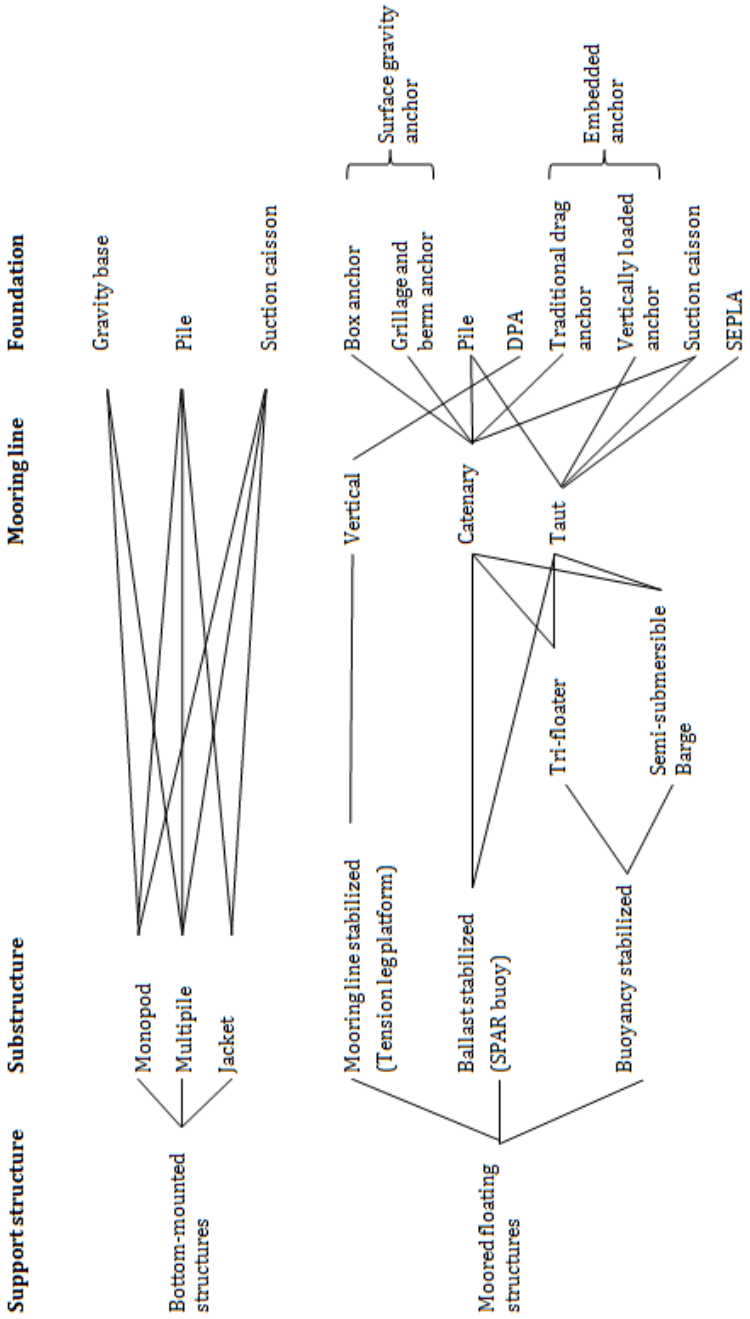

Appendix B
Variation of the global reaction components

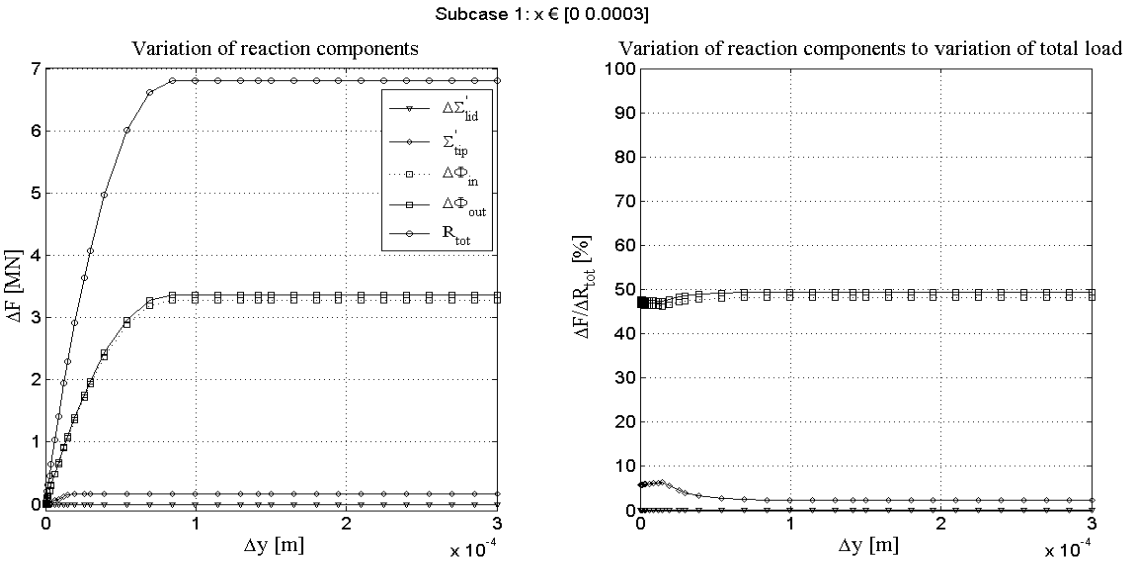

FIGURE B- 1 : Drained traction simulations: variations of the reaction components and variations of the reaction components to variation of the total load for the sub-case 1

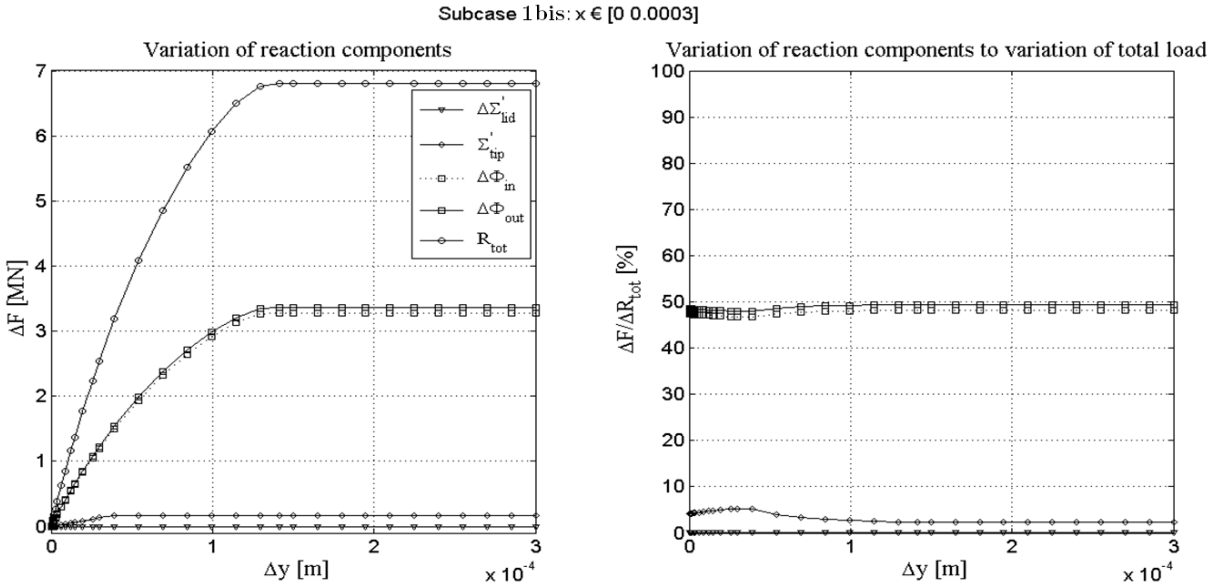

FIGURE B- 2: Drained traction simulations: variations of the reaction components and variations of the reaction components to variation of the total load for the sub-case 1*bis*

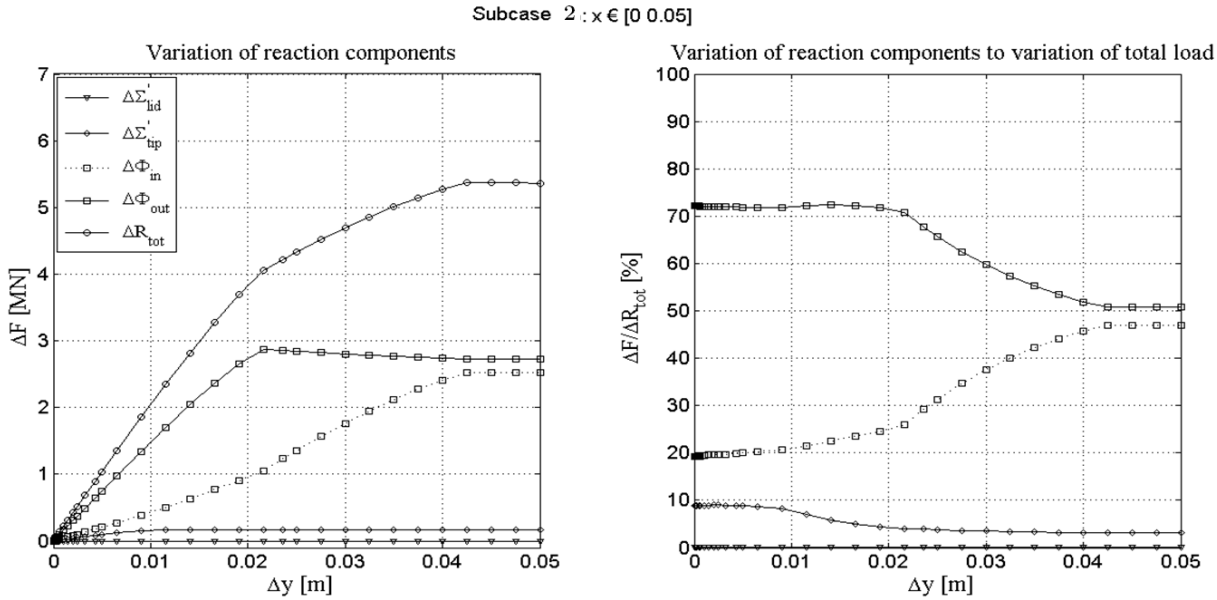

FIGURE B- 3 : Drained traction simulations: variations of the reaction components and variations of the reaction components to variation of the total load for the sub-case 2

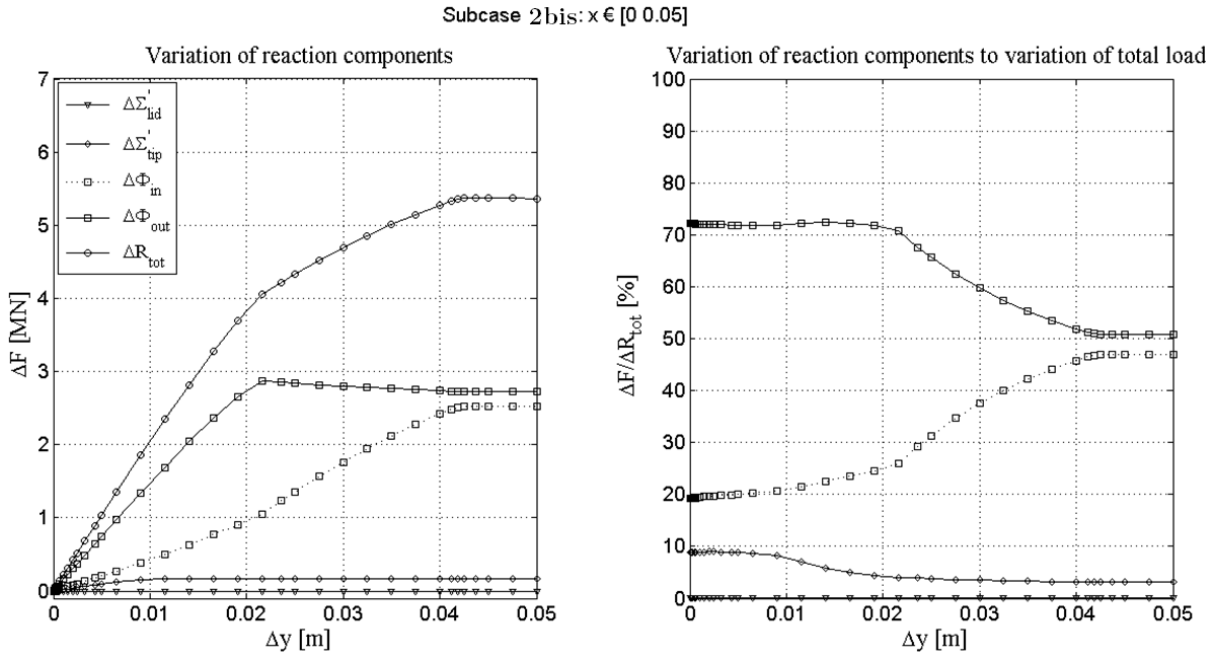

FIGURE B- 4: Drained traction simulations: variations of the reaction components and variations of the reaction components to variation of the total load for the sub-case 2*bis*

Appendix C
Friction - Displacement curves

C.1 Calculation of the maximum available friction under the assumption of a rigid body movement (sub-cases 1 and 1*bis*)

Given

Δy	Displacement increment
ϕ	Friction coefficient at the interface
K_0	Horizontal earth pressure coefficient at rest
K_τ	Tangential penalty coefficient
$\Delta\sigma'_{v,o}$	Effective stress variation
τ	Shear stress at the interface
τ_{mob}	Mobilised shear stress at the interface
τ_{max}	Maximum available shear stress a the interface
Φ	Shear force component along the skirt of the caisson
Φ_{mob}	Mobilised shear force at the interface
Φ_{max}	Maximum available shear force at the interface

Identification of the depth z_0 of mobilisation of the maximum available shear stress τ_{max}, Equation C- 1.

$$\underbrace{\phi K_0 \Delta\sigma'_{v,o} z}_{(1)} = \underbrace{K_\tau \Delta y}_{(2)}$$

$$\Leftrightarrow z_0 = \frac{K_\tau \Delta y}{\phi K_0 \Delta\sigma'_{v,o}} \qquad \text{Equation C- 1}$$

Expression of the final displacement step on the basis of the calculated value of z_0, Equation C- 2.

$$z_{max} = z_0(L)$$

$$\Leftrightarrow \Delta y_{max} = \frac{\phi K_0 \Delta\sigma'_{v,o}}{K_\tau} L \qquad \text{Equation C- 2}$$

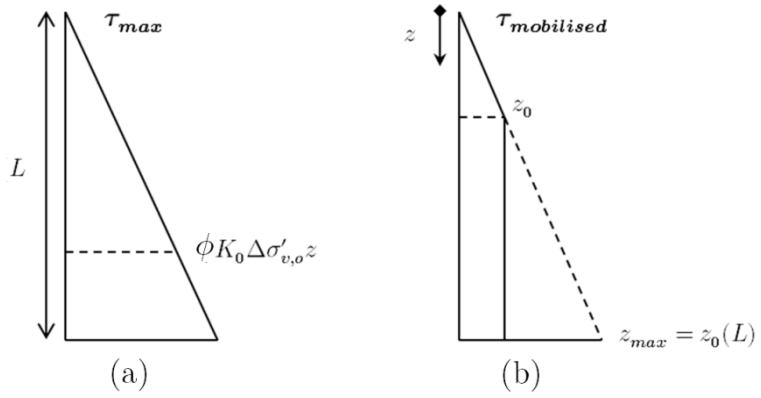

FIGURE C- 1 : Shear stress profile

Calculation of the shear stress associated to each displacement step by integrating a triangular shear stress profile between 0 and z_0, and then a rectangular shear stress profile between z_0 and the total length L all integrated over the cylindrical surface, Equation C- 3.

$$\begin{aligned}
\tau\ \Delta y &= \int_0^{z_0} \phi K_0 \Delta\sigma'_{v,o} z\ dz + \int_{z_0}^{L} K_\tau \Delta y \\
&= \phi K_0 \Delta\sigma'_{v,o} \frac{z_0^2}{2} + K_\tau \Delta y (L - z_0) \\
&= \phi K_0 \frac{\Delta\sigma'_{v,o}}{2}\ \frac{K_\tau^2}{\phi^2 K_0^2 {\Delta\sigma'_{v,o}}^2} + K_\tau \Delta y L - \frac{K_\tau^2 \Delta y^2}{\phi K_0 \Delta\sigma'_{v,o}} \\
&= K_\tau \Delta y L - \frac{1}{2} \frac{K_\tau^2 \Delta y^2}{\phi K_0 \Delta\sigma'_{v,o}}
\end{aligned}$$

EQUATION C- 3

Calculation of the mobilised shear force at the interface by integrating the shear stress over the cylindrical surface, Equation C- 4.

$$\begin{aligned}
\Phi_{mob} &= 2\pi R\ \tau\ \Delta y \\
&= 2\pi R\ \left(K_\tau \Delta y L - \frac{1}{2} \frac{K_\tau^2 \Delta y^2}{\phi K_0 \Delta\sigma'_{v,o}} \right)
\end{aligned}$$

EQUATION C- 4

Calculation of the maximum available shear force at the interface, Equation C- 5.

$$\begin{aligned}
\Phi_{max} &= \Phi_{mob}(\Delta y_{max}) \\
&= 2\pi R\ \tau\ \Delta y_{max} \\
&= 2\pi R \left(\frac{1}{2} \phi K_0 \Delta\sigma'_{v,o} L^2 \right)
\end{aligned}$$

EQUATION C- 5

C.2 Analytical calculation of the friction-displacement curves for a linear elastic soil

From: Randolph M. F. & Wroth C. P. (1978),'Analysis of deformation of vertically loaded piles', Journal of the geotechnical engineering division, No. 12, pp. 1465 - 1488 [75]

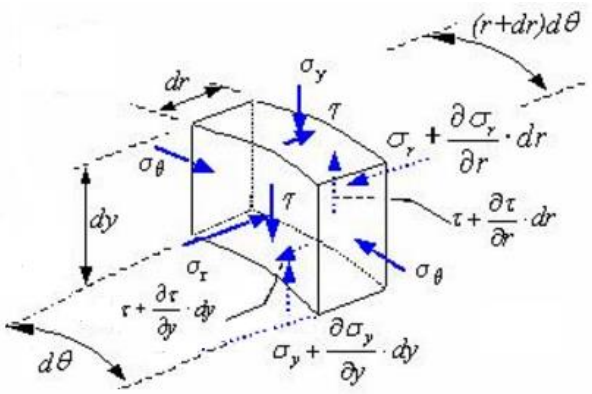

FIGURE C- 2 : Stresses in soil element [75]

Given

τ	Shear stress at the interface
r	Radius of the suction caisson
σ	Stresses on soil element
u	Radial displacement
w	Vertical displacement
γ	Deformation due to shear
G	Shear modulus

$r_m = 2L(1-\nu)$

Step 1: Moment equilibrium around centre O gives Equation C- 6.

$$\left(\tau + \frac{\partial \tau}{\partial r} dr\right)\ d\theta\ dy\ \ r + dr\ \ - \tau\ d\theta\ dy\ r + \left(\sigma_y + \frac{\partial \sigma_y}{\partial y} dy\right)\ dr\ d\theta\ \left(r + \frac{dr}{2}\right) - \sigma_y\ d\theta\ dr\ \left(r + \frac{dr}{2}\right) = 0$$

$$\Leftrightarrow \quad \tau\ d\theta\ dy\ \ r + dr\ + \frac{\partial \tau}{\partial r} dr\ d\theta\ dy\ \ r + dr\ - \tau\ d\theta\ dy\ r + \sigma_y\ dr\ d\theta\ \left(r + \frac{dr}{2}\right) + \frac{\partial \sigma_y}{\partial y} dy\ dr\ d\theta\ \left(r + \frac{dr}{2}\right) - \sigma_y\ d\theta\ dr\ \left(r + \frac{dr}{2}\right) = 0$$

Cancellation of similar terms

$$\Leftrightarrow \quad \tau\ d\theta\ dy\ dr\ + r\frac{\partial \tau}{\partial r} dr\ d\theta\ dy + \frac{\partial \tau}{\partial r} dr^2\ d\theta\ dy + r\frac{\partial \sigma_y}{\partial y} dy\ dr\ d\theta + \frac{\partial \sigma_y}{\partial y} dy\ d\theta \frac{dr^2}{2}$$

Neglecting second order terms

$$\Leftrightarrow \quad \tau + r\frac{\partial \tau}{\partial r} + \frac{\partial \sigma_y}{\partial y}\ r = 0$$

Cancellation of $d\theta\ dy\ dr$

$$\Leftrightarrow \quad \frac{\partial\ r\tau}{\partial r} + \frac{\partial \sigma_y}{\partial y} r = 0 \qquad \text{EQUATION C- 6} \qquad \text{Derivation of a product}$$

Step 2: Simplification formulated on the basis of the assumption that the rate of change of vertical stress with respect to depth is much less than the rate of change of the shear stress with respect to radial distance, during the axial loading. This leads to Equation C- 7:

$$\Leftrightarrow \quad \frac{\partial\ r\tau}{\partial r} = 0 \qquad \text{EQUATION C- 7}$$

Step 3: Integration of Equation C-7 between the caisson's radius r_0 and a radial distance r from the centreline of the caisson gives Equation C- 8.

$$\int_{r_0}^{r} d\,(r\tau) = 0$$

$$\Leftrightarrow \quad \tau\ r\ r - \tau\ r_0\ r_0 = 0$$

$$\Leftrightarrow \quad \tau\ r\ = \tau\ r_0\ \frac{r_0}{r} \qquad \text{EQUATION C- 8}$$

Where

$\tau_0 = \tau\ r_0$	Shear stress at the soil - caisson interface
$\tau_r = \tau\ r_r$	Shear stress at the radial distance r from the centreline of the caisson
r_0	Caisson's radius

Step 4: Deformation due to shear is expressed by Equation C- 9.

$$\tan\gamma = \frac{\Delta l}{l} \approx \gamma$$

$$\gamma = \frac{\left(u + \frac{\partial u}{\partial z} dz\right) - u}{dz} + \frac{\left(w + \frac{\partial w}{\partial r} dr\right) - w}{dr}$$

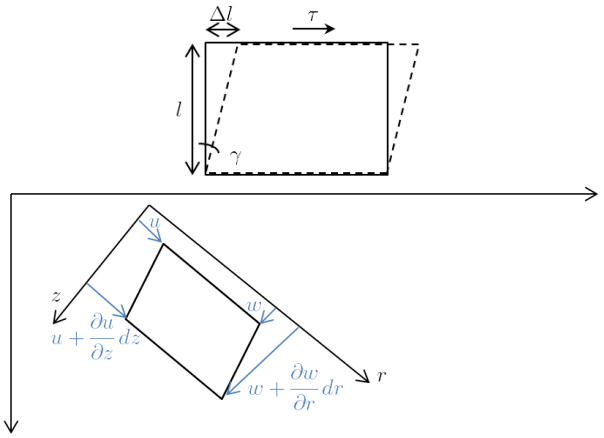

$$\Leftrightarrow \quad \gamma = \frac{\partial u}{\partial z} + \frac{\partial w}{\partial r} \qquad \text{EQUATION C- 9}$$

Where

u	Radial displacement
w	Vertical displacement

Step 5: By making the assumption of a negligible radial displacement compared to vertical displacement of the soil, Equation C- 9 becomes Equation C- 10.

$$\Leftrightarrow \quad \gamma = \frac{\partial w}{\partial r} \qquad \text{EQUATION C- 10}$$

Step 6: By analogy to Hooke's law, it is possible to rewrite Equation C-10 as a shear stress-strain relationship for linear elastic soils denoted by Equation C- 11.

$$\tau\ r\ = G\ r\ \gamma\ r$$

$$\Leftrightarrow \quad \gamma = \frac{\partial w}{\partial r} = \frac{\tau\ r}{G\ r} \qquad \text{EQUATION C- 11}$$

Step 7: By substituting Equation C- 8 into Equation C- 11, one can obtain Equation C- 12.

$$\gamma\ \mathrm{r}\ = \frac{\partial \mathrm{w}}{\partial \mathrm{r}} = \frac{\tau\ \mathrm{r}_0}{\mathrm{G\ r}} \frac{\mathrm{r}_0}{\mathrm{r}} \qquad \text{EQUATION C- 12}$$

Step 8: The extraction length of the caisson shaft $\mathrm{w_s}$ is given by the integration of previous Equation C- 12 assuming a linear elastic soil on the one hand and no radial variation of G on the other hand, meaning that $\mathrm{G\ r}\ = \mathrm{r}$ (Equation C- 13).

$$\mathrm{W_s} = \tau\ r_0\ r_0 \int_{r_0}^{r_m} \frac{dr}{Gr}$$

$$\Leftrightarrow \quad \mathrm{w_s} = \frac{\tau_0 r_0}{G} \ln\left(\frac{r_m}{r_0}\right) \qquad \text{EQUATION C- 13}$$

Step 9: Finally, knowing $\mathrm{w_s}$ from previous step, the final relation between shear stress τ and vertical displacement $\Delta \mathrm{y}$, is given byEquation C- 14.

$$\Leftrightarrow \quad \frac{\tau}{\tau_{\max}} = K_s \Delta \mathrm{y} \qquad \text{EQUATION C- 14}$$

Appendix D
Trend lines of the variation of the calibration parameters

D.1 Variation of the calibration parameters $\zeta_{out,d}$, $\xi_{out,d}$ and $\zeta_{in,d}$ with ν_c

As a general rule, the variation of the calibration parameters $\zeta_{out,d}$ and $\xi_{out,d}$ with ν_c on the outside of the caisson can be interpolated by using second order polynomial equations, whose generic formula is given in Equation D- 1. The exact equations are indicated in Figure D- 1(a) and (b) respectively

$$f\ x\ = p_1 x^2 + p_2 x + p_3 \qquad \text{EQUATION D- 1}$$

As far as the variation of the parameter $\zeta_{in,d}$ is concerned, it is fitted by a general exponential model including two terms as stated in Equation D- 2. Equations are given in Figure D- 2.

$$f\ x\ = a\, exp(bx) + c\, exp(dx) \qquad \text{EQUATION D- 2}$$

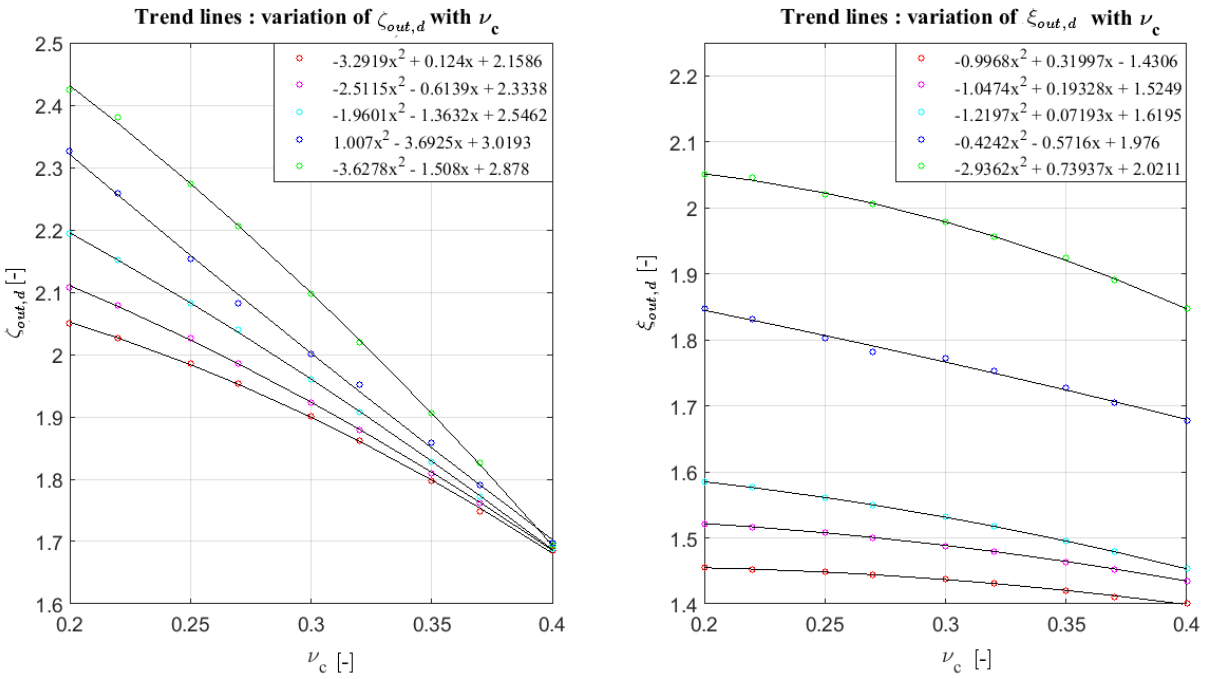

FIGURE D- 1 : Trend lines for the variation of $\zeta_{out,d}$ and $\xi_{out,d}$ with ν_c

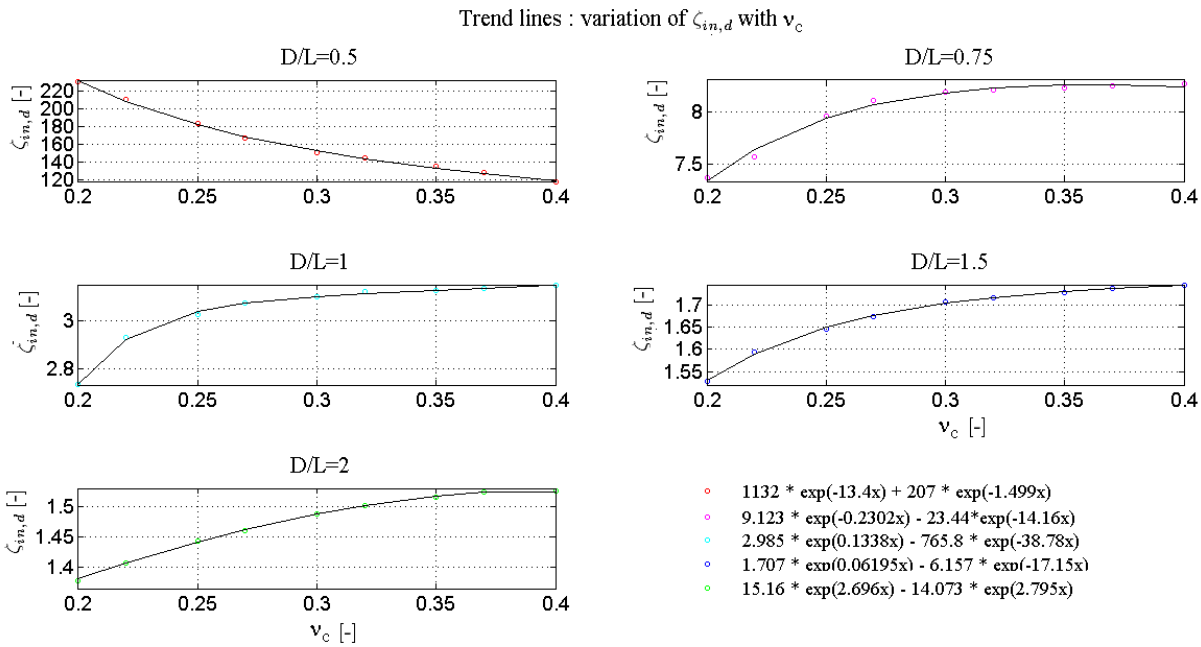

FIGURE D- 2: Trend lines for the variation of $\zeta_{in,d}$ with ν_c

D.2 Variation of the calibration parameters $\zeta_{out,d}$, $\xi_{out,d}$ and $\zeta_{in,d}$ with K_τ

As a general rule, the variation of the calibration parameters $\zeta_{out,d}$, $\xi_{out,d}$ and $\zeta_{in,d}$ with K_τ for both the outside and the inside friction along the skirt of the caisson can be interpolated by using a fitting curve having a 2-terms power Equation D- 3. The exact equations are indicated in Figure D- 3, Figure D- 4 and Figure D- 5 for $\zeta_{\mathrm{out,d}}$, $\xi_{\mathrm{out,d}}$ and $\zeta_{in,d}$ respectively. $[\frac{kN}{m^3}]$

$$f\ x\ = ax^b + c \qquad \text{EQUATION D- 3}$$

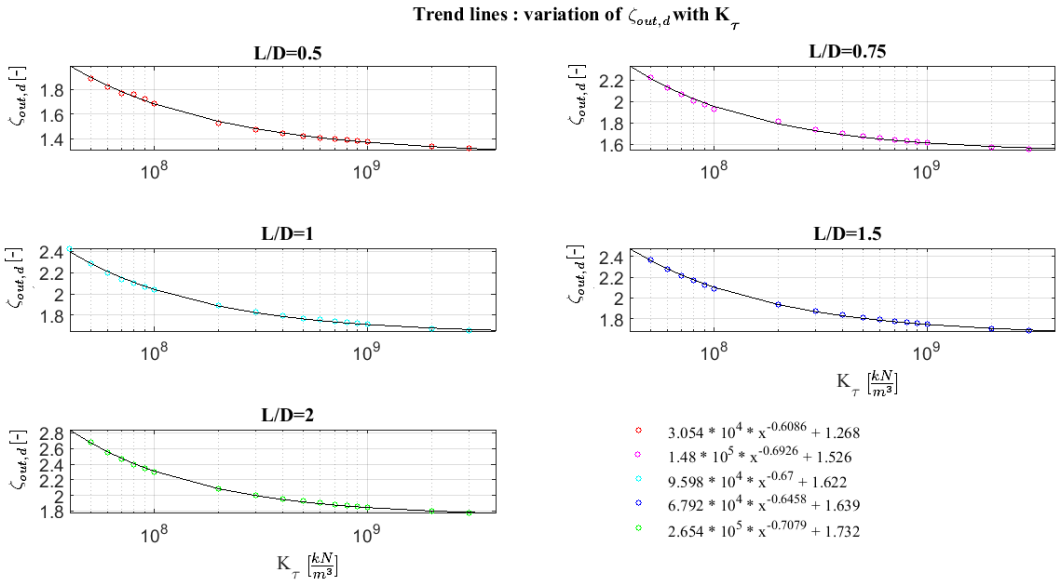

FIGURE D- 3: Trend lines for the variation of $\zeta_{out,d}$ with ν_c

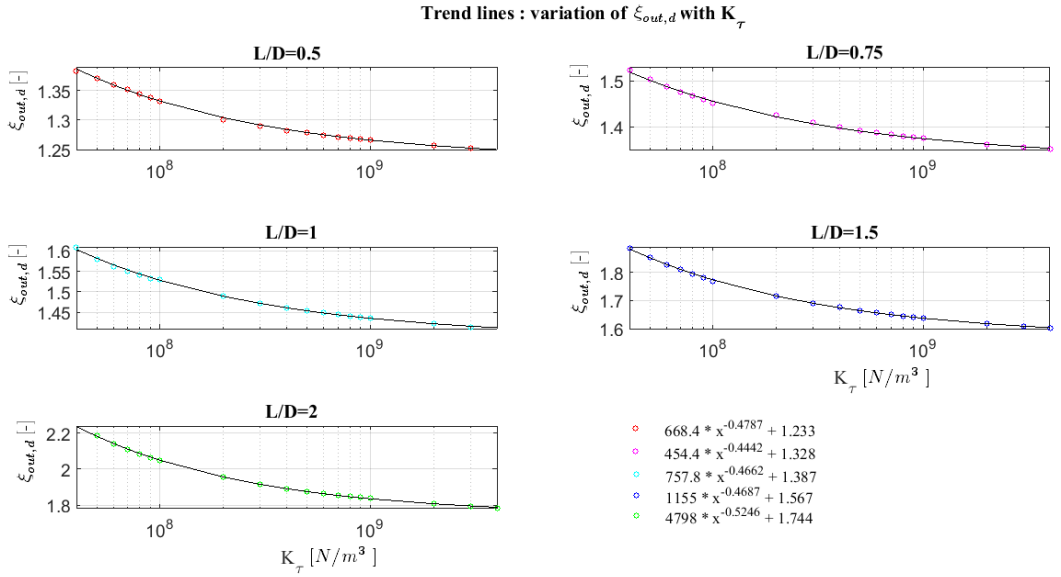

FIGURE D- 4 : Trend lines for the variation of $\xi_{out,d}$ with ν_c

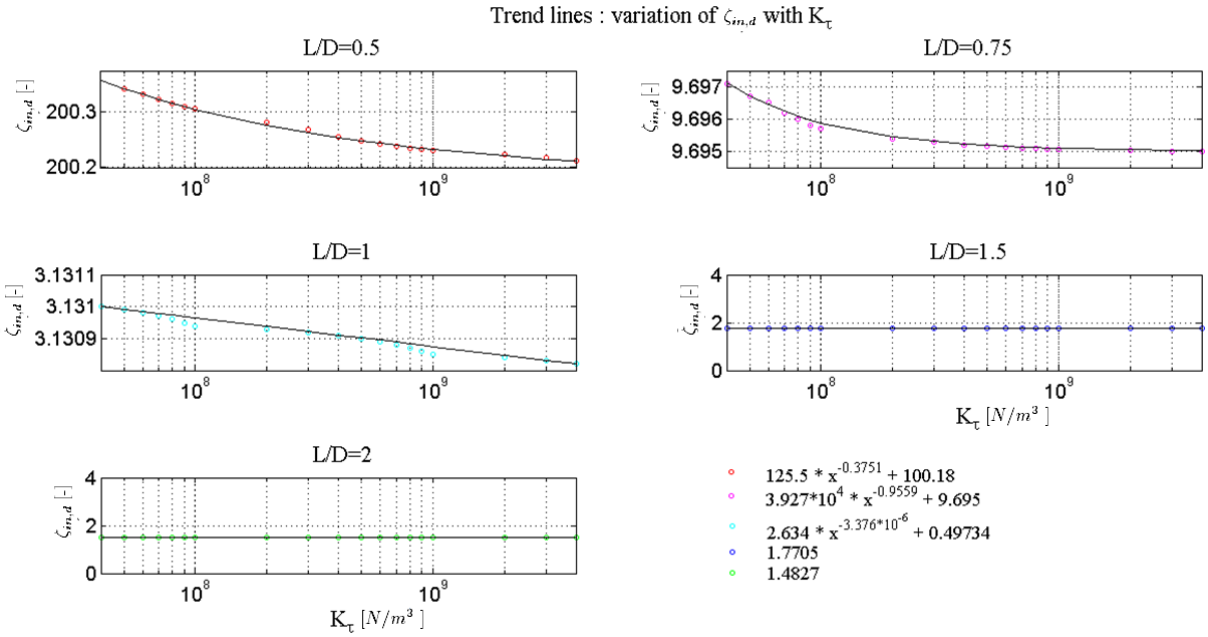

FIGURE D- 5: Trend lines for the variation of $\zeta_{in,d}$ with ν_c

D.3 Variation of the calibration parameters $\zeta_{out,d}$, $\xi_{out,d}$ and $\zeta_{in,d}$ with E_c

As a general rule, the variation of the calibration parameters $\zeta_{out,d}, \xi_{out,d}$ and $\zeta_{in,d}$ with E_c for both the outside and the inside friction along the skirt of the caisson can be interpolated by using a fitting curve having a 2-terms exponential Equation D- 4. The exact equations are indicated in Figure D- 6, Figure D- 7 and Figure D- 8 for $\zeta_{out,d}$, $\xi_{out,d}$ and $\zeta_{in,d}$ respectively.

$$f\ x\ = a\,exp(bx) + c\,exp(dx) \qquad \text{EQUATION D- 4}$$

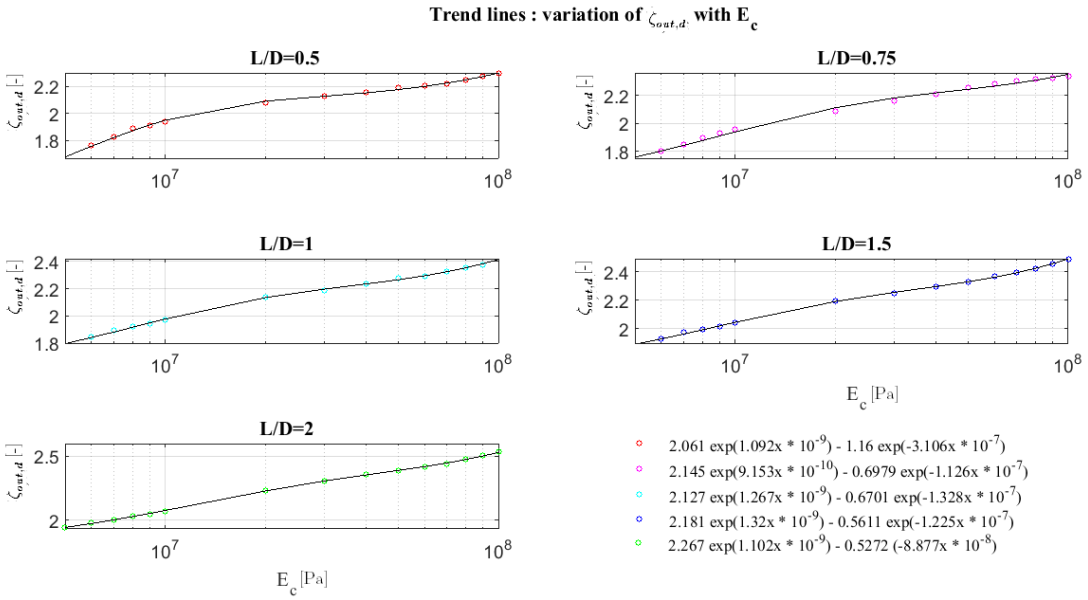

FIGURE D- 6 : Trend lines for the variation of $\zeta_{out,d}$ with E_c

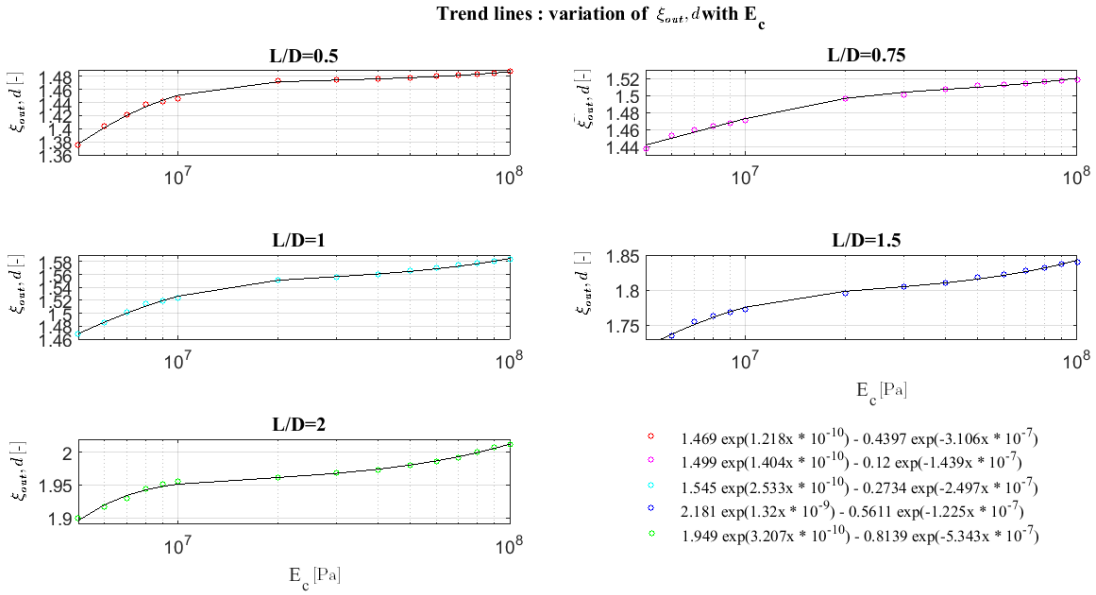

FIGURE D- 7 : Trend lines for the variation of $\xi_{out,d}$ with E_c

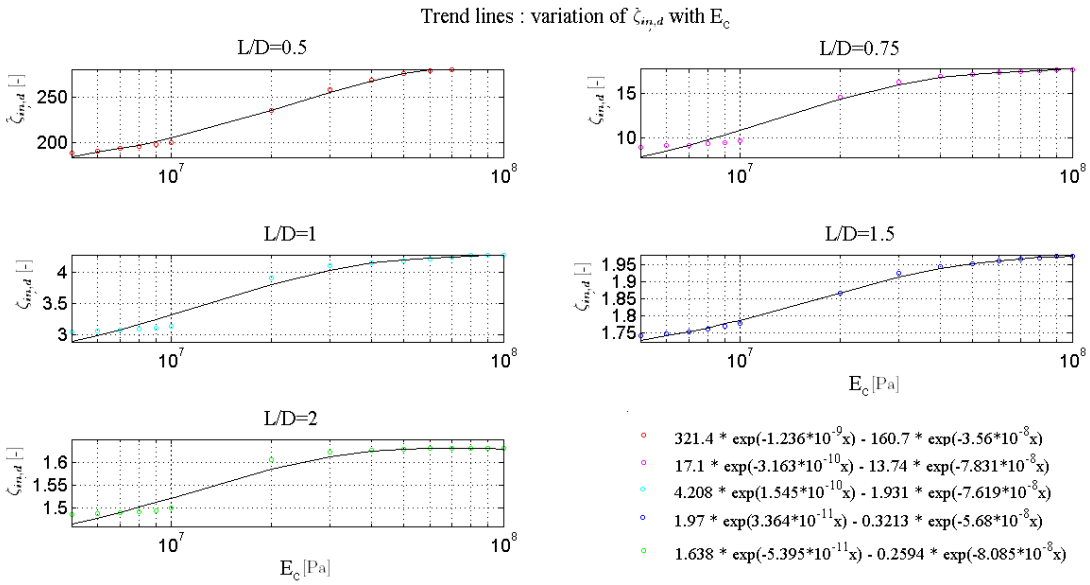

FIGURE D- 8 : Trend lines for the variation of $\zeta_{in,d}$ with E_c

D.4 Variation of the calibration parameter $\xi_{pwp,u,I}$ with k and the loading rate

As a general rule, the variation of the calibration parameter $\xi_{pwp,u,I}$ with the permeability k and the loading rate for the estimation of the excess negative PWPs below the lid can be interpolated by using a fitting curve having a 2-terms power Equation D- 5, with the exact formula's for the different aspect ratio's depicted in Figure D- 9, and Figure D- 10.

$$f\ x\ = ax^b + c \qquad \text{EQUATION D- 5}$$

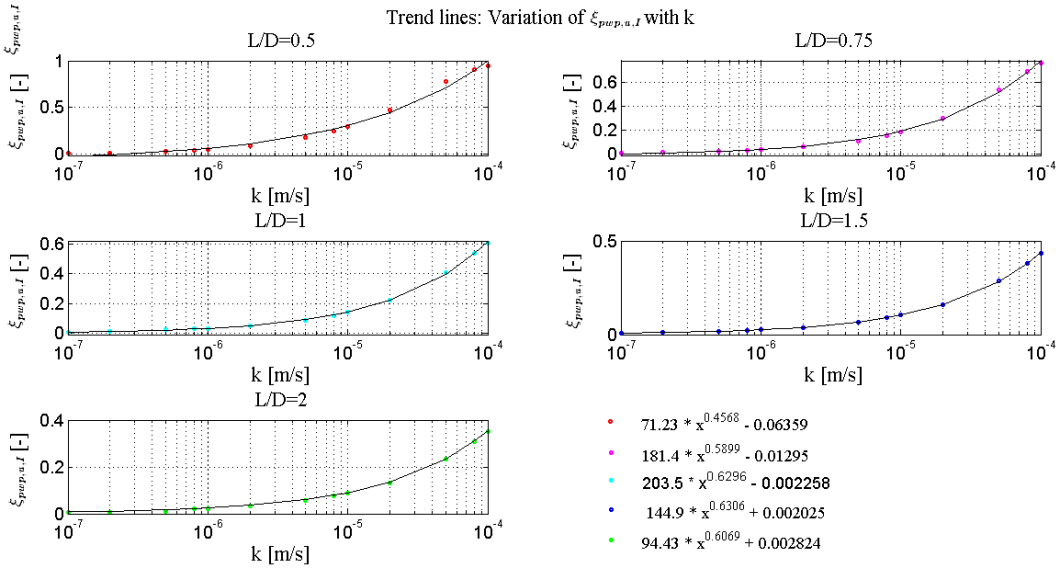

FIGURE D- 9 : Trend lines for the variation of $\xi_{pwp,u,I}$ with k

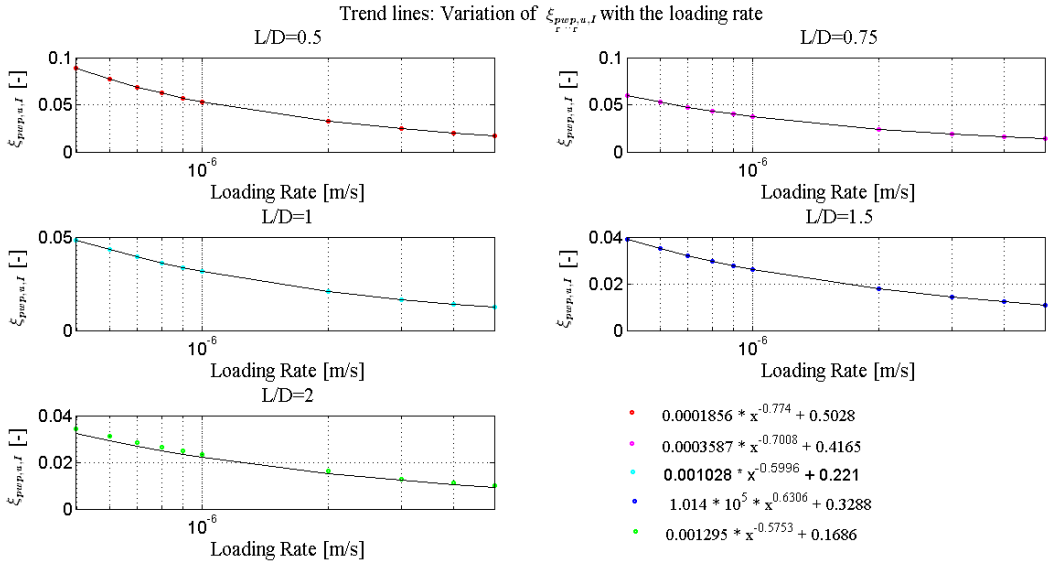

FIGURE D- 10 : Trend lines for the variation of $\xi_{pwp,u,I}$ with the loading rate

D.5 Variation of the calibration parameter $\xi_{pwp,u,II}$ with k and the loading rate

As a general rule, the variation of the calibration parameter $\xi_{pwp,u,II}$ with the permeability k and the loading rate for the estimation of the excess negative PWPs underneath the lid can be interpolated by using a fitting curve having a 2-terms power Equation D- 5, with the exact formula's for the different aspect ratio's depicted in Figure D- 9, and Figure D- 10.

$$f\ x\ = ax^b + c \qquad \text{EQUATION D- 6}$$

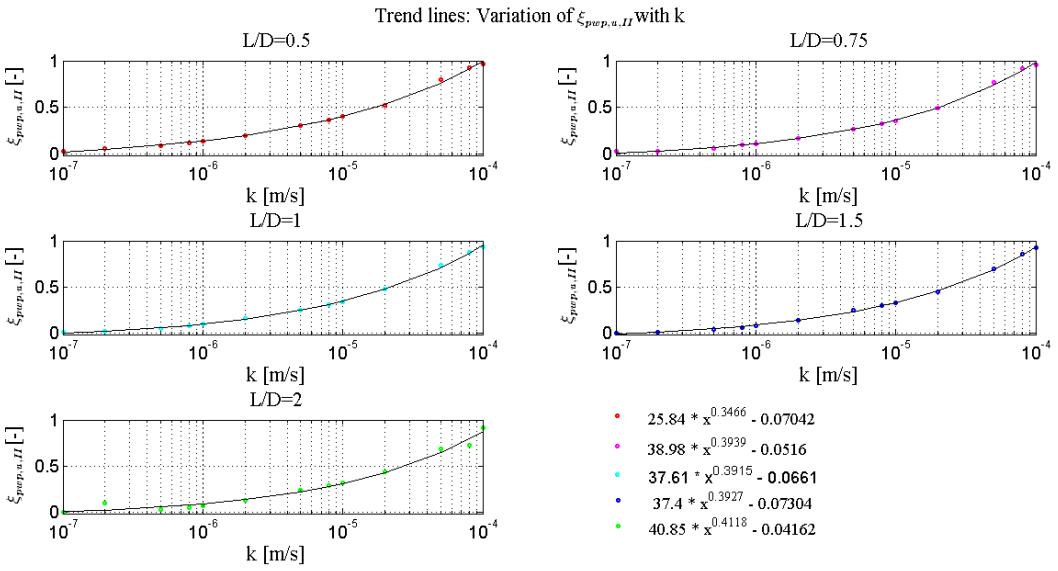

FIGURE D- 11 : Trend lines for the variation of $\xi_{pwp,u,II}$ with k

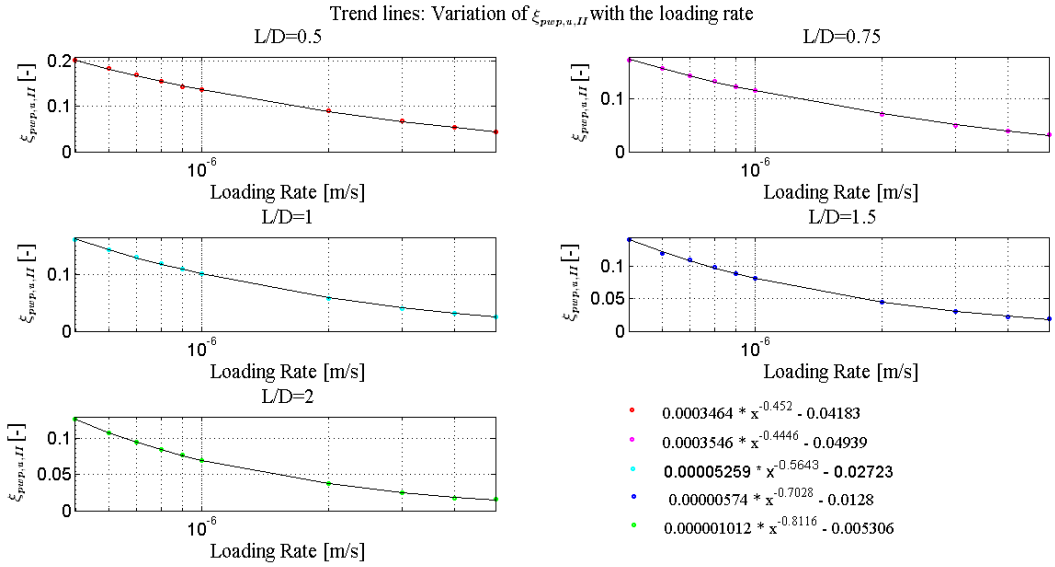

FIGURE D- 12 : Trend lines for the variation of $\xi_{pwp,u,II}$ with the loading rate

D.6 Variation of the calibration parameter $\xi_{out,u}$ with k and the loading rate

As a general rule, the variation of the calibration parameter $\xi_{out,u}$ with k on the outside of the caisson can be interpolated by using a combination of a power term and an exponential term according to the generic formula expressed by Equation D- 7. The exact expressions for the different aspect ratio's are depicted in Figure D- 13.

$$f\ x\ = a\ x^b + \exp\ c \times x\ + d \qquad \text{EQUATION D- 7}$$

As far as the variation of the parameter $\xi_{out,u}$ with the loading rate is concerned, it is fitted by a linear straight line as stated in Equation D- 8, and displayed in Figure D- 14.

$$f\ x\ = ax + b \qquad \text{EQUATION D- 8}$$

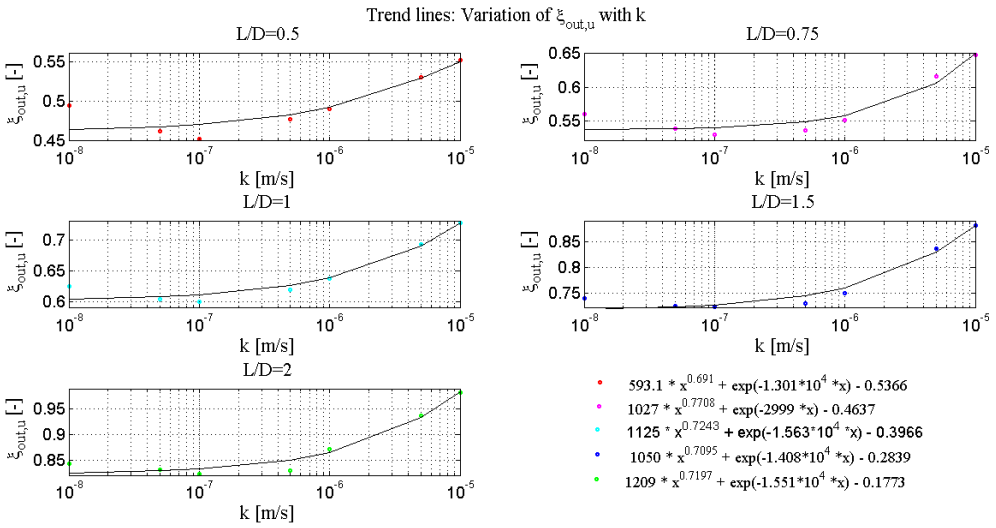

FIGURE D- 13 : Trend lines for the variation of $\xi_{out,u,}$ with the permeability

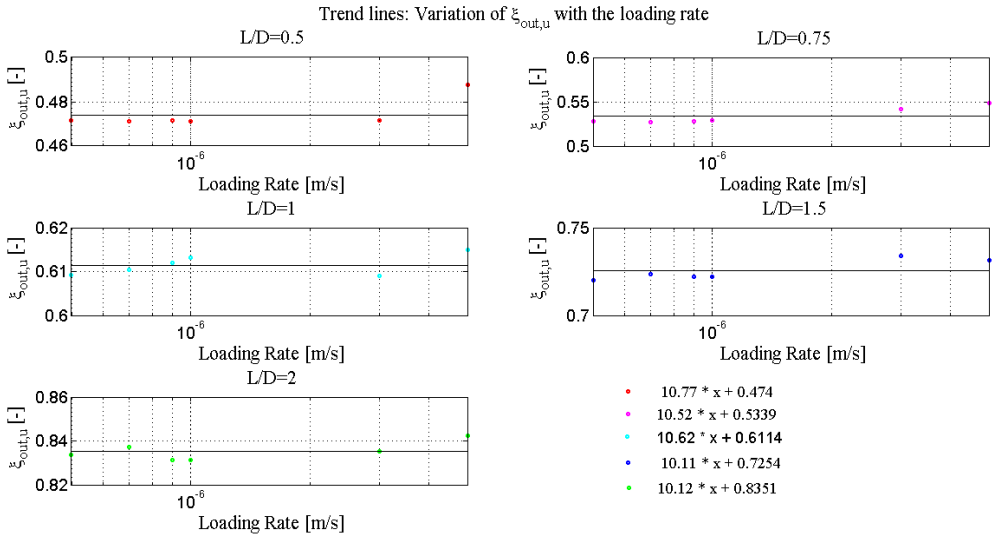

FIGURE D- 14 : Trend lines for the variation of $\xi_{out,u,}$ with the loading rate

D.7 Variation of the calibration parameter $\xi_{in,u}$ with k and the loading rate

As a general rule, the variation of the calibration parameter $\xi_{in,u}$ with k and the loading speed on the inside of the caisson can be interpolated by a fitting curve having a 2-terms power Equation D- 9, with the exact formula's for the different aspect ratio's depicted in Figure D- 15, and Figure D- 16.

$$f\ x\ = ax^b + c \qquad \text{EQUATION D- 9}$$

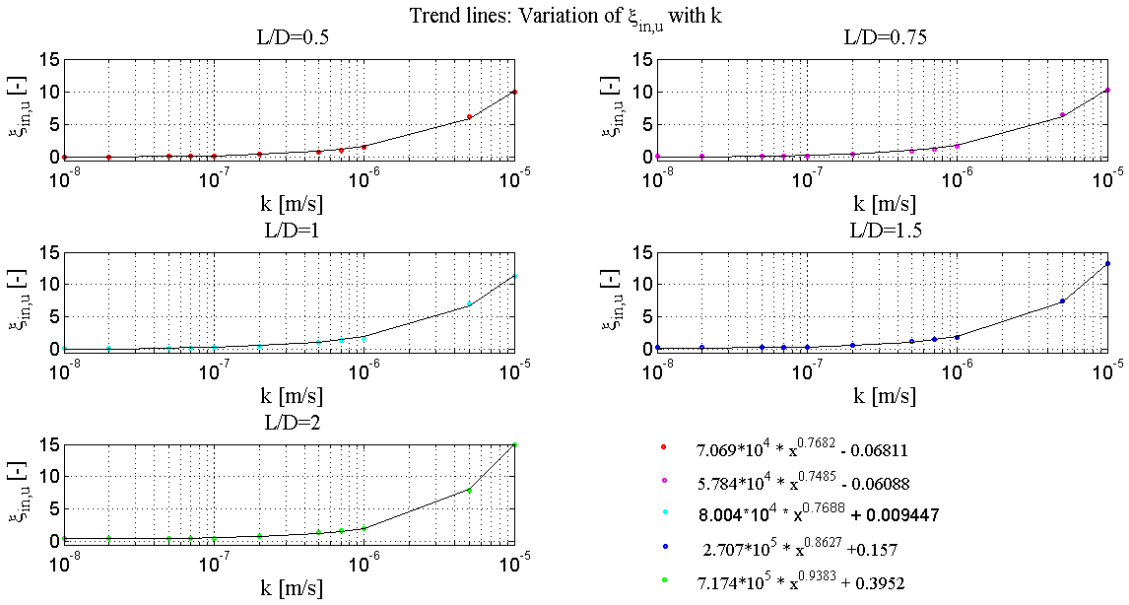

FIGURE D- 15 : Trend lines for the variation of $\xi_{in,u,}$ with the permeability

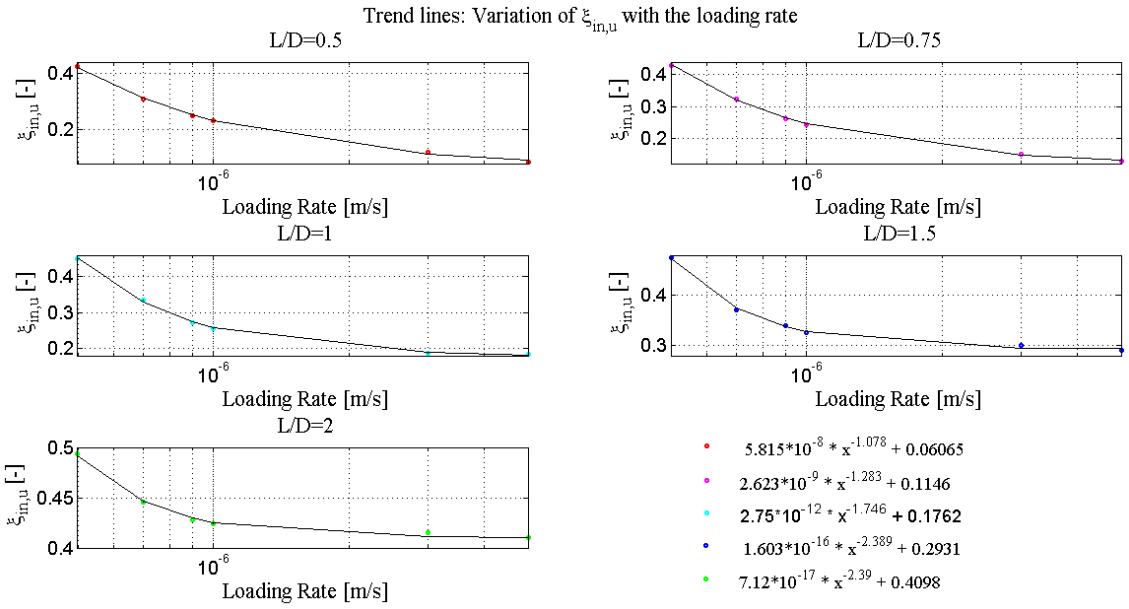

FIGURE D- 16 : Trend lines for the variation of $\xi_{in,u,}$ with the loading rate

D.8 Variation of the calibration parameter $\xi_{plug,u}$ with k and the loading rate

As a general rule, the variation of the calibration parameter $\xi_{plug,u}$ with k can be interpolated by using a combination of a power term and an exponential term according to the generic formula expressed by Equation D-10, and depicted in Figure D-17.

$$f\ x\ = ax + b\ f\ x\ = a\ x^b + \exp\ c \times x\ + d \qquad \text{EQUATION D- 10}$$

As far as the variation of the parameter $\xi_{plug,u}$ with the loading rate is concerned, it is interpolated by a fitting curve having a 2-terms power Equation D-11, with the exact formula's for the different aspect ratio's depicted in Figure D-18.

$$f\ x\ = ax + b \qquad \text{EQUATION D- 11}$$

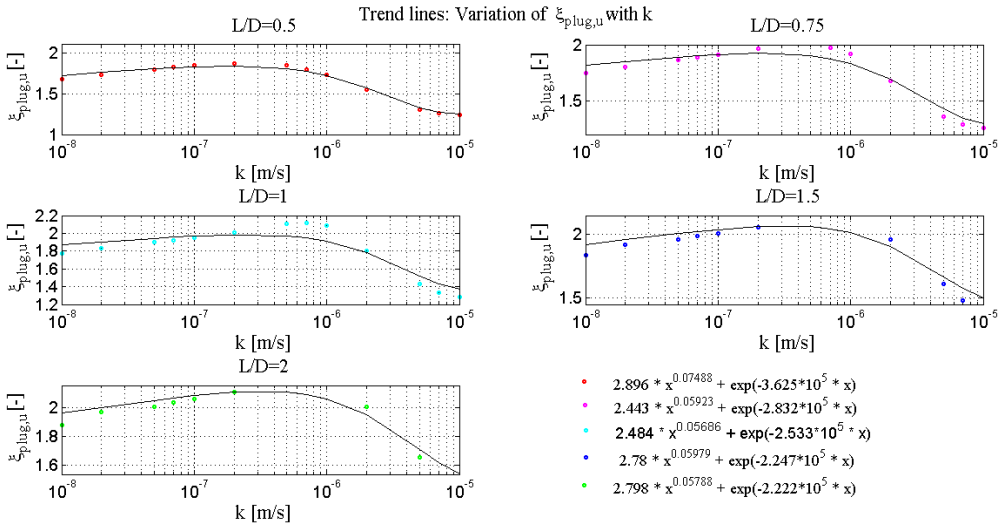

FIGURE D- 17 : Trend lines for the variation of $\xi_{plug,u,}$ with the permeability

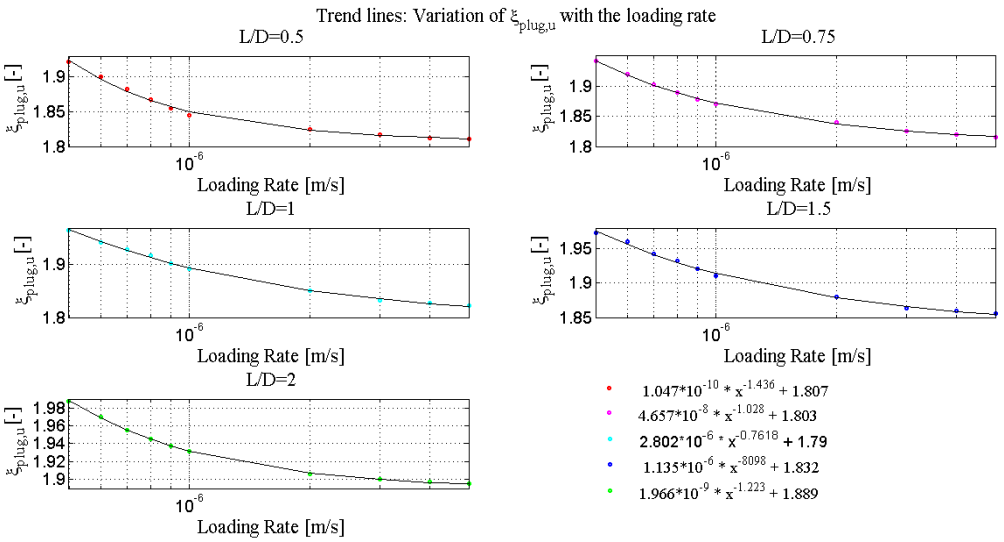

FIGURE D- 18 : Trend lines for the variation of $\xi_{plug,u,}$ with the loading rate

Appendix E
Flow chart for plug uplift

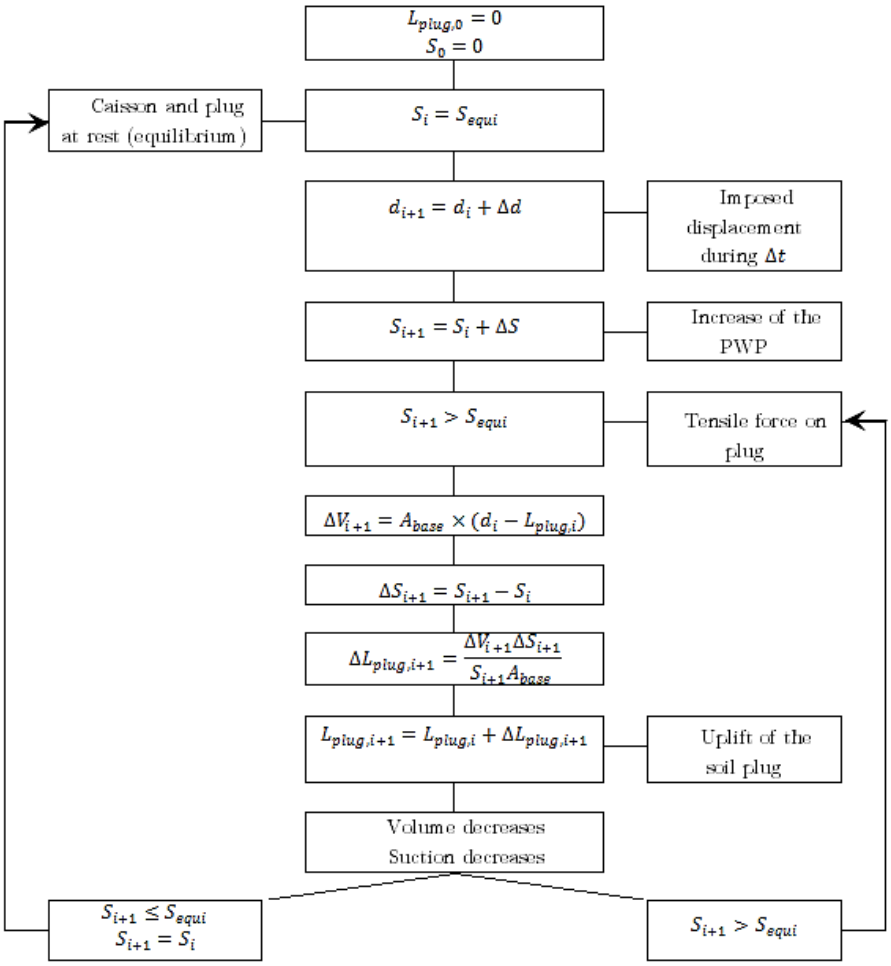

FIGURE E- 1 : Flow chart to assess the plug uplift mechanism

References

[1] Renewable Energy policy Network for the 21st century – REN21 (2016), *'Renewables 2016 : global status report'*

[2] KARYDIS M. (2013), '*Public attitudes and environmental impacts of wind farms : a review'*, Global NEST Journal, Vol. 15, No. 4, pp. 581 – 600

[3] THAYER R. L. & FREEMAN C. M. (1987), '*Altamont: Public perceptions of a wind energy landscape'*, Landscape and urban planning, Vol. 14, pp. 379-398

[4] KADAR P. (2014), '*Pros and cons of the renewable energy application'*, Acta Polytechnica Hungarica, Vol. 11, No. 4

[5] SCHAUMANN P. & LOCHTE-HOLTGRVEN S. & STEPPELER S. (2011), '*Special fatigue aspects in support structures of offshore wind turbines*', Materialwissenschaft und Werkstofftechnik, Vol. 42, No. 12, pp. 1075 – 1081

[6] Wind Energy The Facts (2011), '*Chapter 2 : Projecting targets for the EU-27 up to 2030'*[Online]

Available [Accessed 09/02/2017]: https://www.wind-energy-the-facts.org/

[7] HALUZAN N. (November 2010), '*Wind energy advantages and disadvantages'*, Renewable energy articles and news [Online]

Available [Accessed 09/02/2017] : http://www.renewables-info.com

[8] International Renewable Energy Agency – IRENA (2012), '*Wind power'*, Renewable energy technologies : cost analysis series, Vol. 1

[9] SÖDERHOLM P. & PETTERSSON M. (2010), '*Offshore wind power policy and planning in Sweden : Energy Policy*' Renewable and Sustainable Energy Reviews, Vol. 11, pp. 365-400

[10] European Wind Energy Association – EWEA (2017), '*The European offshore wind industry - Key trends and statistics 2016'*

[11] European Comission (2010), '*A strategy for competitive, sustainable and secure energy'*, Communication from the commission to the European Parliament, the council, the European economic and social committee and the committee of the regions

[12] European Wind Energy Association – EWEA (2017), '*2016 European statistics'*, Wind in power

[13] METSSON E. (July 2016), 'Market overview : Offshore wind energy in Europe as of Q2 2016' Planet OS

[14] Global Wind Energy Council – GWEC (2017), 'Global wind statistics 2016'

[15] BIANCHI F. D. & DE BATTISTA H. & MANTZ R. J. (2007), '*Wind Turbine Control Systems – Principles, modelling and gain scheduling design'*, Advances in industrial control (AIC), Spinger-Verlag London

[16] Wikipedia,'*Wind turbine design'* [Online]

Available [Accessed: 13/02/2017]: https://en.wikipedia.org/wiki/Wind_turbine

[17] DNV (2016),*'Support structures for wind turbines'*, Standard, DNVGL-ST-0126, Det Norske Veritas, Norway

[18] US department of energy – Office of energy efficiency & renewable energy, '*The inside of a wind turbine'* [Online]

Available [Accessed: 09/02/2017]: https://energy.gov/eere/wind/inside-wind-turbine-0

[19] CHARLIER R. (2014-2015), '*Géotechnique : Théorie – Ouvrages, Tome 2'*, Lecture notes, Centrale des cours de l'AEES, Université de Liège

[20] RANDOLPH M. & GOURVENEC S. (2011), '*Offshore geotechnical engineering'* Spon Press

[21] ARSHAD M. & O4KELLY C. B. (2013), '*Offshore wind-turbine structures : a revifloatingew'*, Energy, Vol.166, Issue EN4, Institution of Civil Engineers (ICE) publishing

[22] ESTEBAN M. D. & LOPEZ-GUTIERREZ J. S. & DIEZ J. J. & NEGRO V. (2011), '*Foundations for offshore wind farms'*, Proceedings of the 12th International Conference on Environmental Science and Technology, Rhodes, Greece, pp. 516 – 523

[23] LEBLANC C. (2009), '*Design of offshore wind turbine support structures : selected topics in the field of geotechnical engineering'*, Ph.D. Thesis, Aalborg University, Denmark

[24] Centre for wind energy (August 2012), '*Review of options for offshore foundation substructures*', James Madison University

[25] PEIRE K. & KONNEMAN H. & BOSSCHEM E. (2009), 'Gravity based foundations for the thornton bank offshore wind farm' Terra et Aqua, No. 115, pp. 19 – 29

[26] MENGE P. & GUNST N. (2008), 'Gravity base foundations for the wind turbines on the Thornonbank – Belgium', 15th Innovatieforum Geotechniek

[27] KALLEHAVE D. & BYRNE BW. & LEBLANC THILSTED C. & MIKKELSEN KK. (2015), 'Optimization of monopiles for offshore wind turbines', Philosophical Transactions Royal Society A 373 : 2014100

[28] DEN BOON J. H. & SUTHERLAND J. & WHITEHOUSE R. & SOULSBY R. & STAM C. J. M. & VERHOEVEN K. & HOGEDAL M. & HALD T. (2015), '*Scour behaviour and scour protection for monopile foundations of offshore wind turbines'*

[29] European Wind Energy Association – EWEA (2013), '*Deep water : the next step for offshore wind energy*, Wind in power

[30] BUTTERFIELD S. & MUSIAL W. & JONKMAN J. & SCLAVOUNOS (2007), '*Engineering challenges for floating offshore wind turbines'*, Conference paper, National Re-

newable Laboratory Goldon, CO, USA

[31] International Renewable Energy Agency – IRENA (2016), 'Floating foundations : a game changer for offshore wind power', Innovation outlook : Offshore wind, Abu Dhabi

[32] BACHYNSKI E. E. & MOAN T. (2012), *'Design consideration for tension leg platform wind turbines'*, Marine Structures, Vol. 29, pp. 89 - 114

[33] YICHAO L. & SUNWEI L. & QIAN Y. & DAOYI C. (2016), '*Developments in semi-submersible floating foundations supporting wind turbines : A conprehensive review'*, Renewable and Sustainable Energy Reviews, Vol. 60, pp. 433 – 449

[34] WISER R. & al. (2011), '*Wind Energy in IPCC'* Special Report on Renewable Energy Sources and Climate Change Mitigation, Cambridge and New York: Cambridge University Press

[35] VRYHOF anchor (2010), '*Anchor Manual 2010 – The Guide to Anchoring'*, 4th edition, Yssel, The Netherlands

[36] DI EMIDIO G (2016), '*Lesson 5 : Anchors'*, Offshore foundations, University of Ghent, Laboratory of geotechnics

[37] RICHARDSON M. D. (2008), '*Dynamically installed anchors for floating offshore structures'*, PHD thesis, The University of Western Australia

[38] EHLERS C. J. & YOUNG A. G. & CHEN J. H. (2004), 'Technology assessment of deepwater anchors', Proc. Annu. Offshore Tech. Conf., Houston, Texas, Paper OTC 16840

[39] GAUDIN C. & O'LOUGHLIN C. D. & RANDOLPH M. F. & LOWMASS A. C. (2006), '*Influence of the installation process on the performance of suction embedded plate anchors'*, Géotechnique, Vol. 56 (6), pp. 381 - 391

[40] TJELTA T. I. (2014), '*Installation of suction caissons for offshore wind turbines'*, Danish geotechnical society seminar, statoil

[41] TRAN M. N. (2007), '*Suction caissons : a new offshore foundation concept'*, Australian Geomechanic, Vol. 42, No. 4, pp. 109 – 118

[42] BYRNE B. & HOULSBY G. & MARTIN C. & FISH P. (2002), *'Suction caisson foundation for offshore wind turbines'*, Wind Engineering, Vol. 26, No. 3, pp. 145 – 155

[43] BYRNE B. & HOULSBY G. (2000), '*Suction caisson foundations for offshore wind turbines and anemometer masts*', Wind Engineering, Vol. 24, No. 4, pp. 249 – 255

[44] IBSEN L. B. (2008), *'Implementation of a new foundations concept for offshore wind farms'*, Nordisk geoteknikermøte, No. 15, pp. 19 – 33

[45] ZHANG J. & FOWAI I. & SUN K. (2016), '*A glance at offshore wind turbine foundation structures'*, Shipbuilding : Theory and practice of naval architecture, marine engineering and ocean engineering, Vol. 67, No. 2, pp. 101 – 113

[46] GARUS K. (2014), '*First suction bucket jacket is complete'*, Offshore Wind Industry

[47] ACHMUS M. 1 AKDAG C. T. 1 THIEKEN K. (2013), '*Load-bearing behavior of suction*

bucket foundations in sand', Applied Ocean Research, Vol. 43, pp. 157 – 165

[48] TRAN M. N. (2005), '*Installation of suction caissons in dense sand and the influence of silt and cemented layers*', PhD thesis, The University of Sydney, Sydney, NSW, Australia

[49] FELD T. & RASMUSSEN J. L. & SORENSEN P.H. (1999), '*Structural and economic optimisation of offshore wind turbine support structure and foundation*', Geotechnical engineering group, Aalborg University, Denmark, Engineering Paper No. 15 presented at Proc.18th International Conference on Offshore Mechanics and Artic Engineering, St John's, Canada

[50] LEBLANC C. L. (2009), '*Recent experience and challenges ahead*', Dong Energy Power – The monopod bucket foundation, Hamburg Offshore Wind Conference, Hamburg, Germany

[51] MALHOTRA S. (2011), '*Selection, design and construction of offshore wind turbine foundations*', Wind Turbines, Dr. Ibrahim Al-Bahadly (Ed.), InTech, Open Access Publisher, pp. 231 – 264

[52] DNV (2014), '*Design of offshore wind turbine structures*', Offshore Standard, DNV-OS-J101, Det Norske Veritas, Norway

[53] American Petroleum Institute – API (2002), '*Recommended practice for planning, designing and constructing fixed offshore platforms – working stress design*', API recommended practice 2A – WSD, 21st edition

[54] DNV (2007), '*Environmental conditions and environmental loads*', Recommended Practice, DNV-RP-C205, Det Norske Veritas, Norway

[55] BYRNE B.W. & HOULSBY G.T. (2015),'*Helical piles: an innovative foundation design option for offshore wind turbines*', Philosophical Transactions R. Soc. A, Vol. 373

[56] HOULSBY G.T., IBSEN L.B. & BYRNE B.W. (2005), *'Suction caissons for wind turbines'*, Proc. International Symposium on Frontiers in Offshore Geotechnics (ISFOG), Perth, Australia, Taylor & Francis Group

[57] BYRNE B.W. & HOULSBY G.T. (2003), '*Foundations for offshore wind turbines*', Phil. Trans.R. Soc. Lond., Vol. 361, pp. 2909-2930

[58] ROMP R. H. (2013), '*Installation-effects of suction caissons in non-standard soil conditions*', Master Dissertation, Delft University of Technology

[59] COTTER O.J. & BYRNE B.W. & HOULSBY G.T. (2010), '*Installation of suction caissons for offshore renewable energy structures*', Frontiers in Offshore Geotechnics II, pp 569 – 574 GOUVERNEC S. & WHITE D. (Eds), CRC Press

[60] DI EMIDIO G (2016), '*Lesson 4 : Caissons*, Offshore foundations, University of Ghent, Laboratory of geotechnics

[61] HOULSBY G.T . & BYRNE B.W. (2005), '*Design procedures for installation of suction caissons in clay and other materials*', Geotechnical Engineering, Vol. 158, Issue GE2, pp. 75 – 82

[62] HOULSBY G.T . & BYRNE B.W. (2005), *'Design procedures for installation of suction caissons in sand'*, Geotechnical Engineering, Vol. 158, Issue GE3, pp. 135 – 144

[63] DENG W. & CARTER J.P. (2002), '*A theoretical study of the uplift capacity of suction caissons'*, International Journal of Offshore and Polar Engineering, Vol. 12 (2), pp. 89 – 97

[64] CERFONTAINE B. & COLLIN F. & CHARLIER R. (2015),*'Numerical modelling of transient cyclic vertical loading of suction caissons in sand'*, Géotechnique, Vol. 65, No. 12

[65] DENG W. (2000),*'Uplift capacity of suction caissons'*, Australian Geomechanics, pp. 41 – 54, Centre for Geotechnical Research, The University of Sydney

[66] TERZAGHI K. (1943),*'Theoretical soil mechanics'*, J. Wiley, New-York

[67] PRANDTL L. (1920), '*Über die Eindringungsfestigkeit plastischer Baustoffe und die Festigkeit von Schneiden*', Zeitschrift für angewandte Mathematik und Mechanik, Vol. 1

[68] CAQUOT A. & KERISEL J. (1953), '*Sur la terme de surface dans le calcul des fondationsen milieu pulvérultant'* Proc. of the 3rd international conference on soil mechanics and foundation engineering, Zurich

[69] RANDOLPH M. F. & STEWART D.P. & ERBRICH C. (1998), '*Performance of suction anchors in fine grained calcareous soils'*, Proceedings, Offshore Technology Conference, OTC 8831, Houston, USA, pp. 521 – 529

[70] Association of Swiss Road and Traffic Engineers, '*Characteristic Coefficients of soils'*, Swiss Standard SN 670 010b
Retrieved from: http://www.geotechdata.info/parameter.html

[71] TERZAGHI K. & PECK R. & MESRI G. (1996),*'Soil Mechanics in Engineering Practice'*, Wiley, New York
Retrieved from: http://www.geotechdata.info/parameter.html

[72] HOUGH B. (1969),*'Basic soil engineering'*, Ronald Press Company, New York
Retrieved from: http://www.geotechdata.info/parameter.html

[73] PRAT M. & BISCH E. & MILLARD A. & MESTAT P. & CABOT G. (1995),*'La modelisation des* ouvrages'. Hermes, Paris
http://www.geotechdata.info/parameter.html

[74] KEZDI A. (1974), '*Handbook of Soil Mechanics'*. Elsevier, Amsterdam.
http://www.geotechdata.info/parameter.html

[75] Randolph M. F. & Wroth C. P. (1978),*'Analysis of deformation of vertically loaded piles'*, Journal of the geotechnical engineering division, No. 12, pp. 1465 - 1488

[76] SENDERS M. (2008),*'Suction caissons in sand as tripod foundations for offshore wind turbines'*, Ph. D. thesis, University of western Australia

[77] CERFONTAINE B. (2014),' *The cyclic behaviour of sand, from the Prevost model to offshore geotechnics'*, Ph. D. thesis, Université de Liège

[78] Divya S.K. & GOUVERNEC S. & RANDOLPH M.F. (2014), '*Numerical modelling of seepage beneath skirted foundations subjected to vertical uplift'*, Computers and Geotech-

nics, No. 55, pp. 150 - 157

[79] SENDERS M. & RANDOLPH M.F. (2009), *'CPT-Based Method for the Installation of Suction Caissons in Sand',* Journal of Geotechnical and Geoenvironmental Engineering, Vol. 135, No. 1, pp. 14-25

[80] PLAXIS (2008). Plaxis 2D Version 8.6 Reference Manual. Plaxis bv.

[81] FU D. & GAUDIN C. & TIAN Y. & CASSIDY M.J. & BIENEN B. (2017), 'Uniaxial Capacities of Skirted Circular Foundations in Clay', Journal of Geotechnical and Geoenvironmental Engineering, Vol. 143, No. 7